Katalysatoren für die thermische Sauerstoffentwicklungsreaktion

Dissertation

zur

Erlangung des Doktorgrades (Dr. rer. nat.)

der

Mathematisch-Naturwissenschaftlichen Fakultät

der

Rheinischen Friedrich-Wilhelms-Universität Bonn

vorgelegt von

Benjamin Grimm

aus Bad Segeberg

Bonn

2024

Die vorliegende Arbeit entstand in der Zeit vom 01.04.2021 bis zum 31.03.2024 am Institut für Physikalische und Theoretische Chemie der Mathematisch-Naturwissenschaftlichen Fakultät der Rheinischen Friedrich-Wilhelms-Universität Bonn.

Betreuer/Erstgutachter: Prof. Dr. Thomas Bredow
Zweitgutachter: Prof. Dr. Stefan Grimme
Drittgutachter: Prof. Dr. Sigurd Höger
Viertgutachterin: Priv.-Doz. Dr. Elisabeth Soergel

Tag der Promotion: 27.06.2024
Erscheinungsjahr: 2024

Danksagung

An dieser Stelle möchte ich mich bei allen Menschen bedanken, welche mich bei der Erstellung dieser Arbeit unterstützt haben. Besonderer Dank gilt meinem Betreuer Thomas Bredow für die ausgezeichnete Betreuung dieser Arbeit. Außerdem danke ich Stefan Grimme für die Übernahme der Zweitkorrektur sowie Sigurd Höger und Elisabeth Soergel für die Teilnahme an der Prüfungskommission.
Ich möchte mich gerne bei meinen Kollegen am Institut für die sehr angenehme Arbeitsatmosphäre bedanken. Dabei möchte ich mich insbesondere bei meinem Büronachbarn Michael Häfner, bei Stefan Jütten und bei Berenike Stahl für den anregenden fachlichen Austausch bedanken. Außerdem bedanke ich mich bei Claudia Kronz und Jens Mekelburger für die administrative Unterstützung während meines Promotionsstudiums.
Ich möchte mich beim Paderborn Center for Parallel Computing (PC^2) für die kostenfreie Bereitstellung leistungsstarker Rechner bedanken, ohne diese zahlreiche Rechnungen nicht möglich gewesen werden.
Des Weiteren danke ich meiner Familie für die Unterstützung und die gemeinsame Zeit.

Inhaltsverzeichnis

1. Einleitung

Die globale Energiewende ist eins der größten Themen unserer Zeit. Man steht vor der Herausforderung, den steigenden Energiebedarf zu decken und gleichzeitig die CO_2-Emissionen zu reduzieren, um den Klimawandel zu stoppen. Dies erfordert bis 2050 in allen Sektoren einen nahezu vollständigen Rückgang der Treibhausgasemissionen [1, 2, 3]. Wasserstoff wird mittlerweile als der wichtigste Schlüssel zum Erreichen der langfristigen Klimaziele angesehen [4, 5, 6]. Er gehört zu den Sekundärenergieträgern, da zunächst Primärenergie benötigt wird, um ihn aus Wassermolekülen zu gewinnen, welche nahezu unbegrenzt verfügbar sind. Wasserstoff hat eine sehr hohe Energiedichte von 33 kWh/kg [7] (im Vergleich zu 12 kWh/kg für Diesel [8]), weshalb er zur Speicherung erneuerbarer Energieüberschüsse verwendet werden kann.

Zu den gängigen Herstellungsverfahren für Wasserstoff gehören die Dampfreformierung [9], die Elektrolyse [10] und die Methanpyrolyse [11]. Die entscheidenden Unterschiede dieser Verfahren sind die entstehenden Nebenprodukte, die verwendete Ressource und die Kosten. Die Dampfreformierung ist das günstigste dieser Verfahren, welches Wasserstoff aus Erdgas herstellt, wobei aber pro zwei Wasserstoffmoleküle auch ein CO_2-Molekül entsteht. Dieses Verfahren ist dementsprechend nicht geeignet, um die CO_2-Emissionen zu senken. Die Elektrolyse wird verwendet, um Wasser durch Anlegen eines elektrischen Potentials in Wasserstoff und Sauerstoff zu spalten. Die Kosten für dieses Verfahren sind aufgrund der benötigten elektrischen Energie deutlich höher als für die Dampfreformierung, allerdings ist dieses Verfahren nachhaltig, solange die elektrische Energie aus erneuerbaren Primärenergieträgern stammt. Es ist zwischen Niedrigtemperaturelektrolyse (60 bis 80 °C) und Hochtemperaturelektrolyse (700 - 900 °C) zu unterscheiden [6]. Die Alkali-Elektrolyse (AEC) [12] ist ein Niedrigtemperaturelektrolyseverfahren, welches bereits seit etwa 100 Jahren in der Industrie eingesetzt wird. Es handelt sich dabei um die Elektrolyse von Wasser, welche im stark alkalischen Milieu durchgeführt wird. Die PEM-Elektrolyse

[13] (PEMEC, *engl.* Proton exchange membrane electrolysis) besteht aus einer Elektrolysezelle mit einer protonenleitenden Membran, welche den Transport der Protonen von der Anode zur Kathode ermöglicht. Hochtemperaturelektrolyseverfahren wurden bis vor Kurzem erst in kleinem Maßstab betrieben. Ihnen wird allerdings erhebliches Potential für geringere Kosten und einen erhöhten Wirkungsgrad vorhergesagt. Im Rahmen des GrInHy2.0 Projekts erzielte der weltweit größte Hochtemperatur-Elektrolyseur im Jahr 2022 einen Rekord-Wirkungsgrad von 84 % und produzierte 200 Nm^3 (Normkubikmeter) H_2 pro Stunde [14].

Aktuell wird in Deutschland immer noch 90 % des Wasserstoffs über Dampfreformierung (40 %) und aus fossilen Quellen (50 %) gewonnen. Durch Elektrolyse wird aktuell 7% des benötigten Wasserstoffs hergestellt, was es zum am häufigsten verwendeten nachhaltigen Verfahren zur Wasserstoffgewinnung macht [6]. Die Weiterentwicklung von Elektrolyseverfahren ist von fundamentaler Bedeutung, um die Wettbewerbsfähigkeit von nachhaltig erzeugtem Wasserstoff zu verbessern. Zhao et al. verglichen in einem Übersichtsartikel den aktuellen Stand der Tieftemperaturverfahren AEC und PEMEC und dem aktuell am weitesten entwickelten Hochtemperaturverfahren, der SOEC (*engl.* solid oxide electrolysis cell) [15]. Die PCEC (*engl.* Proton ceramic electrolysis cell) ist eine alternative Form der Hochtemperaturelektrolyse, über welche von Duan et al. in einem Übersichtsartikel berichtet wurde [16]. Dieses Elektrolyseverfahren basiert auf elektrochemisch aktiven Anodenmaterialien, welche bei moderaten Temperaturen im Rahmen der Sauerstoffentwicklungsreaktion (OER) Sauerstoffdefekte bilden. Diese Sauerstoffdefekte werden dann durch die Hydratiserungsreaktion ausgeheilt, wodurch formal adsorbierter Wasserstoff auf der Elektrode entsteht. Protonenkeramiken leiten generell nicht nur Protonen, sondern auch Oxidionen (O^{2-}) und Elektronenlöcher, wodurch unerwünschte Konkurrenzreaktionen auftreten können. Die Hydratisierungsreaktion steht in Konkurrenz zur Reoxidation (Auffüllen der Defekte), weshalb der Temperaturbereich genau so gewählt werden muss, dass die stark exotherme Hydratisierung bevorzugt ist. Die PCEC ist bisher noch nicht so weit entwickelt wie die SOEC, ist aber kürzlich wieder verstärkt ins Interesse aktueller Forschung gerückt. Die PCEC hat einige signifikante Vorteile gegenüber der SOEC, darunter die kleineren Wanderungsbarrieren der Protonen (im Vergleich zu O^{2-}) und die Produktion trockenen Wasserstoffs (Wasserstoff und Wasserdampf sind getrennt).

Fundamental für die PCEC ist neben geeigneten Elektrolyten die Existenz kostengünstiger, protonenleitender Elektrodenmaterialien. Seit 2016 zeigt die Entwicklung solcher Materialien große Fortschritte [16]. Hauptanforderung an solche Materialien ist die reversible Bildung von Defekten bei moderaten Temperaturen (350 - 600 °C) sowie eine Protonenleitfähigkeit im Festkörper und auf der Oberfläche. Des Weiteren ist die Langzeitstabilität des Materials essentiell.

Ziel dieser Arbeit ist es, ein PCEC-Anodenmaterial vorauszusagen, welches ausschließlich kostengünstig und häufig verfügbare Elemente enthält. Perovskite sind aufgrund ihrer Stabilität und der reversiblen temperaturabhängigen OER geeignet für die Suche eines solchen Materials. Geeignete Perovskite sollen bereits bei moderaten Temperaturen Sauerstoffdefekte bilden, keine Dekomposition zeigen sowie protonenleitfähig sein. Hierfür relevante Eigenschaften wie Defektbildungsenthalpien, freie Bildungsenthalpien und Protonenkonzentrationen können experimentell bestimmt werden. Allerdings ist der Einsatz theoretischer Methoden essentiell für die systematische Suche geeigneter Kandidaten. Defektbildungsenthalpien und Bildungsenthalpien können für eine große Anzahl von Perovskiten berechnet werden, wobei entscheidende Trends sichtbar werden. Außerdem können Mechanismen wie der Protonenwanderungsmechanismus auf atomarer Ebene betrachtet werden.

Theoretische Berechnungen von Perovskiten wurden bereits in großer Anzahl durchgeführt, darunter auch zahlreiche auf Hybriddichtefunktionaltheorie-Niveau [17, 18, 19, 20, 21, 22, 23, 24]. Diese Studien berichten übereinstimmend, dass Hybriddichtefunktionale (Hybrid-DFT) genauere Strukturen und Bandlücken als GGA-Funktionale erhalten, allerdings gibt es darunter keinen Methodentest, welcher die Zuverlässigkeit und Genauigkeit unterschiedlicher Hybridfunktionale vergleicht. Des Weiteren liegen bisher keine Untersuchungen auf Hybrid-DFT-Niveau über das Perovskit $CaMnO_3$ vor. Allerdings ist $CaMnO_3$ ein hervorragender Ausgangspunkt für die Suche eines PCEC-Materials, da es nur häufig und kostengünstig verfügbare Elemente enthält und die reversible OER bei verhältnismäßig geringen Temperaturen (etwa 1000 °C) stattfindet.

Bulfin et al. untersuchten die Defektbildungsthermodynamik experimentell [25]. Dabei stießen sie auf das Problem der Dekomposition von $CaMnO_3$ in $CaMn_2O_4$ und Ca_2MnO_4 im für die Defektbildung relevanten Temperaturbereich. Dieses Problem trat allerdings

bei $Ca_{0.8}Sr_{0.2}MnO_3$ nicht mehr auf. Für diese Arbeit war dies der erste Hinweis, dass Kationensubstitution eine wichtige Rolle bei der Suche des Materials spielen wird.
Diese Arbeit beginnt mit einem Methodentest, in welchem die Defektbildungsenthalpien und Defektbildungsentropien von $CaMnO_3$ mit verschiedenen Hybrid- und GGA-Funktionalen berechnet werden (Kapitel 3). Anschließend wird der Effekt der Kationensubstitution auf die OER von $CaMnO_3$ in dieser Arbeit ausführlich untersucht (Kapitel 4). In Kapitel 5 wird sich dann auf die ABO_3-Perovskite aus den häufig und kostengünstig verfügbaren Elementen A=Mg,Ca,Sr und B=Ti,V,Cr,Mn,Fe beschränkt und von diesen die OER auf Hybrid-DFT-Niveau berechnet. Gleichzeitig wird die Stabilität bezüglich Dekomposition in AB_2O_4 und A_2BO_4 untersucht. Aus den vielversprechendsten Kandidaten werden dann Mischverbindungen berechnet, die bezüglich der freien Mischungsenthalpie, der Defektbildungsenergie und der Stabilität bezüglich Dekomposition bewertet werden. Die Thermodynamik der OER wird dann für den vielversprechendsten dieser Kandidaten untersucht. In Kapitel 6 werden alle Niedrigindex-Oberflächen von $CaMnO_3$ berechnet, um aus den Oberflächenenergien den Anteil an der Gesamtoberfläche zu erhalten. Dies ist dann der Ausgangspunkt für die Berechnung von Hydratationsenergien und Protonenmigrationsmechanismen, welche die katalytische Relevanz des Materials bestimmen und daher für andere Perovskite bereits ausführlich untersucht wurden [26, 27, 28, 29]. In Kapitel 7 werden die Protonenmigrationsbarrieren und Hydratationsenergien von $CaMnO_3$ (mit und ohne Kationensubstitution) auf Hybrid-DFT-Level berechnet, um die Protonenleitfähigkeit zu untersuchen. In Kapitel 8 wird der Protonenmigrationsmechanismus von der Oberfläche in den Festkörper berechnet, welcher ebenso essentiell für den katalytischen Einsatz des Materials ist.
Ausgehend von $CaMnO_3$ wird in dieser Arbeit ein Material vorhergesagt, welches vielversprechende Eigenschaften für den Einsatz als PCEC-Material aufweist. Dabei wird gezeigt, dass $Ca_{1-x}Sr_xMn_{1-y}Fe_yO_3$ für x=0.5 und y=0.25 bereits ab 520 K Sauerstoffdefekte bilden kann und keine Dekomposition aufweist. Des Weiteren wird eine hervorragende Protonenleitfähigkeit anhand von Protonenwanderungsbarrieren zwischen 0.2 und 0.5 eV und negativen Hydratationsenergien nachgewiesen. Außerdem kann ein Protonenwanderungsweg von der Oberfläche in niedrigere Schichten berechnet werden, welcher sogar im Vergleich zum bekannten Protonenleiter $BaFeO_3$ vorteilhaft ist.

2. Theoretischer Hintergrund

Diese Arbeit entstammt aus dem Gebiet der Festkörperquantenchemie. Daher werden in diesem Kapitel auf der Basis von Literatur und Quantenchemie-Vorlesungen [30, 31, 32, 33] die Grundlagen der festkörpertheoretischen Methoden dargelegt. Anschließend wird konkret auf die in dieser Arbeit verwendeten Verfahren eingegangen.

2.1. Schrödingergleichung für Mehrelektronensysteme

Die Quantenchemie basiert darauf, die Gesamtenergie eines Mehrelektronensystems durch Lösung der Schrödingergleichung

$$\hat{H}\Psi(\vec{r},\vec{R}) = E\Psi(\vec{r},\vec{R}) \tag{2.1}$$

zu erhalten. Hierbei ist $\hat{H}$ der Hamiltonoperator eines Systems aus M Kernen auf den Positionen $\vec{R}$ und N Elektronen auf den Positionen $\vec{r}$ und $\Psi(\vec{r},\vec{R})$ die Gesamtwellenfunktion des Systems. Den Hamiltonoperator eines solchen Systems kann man schreiben als

$$\hat{H} = -\sum_{i=1}^{N}\frac{\vec{\nabla}_i^2}{2} - \sum_{i=1}^{M}\frac{\vec{\nabla}_i^2}{2M_A} - \sum_{i=1}^{N}\sum_{A=1}^{M}\frac{Z_A}{r_{iA}} + \sum_{i=1}^{N}\sum_{j>i}^{M}\frac{1}{r_{ij}} + \sum_{A=1}^{N}\sum_{B>A}^{M}\frac{Z_A Z_B}{R_{AB}} \tag{2.2}$$

$$= \hat{T}_K + \hat{T}_e + \hat{V}_{KK} + \hat{V}_{eK} + \hat{V}_{ee} \tag{2.3}$$

wobei $\hat{T}$ der Operator der kinetischen und $\hat{V}$ der Operator der potentiellen Energie der Elektronen e und der Kerne K, M_A das Massenverhältnis von Kern und Elektron und Z die Kernladung ist. Mit der Born-Oppenheimer-Näherung [34] können die Bewegungen von Elektron und Kern entkoppelt werden. Da das Elektron erheblich leichter als der Kern ist, kann man die kinetische Energie der Kerne vernachlässigen und die Elektron-Kern-Wechselwirkungen für eine fixierte Position der Kerne berechnen. Dadurch vereinfacht sich Gleichung 2.2 zu

$$\hat{H} = -\sum_{i=1}^{N} \frac{\vec{\nabla}_i^2}{2} - \sum_{i=1}^{N}\sum_{A=1}^{M} \frac{Z_A}{r_{iA}} + \sum_{i=1}^{N}\sum_{j>i}^{M} \frac{1}{r_{ij}} + \sum_{A=1}^{N}\sum_{B>A}^{M} \frac{Z_A Z_B}{R_{AB}} \quad . \tag{2.4}$$

Nach dem Pauli-Prinzip entspricht die Mehrelektronenwellenfunktion einer Slater-Determinante aus N orthonormalen Spinorbitalen $\chi_i(q_i)$:

$$\Psi(1,2,...,N) = \frac{1}{\sqrt{N!}} \begin{vmatrix} \chi_1(q_1) & \chi_2(q_1) & ... & \chi_N(q_1) \\ \chi_1(q_2) & \chi_2(q_2) & ... & \chi_N(q_2) \\ ... & ... & ... & ... \\ \chi_1(q_N) & \chi_2(q_N) & ... & \chi_N(q_N) \end{vmatrix} \tag{2.5}$$

2.2. Dichtefunktionaltheorie

Eine Möglichkeit zur numerischen Lösung der Mehrelektronenschrödingergleichung ist die Dichtefunktionaltheorie (DFT). Hohenberg und Kohn zeigten 1964, dass die Grundzustandsenergie E_{exakt} als Funktional der exakten Elektronendichte $\rho_{\text{exakt}}(r)$ erhalten werden kann [35]:

$$F[\rho_{\text{exakt}}(\vec{r})] = E_{\text{exakt}} \quad . \tag{2.6}$$

Das exakte Energiefunktional F ist bis heute unbekannt. Kohn und Sham formulierten die heute von den meisten Methoden verwendete Separation der Wechselwirkungstherme

$$E_{KS}[\rho(\vec{r})] = T_e[\rho(\vec{r})] + V_{KK} + V_{eK}[\rho(\vec{r})] + J[\rho(\vec{r})] + E_{xc}[\rho(\vec{r})] \quad , \tag{2.7}$$

wobei J die klassische Coulomb-Wechselwirkungsenergie und E_{xc} die Austauschkorrelationsenergie ist. In der DFT werden prinzipiell keine Orbitale benötigt, allerdings können die kinetische Energie T_e und die Austauschkorrelationsenergie E_{xc} nur approximiert werden. Weil die kinetische Energie einen großen Anteil der Gesamtenergie ausmacht, wird durch rein dichtebasierte DFT keine ausreichende Genauigkeit erreicht. Kohn und Sham führten daher Orbitale in die DFT ein, was als Kohn-Sham-Dichtefunktionaltheorie (KS-DFT) bezeichnet wird. Die Elektronendichte wird aus der Wellenfunktion durch

$$\rho(\vec{r}) = N \cdot \int |\Psi(\vec{r}, \vec{r_2}, ..., \vec{r_N})|^2 d\vec{r_2}...d\vec{r_n} = N \cdot \sum_{i=1}^{N} |\psi_i(\vec{r})|^2 \tag{2.8}$$

erhalten, wobei Ψ die Slater-Determinante und ψ_i die Kohn-Sham-Orbitale sind. Die Kohn-Sham-Orbitale können dann durch Lösen der Einelektronenschrödingergleichungen

$$\left\{ -\frac{\vec{\nabla}_i^{\,2}}{2} - \sum_A^M \frac{Z_A}{\left|\vec{r} - \vec{R_A}\right|} + \int \frac{\rho(\vec{r'})}{\left|\vec{r} - \vec{r'}\right|} + V_{xc}(\vec{r}) \right\} \psi_i(\vec{r}) = \epsilon_i \psi_i(\vec{r}) \tag{2.9}$$

bestimmt werden, wobei V_{xc} das Austauschkorrelationspotential und ϵ_i die Energie des Orbitals ψ_i ist.

2.2.1. Jakobsleiter

Die Qualität der Funktionale wird im Wesentlichen durch die Austausch- und Korrelationspotentiale (Gleichung 2.9) bestimmt. Dafür werden diese in guter Näherung separiert:

$$V_{\mathrm{xc}} = V_{\mathrm{x}} + V_{\mathrm{c}} \quad . \tag{2.10}$$

Perdew und Schmidt ordneten die Funktionale in der sogenannten Jakobsleiter [36] nach ihrer Komplexität.

Local (Spin) Density Approximation

Die einfachsten Funktionale basieren auf der **L**ocal **S**pin **D**ensity **A**pproximation (LSDA) für offenschalige Systeme beziehungsweise der **L**ocal **D**ensity **A**pproximation (LDA) für geschlossenschalige Systeme. In dieser Näherung wird eine homogene Elektronendichte im gesamten Raum angenommen. Die Austauschenergie E_x ist somit gegeben als

$$E_x^{\mathrm{LDA}}[\rho] = \int \rho(\vec{r}) \epsilon_x \rho(\vec{r}) d\vec{r} \tag{2.11}$$

mit dem Austauschterm

$$\epsilon_x = -\frac{3}{4} \left(\frac{3}{\pi} \right)^{\frac{1}{3}} [\rho(\vec{r})]^{\frac{1}{3}} \quad . \tag{2.12}$$

Die Korrelationsenergie wird numerisch aus Quanten-Monte-Carlo-Simulationen des homogenen Elektronengases ermittelt. LD(S)A-Funktionale sind eine gute Näherung für Systeme wie Metalle mit einer annähernd homogenen Elektronendichte, allerdings nicht für komplexere Systeme. Die Näherung kann verbessert werden, indem zusätzlich die Gradienten der Elektronendichte betrachtet werden.

Generalized Gradient Approximation

Die Austauschenergie der **G**eneralized **G**radient **A**pproximation (GGA)-Funktionale ist gegeben durch

$$\epsilon_x^{GGA}[\rho] = \epsilon_X^{LDA} F(s) \tag{2.13}$$

wobei der Skalierungsfaktor F(s) vom Elektronendichtegradienten abhängt:

$$s = \frac{|\nabla\rho|}{2(3\pi^2)^{\frac{1}{3}}\rho^{\frac{4}{3}}} \quad . \tag{2.14}$$

Das PBE-Funktional [37] ist ein Standardfunktional, welches auch in dieser Arbeit für komplexe Rechnungen wie Frequenzrechnungen (Abschnitt 2.5.1) verwendet wurde. Für dieses wird F(s) in Abhängigkeit der Parameter κ und μ berechnet, welche an physikalische Eigenschaften von Modellsystemen angepasst wurden.

$$F^{\mathrm{PBE}}(s) = 1 + \kappa - \frac{\kappa}{1 + \mu s^2/\kappa} \tag{2.15}$$

Das PBEsol-Funktional ist eine speziell für Festkörper parametrisierte Version des PBE-Funktionals [38] und wurde im Methodentest dieser Arbeit verwendet.

Die nächste Stufe der Jakobsleiter sind die meta-GGA-Funktionale, bei denen neben den Gradienten auch die zweiten Ableitungen der Elektronendichte (bzw. die kinetische Energiedichte) berücksichtigt werden. Das meta-GGA-Funktional SCAN ist ein bekannter Vertreter dieser Stufe, welches genaue Ergebnisse liefert, besonders für Gitterparameter und schwache Wechselwirkungen [39]. Ein Nachteil des SCAN-Funktionals ist die starke Abhängigkeit von numerischen Integrationsgittern. Um die Recheneffizienz und die Robustheit zu verbessern, wurde das r^{2}SCAN-Funktional entwickelt, welches in VASP eine deutlich schnellere Konvergenz der Gesamtenergie mit der Anzahl der Integrationsgitterpunkte aufweist [40]. Beide Funktionale wurden als Teil des Methodentests in dieser Arbeit verwendet.

Alle Funktionale bis zu dieser Stufe berechnen die Austauschenergie ausschließlich in Abhängigkeit von der Elektronendichte. Durch das Verwenden der Elektronendichte anstatt einzelner Wellenfunktionen werden die Elektronen nicht unterschieden, weshalb die Elektronenwechselwirkung automatisch auch den Selbstwechselwirkungsterm enthält. Diesen Fehler bezeichnet man als Selbstwechselwirkungsfehler (SIE).

Hybridfunktionale

Hybridfunktionale reduzieren den SIE, indem die Austauschenergie mit exakter Fock-Austauschenergie E_x^F gemischt wird, welche aus den KS-Orbitalen als

$$E_x^F = -\frac{1}{2}\sum_{i,j}\int\int \psi_i^*(\vec{r_1})\psi_j^*(\vec{r_2})\frac{1}{r_{12}}\psi_j(\vec{r_1})\psi_i(\vec{r_2})d\vec{r_1}d\vec{r_2} \tag{2.16}$$

berechnet wird. Die sogenannten globalen Hybrid-Funktionale haben eine Austauschenergie der Form

$$E_x^{\text{hyb}} = (1-\alpha)E_x^{GGA} + \alpha E_x^F \quad . \tag{2.17}$$

Das PW1PW-Funktional [51], welches in dieser Arbeit für die meisten Rechnungen verwendet wurde, hat einen Fock-Anteil α von 20 %. Im Methodentest dieser Arbeit wurden des Weiteren die Hybridfunktionale HSE06 [52], PBE0 [53], M06 [54], B1WC [55], B3PW [56, 57] und B3LYP [56, 58] mit Fock-Anteilen α zwischen 16 % und 27 % verwendet. Das M06-Funktional ist dabei ein metaGGA-Hybridfunktional und das HSE06-Funktional reichweitenseparierte. Für reichweitenseparierte Hybridfunktionale berechnet sich die Austauschenergie über

$$E_{\text{x}}^{HSE06} = \alpha E_{\text{x}}^{\text{Fock,SR}}(\omega_{\text{Fock}}) + (1-\alpha)E_{\text{x}}^{\text{GGA,SR}}(\omega_{\text{GGA}}) + E_{\text{x}}^{\text{GGA,LR}}(\omega_{\text{GGA}}) \quad , \tag{2.18}$$

wobei für das HSE06-Funktional $\omega_{\text{Fock}} = 0.106$ und $\omega_{\text{GGA}} = 0.189$ gesetzt sind. Die Parameter ω bestimmen die Aufspaltung des Coulomb-Operators in kurze und lange Reichweiten über

$$\frac{1}{r} = \left(\frac{1-\text{erf}(\omega r)}{r}\right)_{\text{SR}} + \left(\frac{\text{erf}(\omega r)}{r}\right)_{\text{LR}} \quad . \tag{2.19}$$

2.2.2. Hubbard-Modell

Eine weitere Möglichkeit den SIE von GGA-Funktionalen zu reduzieren, ist die DFT+U-Methode. Im Hubbard-Modell [41, 42] werden die intra-atomaren Coulomb- und Austauschintegrale durch die Parameter U und J ersetzt. Dudarev et al. [43] verwenden einen effektiven Parameter $U_{\text{eff}} = U - J$ und berechnen die Energie über

$$E_{\text{DFT+U}} = E_{\text{DFT}} + \frac{U_{\text{eff}}}{2}\sum_{\sigma}\left[\left(\sum_{m_1} n_{m_1,m_2}^{\sigma}\right) - \left(\sum_{m_1,m_2} n_{m_1,m_2}^{\sigma} n_{m_1,m_2}^{\sigma}\right)\right] \quad , \tag{2.20}$$

wobei n die Besetzungszahlen der elektronischen Zustände m_1 und m_2 mit dem Spin σ sind. Die Parameter U_{eff} müssen für jedes Element individuell ermittelt werden

[44, 45, 46, 47]. Dies erfolgt in der Regel empirisch durch Anpassung berechneter elektronische Bandlücken an experimentelle Referenzwerte [48]. Die Entwicklung selbstkonsistenter Methoden zur Berechnung der U_{eff} erfolgt auf Basis des Thomas-Fermi-Screening-Modells [49] oder der linearen Antwortfunktionaltheorie [50].

2.2.3. Dispersionskorrekturen

London-Dispersionskräfte sind langreichweitige Elektronenkorrelationseffekte, welche von der KS-Dichtefunktionaltheorie nicht beschrieben werden. Um diese Wechselwirkungen korrekt zu beschreiben, werden entweder post-Hartree-Fock-Methoden oder parameterbasierte Korrekturen wie die D3(BJ)-Korrektur von Grimme et al. benötigt [59, 60].

D3-Korrektur

Die Dispersionsenergie nach der D3(BJ)-Korrektur wird als Summe aller paarweisen Wechselwirkungen über

$$E_{\text{disp}}^{\text{D3}} = -\sum_{AB}\sum_{n=6,8} s_n \frac{C_n^{AB}}{R_{AB}^n + \left[f_{\text{damp}}^{(n)}(R_{AB})\right]^n} \tag{2.21}$$

berechnet, wobei R_{AB} der Abstand der Kerne ist. Die Dispersionskoeffizienten C_6^{AB} werden über die Casimir-Polder-Gleichung

$$C_6^{AB} = \frac{3}{\pi}\int_0^\infty \alpha^A(i\omega)\alpha^B(i\omega)d\omega \tag{2.22}$$

erhalten, wobei α die Polarisierbarkeit bei der Frequenz ω ist. Diese Koeffizienten werden für einen Satz an Referenzsystemen (Hydride aller Elemente) mit zeitabhängiger Dichtefunktionaltheorie (TD-DFT) berechnet. Die für das berechnete System benötigten Koeffizienten werden dann durch Interpolation aus der Abhängigkeit zwischen C_6^{AB} und der Koordinationszahl erhalten (Gleichung 2.23).

$$\begin{aligned} C_6^{AB}(\text{CN}^A, \text{CN}^B) &= \frac{\sum_i^{N_A}\sum_j^{N_B} C_{6,\text{ref}}^{AB}(\text{CN}_i^A, \text{CN}_j^B) L_{ij}}{\sum_i^{N_A}\sum_j^{N_B} L_{ij}} \\ L_{ij} &= e^{-4[(\text{CN}^A - \text{CN}_i^A)^2 + (\text{CN}^B - \text{CN}_j^B)^2]} \end{aligned} \tag{2.23}$$

Da in Festkörpern häufig höhere Koordinationszahlen als in Molekülen auftreten, liegen zu wenige Koeffizienten für Referenzsysteme mit vergleichbar hohen Koordinationszahlen

vor. In diesem Fall wird der Koeffizient des Referenzsystems mit der höchsten vorhandenen Koordinationszahl verwendet, welcher allgemein zu groß ist [61]. Dies führt wegen Gleichung 2.21 zu einer Überkorrektur der Dispersionsenergie.
Die Koeffizienten C_8^{AB} werden über

$$C_8^{AB} = 3C_6^{AB}\sqrt{Q^A Q^B} \tag{2.24}$$

erhalten, wobei Q von Multipolerwartungswerten und der Kernladung von A und B abhängt. Als Korrektur für kleine Abstände R_{AB} wurde der von Becke und Johnson entwickelte Dämpfungsterm [59] $f_{\text{damp}}^{(n)}(R_{AB})$ implementiert, welcher gegeben ist als

$$f_{\text{damp}}^{(n)}(R_{AB}) = a_1 r_{AB}^0 + a_2 \tag{2.25}$$

mit

$$R_{AB}^0 = \frac{C_8^{AB}}{C_6^{AB}} \tag{2.26}$$

und den empirisch angepassten Parametern a_1 und a_2.

D4-Korrektur

Die D4-Korrektur [62] ist eine Weiterentwicklung der D3-Korrektur. Grundsätzlich wird derselbe Ansatz verfolgt, die Dispersionsenergie über Gleichung 2.21 und die Koeffizienten über die Casimir-Polder-Gleichung (Gleichung 2.22) zu berechnen. Allerdings werden die Polarisierbarkeiten in Gleichung 2.22 auf andere Wege berechnet. Dafür wird eine Ladungsskalierungsfunktion ζ eingeführt:

$$\zeta(z^A, z^{A,\text{ref}}) = \exp\left[\beta_1\left\{1 - \exp\left[\gamma^A\left(1 - \frac{z^{A,\text{ref})}}{z^A}\right)\right]\right\}\right] \tag{2.27}$$

Hierbei ist γ^A die chemische Härte, welche von Ghosh und Islam [63] übernommen wurde, z^A die effektive Kernladung von A und $z^{A,\text{ref}}$ die effektive Kernladung des Referenzsystems und $\beta_1 = 3$ ein Parameter. Die effektive Kernladung wird als Summe der Kernladung Z^A und der Partialladung q^A des Atoms A erhalten:

$$z^A = Z^A + q^A \quad . \tag{2.28}$$

Als Partialladungen q^A werden die EEQ-Partialladungen (*engl.* electronegativity equilibration partial charges) nach Goedecker et. al. [64] verwendet. Die Polarisierbarkeiten der

Referenzsysteme (Gleichung 2.22) werden mit der Ladungsskalierungsfunktion multipliziert:

$$\alpha^{A,\mathrm{ref}} = \alpha^{A,\mathrm{ref}}(i\omega)\zeta(z^A, z^{A,\mathrm{ref}}) \quad . \tag{2.29}$$

Wie auch bei der D3-Korrektur wird die Abhängigkeit der Koeffizienten von der Koordinationszahl fü die Interpolation der Koeffizienten benötigt. Allerdings werden hier die Koordinationszahlen um eine Abhängigkeit von der Elektronegativitätsdifferenz erweitert:

$$\begin{aligned} CN^A &= \sum_A \sum_{B \neq A} \frac{\delta_{AB}^{EN}}{2} \left(1 + \mathrm{erf}\left(-k_0 \left(\frac{R_{AB} - R_{AB}^{\mathrm{cov}}}{R_{AB}^{\mathrm{cov}}}\right)\right)\right) \\ \delta_{AB}^{EN} &= \left(k_1 \mathrm{exp}\left(|\mathrm{EN}_A - \mathrm{EN}_B| + k_2\right)^2\right)/k_3 \end{aligned} \tag{2.30}$$

Hierbei sind die (EN) die Elektronegativitäten nach Pauling, R_{AB} der Abstand der Kerne und $R_{AB}^{\mathrm{cov}} = R_A + R_B$ die Summe der kovalenten Atomradien von A und B.
Mit DFT-D4 können für Moleküle genauere Ergebnisse als mit DFT-D3 erzielt werden. Durch den auf Partialladungen basierenden Ansatz ist eine genauere Interpolation und Extrapolation der Koeffizienten möglich, was auch für den Einsatz für Festkörper vorteilhaft ist.

2.3. Festkörperquantenchemie

Ein idealer kristalliner Festkörper definiert sich über eine dreidimensionale, sich unendlich oft wiederholende Einheitszelle. Die Gitterpunkte innerhalb dieser Zelle können mithilfe der Gittervektoren $\vec{T}$ (einer Linearkombination der Basisvektoren $\vec{a_i}$) auf ihre Bilder übertragen werden:

$$\vec{T} = \sum_{i=1}^{3} n_i \vec{a_i} \quad \text{mit} \quad n_i \in \mathbb{Z} \tag{2.31}$$

Die kleinste sich auf diese Art wiederholende Einheit wird als primitive Einheitszelle bezeichnet. Die konventionelle Einheitszelle ist von größerer Bedeutung, da diese die Symmetrie des Kristalls widerspiegelt. Eine konventionelle Zelle enthält einen bis vier Gitterpunkte und gehört zu einer von 230 Raumgruppen. Alle Positionen $\vec{f}$ innerhalb der Zelle werden durch fraktionale Koordinaten u_i angegeben, welche unabhängig von der Größe der Zelle sind:

$$\vec{f} = \sum_{i=1}^{3} u_i \vec{a_i} \quad \text{mit} \quad u_i \in \mathbb{R} \tag{2.32}$$

Die u_i der Urbilder liegen in der Regel zwischen 0 und 1, die Bilder werden über Gleichung 2.31 konstruiert.

Für die quantenchemische Beschreibung von Festkörpern werden häufig reziproke Gitter mit den Basisvektoren $\vec{b}$ verwendet. Diese ergeben sich aus $\vec{a}$ über

$$\begin{aligned} \vec{b_i} \cdot \vec{a_j} &= 2\pi\delta_{ij} \\ \vec{b_k} &= 2\pi\frac{\vec{a_j} \times \vec{a_i}}{V} \quad \text{mit} \quad i,j,k \in \{1,2,3\} \end{aligned} \tag{2.33}$$

wobei V das Volumen der primitiven Zelle und δ_{ij} das Kroneckerdelta ist. Der Gittervektor $\vec{G}$ ist damit gegeben als

$$\vec{G} = \sum_{i=1}^{3} m_i \vec{b_i} \quad \text{mit} \quad m_i \in \mathbb{Z} \tag{2.34}$$

Ein Position im reziproken Raum wird ist durch den Vektor $\vec{k}$ gegeben:

$$\vec{k} = \sum_{i=1}^{3} k_i \vec{b_i} \quad \text{mit} \quad k_i \in \mathbb{R}. \tag{2.35}$$

Die k_i sind dann die fraktionellen Koordinaten des reziproken Gitters. Die reziproke Einheitszelle ist eine Voronoi-Zelle um den Ursprung des reziproken Gitters, welche in alle Seiten die halbe Entfernung zu den benachbarten Gitterpunkten geht. Das Gegenstück im realen Raum ist die Wigner-Seitz-Zelle.

2.3.1. Bloch-Theorem

Aufgrund der Periodizität des Systems sind das auf die Elektronen wirkende Potential V und der Operator der kinetischen Energie $\hat{T}$ periodisch, sodass gilt

$$\begin{aligned} V(\vec{r}) &= V(\vec{r} + \vec{T}) \\ \hat{T}(\vec{r}) &= \hat{T}(\vec{r} + \vec{T}). \end{aligned} \tag{2.36}$$

Damit kommutiert auch der Hamiltonoperator des Systems mit dem Translationsoperator $\vec{T}$. Die Wellenfunktion setzt sich somit aus einem Phasenfaktor und der Wellenfunktion des Urbilds zusammen:

$$\psi(\vec{r} + \vec{T}) = e^{i\vec{k}\vec{T}}\psi(\vec{r}). \tag{2.37}$$

Mit dieser Grundforderung lautet nach Bloch der Ansatz für die Eigenfunktionen des Hamiltonoperators

$$\psi^{\vec{k}}(\vec{r}) = e^{i\vec{k}\vec{r}}u_k(\vec{r}) \tag{2.38}$$

wobei $u_k(\vec{r})$ eine gitterperiodische Funktion und $e^{i\vec{k}\vec{r}}$ eine ebene Welle ist. Die $\psi^{\vec{k}}(\vec{r})$ werden Blochfunktionen genannt. Die Kristallorbitale $\varphi^{\vec{k}}$ sind eine Linearkombination der Blochfunktionen:

$$\varphi_a^{\vec{k}}(\vec{r}) = \sum_{\mu} c_{\mu a}^{\vec{k}} \psi^{\vec{k}}(\vec{r}) \tag{2.39}$$

2.3.2. Basissätze

Die gitterperiodischen Funktionen u_k unterscheiden sich je nach Programm. In CRYSTAL [65] werden atomzentrierte Orbitale verwendet. Die Basisfunktionen sind wie in Molekülbasissätzen Linearkombinationen (Kontraktionen) primitiver Gaußfunktionen (cGTOs, *contracted Gaussian Type Orbitals*):

$$\chi_j(r) = \sum_{\alpha}^{K} c_\alpha x^u y^v z^w e^{-\alpha r^2} \quad \text{mit} \quad u+v+w = l \quad \text{(Nebenquantenzahl)} \quad . \tag{2.40}$$

Hierbei ist K die Kontraktionslänge. Es bietet sich die Verwendung speziell für Festkörper optimierter Basissätze an. Die rev2-POB-TZVP Basissätze [66, 67, 68, 68], welche in dieser Arbeit verwendet werden, wurden speziell für Festkörper und einen geringeren Basisatzsuperpositionsfehler (BSSE) optimiert. In dieser Arbeit wurden die meisten Rechnungen mit CRYSTAL durchgeführt, da sich im Methodentest die Hybridfunktionale als vorteilhaft erwiesen, welche in CRYSTAL besonders recheneffizient implementiert sind. Im Gegensatz zu ebenen Wellen muss man bei der Linearkombination von cGTOs den Basissatzsuperpositionsfehler (BSSE) beachten, außerdem ist der Basissatzunvollständigkeitsfehler (BSIE) von Bedeutung. Rechnet man beispielsweise die Defektbildungsenergie E_{ODF} von $CaMnO_3$ über

$$E_{ODF} = E_{\mathrm{CaMnO_{3-\delta}}} + \frac{\delta}{2} E_{\mathrm{O_2}} - E_{\mathrm{CaMnO_3}} \tag{2.41}$$

aus, so fehlen bei $CaMnO_{3-\delta}$ die Basisfunktionen an der Defektposition. Der Basissatz der Atome in der Nähe der Defektposition ist im Allgemeinen nicht vollständig genug, um die fehlende Basisfunktion zu kompensieren (BSIE). Der BSIE kann durch das Hinzufügen sogenannter Ghost-Funktionen behoben werden, welche am fehlenden Sauerstoffatom zentriert sind. Im O_2-Molekül sind die Basissätze der O-Atome kleiner als im Festkörper, da weniger umgebende Atome vorhanden sind, deren Basisfunktionen den Basissatz vervollständigen können (BSSE).

Der einfachste Ansatz zur Behebung des BSSE ist die Erweiterung des O-Basissatzes des O_2-Moleküls bis zur Konvergenz. Dafür werden für jeden Orbitaltyp weitere Basisfunktionen mit dem jeweils halben Orbitalexponent der letzten Funktion hinzugefügt, bis sich die Energie um weniger als 1 kJ mol^{-1} ändert.
Das Programm VASP [69, 70, 71] arbeitet mit ebenen Wellen der Form

$$u_{\vec{G}}(\vec{r}) = e^{i\vec{G}\vec{r}} \tag{2.42}$$

abhängig von den reziproken Gittervektoren $\vec{G}$. Die Basissätze sind beschränkt durch die kinetische Cutoff-Energie

$$E_{cut} \geq \frac{1}{2}|\vec{G}|^2 \tag{2.43}$$

Bei ebenen Wellen tritt kein BSSE auf, da die Basisfunktionen nicht atomzentriert, sondern gleichmäßig über den Raum verteilt sind.

2.3.3. Born-von Kármán-Randbedingung

Bisher wurde von einem unendlichen Festkörper ausgegangen. Da man ein solches System in der Praxis nicht beschreiben kann, muss dieser unter Einhaltung der Translationsinvarianz beschränkt werden. Born und von Kármán schlugen dazu vor, den Festkörper in Hauptregionen aufzuteilen, für die gilt

$$\psi(\vec{r} + N_i\vec{a_i}) = \psi(\vec{r}) \quad \text{mit} \quad i \in \{1,2,3\} \quad \text{und} \quad N_i \in \mathbb{N} \quad . \tag{2.44}$$

Wendet man dies auf die Blochfunktionen an, ergibt sich aus Gleichung 2.37 dass

$$e^{i\vec{k}N_i\vec{a_i}} = 1 \quad . \tag{2.45}$$

Aus der Definitionen von $\vec{k}$ (Gleichungen 2.33 und 2.35) ergibt sich damit

$$e^{i\vec{k}N_i\vec{a_i}} = e^{i\sum_{j=1}^{3} k_j\vec{b_i}N_i\vec{a_i}} = e^{i\sum_{j=1}^{3} k_j 2\pi\delta_{ij}N_i} = e^{i2\pi k_i N_i} = 1 \tag{2.46}$$

Damit sind nur alle

$$k_i = \frac{m_i}{N_i} \quad \text{mit} \quad m_i \in \mathbb{Z} \tag{2.47}$$

erlaubt. Aufgrund der Periodizität des Phasenvektors der Blochfunktion (Gleichung 2.38) ist es nun möglich, m_i auf das Intervall $[-\frac{N_i}{2}, \frac{N_i}{2}]$ zu begrenzen.

Das Monkhorst-Pack-Gitter ist eine mögliche Implementierung der Born-von-Kármán-Randbedingung, welche in CRYSTAL und VASP verwendet wird. Hierfür wird das reziproke Gitter durch die vom Benutzer festzulegenden Shrinking-Faktoren N_1, N_2 und N_3 gleichmäßig unterteilt. Die Energieeigenwerte werden dann für alle symmetrieinequivalenten k-Punkte mit $k_i = \frac{m_i}{N_i}$ berechnet.

2.4. Geometrieoptimierung

Die Energie des Systems hängt von den Atompositionen ab, weshalb in einer Geometrieoptimierung die energetisch günstigste Anordnung der Atome gesucht wird. Die Startgeometrie $\mathbf{R}_0$ wird jeden Optimierungsschritt um eine Verschiebung $\mathbf{s}_k$ verändert, welche möglichst so gewählt wird, dass die neue Geometrie energetisch günstiger ist als die vorherige. Es wird angenommen, dass die Energie um $\mathbf{R}_0$ durch eine Taylorentwicklung zweiter Ordnung beschrieben werden kann. Führt man den Gradienten $\mathbf{g}$ mit den Elementen $\mathbf{g} = \frac{\partial E}{\partial \mathbf{R}}$ und die Hesse-Matrix $\mathbf{H}$ mit den Elementen $H_{ij} = \frac{\partial^2 E}{\partial R_i \partial R_j}$ ein, so lässt sich die Taylorentwicklung schreiben als

$$E(\mathbf{R}_{k+1}) = E(\mathbf{R}_k) + \mathbf{g}(\mathbf{R}_k) \cdot \mathbf{s}_k + \frac{1}{2}\mathbf{s}_k \cdot \mathbf{H}(\mathbf{R}_k) \cdot \mathbf{s}_k \quad . \tag{2.48}$$

Die optimale Verschiebung $\mathbf{s}_k$ führt zu einer maximal negativen Energie. Dieses Minimum wird als Nullpunkt der ersten Ableitung berechnet

$$\frac{dE(\mathbf{R}_{k+1})}{d\mathbf{s}_k} = \mathbf{g}(\mathbf{R}_k) + \mathbf{H}(\mathbf{R}_k) \cdot \mathbf{s}_k = 0 \quad . \tag{2.49}$$

Durch Umstellen der Gleichung ergibt sich die optimale Verschiebung

$$\mathbf{s}_k = -\mathbf{H}^{-1}(\mathbf{R}_k) \cdot \mathbf{g}(\mathbf{R}_k) \quad . \tag{2.50}$$

Die Atompositionen werden auf diese Weise jeden Optimierungsschritt aktualisiert, bis die Konvergenzkriterien von Energie und Gradienten erreicht sind. Dieses Verfahren wird als Newton-Raphson-Algorithmus bezeichnet.
Die Berechnung der Hesse-Matrix $\mathbf{H}$ ist sehr zeitaufwändig, weshalb es sich anbietet diese zu approximieren. Man kann sie aus der Änderung des Gradienten zwischen zwei Optimierungsschritten approximieren (Quasi-Newton-Raphson-Algorithmen).

2.4.1. BFGS

Das Standardbeispiel für einen Quasi-Newton-Raphson-Algorithmus ist der BFGS-Optimierer [72, 73, 74, 75]. Die Verschiebung $\mathbf{s}_k$ wird gemäß Gleichung 2.50 berechnet, indem das lineare Gleichungssystem gelöst wird

$$\mathbf{H}(\mathbf{R}_k) \cdot \mathbf{s}_k = -\mathbf{g}(\mathbf{R}_k) \quad . \tag{2.51}$$

Die neue Hesse-Matrix $\mathbf{H}(\mathbf{R}_{k+1})$ wird dann approximiert als

$$\mathbf{H}(\mathbf{R}_{k+1}) = \mathbf{y}_k \mathbf{s}_k^{-1} \quad , \tag{2.52}$$

wobei $\mathbf{y}_k$ die Differenz zwischen den Gradienten ist

$$y_k = \mathbf{g}(\mathbf{R}_{k+1}) - \mathbf{g}(\mathbf{R}_k) \quad . \tag{2.53}$$

Dies kann als Aktualisierung der Hesse-Matrix $\mathbf{H}(\mathbf{R}_k)$ ausgedrückt werden:

$$\mathbf{H}(\mathbf{R}_{k+1}) = \mathbf{H}(\mathbf{R}_k) + \frac{\mathbf{y}_k \cdot \mathbf{y}_k^T}{\mathbf{y}_k^T \cdot \mathbf{s}_k} - \frac{\mathbf{H}(\mathbf{R}_k) \cdot \mathbf{s}_k \cdot \mathbf{s}_k^T \cdot \mathbf{H}(\mathbf{R}_k)}{\mathbf{s}_k^T \cdot \mathbf{H}(\mathbf{R}_{k+1}) \cdot \mathbf{s}_k} \quad . \tag{2.54}$$

2.4.2. LBFGS

Der limited-memory Broyden–Fletcher–Goldfarb–Shanno (LBFGS)-Optimierer [76] ist eine speicherbegrenzte Variante des BFGS-Optimierers. Er verwendet eine diagonale inverse Hesse-Matrix anstelle der Hesse-Matrix . Die kartesische Hesse-Matrix wird diagonalisiert durch

$$\mathbf{X}^{-1}\mathbf{H}\mathbf{X} = \mathbf{H}_d \quad , \tag{2.55}$$

wobei $\mathbf{X}$ die Matrix der Eigenvektoren von $\mathbf{H}$ und ist. Die Eigenvektoren von $\mathbf{H}$ sind die Basis des Normalkoordinatensystems. Anstelle der kartesischen Koordinaten werden die Normalkoordinaten optimiert. Die Verschiebung ist dann gegeben als

$$\mathbf{s}_k = -\mathbf{H}_d^{-1}(\mathbf{R}_k) \cdot \mathbf{g}(\mathbf{R}_k) \quad . \tag{2.56}$$

Dabei ist $\mathbf{R}_k$ der Vektor aller Atompositionen in Normalkoordinaten und $\mathbf{g}(\mathbf{R}_k)$ der Gradient in Normalkoordinaten. Anstatt der Hesse-Matrix wird dann direkt die inverse diagonalisierte Hesse-Matrix aktualisiert:

$$\mathbf{H}_d^{-1}(R_{k+1}) = \mathbf{H}_d^{-1}(R_k) + \frac{(\mathbf{s}_k^T \cdot \mathbf{y}_k + \mathbf{y}_k^T \cdot \mathbf{H}_d^{-1}(\mathbf{R}_k) \cdot \mathbf{y}_k) \cdot (\mathbf{s}_k \cdot \mathbf{s}_k^T)}{(\mathbf{s}_k^T \cdot \mathbf{y}_k)^2} - \frac{\mathbf{H}_d^{-1}(\mathbf{R}_k) \cdot \mathbf{y}_k \cdot \mathbf{s}_k^T + \mathbf{s}_k \cdot \mathbf{y}_k^T \cdot \mathbf{H}_d^{-1}(\mathbf{R}_k)}{\mathbf{s}_k^T \cdot \mathbf{y}_k} \quad . \tag{2.57}$$

2.4.3. precon-LBFGS

Der von Packwood et al. entwickelte precon-LBFGS-Optimierer [77] ist eine Weiterentwicklung des LBFGS-Optimierers, welcher speziell für Festkörper und Molekülkristalle entwickelt wurde. Dieser verwendet ein Liniensuchverfahren, welches die Verschiebung s_k (Gleichung 2.58) allgemein berechnet als

$$\mathbf{s}_k = -\alpha \mathbf{H}_d^{-1}(\mathbf{R}_k) \cdot \mathbf{g}(\mathbf{R}_k) \quad . \tag{2.58}$$

wobei der Parameter α in jedem Optimierungsschritt separat optimiert wird.
Für große Systeme tritt beim normalen LBFGS das Problem auf, dass die Aktualisierung der Hessematrix auf Basis der Gradienten (Gleichung 2.57) nicht genau genug ist. In diesem Optimierer wird durch das sogenannte *metric preconditioning* die initiale Hessematrix der Liniensuche verbessert. Man nimmt an, dass die Hesse-Matrix $\mathbf{H}(\mathbf{R}_{k+1})$ durch eine für den kompletten Optimierungsprozess konstante Hesse-Matrix P ersetzt werden kann, wobei P eine Metrik im Konfigurationsraum definiert. Die Richtung eines *steepest descent* $-\vec{\nabla} f(x_k)$ ist mit Referenz zu der ℓ^2-Norm $||u||_I := (\sum |u_i|^2)^{\frac{1}{2}}$, wobei u eine Richtung im Konfigurationsraum ist. Werden die Abstände im Konfigurationsraum respektiv zur P-Norm $||u||_P = (u^T P u)^{\frac{1}{2}}$ gemessen, so wird der *steepest descent* zu $-P^{-1}\vec{\nabla} f(x_k)$. Definiert man nun $\tilde{x}_k = P^{\frac{1}{2}} x_k$ und $\tilde{f}(\tilde{x}) = f(P^{-\frac{1}{2}}\tilde{x})$ dann ergibt sich $\tilde{x_{k+1}} = \tilde{x_k} - \alpha_k \vec{\nabla} \tilde{f}(\tilde{x}_k)$ (entsprechend Gleichung 2.58). Mit $\vec{\nabla}^2 \tilde{f}(\tilde{x}) = P^{-\frac{1}{2}} \vec{\nabla}^2 f(P^{-\frac{1}{2}}\tilde{x}) P^{-\frac{1}{2}}$ ist die Konvergenzrate $x_k \to x$ aus Gleichung 2.58 zum Grenzwert x gegeben als

$$||x_k - x||_P \lesssim \left(\frac{\kappa_P - 1}{\kappa_P + 1}\right)^k ||x_0 - x||_P \tag{2.59}$$

wobei κ_P die Konditionszahl $P^{-\frac{1}{2}} H P^{-\frac{1}{2}}$ ist. Man erhält P aus dem Eigenwertproblem

$$H\nu = \lambda P \nu \quad . \tag{2.60}$$

H ist hierbei die exakte Hessematrix. Die Approximierung der Hessematrix sollte idealerweise zu $\kappa_p \approx 1$ führen, allerdings kann man sich mit einem sinnvollen Bereich an

Abständen begnügen, welcher zu einer Matrix P und zu einem κ_P abhängig von einer Konstanten führt, was für die meisten Systeme funktioniert. Die Matrix P wird in Abhängigkeit des Cutoff-Radius r_{cc}, des Abstands der nächsten benachbarten Atome r_{nn} und der Parameter A und μ formuliert:

$$\begin{aligned} u^T P u &= \mu \sum_{0 \leq |r_{ij} < r_{\text{cut}}} c_{ij} |u_i - u_j|^2, \\ c_{ij} &= \exp\left(-A\left(\frac{r_{\text{ij}}}{r_{\text{nn}}} - 1\right)\right) \end{aligned} \tag{2.61}$$

wobei die Matrixelemente von P geschrieben werden können als

$$\begin{aligned} P_{ij} &= \begin{cases} -\mu c_{ij}, & |r_{ij}| < r_{\text{cut}} \\ 0, & |r_{ij}| > r_{\text{cut}} \end{cases} \\ P_{ii} &= -\sum_{j \neq i} P_{ij} \quad . \end{aligned} \tag{2.62}$$

Die Parameter werden in der Regel auf $A = 3$ und $r_{\text{cut}} = 2r_{\text{nn}}$ gesetzt. Der Energieskalierungsparameter μ wird so gewählt, dass der LBFGS-Algorithmus die Einheitsschrittlänge als Standard verwenden kann:

$$\begin{aligned} \nu^T \left(\nabla E(x_0 + \nu) - \nabla E(x_0)\right) &= \mu \nu^T P_{\mu=1} \nu \\ \nu(x, y, z) &= M \left(\sin(x/L_x), \sin(y/L_y) \sin(z/L_z)\right) \end{aligned} \tag{2.63}$$

wobei L_i die Längen der periodischen Gittervektoren und M eine benutzerdefinerte Matrix mit dem Standardwert M=$10^{-2} r_{\text{nn}} \mathbb{1}$ ist.

2.5. Thermodynamik

2.5.1. Berechnung der thermodynamischen Funktionen

Die elektronische Energie E_0 einer quantenchemischen Rechnung kann nicht direkt mit experimentellen Ergebnissen verglichen werden. Dafür müssen die thermodynamischen Funktionen berechnet werden, in der Regel die Enthalpie H, die Entropie S und die Gibbs-Energie G. Die Gibbs-Energie G berechnet sich aus der Enthalpie H und der Entropie S:

$$G(T) = H(T) + TS(T) \tag{2.64}$$

Enthalpie und Entropie setzen sich aus Translations-, Rotations-, und Schwingungsbeiträgen zusammen. Da in Festkörpern nur Vibrationen vorhanden sind, beschränkt sich

dort (in der harmonischen Näherung) die Berechnung der Enthalpie und der Entropie auf Gleichungen 2.65 und 2.66.

$$H_{\text{vib}} = E_{\text{el}} + \sum_i \frac{1}{2} h\nu_i + \sum_i \frac{h\nu_i}{e^{\frac{h\nu_i}{kT}} - 1} + pV \tag{2.65}$$

$$S_{\text{vib}} = \frac{1}{T}\left(\sum_i \frac{1}{2} h\nu_i + \sum_i \frac{h\nu_i}{e^{\frac{h\nu_i}{kT}} - 1}\right) + k \cdot \ln\left(\sum_i \frac{e^{\frac{h\nu_i}{2kT}}}{1 - e^{-\frac{h\nu_i}{kT}}}\right) \tag{2.66}$$

Hierbei ist p der Druck, V das Volumen, k die Boltzmann-Konstante, h das Plancksche Wirkungsquantum und ν_i die Schwingungsfrequenzen des Festkörpers oder der Oberfläche. Die Schwingungsfrequenzen werden von CRYSTAL aus den zweiten Ableitungen der Energie im energetischen Minimum erhalten. Für die Berechnung von Gibbs-Energien von Reaktionen, in denen Moleküle und Festkörper vorkommen (wie der Sauerstoffdefektbildung im Perovskit), sind auch die thermodynamischen Funktionen der Moleküle notwendig. In diesem Fall werden diese aus der NIST-Datenbank erhalten [78].

2.5.2. Konfigurationsentropie

Bei der Substitution von Atomen durch Fremdatome oder bei Leerstellen gibt es häufig viele verschiedene Möglichkeiten der Anordnung, welche man Konfigurationen nennt. Jede Konfiguration i hat eine elektronische Energie E_i und eine symmetriebedingte Entartung g_i. Die Wahrscheinlichkeit, dass der Festkörper in einer bestimmten Konfiguration vorliegt, ist dann nach Boltzmann gegeben durch

$$p_i = \frac{\exp\left(-\frac{(E_i - E_0)}{RT}\right)}{\sum_j g_j \exp\left(-\frac{(E_j - E_0)}{RT}\right)} \tag{2.67}$$

wobei E_0 die Energie der stabilsten Konfiguration, R die ideale Gaskonstante und T die Temperatur ist. Aus der statistischen Thermodynamik und Anwendung der Sterlingformel ergibt sich für das thermodynamische Ensemble eine Konfigurationsentropie

$$S_{\text{conf}} = -R \sum_i g_i p_i \ln(p_i) \quad . \tag{2.68}$$

Dieser Ansatz für die Konfigurationsentropie wurde auch bereits schon von Pracht und Grimme verfolgt, um die absolute molekulare Entropie von Rotamer-Konformer-Ensemblen zu berechnen [79]. Diese direkte Möglichkeit, die Konfigurationsentropie zu

erhalten, erfordert die Berechnung der elektronischen Energien aller Konfigurationen. Sind die elektronischen Energien relativ ähnlich (wie zum Beispiel bei Mischungsentropien von Perovskiten), lässt sich die Konfigurationsentropie approximieren als

$$\Delta S_{\text{conf}} = -R\,(x\ln(x) + (1-x)\ln(1-x)) \tag{2.69}$$

wobei x der Anteil an Defekten oder substituierten Atomen ist.

2.6. Übergangszustandssuche

Reaktionspfade sind von signifikantem Interesse, um Aufschluss über Reaktionsmechanismen zu erhalten. Für den Reaktionspfad ist der Übergangszustand zwischen zwei Minimumsstrukturen von größter Bedeutung, um die Reaktionsbarriere zu ermitteln. Übergangszustände entsprechen Sattelpunkten auf der Energiehyperfläche. Die Suche von Sattelpunkten ist für Optimierungsalgorithmen allgemein problematischer als die von Minima. Im Folgenden werden zwei mögliche Ansätze dafür gezeigt.

2.6.1. Direkte Suche

Ein Algorithmus für eine direkte Suche wurde von Nichols et al. [80] publiziert. Ähnlich wie bei der Geometrieoptimierung wird die Energiehyperfläche über Gleichung 2.48 approximiert. Um den Übergangszustand zu erhalten, werden in jedem Optimierungsschritt die Eigenmoden und deren Eigenwerte benötigt. Entlang der Eigenmode mit dem niedrigsten Eigenwert wird das Maximum gesucht, während entlang aller anderen Eigenmoden das Minimum gesucht wird. In CRYSTAL ist die direkte Suche über das Keyword TSOPT verfügbar. Problematisch bei der direkten Suche ist, dass die Startstruktur bereits nah genug am Übergangszustand sein muss. Möglich wäre es, das energetisch höchste Bild aus einer Rechnung mit der Nudged-Elastic-Band-Methode (NEB) (siehe nächstes Kapitel) als Startpunkt für eine direkte Suche zu nehmen. Allerdings wird in jedem Optimierungsschritt eine Hessematrix benötigt, wodurch eine solche Rechnung sehr rechenzeitintensiv ist. Aus diesem Grund wird in dieser Arbeit die NEB-Methode verwendet, welche im folgenden Kapitel erklärt wird.

2.6.2. Nudged-Elastic-Band-Methode

Die Nudged-Elastic-Band-Methode (NEB) [81, 82, 83] wurde in dieser Arbeit verwendet, um den energetisch günstigsten Reaktionspfad zwischen Edukt und Produkt zu finden. Zunächst wird eine bestimmte Anzahl an Zwischenbildern durch Interpolation erzeugt. Die Geometrie der Zwischenbilder wird dann unter der Randbedingung optimiert, dass sich dessen Reaktionskoordinate nicht verändert. Dies wird umgesetzt durch eine Kraft F_i^{NEB} welche auf das i-te Zwischenbild wirkt und gegeben ist als

$$\begin{aligned} F_i^{NEB} &= F_i^{\nabla\perp} + F_i^{S\parallel} \\ F_i^{\nabla\perp} &= -\nabla(R_i) + \nabla(R_i) \cdot \hat{\tau}_i\hat{\tau}_i \\ F_i^{S\parallel} &= k(|R_{i+1} - R_i| - |R_i - R_{i-1}|)\hat{\tau}_i \end{aligned} \tag{2.70}$$

Hierbei sind $F_i^{\nabla\perp}$ die Kraftkomponenten orthogonal zum Reaktionspfad, $F_i^{S\parallel}$ die Komponenten tangential zum Reaktionspfad, R_i die Atompositionen des i-ten Bildes, k die Federkonstante und $\hat{\tau}_i$ der Vektor entlang der Tangente des benachbarten Bildes mit höherer Energie.

Die Climbing-Image Methode ist eine Variante des NEB-Verfahrens, in welcher das Bild mit der höchsten Energie auf den exakten Sattelpunkt optimiert wird. Dazu werden auf dieses Bild keine tangentialen Federkräfte angewendet und die Federkraft orthogonal zum Reaktionspfad invertiert. Dies führt zu einer Maximierung der Energie entlang des Reaktionspfads und einer Minimierung in alle anderen Richtungen. Allerdings kann diese Methode ungleiche Abstände der Bilder entlang des Reaktionspfads erzeugen.

Des Weiteren kann der dynamische NEB-Algorithmus verwendet werden, welcher die Konvergenzkriterien der Bilder in Abhängigkeit der Entfernung vom Sattelpunkt skaliert. Dies kann unter Ausnutzung der größeren Wichtigkeit des Sattelpunkts für den Reaktionspfad Rechenzeit sparen.

Für Festkörper gibt es die Möglichkeit, ein verallgemeinertes Festkörper-NEB durchzuführen, in welchem die Strukturen aller Bilder inklusive der Gittervektoren optimiert werden. Dies ist zum Beispiel für Phasenübergänge von Bedeutung, kann aber für Protonenwanderungsbarrieren wie in dieser Arbeit vernachlässigt werden.

2.6.3. NEB mit CRYSTAL - Codemodifikationen in der ASE

Die Nudged-Elastic-Band-Methode ist in CRYSTAL nicht implementiert. Die Atomic Simulation Environment (ASE) bietet die Möglichkeit, die NEB-Rechnungen in Kombination mit zahlreichen quantenchemischen Programmen durchzuführen [84]. In CRYSTAL wird im Gegensatz zu anderen quantenchemischen Programmen die Symmetrie der Systeme vollständig ausgenutzt. Die ASE kann zwar bereits in Kombination mit CRYSTAL verwendet werden, allerdings werden Atomkoordinaten ausschließlich aus den *fort.34*-Dateien entnommen. Diese enthalten die Positionen aller Atome, wobei CRYSTAL nur die symmetrieinäquivalenten Atompositionen benötigt. Dies hat den Nachteil, dass die ASE daraus nicht die Information erhält, welche Atome symmetrieinäquivalent sind. Für eine Erhaltung der Symmetrie muss die Symmetrie der Gradienten sichergestellt werden, wofür die ASE zwar Funktionen enthält, welche aber nicht in die Schnittstelle zu CRYSTAL eingebaut sind.

In dieser Arbeit wird eine komplett neue Schnittstelle zwischen ASE und CRYSTAL implementiert [85], welche einen alternativen Ansatz verfolgt. Die ASE liest die Geometrie aus einem normalen CRYSTAL-Input-File ein, welches neben der Raumgruppe und den Gitterparametern nur die Positionen der symmetrieinäquivalenten Atome enthält. Alle Informationen für die Rechnung werden aus diesem Input-File ausgelesen, also ist auch die Kombination mit anderen CRYSTAL-Keywords möglich. Die Atompositionen und die Nummern der symmetrieinäquivalenten Atome werden automatisch an die ASE weitergegeben. Durch Kenntnis der symmetrieinäquivalenten Atome ist es möglich, dass für jeden Optimierungsschritt nur diese Atompositionen über das ATOMDISP-Keyword in CRYSTAL verändert werden, wodurch die Erhaltung der Symmetrie sichergestellt ist. Für das NEB wird der Code der Schnittstelle noch bezüglich der Rechenzeit optimiert. Zum einen wird die Dichtematrix für jedes Bild gespeichert, wodurch Folgeoptimierungsschritte der Bilder um den Faktor zwei beschleunigt werden. Zum anderen wird eine einfache Parallelisierungsoption implementiert, welche es ermöglicht, alle Bilder gleichzeitig zu optimieren. Die ASE enthält bereits eine Parallelisierungsoption für NEB-Rechnungen, welche allerdings für CRYSTAL nicht anwendbar ist. Die in dieser Arbeit implementierte Parallelisierung basiert auf der gleichzeitigen Berechnung aller Bilder eines NEB-Schritts, was mithilfe eines einfachen Python-Skripts möglich ist.

2.7. Oberflächenmodelle

Die Oberfläche eines Festkörpers ist entscheidend für seine Reaktivität und seine katalytische Aktivität. Werden die in Kapitel 2.3 vorgestellten Konzepte angewendet, besteht ein Festkörper aus einer in jede Raumrichtung unendlich periodischen Elementarzelle. Dementsprechend hat jedes Atom seine im Festkörper bevorzugte Konfigurationszahl. An der Oberfläche ist dies nicht mehr möglich, da auf dieser zwangsläufig keine Bindungspartner in Richtung der Oberflächennormalen existieren. Diese Unterkoordination der Oberflächenatome erhöht deren Reaktivität. Außerdem hängt die Form des Kristalls direkt von der Stabilität der Oberflächen ab. Nach dem Gibbs-Wulff-Theorem [86] nimmt ein Kristall im thermodynamischen Gleichgewicht die Gestalt minimaler freier Oberflächenenthalpie an.

$$G_{\text{surf}} = \min\left(\sum_i G_{\text{surf},i} A_i\right) \tag{2.71}$$

Hierbei ist A der Flächeninhalt der Oberfläche und $G_{\text{surf},i}$ die freie Enthalpie der Oberfläche relativ zum Bulk. Unter Vernachlässigung der thermischen (und daraus resultierenden thermodynamischen) Effekte werden in der Regel die Oberflächenenergien E_s aller relevanten Oberflächen berechnet.

$$E_s(n) = \frac{E_{\text{slab}}(n) - nE_{\text{bulk}}}{2A} \tag{2.72}$$

Hierbei ist n die Anzahl an Formeleinheiten des Oberflächenmodells, die proportional zur Anzahl der Schichten ist. Oberflächen werden anhand der sogenannten Miller-Indizes h, k und l klassifiziert. Diese Indizes geben an, dass die Achsen der Elementarzelle bei $\frac{1}{h}$, $\frac{1}{k}$ und $\frac{1}{l}$ (in fraktionellen Koordinaten) geschnitten werden. In dieser Arbeit werden die Oberflächen (100),(010),(001),(110),(101) und (011) für $CaMnO_3$ betrachtet. Oberflächenmodelle für eine bestimmte Facette werden durch die Terminierung und die Anzahl der Schichten klassifiziert. Um das jeweils stabilste Modell zu erhalten, müssen alle möglichen Terminierungen berechnet werden und die Schichtanzahl bis zur Konvergenz erhöht werden.

Viele Perovskitoberflächen sind polar nach der Tasker-Klassifikation [87], was die theoretische Modellierung verkompliziert. Noguera et al. identifizierten in einer Studie über $SrTiO_3$ verschiedene Faktoren, welche essentiell für die physikalisch korrekte Beschrei-

bung polarer Oberflächen sind [88]. Oberflächenmodelle sollen symmetrisch zur Oberflächennormalen sein, um Dipolmomente zu vermeiden. Außerdem soll die Anzahl gebrochener Metall-Sauerstoff-Bindungen möglichst gering sein. Des Weiteren soll die Schichtanzahl nicht zu klein sein.

Die Stöchiometrie eines Oberflächenmodells ist essentiell für die korrekte Beschreibung der elektronischen Struktur. Einige Oberflächenmodelle sind nicht automatisch stöchiometrisch. Die Stöchiometrie kann beispielsweise durch das Einbauen von Schottky-Defekten erreicht werden, wie von Bauerfeind et al. diskutiert [89]. Des Weiteren ist es nach Noguera auch möglich, nicht-stöchiometrische Oberflächenmodelle zu berechnen, was allerdings eine sinnvolle Berechnung der Oberflächenenergien erschwert. Eine gemittelte Oberflächenenergie der beiden möglichen Terminierungen X und Y ist dann gegeben als

$$E_{cl}^{X+Y} = \frac{1}{4A}\left(E_{\text{Slab}}^{X} + E_{Slab}^{Y} - nE_{\text{bulk}}\right) \quad . \tag{2.73}$$

Diese kann direkt mit der Oberflächenenergie des defektiven Modells verglichen werden, um zu entscheiden, welcher Ansatz vorteilhaft ist.

2.8. Hochtemperaturelektrolyse

Das übergeordnete Thema dieser Arbeit ist die Eignung von $CaMnO_3$ und anderen nachhaltigen Perovskiten als Katalysator für die thermische Sauerstoffentwicklungsreaktion (OER). Für die Hochtemperaturelektrolyse sind die SOEC (*engl.* solid oxid electrolysis cell)[90] und die PCEC (*engl.* proton ceramic electrolysis cell)[16] zwei konkurrierende Technologien, welche in Abbildung 2.1 schematisch dargestellt sind.

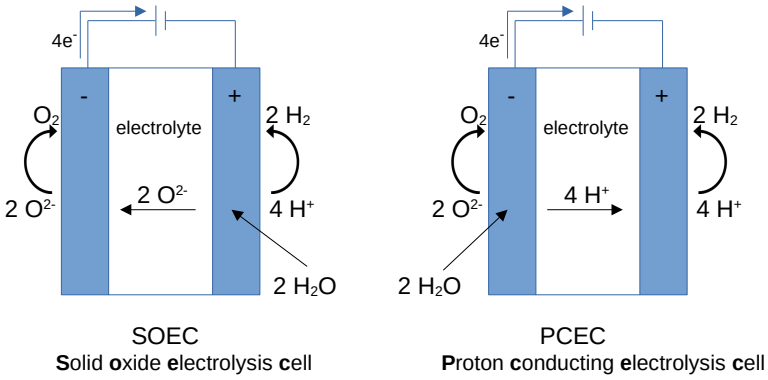

Abbildung 2.1.: Unterschied zwischen SOEC und PCEC

Bei der SOEC wird Wasser an der Kathode adsorbiert und an der Kathode entsteht Wasserstoff. Die Oxidionen wandern dann von der Kathode zur Anode und werden dort zu Sauerstoff oxidiert. Bei der PCEC wird Wasser an der Anode adsorbiert, an welcher Sauerstoff entsteht (OER). Die Protonen wandern von der Anode zur Kathode, um dort zu Wasserstoff reduziert zu werden. Der Vorteil der PCEC ist, dass allgemein die Wanderungsbarrieren der Protonen kleiner sind als die der Oxidionen, weshalb niedrigere Temperaturen erforderlich sind [16]. Des Weiteren wird trockener Wasserstoff hergestellt, weil Wasser und Wasserstoff getrennt sind. Die Herausforderung für die PCEC ist es, geeignete Elektrodenmaterialien mit ausreichend kleinen Protonenwanderungsbarrieren zu finden. Perovskite sind aufgrund ihrer Langzeitstabilität und der reversiblen OER abhängig von der Temperatur vielversprechende Anodenmaterialien für die PCEC. In dieser Arbeit beginnt die Suche beim Perovskit $CaMnO_3$, welches bei verhältnismäßig kleinen Temperaturen Sauerstoffdefekte bildet [25].
Da im Rahmen der OER die Sauerstoffdefekte reversibel und temperaturabhängig gebildet werden, lässt sich das elektrische Potential der Elektrolyse mit dem chemischen Potential der Anode kombinieren. Erhöht man die Temperatur, werden spontan Defekte über Gleichung (2.76) gebildet.

$$\begin{aligned} &\text{Gesamtreaktion:} && CaMnO_3 && \rightarrow CaMnO_{3-\delta} + \tfrac{\delta}{2}\, O_2 \\ &\text{Reduktion:} && 2\, Mn^{4+} + 2\, e^- && \rightarrow 2\, Mn^{3+} \\ &\text{Oxidation:} && O^{2-} && \rightarrow \tfrac{1}{2}\, O_2 + 2\, e^- \end{aligned} \tag{2.74}$$

Sobald genug Sauerstoffdefekte vorhanden sind, wird die Anodenregion nicht weiter erhitzt und abkühlen gelassen. Da die Defektkonzentration nun größer als die Gleichgewichtskonzentration ist, ist die Adsorption von Wasser auf die Defektpositionen begünstigt (Gleichung 2.75).

$$CaMnO_{3-\delta} + \delta H_2O \rightarrow CaMnO_3H_{2\delta} \tag{2.75}$$

Auch wenn diese Reaktion durch die Abkühlung zusätzlich begünstigt wird, ist es wichtig, dass die Hydratationsenergien der defekten Struktur negativ sind. Die Protonen wandern nun durch die Anode durch den Elektrolyten zur Kathode. Die Elektrodenreaktionen, welche die anzulegende Spannung bestimmen, sind

$$\begin{aligned} &\text{Anode :} && 2\, Mn^{3+} && \rightarrow 2\, Mn^{4+} + 2\, e^- \\ &\text{Kathode :} && 2\, H^+ + 2\, e^- && \rightarrow H_2 \quad . \end{aligned} \tag{2.76}$$

Im Folgenden wird zunächst im Rahmen eines Methodentests eine quantenchemische Methode gesucht, welche die experimentellen Werte für die Defektbildungsenthalpien und Defektbildungsentropien der OER von $CaMnO_3$ am besten reproduziert. Anschließend wird der Effekt von Kationensubstitution auf die OER untersucht. Die Betrachtung der Defektbildungsthermodynamik wird erweitert durch die Berechnung aller möglichen ABO_3-Perovskite aus den häufig und kostengünstig verfügbaren Elementen A=Mg,Ca,Sr und B=Ti,V,Cr,Mn,Fe und die Suche eines geeigneten Mischperovskits, welches Defekte in dem für die PCEC gesuchten Temperaturbereich bildet. Als Nächstes werden Protonenwanderungsbarrieren und Hydratationsenergien im Festkörper berechnet, um die Protonenleitfähigkeit sicherzustellen. Als letztes wird ein geeigneter Protonenwanderungsweg von der Oberfläche in den Festkörper berechnet.

3. Oxygen defect Formation Thermodynamics of $CaMnO_3$: A closer look

Benjamin Grimm[†] und Thomas Bredow[*]

Eingereicht am 07.09.2022, Akzeptiert am 20.09.2022, Online veröffentlicht am 29.09.2022

Oxygen defect Formation Thermodynamics of $CaMnO_3$: A closer look, Phys. Status Solidi B, 2023, 260, 2200427. DOI: https://doi.org/10.1002/pssb.202200427

Meine individuellen Beiträge: Ich habe alle Rechnungen für den Artikel selber durchgeführt sowie den Artikel selber verfasst. Thomas Bredow hat mich bei dem strategischen Vorgehen der Forschung beraten sowie den Artikel zur Korrektur gelesen.

[†]Address: Mulliken Center for Theoretical Chemistry, Clausius-Institut für Physikalische und Theoretische Chemie, University of Bonn, Beringstr. 4, 53115 Bonn, Germany.
Email Address: grimm@thch.uni-bonn.de

[*]Address: Mulliken Center for Theoretical Chemistry, Clausius-Institut für Physikalische und Theoretische Chemie, University of Bonn, Beringstr. 4, 53115 Bonn, Germany.
Email Address: bredow@thch.uni-bonn.de

[‡]Anfragen zur Genehmigung der Wiederverwendung von Material aus diesem Kapitel sollten an die Wiley-VCH GmbH gerichtet werden

Als Methodentest werden die Gitterparameter, Bandlücken, Reaktionsenthalpien und Magnetisierungen für perfektes $CaMnO_3$ für eine Auswahl an Funktionalen mit den Programmen VASP und CRYSTAL berechnet und mit dem Experiment verglichen. Mit VASP wurden die Standard-GGA-Funktionale PBE [37] und PBEsol [38] sowie die metaGGA-Funktionale SCAN [39] und r^{2}SCAN [40] verwendet. Alle Funktionale wurden mit und ohne DFT+U-Korrektur nach Dudarev [91] verwendet. In CRYSTAL wurden das Standard-GGA-Funktional PBE und die globalen und reichweitenseparierten Hybridfunktionale PW1PW [51], HSE06 [52], PBE0 [53], M06 [54], B1WC [55], B3PW [56, 57] und B3LYP [56, 58] verwendet. Zusammenfassend kann der $CaMnO_3$-Festkörper am besten mit den Hybridfunktionalen B3PW, PW1PW, HSE06 und M06 beschrieben werden.
Als zweiter Teil des Methodentests wird die Thermodynamik der OER von $CaMnO_3$ genauer betrachtet. Dafür werden zwei Sauerstoffdefekte in einer 2×2×2 Superzelle mit 80 Atomen generiert. Um alle möglichen Defektkonfigurationen zu erfassen, wird das Keyword CONFCOUNT in CRYSTAL verwendet. Von den insgesamt 2256 Möglichkeiten der Anordnung von zwei Defekten in der Superzelle (mit 48 Sauerstoffatomen) verbleiben 50 symmetrieinäquivalente Konfigurationen. Aus den berechneten Energien und den Multiplizitäten der Konfigurationen wurde dann, wie in Kapitel 2.5.2 beschrieben, die Konfigurationsentropie berechnet. Des Weiteren wurden für die Strukturen der stabilsten Konfigurationen Frequenzrechnungen durchgeführt, um die Gibbs-Energie der Defektformation zu berechnen (siehe Kapitel 2.5.1). Die Frequenzrechnungen wurden mit dem PBE-Funktional in CRYSTAL durchgeführt, da die thermodynamischen Korrekturen ($\Delta_{\text{therm}} = \Delta_r G - \Delta_r E$) für das PBE GGA-Funktional und das PW1PW-Hybridfunktional nur geringe Abweichungen aufweisen, und das GGA-Funktional einen erheblich niedrigeren Rechenaufwand verlangt. Die Defektbildungsenergien wurden nun mit allen verwendeten Funktionalen berechnet und die Enthalpien und Entropien aus den thermodynamischen Korrekturen erhalten, welche nun direkt mit dem Experiment verglichen werden können. Insgesamt kann das Hybrid-Funktional PW1PW die experimentelle Defektbildungsenthalpie bei 1273 K am genauesten reproduzieren, mit einer absoluten Abweichung von -10.8 kJ mol^{-1}. Die berechneten Defektbildungsentropien weichen nur um 3.7 J K^{-1} mol^{-1} vom Experiment ab, wobei die Konfigurationsentropie einen signifikanten Anteil von 15.3 % der Gesamtentropie ausmacht. Insgesamt weicht die berechnete Gibb-

senergie für PW1PW-Energien kombiniert mit PBE-Frequenzen um -6 kJ mol^{-1} vom Experiment ab.

Im finalen Teil dieses Artikels werden aus den PW1PW-Energien und den PBE-Frequenzen Phasendiagramme berechnet. Zunächst wird die Gibbs-Energie von Defektbildung und Dekomposition von $CaMnO_3$ in $CaMn_2O_4$ und Ca_2MnO_4 in Abhängigkeit vom Druck bei 1273 K berechnet. Dabei konnte der experimentelle Gleichgewichtsdruck zwischen defektem und perfektem $CaMnO_3$ von 10^{-2} bis 10^{-1} bar [92] reproduziert werden. Abschließend wurde die Gibbs-Energie der OER für verschiedene Temperaturen berechnet, um die Gleichgewichtstemperatur, ab welcher Defekte gebildet werden, zu erhalten. Hierbei wurde eine Gleichgewichtstemperatur von 1351 K bei p_{O_2}= 1 bar erhalten, was eine nahezu quantitative Übereinstimmung mit dem experimentellen Wert von 1368 K [92] darstellt.

Dieser Artikel empfiehlt als Ergebnis eines umfangreichen Methodentests PW1PW als bestes Funktional, um Sauerstoffdefektbildungsenergien und Gibbs-Energien in Kombination mit PBE-Frequenzen zu berechnen. Dies bietet für den weiteren Verlauf der Arbeit die Möglichkeit, den Einfluss von Substitution auf die Gibbs-Energie der Defektbildung zu überprüfen. Ziel ist es auf Basis der gefundenen Methode, ein Perovskit mit einer möglichst kleinen OER-Defektbildungsenergie zu finden, welches im relevanten Temperaturbereich keine Dekomposition aufweist und idealerweise nur häufig verfügbare und kostengünstige Elemente enthält.

4. Partial substitution of the Mn atoms in $CaMnO_3$ by first row transition metal atoms: Effect on oxygen vacancy formation

Benjamin Grimm[†] und Thomas Bredow[*]

Eingereicht am 24.02.2022, Akzeptiert am 18.03.2022, Online veröffentlicht am 27.04.2022

Der Artikel wird im Einverständnis[‡] der Autoren Benjamin Grimm und Thomas Bredow im Appendix B wieder veröffentlicht.

Partial substitution of the Mn atoms in $CaMnO_3$ by first row transition metal atoms: Effect on oxygen vacancy formation, Zeitschrift für Naturforschung B, 2022, 77(6), 405-410. DOI: https://doi.org/10.1515/znb-2022-0025

Meine individuellen Beiträge: Ich habe alle Rechnungen für den Artikel selber durchgeführt sowie den Artikel selber verfasst. Thomas Bredow hat mich bei dem strategischen Vorgehen der Forschung beraten sowie den Artikel zur Korrektur gelesen.

[†]Address: Mulliken Center for Theoretical Chemistry, Clausius-Institut für Physikalische und Theoretische Chemie, University of Bonn, Beringstr. 4, 53115 Bonn, Germany.
Email Address: grimm@thch.uni-bonn.de

[*]Address: Mulliken Center for Theoretical Chemistry, Clausius-Institut für Physikalische und Theoretische Chemie, University of Bonn, Beringstr. 4, 53115 Bonn, Germany.
Email Address: bredow@thch.uni-bonn.de

[‡]Anfragen zur Genehmigung der Wiederverwendung von Material aus diesem Kapitel sollten an die Walter de Gruyter GmbH gerichtet werden

Es wird der Einfluss der Mn-Substitution in $CaMnO_3$ mit den 3*d*-Metallen M=Sc,Ti,V,Cr,Fe,Co,Ni,Cu und Zn auf die OER untersucht. Ausgegangen wurde von einer $CaMnO_3$-Superzelle mit 80 Atomen, bestehend aus vier primitiven Einheitszellen. Zunächst wurden zwei Mn-Atome mit M substituiert, wobei M aus der 3d-Reihe Sc-Zn ist, was der Summenformel $CaMn_{0.75}M_{0.25}O$ entspricht. Es werden alle symmetrieinäquivalenten Konfigurationen berechnet und von diesen die energetisch niedrigste für weitere Rechnungen verwendet. Alle Rechnungen wurden mit dem Hybdridfunktional PW1PW durchgeführt, welches die besten Ergebnisse im Methodentest für $CaMnO_3$ lieferte (Kapitel 3)

Zunächst werden die Magnetisierungen der verschiedenen Elemente (Mn, M und O) für alle Verbindungen verglichen. Die 3d-Metalle mit einem stabilen (+4)-Zustand (Ti,V,Cr) zeigen erwartungsgemäß Magnetisierungen von nahezu null, eins und zwei. Für Fe, Co und Cu werden signifikante Magnetisierungen der Sauerstoffatome beobachtet, was auf die Oxidation von O^{2-}-Ionen hinweist an Stelle der Bildung von instabilen (+4)-Zuständen. Bei Ni wird ein (+4) low spin-Zustand gebildet. Zn liegt erwartungsgemäß im (+2)-Zustand vor, was formal durch die Oxidation von vier O^{2-}-Ionen zu O^{-} kompensiert wird. Sc liegt ebenfalls im stabilen (+3)-Zustand vor, kompensiert durch die formale Oxidation dreier O^{2-}-Ionen zu O^{-}.

Anschließend werden OER-Defektbildungsenergien für die schrittweise Erzeugung von Sauerstofffehlstellen in $CaMn_{0.75}M_{0.25}O_3$-Verbindungen berechnet. Die OER-Defektbildungsenergie $\Delta_{OVF}E_{\delta=0\rightarrow0.125}$ wird für M = Ti, V und Cr größer als bei $CaMnO_3$, während sie für alle anderen Metalle kleiner wird. Dies war zu erwarten, da die anderen Metalle alle stabile (+2) oder (+3) Zustände haben, welche die Sauerstoffdefektbildung begünstigen. Für M=Zn ist $\Delta_{OVF}E_{\delta=0\rightarrow0.125}$ sogar negativ, was belegt, dass $CaMn_{0.75}Zn_{0.25}O_3$ unter Standardbedingungen nicht vorliegt. Für M = Sc, Cu werden sehr kleine $\Delta_{OVF}E_{\delta=0\rightarrow0.125}$ erhalten (27 und 32 kJ mol^{-1}) was für eine geringe Stabilität von $CaMn_{0.75}Sc_{0.25}O_3$ und $CaMn_{0.75}Cu_{0.25}O_3$ spricht. Dies kann durch die Instabilität der Sc und Cu (+4)-Zustände erklärt werden. Die Energie der zweiten Stufe der OER-Defektbildung $\Delta_{OVF}E_{\delta=0.125\rightarrow0.25}$ ist für fast alle Verbindungen (außer M=Mn) deutlich größer als die erste Stufe $\Delta_{OVF}E_{\delta=0\rightarrow0.125}$.

Final wurden die Gleichgewichtstemperaturen T_{eq} der Stufen $\delta = 0 \rightarrow 0.125$ und

$\delta = 0.125 \rightarrow 0.25$ für alle Verbindungen ermittelt. Näherungsweise wurde T_{eq} aus Enthalpie und Entropie über $T_{eq} = \frac{\Delta_{OVF}H}{\Delta_{OVF}S}$ berechnet. Für M=Zn liegt die Defektstruktur mit $\delta = 0.125$ bereits bei 0 K vor, während für M=Sc und M=Cu die ersten Defektbildungsstufen bei 322 K und 278 K erreicht werden. Für M=Fe, Co und Ni werden ebenfalls vergleichsweise geringe T_{eq} für die erste Defektbildungsstufe erhalten (727 K, 464 K und 684 K). Für $CaMnO_3$ liegt T_{eq} für $\delta = 0 \rightarrow 0.125$ bei 1350 K und für M=Ti,V und Cr werden größere Werte erhalten (T_{eq}=1508 K, 1493 K und 1459 K). Die zweite Stufe $\delta = 0.125 \rightarrow 0.25$ zeigt für M=Mn eine geringere T_{eq} als für die erste Stufe, für M=Cu und Ni 260 und 306 K größere T_{eq} und für alle anderen M deutlich größere T_{eq}.

Dieser Artikel zeigt, dass die OER-Defektbildungsenergie von $CaMnO_3$ durch Substitution mit 3d-Metallen signifikant reduziert werden kann. Dies ist für alle 3d-Metalle der Fall, bei denen der (+3)-Zustand stabiler als der (+4)-Zustand ist. Für Substitution von Mn mit M=Fe, Co, und Ni werden bereits zwischen 464 K und 727 K Sauerstoffdefekte gebildet, was deutlich niedriger als 1350 K für unsubstituiertes $CaMnO_3$ ist. Außerdem können durch Substitution mit M=Sc, Cu bereits bei Raumtemperatur Sauerstoffdefekte gebildet werden. Der Extremfall der Substitution mit M=Zn weist eine negative Defektbildungsenergie auf, weshalb das perfekte Perovskit nicht stabil ist. Dementsprechend ist es die Herausforderung für den weiteren Verlauf dieser Arbeit, Materialien mit möglichst geringen OER-Sauerstoffdefektbildungsenergien, aber unter Erhaltung der Stabilität zu finden.

5. Defect formation thermodynamics of (A,A')(B,B')O_3 (A=Mg,Ca,Sr and B=Ti,Mn,Cr,Fe,Mo) perovskites

Benjamin Grimm[†] und Thomas Bredow[*]

Eingereicht am 02.02.2023, Akzeptiert am 08.03.2023, Online veröffentlicht am 22.03.2023

Der Artikel wird im Einverständnis[‡] der Autoren Benjamin Grimm und Thomas Bredow im Appendix C wieder veröffentlicht.

Defect formation thermodynamics of (A,A')(B,B')O_3 (A=Mg,Ca,Sr and B=Ti,Mn,Cr,Fe,Mo) perovskites, Phys. Status Solidi B, 2023, 260, 202300048. DOI: https://doi.org/10.1002/pssb.202300048

Meine individuellen Beiträge: Ich habe alle Rechnungen für den Artikel selber durchgeführt sowie den Artikel selber verfasst. Thomas Bredow hat mich bei dem strategischen Vorgehen der Forschung beraten sowie den Artikel zur Korrektur gelesen.

[†]Address: Mulliken Center for Theoretical Chemistry, Clausius-Institut für Physikalische und Theoretische Chemie, University of Bonn, Beringstr. 4, 53115 Bonn, Germany.
Email Address: grimm@thch.uni-bonn.de

[*]Address: Mulliken Center for Theoretical Chemistry, Clausius-Institut für Physikalische und Theoretische Chemie, University of Bonn, Beringstr. 4, 53115 Bonn, Germany.
Email Address: bredow@thch.uni-bonn.de

[‡]Anfragen zur Genehmigung der Wiederverwendung von Material aus diesem Kapitel sollten an die Wiley-VCH GmbH gerichtet werden

Es werden alle Perovskite (A,A')(B,B')O_3 der häufig und kostengünstig verfügbaren Elemente A=Mg,Ca,Sr und B=Ti,Mn,Cr,Fe,Mo mit dem Hybrid-Funktional PW1PW betrachtet. Zunächst wird die stabilste Raumgruppe für alle Verbindungen ermittelt. Hierzu werden alle Raumgruppen für ABO_3-Verbindungen dieser Elemente aus der Materials Project-Datenbank [93] einbezogen. Für alle Raumgruppen wird anhand der relativen Energien die Stabilste bestimmt und mit dem Experiment verglichen. Für die meisten Perovskite stimmt die energetisch niedrigste Raumgruppe mit dem Experiment überein. Teilweise werden jedoch ähnliche oder leicht niedrigere Energien für Raumgruppen niedrigerer Symmetrie erhalten.

Für die stabilsten Polymorphe aller Verbindungen werden die OER-Defektbildungsenergien von $ABO_{3-\delta}$ (für $\delta = 0 \rightarrow 0.0625$) und die Energien der Dekomposition in AB_2O_4 und A_2BO_4 berechnet. Nur für B=Fe wird eine geringere Defektbildungsenergie im Vergleich zu B=Mn erhalten. Für die Metalle A=Mg,Ca,Sr werden für Ca und Sr ähnliche Werte für die Defektbildungsenergien erhalten. Die Dekompositionsenergien werden allgemein für Fe kleiner als für Mn sowie für Sr größer als für Ca.

Gesucht ist die optimale Kombination einer möglichst kleinen OER-Defektbildungsenergie und einer möglichst großen Dekompositionsenergie. Dafür werden verschiedene Mischperovskite (A,A')(B,B')O_3 mit A,A'=Ca,Sr und B,B'=Mn,Fe berechnet, um die optimale Verbindung zu finden.

Zunächst werden die Mischungsenergien für alle Mischperovskite berechnet. Dabei wird neben der elektronischen Energie des Mischperovskits auch die Konfigurationsentropie bei 800 K berechnet, um die freie Mischungsenthalpie $\Delta G_{\mathrm{mix}}^{\mathrm{approx}}$ zu approximieren. Insgesamt werden dabei sechs verschiedene Mischperovskite mit $\Delta G_{\mathrm{mix}}^{approx} < -1$ kJ mol^{-1} erhalten. Für diese sechs Mischperovskite werden dann die ersten beiden OER-Defektbildungsenergien der $Ca_xSr_{1-x}Mn_yFe_{1-y}O_{3-\delta}$ ($\delta = 0 \rightarrow 0.0625$ und $\delta = 0.0625 \rightarrow 0.125$) sowie die Dekompositionsenergie berechnet. Dabei zeigt die Verbindung $Ca_{0.5}Sr_{0.5}Fe_{0.25}Mn_{0.75}O_3$ mit den ersten beiden Defektbildungsenergien von 78.0 und 79.9 kJ mol^{-1} sowie einer Dekompositionsenergie von 606.5 kJ mol^{-1} die vielversprechendste Kombination aus niedrigen Defektbildungsenergien und hohen Dekompositionsenergien.

Für $\delta = 0.0625 \rightarrow 0.125$ wird dann das Phasendiagramm berechnet, indem Frequenzrechnungen für die Strukturen mit 1 bis 3 Sauerstoffdefekten ($\delta = 0.0625$,$\delta = 0.125$,$\delta = 0.1875$), sowie die entsprechenden für die freien Dekompositionsenthalpien benötigten AB_2O_4- und A_2BO_4-Strukturen, durchgeführt werden. Das Phasendiagramm zeigt, dass die Defektbildung bereits bei 520 K auftritt, was eine deutlich kleinere Temperatur als die 1350 K für $CaMnO_3$ ist. Dekomposition tritt im gesamten betrachteten Temperaturbereich nicht auf.

In dem Artikel kann gezeigt werden, dass Mischperovskite (A,A')(B,B')O_3 mit A,A'=Ca,Sr und B,B'=Mn,Fe eine vielversprechende Kombination aus kleinen Defektbildungsenergien und großen Dekompositionsenergien aufweisen. Die Verbindung $Ca_{0.5}Sr_{0.5}Fe_{0.25}Mn_{0.75}O_3$ erfüllt diese Anforderungen dabei am besten mit Defekbildungsenergien von 78.0 und 79.9 kJ mol^{-1} sowie einer Dekompositionsenergie von 606.5 kJ mol^{-1}. Das Phasendiagramm sagt eine Defektbildung bereits bei 520 K voraus und schließt eine Dekomposition bei bei für die Anwendung relevanten Temperaturen aus. Damit sind bereits zwei wichtige Kriterien für einen Einsatz als PCEC-Material erfüllt.

6. Effect of surface energetics on phase stability of $CaMnO_3$

Benjamin Grimm[†] und Thomas Bredow[*]

Eingereicht am 20.01.2023, Akzeptiert am 05.05.2023, Online veröffentlicht am 21.05.2023

Der Artikel wird im Einverständnis[‡] der Autoren Benjamin Grimm und Thomas Bredow im Appendix D wieder veröffentlicht.

Effect of surface energetics on phase stability of $CaMnO_3$, Phys. Status Solidi B, 2023, 260, 2300031. DOI: https://doi.org/10.1002/pssb.202300031

Meine individuellen Beiträge: Ich habe alle Rechnungen für den Artikel selber durchgeführt sowie den Artikel selber verfasst. Thomas Bredow hat mich bei dem strategischen Vorgehen der Forschung beraten sowie den Artikel zur Korrektur gelesen.

[†]Address: Mulliken Center for Theoretical Chemistry, Clausius-Institut für Physikalische und Theoretische Chemie, University of Bonn, Beringstr. 4, 53115 Bonn, Germany.
Email Address: grimm@thch.uni-bonn.de

[*]Address: Mulliken Center for Theoretical Chemistry, Clausius-Institut für Physikalische und Theoretische Chemie, University of Bonn, Beringstr. 4, 53115 Bonn, Germany.
Email Address: bredow@thch.uni-bonn.de

[‡]Anfragen zur Genehmigung der Wiederverwendung von Material aus diesem Kapitel sollten an die Wiley-VCH GmbH gerichtet werden

In diesem Artikel werden die Oberflächenmodelle zweier orthorhombischer Polymorphe (Raumgruppen Nr. 62 und Nr. 20) von $CaMnO_3$ berechnet. Das Polymorph mit RG 62 ist die experimentelle Tieftemperaturphase, während das Polymorph mit RG 20 mit dem Hybridfunktional PW1PW als genauso stabil bestimmt wurde (Kapitel 5). Es wurden für beide Polymorphe Oberflächenmodelle für die (100), (010), (001), (101), (011) und (110)-Oberflächen erstellt.

Zunächst werden die Oberflächen des Polymorphs mit RG 62 berechnet. Für die (100)- und die (010)- Oberfläche liegen die Ca- und Mn-Atome in derselben Ebene, weshalb keine verschiedenen Terminierungen zu unterscheiden sind. Des Weiteren sind die beiden Oberflächenmodelle stöchiometrisch. Alle Schichten bestehen aus $Ca_2Mn_2O_6$-Einheiten. Diese beiden Oberflächen haben die kleinsten Oberflächenenergien (1.306 und 1.312 Jm^{-2}). In diesen Fällen muss nur eine Metall-Sauerstoff-Bindung gebrochen werden, was anhand der Koordinationszahlen im Vergleich zum Bulk (ΔC_{M-O}=-1.408 und -0.999) zu sehen ist.

In allen anderen Fällen sind Ca- und Mn-terminierte Modelle möglich, welche jeweils berechnet und verglichen werden. Des Weiteren sind diese Oberflächenmodelle nicht stöchiometrisch. Wie in Kapitel 2.7 beschrieben, werden defektive und nicht-stöchiometrische Modelle berechnet und bezüglich ihrer Oberflächenenergie (defektive Modelle) und ihrer gemittelten Oberflächenenergie beider Terminierungen (nicht-stöchiometrische Modelle) verglichen. Für die (010)-Oberfläche liegen stabile nicht-stöchiometrische Modelle mit einer gemittelten Oberflächenenergie von 1.506 Jm^{-2} vor, was deutlich stabiler als die Oberflächenenergien 2.249 Jm^{-2} und 2.000 Jm^{-2} der Ca- und Mn-terminierten defektiven Modelle ist. Für die (101)-Oberfläche ist das Mn-terminierte defektive Modell am stabilsten mit einer Oberflächenenergie von 1.359 Jm^{-2}, was stabiler als die gemittelte Oberflächenenergie der nicht-stöchiometrischen Modelle (1.546 Jm^{-2}) und die Oberflächenenergie des Ca-terminierten defektiven Modells (2.170 J/m^2) ist. Für die (011)- und die (110)-Oberfläche ist jeweils das Ca-terminierte defektive Modell am stabilsten, mit Oberflächenenergien von 1.733 und 1.986 Jm^{-2}. Mit dem Gibbs-Wulff-Theorem wird der Anteil der Oberflächen an der Gesamtoberfläche des Einkristalls aus den Oberflächenenergien der stabilsten Modelle berechnet. Den größten Anteil hat die (101)-Oberfläche (30.5 %), gefolgt von der (010)-Oberfläche (27.0 %), der (100)-Oberfläche (20.1 %), der (001)-Oberfläche (14.9 %) und der (011)-Oberfläche (7.5 %). Die (110)-Oberfläche

hat keinen Anteil an der Gesamtoberfläche.

Analog wurden die Oberflächenenergien und Anteile an der Gesamtoberfläche auch für das Polymorph mit RG 20 berechnet. Die Oberflächenenergien sind hier im Allgemeinen kleiner (1.029 bis 1.457 Jm^{-2} für alle relevanten Oberflächen), mit der Ausnahme der instabilen (001)-Oberfläche (2.113 Jm^{-2}). Daher liegt es nahe, dass bei kleinerer Partikelgröße die Raumgruppe 20 gegenüber der experimentell beobachteten Raumgruppe 62 bevorzugt ist. Aus den Oberflächenenergien und der experimentellen spezifischen Oberfläche (A_{sp}=11.04 m^2g^{-1}) [94] wurde die relative Stabilität der Oberflächen der Polymorphe in Abhängigkeit von der Partikelgröße berechnet. Dabei konnte gezeigt werden, dass für Nanopartikel mit Durchmesser von unter 10 nm das Polymorph mit RG 20 deutlich begünstigt ist. Die Bevorzugung dieser Struktur für Nanopartikel wurde bereits experimentell für $SrMnO_3$ gefunden [95], ist aber für $CaMnO_3$ eine komplett neue Erkenntnis. In diesem Artikel kann gezeigt werden, welche Oberflächen zweier stabiler Polymorphe von $CaMnO_3$ am stabilsten sind und welchen Anteil sie an der Gesamtoberfläche haben. Für die experimentelle Struktur haben die (101)-Oberfläche, die (100)-Oberfläche und die (010)-Oberfläche zusammen einen Anteil von 78 % an der Gesamtoberfläche, während sich die Oberfläche der theoretisch bestimmten Struktur mit RG20 zu 85 % aus der (110)- der (011)- und der (010)-Oberfläche zusammensetzt. Die Kenntnis der relevanten Oberflächen ist essentiell für die Berechnung der katalytischen Aktivität des Materials, da die für die PCEC relevanten Prozesse an der Oberfläche stattfinden. Während sich das nächste Kapitel mit der Protonenmigration im Festkörper befasst, wird final der Wanderungsweg der Protonen von der Oberfläche in den Festkörper untersucht, wobei die hier gewonnenen Erkentnisse über die stabilsten Oberflächen benötigt werden.

7. Revisiting $CaMnO_3$ as a Proton Conductor - A Theoretical Perspective

Benjamin Grimm[†] und Thomas Bredow[*]

Eingereicht am 17.11.2023 bei J. Phys. Chem. C, Akzeptiert am 13.03.2024 , Online veröffentlicht am 25.03.2024

Der Artikel wird im Einverständnis [‡] der Autoren Benjamin Grimm und Thomas Bredow im Appendix E wieder veröffentlicht.

Revisiting $CaMnO_3$ as a Proton Conductor - A Theoretical Perspective , J. Phys. Chem. C, 2024. DOI: https://doi.org/10.1021/acs.jpcc.3c07594

Meine individuellen Beiträge: Ich habe alle Rechnungen für den Artikel selber durchgeführt sowie den Artikel selber verfasst. Thomas Bredow hat mich bei dem strategischen Vorgehen der Forschung beraten sowie den Artikel zur Korrektur gelesen.

[†]Address: Mulliken Center for Theoretical Chemistry, Clausius-Institut für Physikalische und Theoretische Chemie, University of Bonn, Beringstr. 4, 53115 Bonn, Germany.
Email Address: grimm@thch.uni-bonn.de

[*]Address: Mulliken Center for Theoretical Chemistry, Clausius-Institut für Physikalische und Theoretische Chemie, University of Bonn, Beringstr. 4, 53115 Bonn, Germany.
Email Address: bredow@thch.uni-bonn.de

[‡]Anfragen zur Genehmigung der Wiederverwendung von Material aus diesem Kapitel sollten an die American Chemical Society gerichtet werden

In diesem Artikel werden die Protonenwanderungsbarrieren im $CaMnO_3$-Festkörper berechnet. In einer theoretischen Studie von Bork et al. [96] wurden bereits Protonensprungbarrieren von 1.8 eV für kubisches $CaMnO_3$ berechnet, was deutlich größer als der typische Bereich für Protonenwanderungsbarrieren von Perovskite (0.25 bis 0.5 eV) [97, 98, 99, 100, 101] ist. In diesem Artikel soll diese Barriere mit unseren Methoden (CRYSTAL-PW1PW) überprüft und außerdem die Protonenleitfähigkeit von $Ca_{0.75}Sr_{0.25}Mn_{0.875}Fe_{0.125}O_3$ berechnet werden. Dafür werden zunächst die Sprung- und Rotationsbarrieren für kubisches $CaMnO_3$ berechnet. Die kubische Phase von $CaMnO_{3-\delta}$ ist nur bei über 913° C und $\delta \approx 0.5$ existent [102] weshalb diese Barrieren keine experimentelle Relevanz haben, allerdings für den Vergleich mit der Arbeit von Bork et al. benötigt werden. Für den intra-oktraedrischen Sprung wird vorwärts eine Barriere von 0.15 eV und rückwärts eine von 0.27 eV erhalten, während für den inter-oktaedrischen Sprung eine Barriere von 0.18 eV in beide Richtungen erhalten wird. Diese Werte sind im Gegensatz zu den von Bork et al. erhaltenen 1.8 eV im Bereich typischer Protonenwanderungsbarrieren in Perovskiten, weshalb ein technisches Problem in den dort publizierten Rechnungen für $CaMnO_3$ vermutet werden kann. Die PW1PW-Rotationsbarriere von 0.36 eV vorwärts und 0.24 eV rückwärts unterscheidet sich nur geringfügig von den 0.32 eV von Bork et al..

Als nächstes wird ein Protonenwanderungspfad im orthorhombischen $CaMnO_3$ (RG 62) berechnet. Dafür werden die Barrieren für einen inter-oktaedrischen Sprung, gefolgt von einer Rotation und zwei inter-okataedrischen Sprüngen berechnet. Dadurch soll gezeigt werden, dass das Proton sich über solche Sprungmechanismen durch den gesamten Festkörper bewegen kann. Die Barriere für den inter-oktaedrischen Sprung beträgt 0.20 eV in beiden Richtungen und die Barriere für die Rotation 0.35 eV vorwärts und 0.39 eV rückwärts. Die erste inter-oktaedrische Sprungbarriere beträgt 0.37 eV vorwärts und 0.28 eV rückwärts, während die zweite 0.33 eV vorwärts und 0.42 eV rückwärts beträgt. Insgesamt lässt sich also ein durchlaufender Pfad durch den orthorhombischen $CaMnO_3$-Festkörper mit Barrieren zwischen 0.20 eV und 0.42 eV finden, was die Protonenleitfähigkeit in $CaMnO_3$ belegt.

Wie in Kapitel 5 erwähnt ist Mn/Fe und Ca/Sr-Substitution notwendig, um $CaMnO_3$ als PCEC-Material einzusetzen. Dies liegt daran, dass dadurch die OER-

Defektbildungsenergie gesenkt und die Dekomposition in Ca_2MnO_4 und $CaMn_2O_4$ verhindert wird. Daher wird in der Folge überprüft, wie sich Mn/Fe und Ca/Sr-Substitution auf die Barrieren auswirkt. Die Barrieren werden für $CaMn_{0.875}Fe_{0.125}O_3$ und $Ca_{0.75}Sr_{0.25}Mn_{0.875}Fe_{0.125}O_3$ berechnet, da in diesen Verbindungen die Fremdatomanteile gering genug sind, um den Erhalt der Raumgruppe zu gewährleisten. Für beide Strukturen wurden der Fall benachbarter Fe-Atome und der Fall weit entfernter Eisenatome getrennt betrachtet. In allen Fällen bewegen sich die berechneten Barrieren zwischen 0.1 und 0.5 eV, was keine signifikante Veränderung zum unsubstituierten $CaMnO_3$ darstellt. Für die Protonenleitfähigkeit sind neben den Wanderungsbarrieren auch negative Hydratationsenergien wichtig. Die Hydratationsenergien wurden daher für orthorhombisches $CaMnO_3$ mit und ohne Substitution berechnet. Dabei zeigt sich, dass die Hydratationsenergien für unsubstituiertes $CaMnO_3$ positiv ist (40.2 bis 40.9 kJ mol^{-1}), aber durch Mn/Fe-Substitution auf -29.3 bis -83.5 kJ mol^{-1} abgesenkt wird. Ca/Sr-Substitution schwächt diesen Effekt leicht ab (Hydratationsenergien von -64.2 bis 9.9 kJ mol^{-1}).
In diesem Artikel konnte gezeigt werden, dass substituiertes $CaMnO_3$ ein guter Protonenleiter mit Wanderungsbarrieren zwischen 0.2 und 0.5 eV ist. Die Barrieren werden durch Ca/Sr und Mn/Fe-Substitution nicht signifikant verändert, allerdings ist die Substitution essentiell, um negative Hydratationsenergien zu erhalten. Mit diesen Ergebnissen ist $Ca_{0.75}Sr_{0.25}Mn_{0.875}Fe_{0.125}O_3$ bereits ein sehr vielversprechender Kandidat für ein PCEC-Material, allerdings muss noch der Protonentransport von der Oberfläche in den Festkörper sichergestellt werden. Dies ist das Thema des finalen Kapitels dieser Arbeit.

8. A theoretical study on proton migration on the $CaMnO_3$ surface

Benjamin Grimm[†] und Thomas Bredow[*]

Eingereicht am 28.03.2024 bei J. Phys. Chem. C

Meine individuellen Beiträge: Ich habe alle Rechnungen für den Artikel selber durchgeführt sowie den Artikel selber verfasst. Thomas Bredow hat mich bei dem strategischen Vorgehen der Forschung beraten sowie den Artikel zur Korrektur gelesen.

[†]Address: Mulliken Center for Theoretical Chemistry, Clausius-Institut für Physikalische und Theoretische Chemie, University of Bonn, Beringstr. 4, 53115 Bonn, Germany.
Email Address: grimm@thch.uni-bonn.de

[*]Address: Mulliken Center for Theoretical Chemistry, Clausius-Institut für Physikalische und Theoretische Chemie, University of Bonn, Beringstr. 4, 53115 Bonn, Germany.
Email Address: bredow@thch.uni-bonn.de

Für orthorhombisches $CaMnO_3$ und $CaMn_{0.75}Fe_{0.25}O_3$ wurde der Protonenwanderungsmechanismus ausgehend von der Oberfläche in den Festkörper untersucht. Dafür wurden die (100)- und die (010)-Oberflächen betrachtet, welche nach den Berechnungen in Kapitel 6 zusammen 47 % der Gesamtoberfläche ausmachen. Zuerst wurden die OER-Defektbildungsenergien und Hydratationsenergien für die ersten vier Schichten berechnet. Die (100)-Oberfläche zeigt Defektbildungsenergien zwischen 135.7 kJ mol^{-1} (erste Schicht) und 173.9 kJ mol^{-1} (oberflächenferne Schichten) sowie Hydratationsenergien zwischen -316.0 und -130.0 kJ mol^{-1}. Die (010)-Oberfläche zeigt größere Defektbildungsenergien (275.5 kJ mol^{-1} in der ersten und 179.6 kJ mol^{-1} in oberflächenfernen Schichten), weshalb die Defekte an der (100)-Oberfläche gebildet werden.

Für $CaMn_{0.75}Fe_{0.25}O_3$ werden kleinere Defektbildungsenergien als für $CaMnO_3$ erhalten(22.5 bis 134.7 kJ mol^{-1} für die (100)-Oberfläche und 94.1 bis 119.3 kJ mol^{-1} für die (010)-Oberfläche). Die Hydratationsenergien für die (100)-Oberfläche sind größer (-231.9 bis -4.6 kJ mol^{-1}), aber steigen weiterhin deutlich an. Die Hydratationsenergien für die (010)-Oberfläche (-229.9 bis -191.4 kJ mol^{-1}) zeigen allerdings einen Anstieg von nur 30 kJ mol^{-1} zwischen oberflächennahen und oberflächenfernen Schichten, was deutlich kleinere Barrieren im Protenwanderungsmechanismus im Vergleich zu $CaMnO_3$ ermöglicht. Die kleineren Defektbildungsenergien als bei $CaMnO_3$ ermöglichen die Bildung von Defekten auf der (010)-Oberfläche.

Im Folgenden wird der Protonenwanderungsweg für die unsubstituierte (100)-Oberfläche und die Mn/Fe-substituierte (010)-Oberfläche mithilfe von je drei NEB-Rechnungen berechnet. Für die unsubstituierte (100)-Oberfläche werden Barrieren von 1.12 (0.03) , 0.66 (0.19) und 0.28 (0.12) eV erhalten (Zahlen in Klammern entsprechen Barrieren in Gegenrichtung). Da die erste Barriere in Gegenrichtung nahezu Null ist, müssen die ersten beiden Barrieren zusammen überwunden werden, was einer summierten Barriere von 1.78 eV entspricht. Dieser ungünstige Wanderungsmechanismus erklärt sich durch die deutlich positiveren Hydratationsenergien in den niedrigeren Schichten. Für die (010)-Oberfläche von $CaMn_{0.75}Fe_{0.25}O_3$ werden Barrieren von 1.45 (0.25), 0.21 (0.97) und 0.46 (0.40) eV erhalten. Dieser Wanderungsmechanismus ist deutlich vorteilhafter, was durch die deutlich negativeren Hydratationsenergien der dritten und vierten Schicht im Vergleich zur zweiten Schicht zu erklären ist. Der Vergleich der relativen Energien der Wasserstoffad-

sorptionspositionen zwischen oberflächennahen und -fernen Schichten mit dem bekannten Protonenleiter $BaFeO_3$ zeigt, dass $BaFeO_3$ genauso wie $CaMnO_3$ (mit und ohne Mn/Fe-Substitution) eine Energiedifferenz von etwa 1 eV zwischen den ersten beiden Schichten aufweist. Die Überwindung der daraus resultierenden Barrieren (z.B. 1.48 eV für $CaMn_{0.75}Fe_{0.25}O_3$) ist nur bei erhöhten Temperaturen möglich. Da allerdings für den bekannten Protonenleiter $BaFeO_3$ aufgrund der ähnlichen Energiedifferenz eine ähnlich hohe Barriere zu erwarten ist, kann davon ausgegangen werden, dass dies in der Praxis kein unlösbares Problem darstellt. Beispielsweise kann der hohe Wasserdampfpartialdruck auf der Oberfläche (welcher in der PCEC auftritt [16]) die Protonenwanderung von der ersten in die zweite Schicht thermodynamisch begünstigen.

Für die (100)-Oberfläche von $CaMnO_3$ sind die relativen Energien in oberflächenfernen Schichten erheblich größer als in der zweiten, während sie in $BaFeO_3$ vergleichbar groß sind. Die (010)-Oberfläche von $CaMn_{0.75}Fe_{0.25}O_3$ zeigt in oberflächenfernen Schichten sogar kleinere relative Energien als in der zweiten, wodurch der Protonenwanderungsmechanismus sogar vorteilhafter als bei $BaFeO_3$ ist.

Dieser Artikel zeigt, dass auf der (010)-Oberfläche von $CaMn_{0.75}Fe_{0.25}O_3$ ein Protonenwanderungsmechanismus von der ersten zur vierten Schicht existiert, welcher sogar vorteilhafter als bei dem bekannten Protonenleiter $BaFeO_3$ ist. Da bereits aus dem vorherigen Kapitel bekannt ist, dass $Ca_{0.75}Sr_{0.25}Mn_{0.875}Fe_{0.125}O_3$ im Festkörper ein hervorragender Protonenleiter ist, kann also vorhergesagt werden, dass Ca/Sr und Mn/Fe substituiertes $CaMnO_3$ Protonen sowohl auf der Oberfläche als auch im Festkörper leitet. In Kombination mit den moderaten Defektbildungsenergien von etwa 100 kJ mol^{-1} sind damit die wichtigsten Kriterien für ein vielversprechendes PCEC-Anodenmaterial erfüllt.

9. Zusammenfassung und Ausblick

In dieser Arbeit wurde die Eignung verschiedener Perovskite als PCEC-Anodenmaterial theoretisch untersucht. Dafür wurden als wichtigste Kriterien die Langzeitstabilität, die Sauerstoffentwicklungsreaktion bei moderaten Temperaturen und die Protonenleitfähigkeit herangezogen. Ziel dabei war es, ein dafür besonders geeignetes Material zu finden. $CaMnO_3$ ist ein guter Ausgangspunkt für die Suche eines solchen Materials, da es bei verhältnismäßig niedrigen Temperaturen Sauerstoffdefekte bildet und ausschließlich häufige, gesundheitlich unbedenkliche und kostengünstig verfügbare Elemente enthält.
In Kapitel 3 wurde zunächst ein Methodentest für $CaMnO_3$ durchgeführt, in welchem das Funktional, welches die OER-Sauerstoffdefektbildungsenthalpien und -entropien am genausten reproduzieren kann, ermittelt wurde. Eine Kombination aus PW1PW-Energien und PBE-Schwingungsfrequenzen) konnte dabei die experimentelle Defektbildungsenthalpie bei 1273 K mit einer Abweichung von -10.8 kJ mol^{-1} reproduzieren, was die geringste Abweichung im gesamten Methodentest war. Die Defektbildungsentropie weicht nur 3.7 $JK^{-1}mol^{-1}$ vom Experiment ab, wobei die Konfigurationsentropie einen signifikanten Anteil von 15.3 % der Gesamtentropie ausmacht. Die gesamte Gibbs-Energie der Defektbildung weicht nur -6 kJ mol^{-1} vom Experiment ab. Diese akkurate Berechnung der Defektbildungsthermodynamik ermöglichte es, den experimentellen Gleichgewichtsdruck sowie die experimentelle Gleichgewichtstemperatur der Defektbildung zu reproduzieren. Dadurch ist die Berechnung aussagekräftiger Phasendiagramme möglich.
In Kapitel 4 wurde der Einfluss der Kationensubstitution auf die Sauerstoffdefektbildung in $CaMnO_3$ untersucht. Dafür wurde Mn anteilig mit den 3d-Metallen M=Sc ,Ti, V, Cr, Fe, Co, Ni, Cu und Zn substituiert. Dabei wurden für die 3d-Metalle mit stabileren (+4)-Zuständen als den (+3)-Zuständen (Ti, V, Cr) höhere OER-Defektbildungsenergien als für reines $CaMnO_3$ erzielt, wobei die Defektbildungsenergien für alle anderen Metalle kleiner wurden. Für die Elemente M=Sc, Cu, Zn sind die (+4)-Zustände nicht existent, weshalb

Sauerstoffdefekte bereits bei Raumtemperatur (Sc,Cu) oder sogar bei 0 K (Zn) gebildet werden. Dadurch resultiert eine sehr geringe Langzeitstabilität der perfekten Perovskite für diese Metalle. Als besonders vorteilhaft erwies sich die Substitution von Mn mit Fe, Co oder Ni. Eine näherungsweise Berechnung der Gleichgewichtstemperaturen der Defektbildung zeigte, dass zwischen 464 K und 727 K Sauerstoffdefekte gebildet werden, was genau im Temperaturbereich der Hochtemperaturelektrolyse liegt.

In Kapitel 5 wurden alle Perovskite (A,A')(B,B')O_3 der häufig und kostengünstig verfügbaren Elemente A=Mg,Ca,Sr und B=Ti,Mn,Cr,Fe,Mo mit dem Hybridfunktional PW1PW berechnet. Zuerst wurden für alle ABO_3-Perovskite die stabilsten Polymorphe ermittelt und für diese die Defektbildungsenergien und die Dekompositionsenergien in AB_2O_4 und A_2BO_4 berechnet. Dabei zeigte sich, dass Fe als einziges der Metalle B=Ti,Mn,Cr,Fe,Mo die Defektbildungsenergie im Vergleich zu $CaMnO_3$ verringert. Für A=Mg,Ca,Sr sind die Defektbildungsenergien ähnlich, allerdings wird mit Sr die Dekompositionsenergie im Vergleich zu Ca vergrößert, während sie mit Mg verringert wird. In der Folge wurden alle Mischperovskite (A,A')(B,B')O_3 für A=Ca,Sr und B=Mn,Fe berechnet und anhand ihrer Mischungsentropien verglichen. Unter den Mischperovskiten mit freien Mischungsenthalpien unter -1 kJ mol^{-1} zeigt die Verbindung $Ca_{0.5}Sr_{0.5}Fe_{0.25}Mn_{0.75}O_3$ die vielversprechendste Kombination aus niedrigen Defektbildungsenergien (78.0 und 79.9 kJ mol^{-1} für die ersten beiden Stufen) und einer hohen Dekompositionsenergie (600.5 kJ mol^{-1}). Das berechnete Phasendiagramm zeigte Defektbildung bereits bei 520 K, was eine signifikante Verbesserung zu den 1350 K von $CaMnO_3$ ist.

In Kapitel 6 wurden die Oberflächenmodelle von $CaMnO_3$ berechnet, um die Oberflächenenergien und Anteile an der Gesamtoberfläche aller Niedrigindexoberflächen zu erhalten. Neben dem experimentell bekannten orthorhomischen Polymorph mit der Raumgruppe Nr. 62 wurden auch für das ebenfalls orhthorhombische Polymorph mit der Raumgruppe Nr. 20, welches von den Rechnungen in Kapitel 5 als genauso stabil vorausgesagt wird, Oberflächenmodelle erstellt. Für das Polymorph mit RG 62 haben die (101)-Oberfläche (30.5 %), die (010)-Oberfläche (27 %) und die (100)-Oberfläche (20,1 %) die größten Anteile an der Gesamtoberfläche. Insgesamt sind die Oberflächenenergien des Polymorphs mit RG 20 kleiner als die der experimentell bei niedrigen und moderaten Temperaturen bestätigten Struktur mit RG 62. Da sich die Energien beider Polymorphe

im Festkörper nicht signifikant unterscheiden, wurde die relative Energie beider Polymorphe in Abhängigkeit von der Partikelgröße berechnet. Dabei konnte gezeigt werden, dass die Struktur mit RG 20 für Partikel mit einem Durchmesser unter 10 nm begünstigt ist. Dies ist bisher für $CaMnO_3$ noch nicht bekannt, allerdings zeigen Experimente für $SrMnO_3$ ebenfalls eine Bevorzugung der Raumgruppe 20 für kleine Partikel.
In Kapitel 7 wurde das Energieprofil eines Protonenwanderungswegs durch den $CaMnO_3$-Festkörper berechnet. Dafür wurden vier NEB-Rechnungen durchgeführt, welche einen zusammenhängenden Wanderungspfad mit Barrieren zwischen 0.2 und 0.5 eV berechneten. Ähnliche Barrieren wurden auch für substituiertes $CaMnO_3$ berechnet, wobei sich zeigte dass Ca/Sr- und Mn/Fe-Substitution die Barrieren nicht signifikant verändert. Zusätzlich sind für die Protonenleitfähigkeit eines Festkörpers negative Hydratationsenergien wichtig. Für $CaMnO_3$ werden positive Hydratationsenergien erhalten, allerdings können diese durch Mn/Fe-Substitution deutlich abgesenkt werden, sodass sie negativ sind (-29.3 bis -83.5 kJ/mol). Durch Ca/Sr-Substitution wird der Effekt nur leicht abgeschwächt. Die daraus resultierende Protonenleitfähigkeit für substituiertes $CaMnO_3$ ist eine sehr wichtige Erkenntnis, da diese essentiell für den Einsatz als PCEC-Material ist.
In Kapitel 8 wurde das Energieprofil eines vollständigen Protonenwanderungswegs von der Oberfläche in den Festkörper für $CaMn_{0.75}Fe_{0.25}O_3$ und $CaMnO_3$ berechnet. Die berechneten Hydratationsenergien zeigten für (010)-Oberfläche von $CaMn_{0.75}Fe_{0.25}O_3$ eine sehr kleine Differenz von 30 kJ mol^{-1} zwischen oberflächennahen und -fernen Schichten, was zu einem sehr vorteilhaften Protonenwanderungsmechanismus von der Oberfläche in den Festkörper führt. Die OER-Defektbildungsenergien sind zwar analog zu $CaMnO_3$ für die (100)-Oberfläche kleiner, allerdings wird angenommen, dass sich dieser Effekt durch verstärkte Fe/Mn-Substitution an der (010)-Oberfläche statt an der (100)-Oberfläche korrigieren lässt. Des Weiteren sind die OER-Defektbildungsenergien insgesamt deutlich kleiner als bei $CaMnO_3$, weswegen im relevanten Temperaturbereich ohnehin an beiden Oberflächen Defekte gebildet werden. Für die (010)-Oberfläche von $CaMn_{0.75}Fe_{0.25}O_3$ wird aus den NEB-Rechnungen ein vollständiger Wanderungsweg erhalten, welcher außer der Barriere zwischen erster und zweiter Schicht nur kleine Barrieren zwischen 0.2 und 0.5 eV enthält. Die Barriere von 1.45 eV zwischen den ersten beiden Schichten resultiert aus der Energiedifferenz von 1.15 eV zwischen den Wasserstoffpositionen beider Schichten. Ein

Vergleich der relativen Energien der Wasserstoffpositionen mit dem bekannten Protonenleiter $BaFeO_3$ zeigt, dass auch dort eine vergleichbar hohe Energiedifferenz zwischen den ersten beiden Schichten existiert. Insgesamt ist der Protonenwanderungsmechanismus von $CaMn_{0.75}Fe_{0.25}O_3$ aufgrund der niedrigeren relativen Energien in oberflächenfernen Schichten sogar vorteilhafter als in $BaFeO_3$.

Zusammenfassend konnte diese Arbeit zeigen, dass $CaMnO_3$ mit Ca/Sr- und Mn/Fe-Substitution ein vielversprechendes PCEC-Material ist. Die OER ist bereits ab 520 K möglich, außerdem wurde die Dekomposition in AB_2O_4 und in A_2BO_4 ausgeschlossen. Es wurden negative Hydratationsenergien sowie ein durchgehender Protonenwanderungsmechanismus im Festkörper mit kleinen Barrieren zwischen 0.2 und 0.5 eV berechnet. Der Protonenwanderungsmechanismus von der (010)-Oberfläche in den Festkörper ist sogar vorteilhafter als bei $BaFeO_3$.

Trotzdem bedarf es noch weiterer Forschung, um einen Einsatz dieses Materials endgültig zu bestätigen. Die PCEC befindet sich noch in der Entwicklungsphase. Die größten bisher auftretenden Probleme wurden von Duan et al. zusammengefasst [103]. Eines der größten Probleme sind dabei geringe Faradaysche Effizienzen, welche durch die Konkurrenzreaktion der Rückoxidiation der Sauerstoffdefekte anstatt der Hydratisierung zustande kommen. An der Grenzfläche zwischen Elektrode und Elektrolyt darf dabei der Partialdruck von O_2 im Vergleich zum Partialdruck von H_2O nicht zu groß sein. Inwiefern solche Probleme in der Praxis zwischen der $Ca_{1-x}Sr_xMn_{1-y}Fe_yO_3$-Elektrode und dem Elektrolyten auftreten, muss experimentell getestet werden. Ein weiteres Problem ist die Langzeitstabilität der Anodenmaterialien, welche durchgehend Wasserdampf ausgesetzt sind. Das von Vollestad et al. getestete Perovskit $Ba_{1-x}Gd_{0.8}La_{0.2+x}Co_2O_{6-\delta}$ lieferte beispielsweise in den ersten 65 Stunden eine exzellente Performance, welche danach durch Dekomposition komplett einbrach [104]. Auch wenn in dieser Arbeit die Dekomposition A_2BO_4 und AB_2O_4 ausgeschlossen wurde, ist eine weitreichende Betrachtung der Dekomposition bei ausreichend hohen Wasserdampf-Partialdrücken notwendig.

10. Literaturverzeichnis

[1] Williams, J. H.; DeBenedictis, A.; Ghanadan, R.; Mahone, A.; Moore, J.; Morrow III, W. R.; Price, S.; Torn, M. S. The technology path to deep greenhouse gas emissions cuts by 2050: the pivotal role of electricity. *science* **2012**, *335*, 53–59.

[2] Bennetzen, E. H.; Smith, P.; Porter, J. R. Decoupling of greenhouse gas emissions from global agricultural production: 1970–2050. *Glob. Change Biol.* **2016**, *22*, 763–781.

[3] Heal, G. Reflections—What would it take to reduce US greenhouse gas emissions 80 percent by 2050? *Rev. Environ. Econ. Policy* **2017**,

[4] IEA, I. Global hydrogen review 2021. *Public Report* **2021**,

[5] Global Energy, . Net Zero by 2050. http://thegreentimes.co.za/wp-content/uploads/2021/05/net-zero-by-2050.pdf, 2021; Accessed: 29.03.2024.

[6] Deutsche Industrie-und Handelskammern, . Wasserstoff - DIHK Faktenpapier. https://www.dihk.de/resource/blob/24872/fd2c89df9484cf912199041a9587a3d6/dihk-faktenpapier-wasserstoff-data.pdf, 2020; Accessed: 07.03.2024.

[7] Pielecha, I.; Engelmann, D.; Merkisz, J. Use of hydrogen fuel in drive systems of rail vehicles. *Rail Vehicles/Pojazdy Szynowe* **2022**, 10–19.

[8] Wildgruber, O. Hydrogen as energy source: an introduction. *Energy & Environment* **2006**, *17*, 275–279.

[9] Palo, D. R.; Dagle, R. A.; Holladay, J. D. Methanol steam reforming for hydrogen production. *Chem. Rev.* **2007**, *107*, 3992–4021.

[10] Wang, M.; Wang, Z.; Gong, X.; Guo, Z. The intensification technologies to water electrolysis for hydrogen production–A review. *Renew. Sustain. Energy Rev.* **2014**, *29*, 573–588.

[11] Scheiblehner, D.; Neuschitzer, D.; Wibner, S.; Sprung, A.; Antrekowitsch, H. Hydrogen production by methane pyrolysis in molten binary copper alloys. *Int. J. Hydrogen Energy* **2023**, *48*, 6233–6243.

[12] Brauns, J.; Turek, T. Alkaline water electrolysis powered by renewable energy: A review. *Processes* **2020**, *8*, 248.

[13] Carmo, M.; Fritz, D. L.; Mergel, J.; Stolten, D. A comprehensive review on PEM water electrolysis. *Int. J. Hydrogen Energy* **2013**, *38*, 4901–4934.

[14] Salzgitter AG, . Weltweit größter Hochtemperatur-Elektrolyseur erzielt Rekord-Wirkungsgrad. https://www.salzgitter-ag.com/de/newsroom/pressemeldungen/details/weltweit-groesster-hochtemperatur-elektrolyseur-erzielt-rekord-wirkungsgrad-19500.html, 2022; Accessed: 07.03.2024.

[15] Zhao, G.; Kraglund, M. R.; Frandsen, H. L.; Wulff, A. C.; Jensen, S. H.; Chen, M.; Graves, C. R. Life cycle assessment of H2O electrolysis technologies. *Int. J. Hydrog. Energy* **2020**, *45*, 23765–23781.

[16] Duan, C.; Huang, J.; Sullivan, N.; O'Hayre, R. Proton-conducting oxides for energy conversion and storage. *Appl. Phys. Rev.* **2020**, *7*, 011314.

[17] Rusevich, L.; Kotomin, E.; Zvejnieks, G.; Popov, A. Ab initio calculations of structural, electronic and vibrational properties of BaTiO3 and SrTiO3 perovskite crystals with oxygen vacancies. *Low Temp. Phys.* **2020**, *46*, 1185–1195.

[18] Rusevich, L. L.; Zvejnieks, G.; Kotomin, E. A.; Krzmanc, M. M.; Meden, A.; Kunej, S.; Vlaicu, I. D. Theoretical and experimental study of (Ba, Sr) TiO3 perovskite solid solutions and BaTiO3/SrTiO3 heterostructures. *J. Phys. Chem. C* **2019**, *123*, 2031–2036.

[19] Kotomin, E.; Zhukovskii, Y. F.; Piskunov, S.; Ellis, D. Hybrid DFT calculations of the F centers in cubic ABO3 perovskites. J. Phys. Conf. Ser. 2008; p 012019.

[20] Heifets, E.; Kotomin, E.; Trepakov, V. Calculations for antiferrodistortive phase of SrTiO3 perovskite: hybrid density functional study. *J. Condens. Matter Phys.* **2006**, *18*, 4845.

[21] Kotomin, E. A.; Kuzmin, A.; Purans, J.; Timoshenko, J.; Piskunov, S.; Merkle, R.; Maier, J. Theoretical and Experimental Studies of Charge Ordering in CaFeO3 and SrFeO3 Crystals. *Phys. Status Solidi B* **2022**, *259*, 2100238.

[22] Zvejnieks, G.; Zavickis, D.; Kotomin, E. A.; Gryaznov, D. BaCoO 3 monoclinic structure and chemical bonding analysis: hybrid DFT calculations. *Phys. Chem. Chem. Phys.* **2021**, *23*, 17493–17501.

[23] Rusevich, L.; Kotomin, E.; Zvejnieks, G.; Popov, A. Ab initio calculations of structural, electronic and vibrational properties of BaTiO3 and SrTiO3 perovskite crystals with oxygen vacancies. *Low Temp. Phys.* **2020**, *46*, 1185–1195.

[24] Wang, M.; Wang, C.; Liu, Y.; Zhou, X. Hybrid density functional theory description of non-metal doping in perovskite BaTiO3 for visible-light photocatalysis. *J. Solid State Chem.* **2019**, *280*, 121018.

[25] Bulfin, B.; Vieten, J.; Starr, D.; Azarpira, A.; Zachäus, C.; Hävecker, M.; Skorupska, K.; Schmücker, M.; Roeb, M.; Sattler, C. Redox chemistry of $CaMnO_3$ and $Ca_{0.8}Sr_{0.2}MnO_3$ oxygen storage perovskites. *J. Mater. Chem. A* **2017**, *5*, 7912–7919.

[26] Poetzsch, D.; Merkle, R.; Maier, J. Stoichiometry variation in materials with three mobile carriers—thermodynamics and transport kinetics exemplified for protons, oxygen vacancies, and holes. *Adv. Funct. Mater.* **2015**, *25*, 1542–1557.

[27] Merkle, R.; Hoedl, M. F.; Raimondi, G.; Zohourian, R.; Maier, J. Oxides with mixed protonic and electronic conductivity. *Annu. Rev. Mater. Res.* **2021**, *51*, 461–493.

[28] Zohourian, R.; Merkle, R.; Raimondi, G.; Maier, J. Mixed-conducting perovskites as cathode materials for protonic ceramic fuel cells: understanding the trends in proton uptake. *Adv. Funct. Mater.* **2018**, *28*, 1801241.

[29] Hoedl, M.; Chesnokov, A.; Gryaznov, D.; Merkle, R.; Kotomin, E.; Maier, J. Proton migration barriers in BaFeO 3- δ–insights from DFT calculations. *J. Mater. Chem. A* **2023**, *11*, 6336–6348.

[30] Koch, W.; Holthausen, M. C. *A chemist's guide to density functional theory*; John Wiley & Sons, 2015.

[31] Reinhold, J. *Quantentheorie der Moleküle: Eine Einführung*; Springer-Verlag, 2012.

[32] Bredow, T. *Quantum-chemical treatment of crystalline solids and their surfaces*; Vorlesungsskript, 2015.

[33] Jensen, F. *Introduction to Computational Chemistry*, 1st ed.; John Wiley & Sons: Chichester, 1999.

[34] Born, M.; Heisenberg, W. Zur quantentheorie der molekeln. *Original Scientific Papers Wissenschaftliche Originalarbeiten* **1985**, 216–246.

[35] Hohenberg, P.; Kohn, W. Inhomogeneous electron gas. *Phys. Rev.* **1964**, *136*, B864.

[36] Perdew, J. P.; Schmidt, K. Jacob's ladder of density functional approximations for the exchange-correlation energy. AIP Conference Proceedings. 2001; pp 1–20.

[37] Perdew, J. P.; Burke, K.; Ernzerhof, M. Generalized gradient approximation made simple. *Phys. Rev. Lett.* **1996**, *77*, 3865.

[38] Perdew, J. P.; Ruzsinszky, A.; Csonka, G. I.; Vydrov, O. A.; Scuseria, G. E.; Constantin, L. A.; Zhou, X.; Burke, K. Restoring the density-gradient expansion for exchange in solids and surfaces. *Phys. Rev. Lett.* **2008**, *100*, 136406.

[39] Sun, J.; Ruzsinszky, A.; Perdew, J. P. Strongly constrained and appropriately normed semilocal density functional. *Phys. Rev. Lett.* **2015**, *115*, 036402.

[40] Furness, J. W.; Kaplan, A. D.; Ning, J.; Perdew, J. P.; Sun, J. Accurate and numerically efficient r2SCAN meta-generalized gradient approximation. *J. Phys. Chem. Lett.* **2020**, *11*, 8208–8215.

[41] Anisimov, V. I.; Zaanen, J.; Andersen, O. K. Band theory and Mott insulators: Hubbard U instead of Stoner I. *Phys. Rev. B* **1991**, *44*, 943.

[42] Anisimov, V. I.; Aryasetiawan, F.; Lichtenstein, A. First-principles calculations of the electronic structure and spectra of strongly correlated systems: the LDA+ U method. *J. Phys.* **1997**, *9*, 767.

[43] Dudarev, S. L.; Botton, G. A.; Savrasov, S. Y.; Humphreys, C.; Sutton, A. P. Electron-energy-loss spectra and the structural stability of nickel oxide: An LSDA+ U study. *Phys. Rev. B* **1998**, *57*, 1505.

[44] Wang, Y.-C.; Chen, Z.-H.; Jiang, H. The local projection in the density functional theory plus U approach: A critical assessment. *J. Chem. Phys.* **2016**, *144*.

[45] Da Silva, J. L.; Ganduglia-Pirovano, M. V.; Sauer, J.; Bayer, V.; Kresse, G. Hybrid functionals applied to rare-earth oxides: The example of ceria. *Phys. Rev. B* **2007**, *75*, 045121.

[46] Meng, Y.; Liu, X.-W.; Huo, C.-F.; Guo, W.-P.; Cao, D.-B.; Peng, Q.; Dearden, A.; Gonze, X.; Yang, Y.; Wang, J., et al. When density functional approximations meet iron oxides. *J. Chem. Theory Comput.* **2016**, *12*, 5132–5144.

[47] Tran, F.; Schweifer, J.; Blaha, P.; Schwarz, K.; Novák, P. PBE+ U calculations of the Jahn-Teller effect in Pr O 2. *Phys. Rev. B* **2008**, *77*, 085123.

[48] Stahl, B.; Bredow, T. Critical assessment of the DFT+ U approach for the prediction of vanadium dioxide properties. *J. Comput. Chem.* **2020**, *41*, 258–265.

[49] Wang, Y.-C.; Jiang, H. Local screened Coulomb correction approach to strongly correlated d-electron systems. *J. Chem. Phys.* **2019**, *150*.

[50] Shishkin, M.; Sato, H. Self-consistent parametrization of DFT+ U framework using linear response approach: Application to evaluation of redox potentials of battery cathodes. *Phys. Rev. B* **2016**, *93*, 085135.

[51] Bredow, T.; Gerson, A. R. Effect of exchange and correlation on bulk properties of MgO, NiO, and CoO. *Phys. Rev. B* **2000**, *61*, 5194.

[52] Heyd, J.; Scuseria, G. E.; Ernzerhof, M. Hybrid functionals based on a screened Coulomb potential. *J. Chem. Phys.* **2003**, *118*, 8207–8215.

[53] Perdew, J. P.; Ernzerhof, M.; Burke, K. Rationale for mixing exact exchange with density functional approximations. *J. Chem. Phys.* **1996**, *105*, 9982–9985.

[54] Zhao, Y.; Truhlar, D. G. The M06 suite of density functionals for main group thermochemistry, thermochemical kinetics, noncovalent interactions, excited states, and transition elements: two new functionals and systematic testing of four M06-class functionals and 12 other functionals. *Theor. Chim. Acta* **2008**, *120*, 215–241.

[55] Bilc, D.; Orlando, R.; Shaltaf, R.; Rignanese, G.-M.; Íñiguez, J.; Ghosez, P. Hybrid exchange-correlation functional for accurate prediction of the electronic and structural properties of ferroelectric oxides. *Phys. Rev. B* **2008**, *77*, 165107.

[56] Becke, A. D. Density-functional exchange-energy approximation with correct asymptotic behavior. *Phys. Rev. A* **1988**, *38*, 3098.

[57] Perdew, J. P. Unified theory of exchange and correlation beyond the local density approximation. *Electronic structure of solids' 91* **1991**, *11*.

[58] Lee, C.; Yang, W.; Parr, R. G. Development of the Colle-Salvetti correlation-energy formula into a functional of the electron density. *Phys. Rev. B* **1988**, *37*, 785.

[59] Grimme, S.; Ehrlich, S.; Goerigk, L. Effect of the damping function in dispersion corrected density functional theory. *J. Comp. Chem.* **2011**, *32*, 1456–1465.

[60] Grimme, S.; Antony, J.; Ehrlich, S.; Krieg, H. A consistent and accurate ab initio parametrization of density functional dispersion correction (DFT-D) for the 94 elements H-Pu. *J. Chem. Phys.* **2010**, *132*.

[61] Ehrlich, S.; Moellmann, J.; Reckien, W.; Bredow, T.; Grimme, S. System-dependent dispersion coefficients for the DFT-D3 treatment of adsorption processes on ionic surfaces. *ChemPhysChem* **2011**, *12*, 3414–3420.

[62] Caldeweyher, E.; Ehlert, S.; Hansen, A.; Neugebauer, H.; Spicher, S.; Bannwarth, C.; Grimme, S. A generally applicable atomic-charge dependent London dispersion correction. *J. Chem. Phys.* **2019**, *150*, 154122.

[63] Ghosh, D. C.; Islam, N. Semiempirical evaluation of the global hardness of the atoms of 103 elements of the periodic table using the most probable radii as their size descriptors. *Int. J. Quantum Chem.* **2010**, *110*, 1206–1213.

[64] Ghasemi, S. A.; Hofstetter, A.; Saha, S.; Goedecker, S. Interatomic potentials for ionic systems with density functional accuracy based on charge densities obtained by a neural network. *Phys. Rev. B* **2015**, *92*, 045131.

[65] Dovesi, R.; Erba, A.; Orlando, R.; Zicovich-Wilson, C. M.; Civalleri, B.; Maschio, L.; Rérat, M.; Casassa, S.; Baima, J.; Salustro, S., et al. Quantum-mechanical condensed matter simulations with CRYSTAL. *Wiley Interdiscip. Rev. Comput. Mol. Sci.* **2018**, *8*, e1360.

[66] Peintinger, M. F.; Oliveira, D. V.; Bredow, T. Consistent Gaussian basis sets of triple-zeta valence with polarization quality for solid-state calculations. *J. Comp. Chem.* **2013**, *34*, 451–459.

[67] Laun, J.; Vilela Oliveira, D.; Bredow, T. Consistent gaussian basis sets of double- and triple-zeta valence with polarization quality of the fifth period for solid-state calculations. *J. Comp. Chem.* **2018**, *39*, 1285–1290.

[68] Vilela Oliveira, D.; Laun, J.; Peintinger, M. F.; Bredow, T. BSSE-correction scheme for consistent gaussian basis sets of double-and triple-zeta valence with polarization quality for solid-state calculations. *J. Comp. Chem.* **2019**, *40*, 2364–2376.

[69] Kresse, G.; Hafner, J. Ab initio molecular dynamics for liquid metals. *Phys. Rev. B* **1993**, *47*, 558.

[70] Kresse, G.; Furthmüller, J. Efficiency of ab-initio total energy calculations for metals and semiconductors using a plane-wave basis set. *Comput. Mater. Sci.* **1996**, *6*, 15–50.

[71] Kresse, G.; Furthmüller, J. Efficient iterative schemes for ab initio total-energy calculations using a plane-wave basis set. *Phys. Rev. B* **1996**, *54*, 11169.

[72] BROYDEN, C. G. The Convergence of a Class of Double-rank Minimization Algorithms 1. General Considerations. *IMA J. Appl. Math.* **1970**, *6*, 76–90.

[73] Fletcher, R. A new approach to variable metric algorithms. *Comput. J.* **1970**, *13*, 317–322.

[74] Goldfarb, D. A family of variable-metric methods derived by variational means. *Math. Comput.* **1970**, *24*, 23–26.

[75] Shanno, D. F. Conditioning of quasi-Newton methods for function minimization. *Math. Comput.* **1970**, *24*, 647–656.

[76] Liu, D. C.; Nocedal, J. On the limited memory BFGS method for large scale optimization. *Math. Program.* **1989**, *45*, 503–528.

[77] Packwood, D.; Kermode, J.; Mones, L.; Bernstein, N.; Woolley, J.; Gould, N.; Ortner, C.; Csányi, G. A universal preconditioner for simulating condensed phase materials. *J. Chem. Phys.* **2016**, *144*.

[78] Linstrom, P. J. NIST chemistry webbook. *http://webbook. nist. gov* **2005**,

[79] Pracht, P.; Grimme, S. Calculation of absolute molecular entropies and heat capacities made simple. *Chem. Sci.* **2021**, *12*, 6551–6568.

[80] Nichols, J.; Taylor, H.; Schmidt, P.; Simons, J. Walking on potential energy surfaces. *J. Chem. Phys.* **1990**, *92*, 340–346.

[81] Sheppard, D.; Terrell, R.; Henkelman, G. Nudged elastic band method for finding minimum energy paths of transitions. *J. Chem. Phys* **2008**, *128*, 134106.

[82] Henkelman, G.; Jóhannesson, G.; Jónsson, H. Methods for finding saddle points and minimum energy paths. *Theoretical methods in condensed phase chemistry* **2002**, 269–302.

[83] Jónsson, H.; Mills, G.; Jacobsen, K. W. *Classical and quantum dynamics in condensed phase simulations*; World Scientific, 1998; pp 385–404.

[84] Atomic Simulation Environment. Main ASE repo: Accessed: 2022-11-01, https://gitlab.com/ase/ase.

[85] Atomic Simulation Environment. ASE fork: Accessed: 2023-10-01, https://gitlab.com/waldlaubsaengernest/ase.

[86] Wulff, G. XXV. Zur Frage der Geschwindigkeit des Wachsthums und der Auflösung der Krystallflächen. *Zeitschrift für Kristallographie-Crystalline Materials* **1901**, *34*, 449–530.

[87] Tasker, P. W. The stability of ionic crystal surfaces. *J. Phys. C* **1979**, *12*, 4977–4984.

[88] Bottin, F.; Finocchi, F.; Noguera, C. Stability and electronic structure of the (1× 1) SrTiO 3 (110) polar surfaces by first-principles calculations. *Phys. Rev. B* **2003**, *68*, 035418.

[89] Bauerfeind, K. C. L.; Roß, R.; Bredow, T. Theoretical Study of Polar Spinel Surfaces: Effect of Termination and Cation Inversion on Structure and Stability. **2020**, *124*, 28520–28530.

[90] Hauch, A.; Küngas, R.; Blennow, P.; Hansen, A. B.; Hansen, J. B.; Mathiesen, B. V.; Mogensen, M. B. Recent advances in solid oxide cell technology for electrolysis. *Science* **2020**, *370*, eaba6118.

[91] Dudarev, S.; Peng, L.-M.; Savrasov, S.; Zuo, J.-M. Correlation effects in the ground-state charge density of Mott insulating NiO: A comparison of ab initio calculations and high-energy electron diffraction measurements. *Phys. Rev. B* **2000**, *61*, 2506.

[92] Bakken, E.; Norby, T.; Stølen, S. Nonstoichiometry and reductive decomposition of $CaMnO_{3-\delta}$. *Solid State Ion.* **2005**, *176*, 217–223.

[93] Jain, A.; Ong, S. P.; Hautier, G.; Chen, W.; Richards, W. D.; Dacek, S.; Cholia, S.; Gunter, D.; Skinner, D.; Ceder, G., et al. Commentary: The Materials Project:

A materials genome approach to accelerating materials innovation. *APL materials* **2013**, *1*, 011002.

[94] Paul, D.; Das, G. Efficient solid-state synthesis of biomineralized vaterite-derived pure CaMnO 3 perovskite for effective photocatalysis. *CrystEngComm* **2021**, *23*, 4050–4058.

[95] González-Jiménez, I. N.; Climent, E.; Torres-Pardo, A.; Hernando, M.; Sánchez-Peláez, A. E.; Fernández-Martínez, F.; Díaz, M. T. F.; González-Calbet, J. M.; de Andrés, A.; Varela, Á., et al. SrMnO3 thermochromic behavior governed by size-dependent structural distortions. *Inorg. Chem.* **2016**, *55*, 3980–3991.

[96] Bork, N.; Bonanos, N.; Rossmeisl, J.; Vegge, T. Simple descriptors for proton-conducting perovskites from density functional theory. *Phys. Rev. B* **2010**, *82*, 014103.

[97] Wang, Z.; Yang, W.; Zhu, Z.; Peng, R.; Wu, X.; Xia, C.; Lu, Y. First-principles study of O 2 reduction on BaZr 1- x Co x O 3 cathodes in protonic-solid oxide fuel cells. *J. Mater. Chem. A* **2014**, *2*, 16707–16714.

[98] Munoz-Garcia, A. B.; Pavone, M. First-principles design of new electrodes for proton-conducting solid-oxide electrochemical cells: A-site doped Sr2Fe1. 5Mo0. 5O6- δ perovskite. *Chem. Mater.* **2016**, *28*, 490–500.

[99] Xu, X.; Wang, H.; Ma, J.; Liu, W.; Wang, X.; Fronzi, M.; Bi, L. Impressive performance of proton-conducting solid oxide fuel cells using a first-generation cathode with tailored cations. *J. Mater. Chem. A* **2019**, *7*, 18792–18798.

[100] Lan, C.; Li, H.; Zhao, S. A first-principles study of the proton and oxygen migration behavior in the rare-earth perovskite SmNiO 3. *J. Comput. Electron.* **2020**, *19*, 905–909.

[101] Ding, H.; Wu, W.; Jiang, C.; Ding, Y.; Bian, W.; Hu, B.; Singh, P.; Orme, C. J.; Wang, L.; Zhang, Y., et al. Self-sustainable protonic ceramic electrochemical cells using a triple conducting electrode for hydrogen and power production. *Nat. Commun.* **2020**, *11*, 1907.

[102] Taguchi, H.; Nagao, M.; Sato, T.; Shimada, M. High-temperature phase transition of CaMnO3- δ. *J. of Solid State Chem.* **1989**, *78*, 312–315.

[103] Du, J.; Zhang, T.; Cheng, F.; Chu, W.; Wu, Z.; Chen, J. Nonstoichiometric perovskite CaMnO3- δ for oxygen electrocatalysis with high activity. *Inorg. Chem.* **2014**, *53*, 9106–9114.

[104] Vøllestad, E.; Strandbakke, R.; Tarach, M.; Catalán-Martínez, D.; Fontaine, M.-L.; Beeaff, D.; Clark, D. R.; Serra, J. M.; Norby, T. Mixed proton and electron conducting double perovskite anodes for stable and efficient tubular proton ceramic electrolysers. *Nat. Mater.* **2019**, *18*, 752–759.

A. Oxygen defect Formation Thermodynamics of $CaMnO_3$: A closer look

Benjamin Grimm[†] und Thomas Bredow[*]

Eingereicht am 07.09.2022, Akzeptiert am 20.09.2022, Online veröffentlicht am 29.09.2022

Der Artikel wird im Einverständnis[‡] der Autoren Benjamin Grimm und Thomas Bredow im Appendix A wieder veröffentlicht.

Oxygen defect Formation Thermodynamics of $CaMnO_3$: A closer look, Phys. Status Solidi B,2023,260,2200427. DOI:https://doi.org/10.1002/pssb.202200427

[†]Address: Mulliken Center for Theoretical Chemistry, Clausius-Institut für Physikalische und Theoretische Chemie, University of Bonn, Beringstr. 4, 53115 Bonn, Germany.
Email Address: grimm@thch.uni-bonn.de

[*]Address: Mulliken Center for Theoretical Chemistry, Clausius-Institut für Physikalische und Theoretische Chemie, University of Bonn, Beringstr. 4, 53115 Bonn, Germany.
Email Address: bredow@thch.uni-bonn.de

[‡]Anfragen zur Genehmigung der Wiederverwendung von Material aus diesem Kapitel sollten an die Wiley-VCH GmbH gerichtet werden

RESEARCH ARTICLE

physica status solidi b

www.pss-b.com

Oxygen Defect Formation Thermodynamics of $CaMnO_3$: A Closer Look

Benjamin Grimm and Thomas Bredow*

Sustainable hydrogen production is one of the most important topics in modern energy economics. Of technological relevance are, for example, electrochemical and thermal splitting of water. For such processes anode materials with a variable concentration of oxygen defects are required. Herein, the oxygen defect thermochemistry of a possible anode material, the perovskite $CaMnO_3$, is investigated theoretically. The aim of this work is to identify reliable quantum chemical methods for the calculation of oxygen defect formation enthalpies and entropies, including configuration entropy, which is usually neglected. All possible defect configurations in a supercell are computed to obtain the configuration entropy using Boltzmann statistics. Various generalized gradient approximation (GGA), meta-GGA, and hybrid functionals as implemented in the solid-state programs CRYSTAL and VASP are evaluated for the calculation of structure parameters, electronic and magnetic properties, and reaction energies of $CaMnO_3$. The global hybrid functional PW1PW gives the most accurate overall description of $CaMnO_3$ and is therefore recommended for future theoretical studies of more efficient water-splitting catalysts based on calcium manganate.

1. Introduction

Hydrogen is one of the most promising future energy sources.[1] In contrast to conventional energy sources, only water is produced during its combustion. At present, a large amount of hydrogen is still obtained from hydrocarbons by steam reforming.[2] However, for every two molecules of hydrogen, one molecule of carbon dioxide is also produced, therefore this process is not climate neutral. Therefore, the sustainable production of hydrogen is of primary interest for the future of the energy industry.[3] One possibility is electrolytic water splitting.[4] The problem, however, is the high demand for environmentally friendly-generated electricity, which is not yet sufficiently available. A promising alternative is solar or solar–thermal water splitting by electrolysis, thermochemistry or photocatalysis. This is not yet feasible on a large scale due to technical and economic challenges. Photocatalysis, on the other hand, does not depend on an external supply of electricity or heat, but requires special catalysts that are often too expensive or resource critical.

In this respect, the combination of chemical and electrical potentials is advantageous. If an anode material is used which is itself redox active, the potential required for electrolysis can be reduced. Perovskites ABO_3 are suitable materials due to their stability and temperature-dependent reversible loss of oxygen and high oxygen mobility in the lattice.[5,6] One of the perovskites which have recently attracted interest is $CaMnO_3$. Poeppelmeier et al. discuss the low-temperature synthesis of oxygen-deficient $CaMnO_{2.5}$ starting from polycrystalline $CaMnO_3$.[7] X-ray and neutron diffraction patterns were used to determine the crystal structure and distribution of oxygen vacancies in $CaMnO_{2.5}$. Jung et al. determined the electronic band structures of $CaMnO_3$ and $LaMnO_3$ measuring reflectivity spectra at room temperature.[8] Wollan and Koehler studied the magnetic properties of perovskite-type compounds

$[La_{(1-x)}, Ca_x]MnO_3$ uses neutron diffraction.[9] Several antiferromagnetic (AFM) spin states were found for $x = 0$ and $x \geq 0.5$. Between $x = 0$ and $x = 0.5$, they observed simultaneous occurrence of ferromagnetic and AFM structures. In a narrow range around $x = 0.35$ the structure was found to be ferromagnetic. The measured magnetic moments decrease with higher x values. Bakken et al. measured the variation of oxygen nonstoichiometry of $CaMnO_{3-\delta}$ with the oxygen partial pressure at 1223, 1273, and 1323 K.[10] The dependence of partial molar enthalpy and entropy from δ was derived. Bulfin et al. measured the equilibrium nonstoichiometry of $CaMnO_3$ and $Ca_{0.8}Sr_{0.2}MnO_3$ for temperatures in the range 400–1200 °C and different oxygen partial pressures.[11] $Ca_{0.8}Sr_{0.2}MnO_3$ showed a lower enthalpy of reduction and was also robust against phase transition, different from $CaMnO_3$ at high temperatures.

Also a number of computational studies on $CaMnO_3$ using density functional theory (DFT) have been published. Molinari et al. calculated the structural, electronic, and thermoelectric properties of orthorhombic $CaMnO_3$ and $CaMnO_{3-\delta}$ on

B. Grimm, T. Bredow
Mulliken Center for Theoretical Chemistry
Clausius-Institut für Physikalische und Theoretische Chemie
University of Bonn
Beringstr. 4, 53115 Bonn, Germany
E-mail: grimm@thch.uni-bonn.de

The ORCID identification number(s) for the author(s) of this article can be found under https://doi.org/10.1002/pssb.202200427.

DOI: 10.1002/pssb.202200427

GGA + U level (generalized gradient approximation of DFT with Hubbard correction).[12] The obtained bandgap of 1.42 eV is far from the experimental value 3.07 eV.[8] Du et al.[13] investigated the suitability of $CaMnO_3$ and $CaMnO_{3-\delta}$ as catalysts for electrochemical oxygen evolution and oxygen reduction reaction. They showed that the electrocatalytic activity is enhanced by oxygen defects. They used various DFT methods to calculate the electronic structure of $CaMnO_{3-\delta}$. The PW91 + U method was used for geometry optimization and the range-separated hybrid functional HSE06 for electronic properties. However, the obtained bandgap, 1.56 eV, is also too small. Aschauer et al. calculated oxygen vacancy formation (OVF) energies of $CaMnO_3$ with PBEsol + U ($U = 3.0$ eV) and plane waves.[14] They approximated the orthorhombic structure by a tetragonal model which was derived from the cubic calcium manganate modification, and obtained an OVF energy of 2.0 eV, which corresponds to 193 kJ mol^{-1} per O atom.

The aim of the present work is to find an optimal theoretical approach to compute the oxygen defect formation thermochemistry of $CaMnO_3$, which is also suited for the calculation of structural and electronic properties. For this benchmark study, we consider the two reference values for OVF enthalpy[15] measured by Roermark et al. For small defect concentrations, $\delta = 0.23$ in $CaMnO_{3-\delta}$, a value of 325 kJ mol^{-1} (per O_2 molecule) was reported there, corresponding to 162.5 kJ mol^{-1} or 1.68 eV per O atom. For larger defect concentrations, $\delta = 0.47$, 356 kJ mol^{-1} (per O_2 molecule) was measured, which corresponds to 178 kJ mol^{-1} or 1.84 eV per O atom. Aschauer et al. removed one O atom from a $Ca_8Mn_8O_{24}$ supercell, corresponding to $\delta = 0.125$. Therefore the low-concentration value of 162.5 kJ mol^{-1} per O atom is more appropriate as reference. Thus, the rather large deviation of the PBEsol + U value, 193 kJ mol^{-1}, from the experiment indicates that there is a need to test other methods beyond DFT + U. Furthermore, thermal contributions from lattice vibrations and the defect configuration entropy were completely neglected.

As far as the authors are aware, no method test is yet available for $CaMnO_3$ evaluating a wider range of DFT methods. For other perovskites, however, there are a large number of theoretical studies at various theoretical levels, including hybrid DFT and quantum Monte Carlo (QMC).

Rusevich et al. calculated the structural, electronic, and vibrational properties of $BaTiO_3$ and $SrTiO_3$ using CRYSTAL17 and the B1WC hybrid exchange functional.[16] They used the Hay-Wadt small core effective pseudopotential basis set[17] for the metals and all-electron basis sets for oxygen.[18] $2 \times 2 \times 2$ supercells consisting of 40 atoms ($BaTiO_3$) and 20 atoms ($SrTiO_3$) were used. Rusevich et al. did a theoretical and experimental study on $(Ba, Sr)TiO_3$ perovskite solid solutions and $BaTiO_3/SrTiO_3$ heterostructures,[19] using the hybrid functionals PBE0, B1WC, and B3LYP. The structural, electronic, and vibrational properties of $BaTiO_3$ and $SrTiO_3$ were studied with B1WC.[16] Kotomin et al. studied F-centers in $PbTiO_3$, $PbZrO_3$, and $SrTiO_3$ with CRYSTAL03 and the B3PW hybrid functional using the same basis sets as in the two previously discussed studies.[20] They used larger $3 \times 3 \times 3$ supercells consisting of 135 atoms. Heifets et al. calculated the antiferrodistortive phase of $SrTiO_3$ using CRYSTAL03 and B3PW. The basis sets 8-411(1d)G (O), 8-411(311d)G (Ti), and Hay-Wadt-311(1d)G (Sr) were used. Wang et al. studied anion doping of $BaTiO_3$ using the VASP code and plane wave basis sets.[21] They used Perdew–Burke–Ernzerhof (PBE) for geometry optimizations and the range-separated hybrid functional HSE06 for electronic structure calculations. Santana et al. computed the equations of state, formation energy, and migration barriers of oxygen vacancies in $SrFeO_3$ and $LaFeO_3$[22] using diffusion QMC with $2 \times 2 \times 2$ supercells consisting of 40 atoms. Park et al. studied the effects of temperature and oxygen vacancy on bandgap renormalization in $LaCrO_3$ on PBE + U level using VASP[23]. Heifets et al. performed a hybrid DFT study on the possible phases of $SrFeO_3 - \delta$ with $\delta = 0.0 - 0.5$.[24] They computed a phase diagram for temperatures between 0 and 2000 K and pressures between 10^{-30} and 10^{10} bar and concluded that $SrFeO_{2.5}$ is the only stable defect phase. $2 \times 2 \times 2$ supercells consisting of 40 atoms were used for $SrFeO_3$ and a larger supercell consisting of 72 atoms for $SrFeO_{2.5}$. Kotomin et al. did a combined theoretical and experimental study of charge ordering in $CaFeO_3$ and $SrFeO_3$ on hybrid DFT (B3PW) level.[25] Zwejnieks et al. performed a chemical bonding analysis on the monoclinic $BaCoO_3$ structure using the same functional.[26]

The DFT studies listed earlier agree that the use of hybrid DFT leads to more accurate bandgaps and structures than GGA. However, a detailed assessment of various types of hybrid DFT methods is still lacking. This work will show that the choice of the hybrid DFT method is of importance for accurate defect formation energies. We will also show that large unit cells are required to find the most stable defect conformation due to relaxation effects. Furthermore, defect conformation energies are key to compute the conformational entropy. Combining conformational entropies at the hybrid DFT level with vibrational entropies at the GGA level significantly improves agreement with experiment. As far the authors are aware, this is the first theoretical study on $CaMnO_3$ which calculates conformational entropies by explicitly taking into account all possible defect conformations in a large supercell. As entropy effects are expected to be relevant at higher temperatures (around 1000 K), this is a significant improvement.

Structural, electronic, and magnetic properties as well as OVF thermodynamics of $CaMnO_3$ were calculated using the programs VASP and CRYSTAL. Representative GGA, GGA + U, and meta-GGA methods were tested as well as hybrid DFT methods. In a first step, the electronic ground state of $CaMnO_3$ was determined by calculating all AFM and ferromagnetic configurations. The OVF energies of $CaMnO_{3-\delta}$ were calculated for $\delta = 0.03125$, 0.0625, 0.125, and 0.25 and compared with the experimental results of Roermark et al.[15] and Bulfin et al.[11] For $\delta = 0.125$, the most stable defect configurations of two defects in a $Ca_{16}Mn_{16}O_{46}$ supercell were considered. Boltzmann statistics of all-symmetry-inequivalent defect configurations was used to calculate configuration enthalpies and entropies. Frequency calculations were performed with CRYSTAL/PBE to obtain the thermodynamic contributions of lattice vibrations. Based on the calculated free energies, pressure-dependent phase diagrams were obtained for $CaMnO_3$, $CaMnO_{3-\delta}$, and the most important decomposition products. Furthermore, the temperature dependence of OVF free energy was calculated.

2. Computational Details

To assess the performance of representative quantum chemical methods, and also to evaluate the effect of different basis set types, the complementary solid-state programs VASP (version 6.1.2)[27–29] and CRYSTAL17 (version 1.0.2)[30] were used. VASP uses plane waves and CRYSTAL linear combinations of Gaussian-type atomic orbitals as basis functions of the crystal orbitals.

In VASP, the standard GGA functionals PBE[31] and PBEsol[32] and the meta-GGA functionals SCAN[33] and r^{2}SCAN[34] were considered. SCAN has been shown to be reliable for energetics and structures of solids.[35] The functional r^{2}SCAN is a recent modification of SCAN providing very promising results for molecules.[34] All functionals were used with and without the rotationally invariant DFT + U correction by Dudarev.[36] The Hubbard parameter $U_{\text{eff}} = U - J$ was set to 3.5 eV for the Mn 3d orbitals, similar as in a previous study.[37] To assess the relevance of London dispersion in the present case, the D4 correction[38] was used in combination with PBE in some calculations. The wave functions were expanded in a plane wave basis delimited by a cutoff of 600 eV, which is considered as converged for insulators and semiconductors. Core electrons were described with the projector augmented wave (PAW) method.[39,40] The potPAW_PBE.54 POTCAR files Mn_sv, Ca_sv, and O were used. A 4×4×4 Monkhorst–Pack k-point mesh was used for the conventional cell. For the supercells, correspondingly smaller Monkhorst–Pack nets were used. Initial atomic magnetic moments were explicitly specified for all transition metal atoms in MnO_2 and $CaMnO_3$. More details can be found in Supporting Information (SI).

In CRYSTAL, the standard GGA-functional PBE and the global hybrid functionals PW1PW,[41] HSE06,[42] PBE0,[43] M06,[44] B1WC,[45] B3PW,[46,47] and B3LYP[46,48] were used. This selection is mainly based on the benchmark test by Tran et al.[35] and the previous works by Heifets et al., Kotomin et al., Rusevich et al., and Zwejnieks et al. mentioned in the introduction.[16,16–26] Hybrid functionals were only applied in CRYSTAL calculations because the implementation of Fock exchange is more efficient than in VASP. As the D4 method is not yet implemented in CRYSTAL, the D3(BJ) correction was used in combination with PBE and PBE0 for some calculations.[49] Furthermore the self-consistent (SC) hybrid functionals SC-PBE0 and SC-PW1PW were applied. In SC hybrid methods, the optimal exchange fraction in the exchange functional of a hybrid functional is determined individually for each compound based on its dielectric constant.[50] SC versions of PBE0 and PW1PW were generated for the perfect solid of $CaMnO_3$ in the primitive orthorhombic cell. Optimized Fock exchange fractions $\alpha = 0.129$ (0.128) were obtained for SC-PBE0 (SC-PW1PW). These values were used for all SC hybrid calculations in this work, because using different exchange fractions for the reference systems in reaction energy calculations would be inconsistent. All calculations were performed using the pob-TZVP-rev2 basis sets,[51] which are particularly optimized for solids and reduction of basis set superposition errors. The integration truncation parameters, which are based on overlap integrals, were set to 10^{-7}, 10^{-7}, 10^{-7}, 10^{-14}, and 10^{-42}. In particular the latter two parameters were set to more strict values compared with the CRYSTAL standard, as recommended for hybrid functionals. Similar Monkhorst–Pack grids were applied as in VASP calculations.

We first present results for pristine $CaMnO_3$. According to the experimental phase diagram,[52] the orthorhombic polymorph (space group $Pmna$)[7] is the most stable form at low temperatures and small defect concentrations. A tetragonal polymorph occurs at defect concentrations δ between 0.04 and 0.12. The high-temperature phase is cubic (space group $Pm\bar{3}m$[53]). At defect concentrations above $\delta = 0.14$ and $T > 1000$ K, $CaMnO_3$ decomposes into Ca_2MnO_4 and $CaMn_2O_4$.[53] Thus, for the calculation of the perfect $CaMnO_3$ solid at temperatures below 950 K, it is sufficient to focus on the orthorhombic structure. Its primitive cell contains four formula units. Experimental room-temperature lattice parameters are $a = 5.279$, $b = 7.448$, and $c = 5.264$ Å.[7] Ca occupies the 4a Wyckoff site (0.0331,0.25,0.9943), Mn the 4b site (0.0,0.0,0.5), and O the 8d (0.2127,0.5336,0.2121) and the 4c site (0.0111,0.75,0.5659) (see Figure 3). Formally, $CaMnO_3$ is composed of Ca^{2+}, Mn^{4+}, and O^{2-} ions. The Mn^{4+} ions have a d^3 configuration and are assumed in a high-spin quartet state (t_{2g}^3).

The so-called G-AFM spin configuration (**Figure 1**) has been determined as magnetic ground state.[9] This magnetic structure consists of two interpenetrating face-centered lattices with opposite spin. Each Mn ion is surrounded by six Mn neighbors with opposite spin. This configuration was used for all subsequent calculations of the perfect $CaMnO_3$ solid.

In the first method assessment, the structural parameters of $CaMnO_3$, the electronic bandgap, and the free energy of the formation reaction (Equation (1)).

$$MnO_2(s) + CaO(s) = CaMnO_3(s) \quad (1)$$

were calculated. For the reference energies in Equation (1), we assumed the rutile structure for MnO_2[54] in an AFM state and the rocksalt structure for CaO.[55] The free reaction enthalpy $\Delta_r G$ is calculated from free reaction enthalpy $\Delta_r H$ and reaction entropy $\Delta_r S$ (Equation (2)).

$$\Delta_r G = \Delta_r H - T\Delta_r S \quad (2)$$

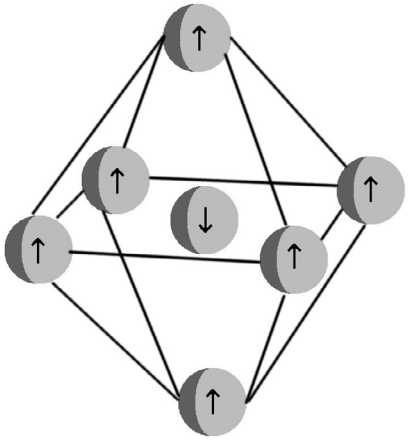

Figure 1. G-AFM spin configuration in orthorhombic $CaMnO_3$.[9]

$\Delta_r H$ and $\Delta_r S$ are calculated as the sum of the individual components for translation, rotation, vibration, and electronic excitation. Translation and rotation degrees of freedom are not present in solids. Electronic excitations were neglected because the fundamental bandgaps were larger than the thermal energy kT (1.67 eV (MnO_2), 6.68 eV (CaO), and 2.50 eV ($CaMnO_3$) on PW1PW level).

$$\Delta_r G = H_{vib}^{CaMnO_3} - H_{vib}^{MnO_2} - H_{vib}^{CaO} - T\left(S_{vib}^{CaMnO_3} - S_{vib}^{MnO_2} - S_{vib}^{CaO}\right) \quad (3)$$

The vibrational enthalpy and entropy were calculated from the vibrational frequencies ν_i, the temperature T, the pressure p, and cell volume V (using the Boltzmann constant k, and the Planck constant h).

$$H_{vib} = E_{el} + \sum_i \frac{1}{2} h\nu_i + \sum_i \frac{h\nu_i}{e^{\frac{h\nu_i}{kT}} - 1} + pV \quad (4)$$

$$S_{vib} = \frac{1}{T}\left(\sum_i \frac{1}{2} h\nu_i + \sum_i \frac{h\nu_i}{e^{\frac{h\nu_i}{kT}} - 1}\right) + k\ln\left(\sum_i \frac{e^{\frac{h\nu_i}{2kT}}}{1 - e^{-\frac{h\nu_i}{kT}}}\right) \quad (5)$$

The thermodynamic correction to the electronic energy was defined as

$$\Delta_{therm} = \Delta_r G - \Delta_r E_{el} \quad (6)$$

The thermodynamic corrections (Equation (6)) were calculated with CRYSTAL/PBE because of higher numerical stability compared with VASP/PBE. The other methods, in particular hybrid functionals, are too demanding for phonon calculations of larger supercells. Test calculations showed that the differences in Δ_{therm} between CRYSTAL/PBE and CRYSTAL/PW1PW are only a few kJ mol^{-1}. The entropies and enthalpies of O_2 were taken from the NIST chemical webbook.[56]

The second method assessment was based on the calculated OVF energy. For the $CaMnO_3$ defect structures, $Ca_8Mn_8O_{24}$ supercells were generated from the primitive cell with a ((−1,0,−1),(0,1,0),(1,0,−1)) transformation matrix and one oxygen atom was removed. For the calculation of the defect structures, the fully optimized structure of the perfect solid was taken as the starting point for each method, and all atomic positions were optimized after removal of an oxygen atom fixing the lattice constants. It was checked that a full optimization of the defective supercell was not necessary because energies and lattice parameters do not change significantly up to $\delta = 0.125$. Only for larger δ values, the lattice parameters were also optimized. The initial spin settings at Mn atoms were not altered compared with the nondefective calculations.

VASP calculations with r^{2}SCAN, SCAN, PBE, and PBE + U consistently showed that the 8d oxygen atom is preferentially removed, which is in agreement with the previous theoretical study of Aschauer et al.[14] In the CRYSTAL calculations, a counterpoise correction was performed for the optimized structures by placing a ghost atom with full O basis set at the position of the oxygen vacancy. The defect formation energies were calculated with respect to the O_2 molecule in its triplet ground state. In VASP calculations, a large orthorhombic box with converged cell parameters was used for the O_2 calculation; in the CRYSTAL reference calculation, the oxygen basis set was converged out by adding more diffuse functions.

3. Results and Discussion

3.1. First Method Assessment: Properties of Pristine $CaMnO_3$

3.1.1. Lattice Parameters

Figure 2 and Table S1 in the Supporting Information show the calculated lattice parameters and their deviations from the experiment for all selected functionals.

In Figure 2 and Table S1 in the Supporting Information, Δ is the average relative deviation of the three lattice parameters from the experimental reference. The results of the tested methods can be grouped into very accurate (Δ < 0.35%), accurate (0.35 < Δ < 0.66%), and less accurate (Δ > 0.66%).[57] The hybrid functionals B3PW, PBE0, SC-PBE0, PW1PW, HSE06, and M06 as well as the GGA functionals PBE-D3 (CRYSTAL), PBE-D4 (VASP) and the meta-GGA-functionals SCAN + U, and r^{2}SCAN + U (VASP) prove to be very accurate. The VASP results obtained with PBE, r^{2}SCAN, SCAN, and PBEsol + U and the CRYSTAL results with B3LYP can be classified as accurate. Less accurate are the CRYSTAL results with B1WC, PBE, and PBE0-D3 and the VASP results with PBE + U.

3.1.2. Atom Positions

The calculated atomic positions are given in **Figure 3** and Table S2 in the Supporting Information. The deviations from the experiment are given as root-mean-squared deviation (RMSD) (from the experimental reference) in fractional coordinates. There are no significant differences in the accuracy of all considered methods. The smallest deviation is obtained with CRYSTAL and PBE or B3LYP and with VASP/r^{2}SCAN. Surprisingly, the VASP/PBE deviation (0.0029) is considerably larger than that of CRYSTAL/PBE (0.0011). Large differences

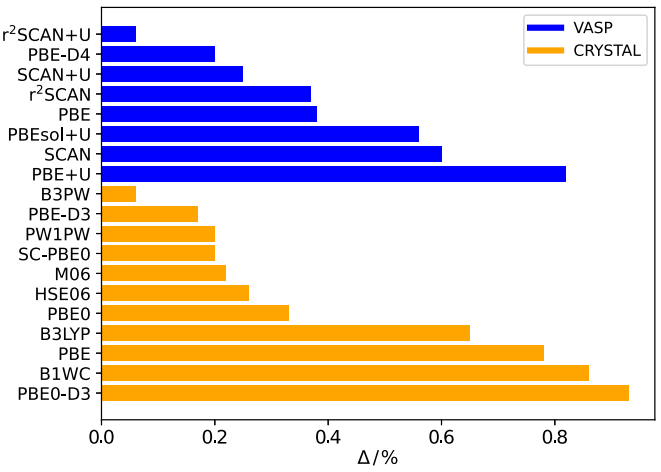

Figure 2. Calculated lattice parameters of orthorhombic $CaMnO_3$ (Å) and percental error (%) with respect to measured values. Experimental reference data are taken from the study by Poeppelmeier et al.[7]

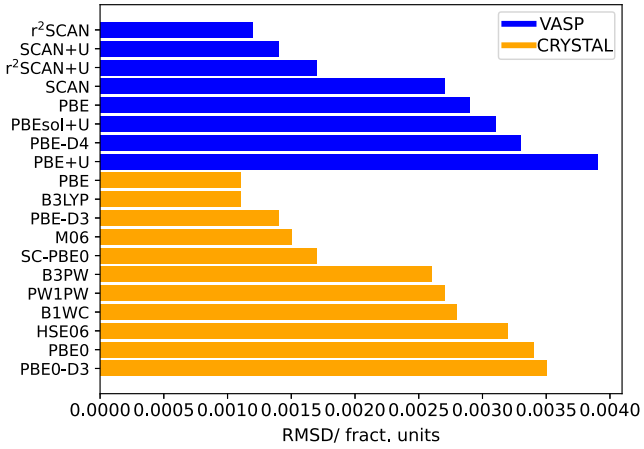

Figure 3. Comparison of calculated and experimental atom positions of orthorhombic $CaMnO_3$. The coordinates of the high-symmetry 4*a* Mn site (0.0, 0.0, 0.5) were not optimized. Experimental data from ref. [7].

between the two implementations were also found for the computed lattice parameters. This is most probably due to an error compensation in CRYSTAL due to the finite size of the atomic basis set. In both cases, dispersion correction slightly deteriorates the quality of the calculated atomic structure. The Hubbard U_{eff} correction of 3.5 eV does not significantly improve the results.

3.2. Bandgaps

The calculated fundamental bandgaps can be found in **Figure 4** and Table S3 in the Supporting Information.

All methods underestimate the experimental value of 3.07 eV.[8] Here it has to be noted that the measured value corresponds to an optical gap. Usually optical gaps are smaller than fundamental bandgaps by some tenth of an eV due to excitonic effects. Thus the deviations between computed and (unavailable) experimental electronic gap are expected to be slightly larger than those given in Figure 4. As expected, only hybrid functionals (PW1PW, HSE06, M06, PBE0, B3PW, B3LYP, B1WC) come reasonably close (with deviations smaller than 0.8 eV) to the

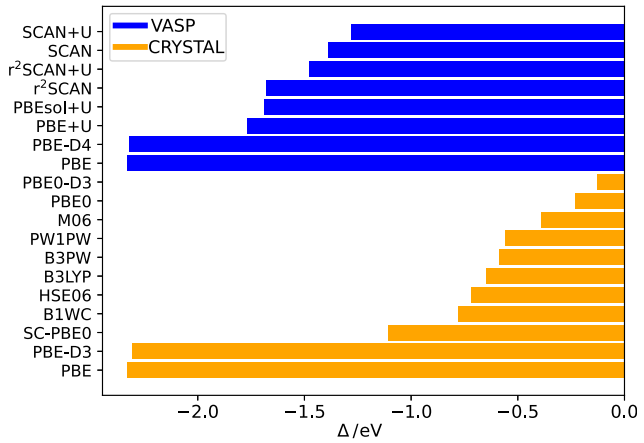

Figure 4. Fundamental bandgap (eV) of orthorhombic $CaMnO_3$, the absolute deviation Δ given in eV. Experimental data from ref. [8] (optical gap).

reference value. In the VASP calculations, the meta-GGA, meta-GGA + *U*, as well as GGA + *U* bandgaps strongly deviate from experiment (by 1.3–1.8 eV), similar to previous GGA + *U* results.[12,13] This shows that the self-interaction error (SIE) is still present in meta-GGA functionals as found before.[58] As for the GGA functionals, the Hubbard U_{eff} correction of 3.5 eV does not significantly improve the results. Large values for U_{eff} would be necessary for this purpose. However, this strategy was not followed in the present study, as our focus was on thermodynamic properties. For the GGA calculations (CRYSTAL/PBE and VASP/PBE, also for the geometries obtained with dispersion correction), the deviations from the literature value are even larger, > 2 eV.

3.3. Free Reaction Enthalpies

The calculated free reaction enthalpies of the Equation (1) are shown in **Figure 5** and Table S4 in the Supporting Information.

First it has to be noted that the thermal contributions to the reaction enthalpy and entropy in Equation (6) are negligible due to cancellation effects. The most accurate results were obtained with CRYSTAL and the dispersion-corrected functionals PBE-D3 and PBE0-D3 (deviations below 1 kJ mol^{-1}). The hybrid functionals B1WC, PBE0, SC-PBE0, PW1PW, HSE06, and M06 show deviations ≤ 5 kJ mol^{-1} which is still close to chemical accuracy. For both functionals PBE and PBE0, the D3 correction improved the agreement with experiment by $\approx$5 kJ mol^{-1}. On the other hand, the SC optimization of the Fock exchange contribution in SC-PBE0 did not lead to a notable change compared with PBE0. CRYSTAL/PBE and B3PW give slightly less accurate results than the hybrid functionals (deviation 6.4 and 6.2 kJ mol^{-1}). Notable is that the hybrid functional B3LYP is the only hybrid functional in this selection which has a deviation of > 10 kJ mol^{-1}.

Striking is the large difference between VASP/PBE (−53.5 kJ mol^{-1}) and CRYSTAL/PBE (−82.6 kJ mol^{-1}). We checked if this discrepancy was due to BSSE in CRYSTAL by adding more diffuse basis functions, but without notable

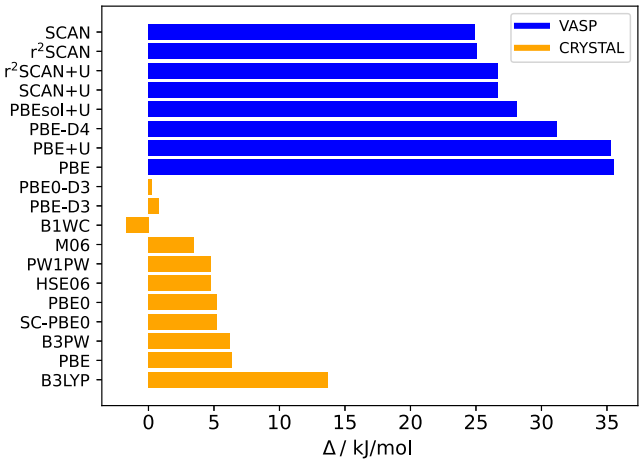

Figure 5. Calculated reaction energies and free energies of reaction (1) in kJ mol^{-1}. Δ is the deviation from the experimental free energy at 298 K in kJ mol^{-1}. Experimental data from ref. [15].

effects. VASP calculations were repeated with different POTCAR files, as well as more exact settings, which changed the result however only slightly. For all tested functionals, agreement with experiment is better when atom-centered basis functions are applied. Therefore we conclude that similar error cancellation effects occur as discussed earlier for the geometry. The meta-GGA functionals perform better than the GGA functionals in VASP, while the addition of a Hubbard U has almost no effect.

3.4. Magnetizations

Experimental data are available for the magnetization of the Mn ions.[9] The calculated magnetizations are compared with the measured value in **Figure 6** and in Table S5 in the Supporting Information.

The experimental value was best reproduced with CRYSTAL/PBE. VASP/meta-GGA, VASP/GGA, VASP/GGA-D4, and CRYSTAL/GGA-D3 can also approximate the experimental value quite accurately (with deviations smaller than 0.1 a.u.). Addition of a U correction does not have a large effect for most functionals except r^{2}SCAN. Hybrid functionals overestimate the experimental value by 0.17–0.4 a.u. This is unexpected as hybrid functionals usually give the best representation of magnetic properties.[59]

In summary, the hybrid functionals B3PW, PW1PW, SC-PBE0, HSE06, and M06 give the best results for lattice parameters, bandgaps, and reaction enthalpies. For atomic positions, similar results are obtained for all functionals. Therefore, CRYSTAL in combination with one of these hybrid functionals can be recommended for the calculation of $CaMnO_3$.

3.5. Second Method Assessment: Oxygen Vacancy Formation Thermodynamics

The selected methods were assessed for the calculation of the OVF enthalpy as experimental reference values are available.[10] However, before comparing theory and experiment, we tested the effect of the O vacancy concentration and the defect configuration on the OVF energy.

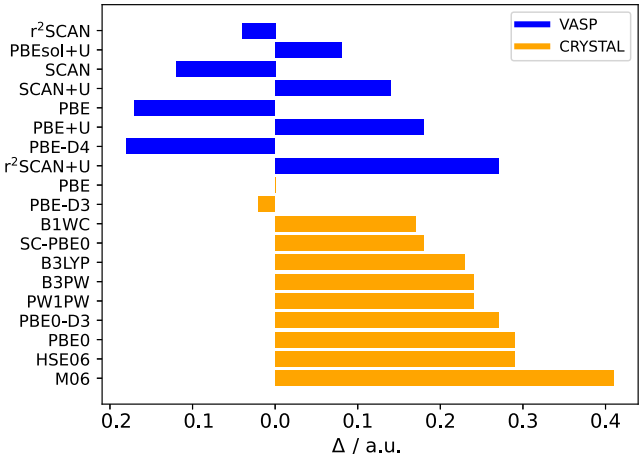

Figure 6. Calculated magnetization (a.u.) of Mn and deviation Δ from experiment in orthorhombic $CaMnO_3$. Experimental data from ref. [9].

3.5.1. Oxygen Vacancy Formation Energies as a Function of δ

As a first step, the OVF energy of $CaMnO_3$ was calculated in dependence of the defect concentration δ to investigate possible defect–defect interaction. For these calculations we employed the hybrid functional PW1PW, which most accurately reproduced the experimental OVF enthalpy (see Section 3.5.3). Oxygen vacancy concentrations δ ranging from 0.03125 to 0.25 were obtained by varying the size of the supercell. $\delta = 0.25$ is obtained by removing an oxygen atom from the primitive $Ca_4Mn_4O_8$ cell. Removal of one oxygen atom from the above mentioned $Ca_8Mn_8O_{24}$ supercell leads to $\delta = 0.125$. $Ca_{16}Mn_{16}O_{48}$ and $Ca_{32}Mn_{32}O_{96}$ supercells are generated with $2 \times 1 \times 2$ and $2 \times 2 \times 2$ transformation matrices. One oxygen vacancy in these cells corresponds to $\delta = 0.0625$ and 0.03125, respectively.

Table 1 shows the PW1PW OVF energies for the selected values for δ. In all cases we considered both oxygen sites 4*c* and 8*d* and performed a BSSE correction by placing a ghost atom at the vacancy site. The stabilization of the defect structures is quantified by the relaxation energy E_{relax} which is defined as energy difference between relaxed and initial structures where the atoms are located at the positions of the pristine bulk as optimized with PW1PW.

In almost all supercell calculations, $\Delta E(8d)$ is comparable with $\Delta E(4c)$. The only exception is the $Ca_{16}Mn_{16}O_{48}$ supercell ($\delta = 0.0625$) result, which we consider as a numerical artifact. The relaxation energy increases with increasing supercell size due to the increased degrees of freedom for the atoms surrounding the defect but is close to convergence for the largest cell. The variation of E_{relax} is the main cause for the decrease of ΔE with decreasing δ. The direct defect–defect interaction appears to be small, which is consistent with formation of a neutral vacancy, in Kröger–Vink notation

$$O_O^{\times} + 2Mn_{Mn}^{\times} = V_O^{\cdot\cdot} + 2Mn_{Mn}' + \frac{1}{2}O_2(g) \quad (7)$$

This is also confirmed by a Mulliken population of only 0.1 at the ghost atom and a small counterpoise correction of ≈15 kJ mol^{-1}. The distribution of the reduced Mn$'$ atoms will be important in the configuration analysis.

Table 1. OVF energies ΔE and relaxation energies E_{relax} (kJ mol^{-1}) of orthorhombic $CaMnO_3$ calculated with PW1PW.

δ	ΔE	E_{relax}
0.03125 (8*d*)	176.4	−100.5
0.03125 (4*c*)	174.7	−102.2
0.0625 (8*d*)	178.9	−95.4
0.0625 (4*c*)	188.4	−94.7
0.125 (8*d*)	216.4	−65.9
0.125 (4*c*)	217.3	−63.4
0.25 (8*d*)	230.1	−58.6
0.25 (4*c*)	229.9	−58.0

3.5.2. Oxygen Vacancy Defect Configurations

So far, only well-ordered defect structures were considered by removing only one oxygen atom per unit cell. From previous studies,[60] it is known that the defect configuration can have a substantial effect on the defect formation energy. In order to check this, we generated all possible symmetry-inequivalent configurations of two oxygen defects in the $Ca_{16}Mn_{16}O_{48}$ supercell with the CRYSTAL CONFCOUNT tool. The calculated relaxation energies, OVF energies, and defect–defect distances for all configurations are given in Table S8 in the Supporting Information. There is no correlation between the defect–defect distance r_{O1-O2} and the defect formation energy ΔE. In the most stable configuration (1), the O1–O2 distance is 7.87 Å (it was carefully checked that this corresponds to the smallest distance), but in the next most stable configurations (2)–(4), r_{O1-O2} is only $\approx$ 3Å. On the other hand, configurations 42–44 and 47–49 with very short O1–O2 distances (2.7 Å) contain fourfold coordinated Mn atoms and are therefore unstable. As for the single-vacancy calculations, ΔE is mainly determined by the relaxation energy E_{relax}. Configurations 40 and 41 in Table S8 (Supporting Information) are identical to the regular defect structure for $\delta = 0.125$ in Table 1. The calculated ΔE and E_{relax} values are therefore similar. There are, however, many O1–O2 configurations with considerably smaller OVF energies. The reduced lattice symmetry introduced by the nonequivalent O vacancy sites in configurations 1–39 allowed stronger relaxation of the atoms surrounding the empty sites and therefore more negative relaxation energies. For the calculation of defect thermochemistry at elevated temperatures, not only the lowest-energy configurations are relevant, but also slightly less-stable structures can contribute according to their statistical weight. The Boltzmann probability p_i of configuration i can be calculated via Equation (8)

$$p_i = \frac{\exp\left(-\frac{(E_i - E_0)}{RT}\right)}{\sum_j g_j \exp\left(-\frac{(E_j - E_0)}{RT}\right)} \quad (8)$$

where g_j is the degeneracy or multiplicity of the configuration and R the ideal gas constant. The probability of a state with energy E_i is the product of degeneracy and probability. At 1273 K, a temperature where thermodynamical properties of $CaMnO_3$ has been measured, the first four configurations from Table S8 (Supporting Information) have Boltzmann weights $p_i g_i$ of 44.67%, 26.87%, 17.98%, and 1.87%. All other configurations have $p_i g_i$ below 1 %. Therefore only the first three configurations have a significant Boltzmann weight.

Figure 7 shows the most stable configuration (1) before and after optimization. During optimization the two nearest oxygen atoms move closer to the vacancy site, while the neighbor Ca atoms move away. The calculated OVF energy, 152.8 kJ mol^{-1}, is much smaller than the value 217.3 kJ mol^{-1} obtained for a single oxygen vacancy in the $Ca_8Mn_8O_{24}$ supercell.

3.5.3. Oxygen Vacancy Formation Enthalpies for $\delta = 0.125$

To calculate the OVF enthalpy, the thermal vibration contribution was obtained with CRYSTAL/PBE for the $Ca_{16}Mn_{16}O_{46}$ supercell. Its value is almost independent from the defect structure and also from the supercell size. **Figure 8** and Table S6 in the Supporting Information show the calculated OVF energies and enthalpies at 1273 K. For the defect structure, the most stable configuration (1) of the $Ca_{16}Mn_{16}O_{46}$ supercell was used. The OVF enthalpy consists of vibrational, rotational, and translational contributions as described in more detail for the entropy in Section 3.5.4. In addition, the configuration enthalpy ΔH_{conf} was estimated using Equation (9) and (8) based on the calculated ΔE values in Table S8 (Supporting Information), here denoted as E_i. E_0 is the OVF energy of configuration (1).

$$\Delta H_{conf} = \sum_i (E_i - E_0) g_i p_i \quad (9)$$

The energy differences $E_i - E_0$ should be corrected by the differences between the vibrational enthalpies $H_{vib,\,i}$. Due to the observed small variation of $H_{vib,\,i}$ with i and to reduce computational cost, the individual contributions of the vibrations were neglected. The remaining components of the OVF entropy are summarized in ΔH_{therm} (Equation (10)).

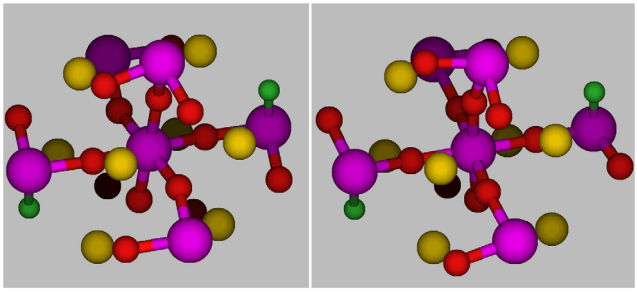

Figure 7. Most stable defect configuration (1) before and (2) after optimization. Defect oxygen (green), oxygen (red), manganese (purple), and calcium (yellow).

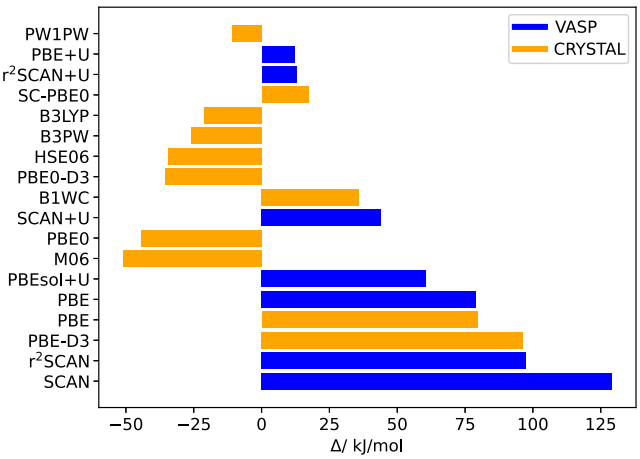

Figure 8. OVF enthalpies ΔH at 1273 K of $CaMnO_3$ ($\delta = 0.125$), including thermodynamic corrections calculated with CRYSTAL/PBE, absolute deviations Δ, all in kJ mol^{-1}. Experimental reference value from ref. [10].

$$\Delta H_{\text{therm}} = H_{\text{vib}}^{\text{CaMnO}_{3-\delta}} - H_{\text{vib}}^{\text{CaMnO}_3} - 0.5\left(H_{\text{vib}}^{\text{O}_2} + H_{\text{rot}}^{\text{O}_2} + H_{\text{trans}}^{\text{O}_2}\right) \quad (10)$$

The OVF enthalpy contributions are relatively small and partly cancel each other. ΔH_{therm} is $-7.2\,\text{kJ mol}^{-1}$, ΔH_{conf} is $+6.6\,\text{kJ mol}^{-1}$ at 1273 K, and $\delta = 0.125$. Therefore the OVF energies of the selected DFT methods are corrected by only $-0.6\,\text{kJ mol}^{-1}$.

The experimental OVF enthalpy, $163.5\,\text{kJ mol}^{-1}$,[10] is best reproduced with CRYSTAL/PW1PW with a deviation of -10.8 kJ/mol. Accurate results were also obtained with VASP/PBE + U and VASP/r^{2}SCAN + U (deviations 12.1 and $12.9\,\text{kJ mol}^{-1}$) and CRYSTAL/SC-PBE0 ($\Delta = 17.3\,\text{kJ mol}^{-1}$). However, Figure 5 shows that the latter two methods have considerably larger deviations for the $CaMnO_3$ formation energy than the hybrid methods. Therefore, r^{2}SCAN + U and PBE + U cannot be considered as overall reliable. The other hybrid methods PBE0, SC-PBE0, and M06, that were among the most accurate methods in the first part of the method assessment, have larger errors in the OVF enthalpy than PW1PW, ranging from $+17.3$ to $-51.0\,\text{kJ mol}^{-1}$. PBE-D3, which was quite accurate for the calculation of the reaction energy (Equation (1)), predicts a much too high defect formation enthalpy ($\Delta = 96.2\,\text{kJ mol}^{-1}$). The present PBEsol + U result, $224\,\text{kJ mol}^{-1}$, has an even larger deviation from the experiment than that reported by Asch et al.,[14] $193\,\text{kJ mol}^{-1}$. The difference is probably due to different settings in the calculations.

After both parts of the assessment, PW1PW can be recommended for the calculation of energetic properties of $CaMnO_3$. PW1PW is therefore used in the following for the calculation of the phase diagram. Since this is based on the Gibbs free enthalpies, entropy contributions must be taken into account.

3.5.4. Oxygen Vacancy Formation Entropy

The OVF entropy is calculated as the sum of the individual components for translation, rotation, vibration, and electronic excitation. Translation and rotation are only present in the O_2 gas-phase molecule. Electronic excitations were neglected because the bandgaps were larger than the thermal energy RT (between 0.8 and 2.1 eV for the relevant defect configuration and 2.5 eV for the perfect solid on PW1PW level). In the defect structure, an additional configuration entropy arises from the occupation of the different defect configurations from Table S8 (Supporting Information). It was calculated via the Gibbs entropy formula (Equation (11)).

$$\Delta S_{\text{conf}} = -R\sum_i g_i p_i \ln(p_i) \quad (11)$$

The remaining components of the OVF entropy are summarized in ΔS_{therm} (Equation (12)).

$$\Delta S_{\text{therm}} = S_{\text{vib}}^{\text{CaMnO}_{3-\delta}} - S_{\text{vib}}^{\text{CaMnO}_3} - 0.5\,(S_{\text{vib}}^{\text{O}_2} + S_{\text{rot}}^{\text{O}_2} + S_{\text{trans}}^{\text{O}_2}) \quad (12)$$

For comparison with the experimental values of Bakken et al.,[10] the oxygen partial pressure dependence of entropy needs to be taken into account. The experimental oxygen equilibrium pressure of $CaMnO_{2.875}$ is around $p_{O_2} = 0.1$ bar.[10] Therefore the entropy has to be corrected by Equation (13).

$$\Delta S_{\text{pressure}} = \Delta S_{p=0.1\,\text{bar}} - \Delta S_{p=1\,\text{bar}} = -R\ln(0.1) \quad (13)$$

Table 2 shows the obtained values for the OVF entropy.

The deviation from the experiment is only $3.7\,\text{J (K mol)}^{-1}$, which justifies the choice of the CRYSTAL/PBE method for this purpose.

3.5.5. Oxygen Vacancy Formation Free Enthalpy

The OVF free enthalpy was calculated from Table 2 and the PBE enthalpy corrections using Equation (14).

$$\Delta G^{\text{OVF}} = \Delta H^{\text{OVF}} - T\Delta S^{\text{OVF}} \quad (14)$$

The results are shown in **Table 3**.

By combining PW1PW OVF energies with vibration contributions from CRYSTAL/PBE, the experimental OVF free enthalpy is reproduced with a deviation of $-6\,\text{kJ mol}^{-1}$.

3.5.6. Phase Diagram

For the calculation of the $CaMnO_3$ phase diagram, free energies were computed for the decomposition products Ca_2MnO_4 and $CaMn_2O_4$ and for the reported oxygen-deficient phase $Ca_2Mn_2O_5$. The free energy of the defect structure was calculated with Equation (15).

$$G^{\text{CaMnO}_{3-\delta}} = H_{\text{therm}}^{\text{CaMnO}_{3-\delta}} + H_{\text{conf}}^{\text{CaMnO}_{3-\delta}} - T\left(S_{\text{therm}}^{\text{CaMnO}_{3-\delta}} + S_{\text{conf}}^{\text{CaMnO}_{3-\delta}}\right) \quad (15)$$

The following solid–gas and solid–solid reactions were considered

$$\text{CaMnO}_3 \rightleftharpoons \text{CaMnO}_{2.875} + \frac{1}{16}\text{O}_2 \quad (16)$$

$$\text{CaMnO}_3 \rightleftharpoons \frac{1}{3}\text{Ca}_2\text{MnO}_4 + \frac{1}{3}\text{CaMn}_2\text{O}_4 + \frac{1}{6}\text{O}_2 \quad (17)$$

$$\text{CaMnO}_3 \rightleftharpoons \frac{1}{2}\text{Ca}_2\text{Mn}_2\text{O}_5 + \frac{1}{4}\text{O}_2 \quad (18)$$

Table 2. OVF entropies at 1273 K of $CaMnO_3$ ($\delta = 0.125$) calculated with CRYSTAL/PBE in J (K mol)$^{-1}$. Reference value from the study by Bakken et al.[10]

Method	ΔS_{therm}	ΔS_{conf}	$\Delta S_{\text{pressure}}$	ΔS_{tot}
CRYSTAL/PBE	85.5	17.2	9.6	112.3
Experiment				116

Table 3. Calculated defect formation enthalpy ΔH^{OVF}, free enthalpy ΔG^{OVF} (kJ mol^{-1}), and entropy ΔS^{OVF} (J K^{-1}mol^{-1}) at 1273 K of $CaMnO_3$ ($\delta = 0.125$). Energies calculated with PW1PW and vibration contributions with CRYSTAL/PBE. Experimental reference value from the study by Bakken et al.[10]

Method	ΔH^{OVF}	ΔS^{OVF}	ΔG^{OVF}
PW1PW/PBE	152.7	112	10
Experiment	163.5	116	16

Figure 9 shows the calculated reaction free energies of these reactions depending on pressure.

According to the calculations, $CaMnO_3$ decomposes into Ca_2MnO_4 and $CaMn_2O_4$ at 1273 K and pressures of 10^4 bar. This is larger than the equilibrium oxygen partial pressure ($10^{-3} - 10^{-2}$ bar) measured by Bakken et al.[10] On the other hand, the equilibrium pressure of the OVF reaction (16), $10^{-2} - 10^{-1}$ bar, is in agreement with experiment.

3.5.7. Temperature Dependence of Oxygen Vacancy Formation Free Enthalpy

Figure 10 shows the OVF free enthalpy (G), enthalpy (H), entropy (S), and energy (E) dependent on the temperature.

The OVF enthalpy is almost independent from temperature while the entropy decreases with increasing temperature. The equilibrium temperature of $CaMnO_{2.875}$ at $p_{O_2} = 1$ bar is 1351 K, which is in good agreement with $T = 1368$ K, as measured by

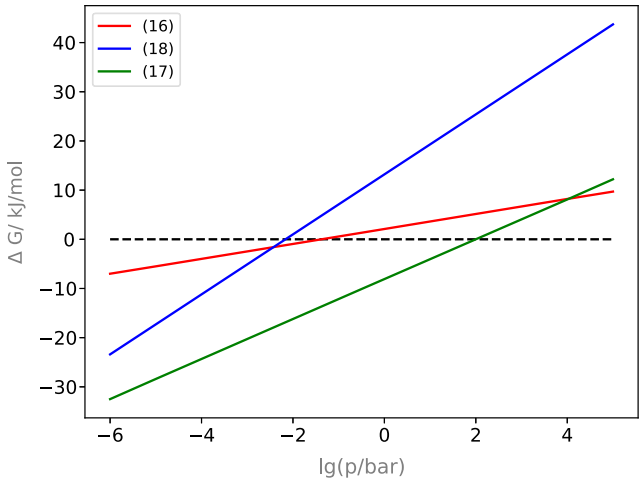

Figure 9. Reaction free energies dependent on pressure at 1273 K of reactions (16)–(18) calculated with PW1PW/PBE.

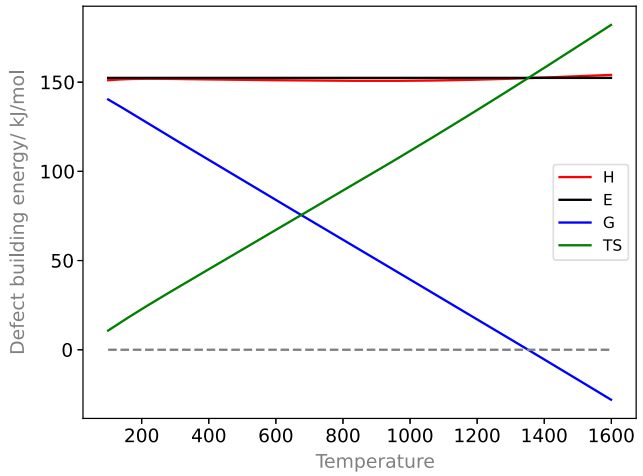

Figure 10. Reaction free energies dependent at $\delta = 0.125$ on temperature (at $p_{O_2} = 1$ bar) on PW1PW level.

Bulfin et al.[11] The suggested combination of methods and models is therefore suitable to reproduce the most relevant quantity for the use of $CaMnO_3$ as an anode material for thermal water splitting.

4. Conclusion

A method test was performed for the calculation of thermodynamic, electronic, and structural properties of $CaMnO_3$. Standard GGA, SC-hybrid, and hybrid functionals as implemented in CRYSTAL and GGA and meta-GGA functionals implemented in VASP were assessed. In addition, the effects of London dispersion and on-site Hubbard corrections were assessed. Among the present selection, the PW1PW hybrid functional without dispersion correction provides most accurate results for the OVF energies and reaction energies of $CaMnO_3$. Vibrational contributions to the thermodynamic functions are calculated with CRYSTAL/PBE, which is computationally more efficient. It was observed that the use of atom-centered basis sets leads to an error cancellation in calculations of structural properties and defect formation energies. Furthermore, accurate defect formation entropies and free enthalpies can be achieved by taking conformational entropies into account. The calculation of all possible defect conformations within a given supercell gives the possibility to achieve accurate conformational entropies using the Boltzmann statistics. With this combination of methods and basis set, the experimental oxygen equilibrium pressure of $CaMnO_3$ is reproduced with reasonable accuracy. Accordingly, it can be assumed that the CRYSTAL implementation of PW1PW/PBE can also be applied for studies of substituted $CaMnO_3$ in the search for the best possible electrode material for water electrolysis. It already showed promising results for the substitution of Mn in $CaMnO_3$.[61]

Supporting Information

Supporting Information is available from the Wiley Online Library or from the author.

Acknowledgements

Open Access funding enabled and organized by Projekt DEAL.

Conflict of Interest

The authors declare no conflict of interest.

Data Availability Statement

Research data are not shared.

Keywords

$CaMnO_3$, configuration entropies, hybrid density functional theory, oxygen defect thermochemistry, phase diagrams

Received: September 7, 2022
Published online: September 29, 2022

[1] J. O. Abe, A. Popoola, E. Ajenifuja, O. Popoola, *Int. J. Hydrogen Energy* **2019**, *44*, 15072.
[2] D. R. Palo, R. A. Dagle, J. D. Holladay, *Chem. Rev.* **2007**, *107*, 3992.
[3] I. Dincer, *Int. J. Hydrogen Energy* **2012**, *37*, 1954.
[4] G. Gahleitner, *Int. J. Hydrogen Energy* **2013**, *38*, 2039.
[5] P. P. Lopes, D. Y. Chung, X. Rui, H. Zheng, H. He, P. Farinazzo Bergamo Dias Martins, D. Strmcnik, V. R. Stamenkovic, P. Zapol, J. Mitchell, R. F. Klie, N. M. Markovic, *J. Am. Chem. Soc.* **2021**, *143*, 2741.
[6] J. S. Yoo, X. Rong, Y. Liu, A. M. Kolpak, *ACS Catal.* **2018**, *8*, 4628.
[7] K. R. Poeppelmeier, M. Leonowicz, J. Scanlon, J. Longo, W. Yelon, *J. Solid State Chem.* **1982**, *45*, 71.
[8] J. H. Jung, K. H. Kim, D. J. Eom, T. W. Noh, E. J. Choi, J. Yu, Y. S. Kwon, Y. Chung, *Phys. Rev. B* **1997**, *55*, 15489.
[9] E. Wollan, W. Koehler, *Phys. Rev.* **1955**, *100*, 545.
[10] E. Bakken, T. Norby, S. Stølen, *Solid State Ion.* **2005**, *176*, 217.
[11] B. Bulfin, J. Vieten, D. Starr, A. Azarpira, C. Zachäus, M. Hävecker, K. Skorupska, M. Schmücker, M. Roeb, C. Sattler, *J. Mater. Chem. A* **2017**, *5*, 7912.
[12] M. Molinari, D. A. Tompsett, S. C. Parker, F. Azough, R. Freer, *J. Mater. Chem. A* **2014**, *2*, 14109.
[13] J. Du, T. Zhang, F. Cheng, W. Chu, Z. Wu, J. Chen, *Inorg. Chem.* **2014**, *53*, 9106.
[14] U. Aschauer, R. Pfenninger, S. M. Selbach, T. Grande, N. A. Spaldin, *Phys. Rev. B* **2013**, *88*, 054111.
[15] L. Rørmark, A. B. Mørch, K. Wiik, S. Stølen, T. Grande, *Chem. Mater.* **2001**, *13*, 4005.
[16] L. Rusevich, E. Kotomin, G. Zvejnieks, A. Popov, *Low Temp. Phys.* **2020**, *46*, 1185.
[17] S. Piskunov, E. Heifets, R. Eglitis, G. Borstel, *Comput. Mater. Sci.* **2004**, *29*, 165.
[18] T. Bredow, K. Jug, R. A. Evarestov, *Phys. Status Solidi B* **2006**, *243*, R10.
[19] L. L. Rusevich, G. Zvejnieks, E. A. Kotomin, M. M. Krzmanc, A. Meden, S. Kunej, I. D. Vlaicu, *J. Phys. Chem. C* **2019**, *123*, 2031.
[20] E. Heifets, E. Kotomin, V. Trepakov, *J. Phys.: Condens. Matter* **2006**, *18*, 4845.
[21] M. Wang, C. Wang, Y. Liu, X. Zhou, *J. Solid State Chem.* **2019**, *280*, 121018.
[22] J. A. Santana, J. T. Krogel, P. R. Kent, F. A. Reboredo, *J. Chem. Phys.* **2017**, *147*, 034701.
[23] J. Park, W. A. Saidi, J. K. Wuenschell, B. H. Howard, B. Chorpening, Y. Duan, *ACS Appl. Mater. Interfaces* **2021**, *13*, 17717.
[24] E. Heifets, E. A. Kotomin, A. A. Bagaturyants, J. Maier, *Phys. Chem. Chem. Phys.* **2019**, *21*, 3918.
[25] E. A. Kotomin, A. Kuzmin, J. Purans, J. Timoshenko, S. Piskunov, R. Merkle, J. Maier, *Phys. Status Solidi B* **2022**, *259*, 2100238.
[26] G. Zvejnieks, D. Zavickis, E. A. Kotomin, D. Gryaznov, *Phys. Chem. Chem. Phys.* **2021**, *23*, 17493.
[27] G. Kresse, J. Hafner, *Phys. Rev. B* **1993**, *47*, 558.
[28] G. Kresse, J. Furthmüller, *Comput. Mater. Sci.* **1996**, *6*, 15.
[29] G. Kresse, J. Furthmüller, *Phys. Rev. B* **1996**, *54*, 11169.
[30] R. Dovesi, A. Erba, R. Orlando, C. M. Zicovich-Wilson, B. Civalleri, L. Maschio, M. Rérat, S. Casassa, J. Baima, S. Salustro, B. Kirtman, *Wiley Interdiscip. Rev. Comput. Mol. Sci.* **2018**, *8*, e1360.
[31] J. P. Perdew, K. Burke, M. Ernzerhof, *Phys. Rev. Lett.* **1996**, *77*, 3865.
[32] J. P. Perdew, A. Ruzsinszky, G. I. Csonka, O. A. Vydrov, G. E. Scuseria, L. A. Constantin, X. Zhou, K. Burke, *Phys. Rev. Lett.* **2008**, *100*, 136406.
[33] J. Sun, A. Ruzsinszky, J. P. Perdew, *Phys. Rev. Lett.* **2015**, *115*, 036402.
[34] J. W. Furness, A. D. Kaplan, J. Ning, J. P. Perdew, J. Sun, *J. Phys. Chem. Lett.* **2020**, *11*, 8208.
[35] F. Tran, J. Stelzl, P. Blaha, *J. Chem. Phys.* **2016**, *144*, 204120.
[36] S. Dudarev, L.-M. Peng, S. Savrasov, J.-M. Zuo, *Phys. Rev. B* **2000**, *61*, 2506.
[37] E. S. Sasioglu, I. Galanakis, C. Friedrich, S. Blügel, *Phys. Rev. B* **2013**, *88*, 134402.
[38] E. Caldeweyher, S. Ehlert, A. Hansen, H. Neugebauer, S. Spicher, C. Bannwarth, S. Grimme, *J. Chem. Phys.* **2019**, *150*, 154122.
[39] P. E. Blöchl, *Phys. Rev. B* **1994**, *50*, 17953.
[40] M. Torrent, N. Holzwarth, F. Jollet, D. Harris, N. Lepley, X. Xu, *Comput. Phys. Commun.* **2010**, *181*, 1862.
[41] T. Bredow, A. R. Gerson, *Phys. Rev. B* **2000**, *61*, 5194.
[42] J. Heyd, G. E. Scuseria, M. Ernzerhof, *J. Chem. Phys.* **2003**, *118*, 8207.
[43] J. P. Perdew, M. Ernzerhof, K. Burke, *J. Chem. Phys.* **1996**, *105*, 9982.
[44] Y. Zhao, D. G. Truhlar, *Theor. Chem. Acc.* **2008**, *120*, 215.
[45] D. Bilc, R. Orlando, R. Shaltaf, G.-M. Rignanese, J. Íñiguez, P. Ghosez, *Phys. Rev. B* **2008**, *77*, 165107.
[46] A. D. Becke, *Phys. Rev. A* **1988**, *38*, 3098.
[47] C. Lee, W. Yang, R. G. Parr, *Phys. Rev. B* **1988**, *37*, 785.
[48] J. P. Perdew, in *Electronic Structure of Solids' 91* (Eds: P. Ziesche, H. Eschrig), Akademie Verlag, Berlin **1991**, p. 11.
[49] S. Grimme, S. Ehrlich, L. Goerigk, *J. Comput. Chem.* **2011**, *32*, 1456.
[50] J. H. Skone, M. Govoni, G. Galli, *Phys. Rev. B* **2014**, *89*, 195112.
[51] D. Vilela Oliveira, J. Laun, M. F. Peintinger, T. Bredow, *J. Comput. Chem.* **2019**, *40*, 2364.
[52] E. I. Leonidova, I. A. Leonidov, M. V. Patrakeev, V. L. Kozhevnikov, *J. Solid State Electrochem.* **2011**, *15*, 1071.
[53] H. Taguchi, M. Nagao, T. Sato, M. Shimada, *J. Solid State Chem.* **1989**, *78*, 312.
[54] W. H. Baur, *Acta Crystallogr., Sect. B: Struct. Sci.* **1976**, *32*, 2200.
[55] E. Perez-Albuerne, H. Drickamer, *J. Chem. Phys.* **1965**, *43*, 1381.
[56] *NIST Chemistry WebBook*, NIST Standard Reference Database Number 69 (Eds: P.J. Linstrom, W.G. Mallard), National Institute of Standards and Technology, Gaithersburg, MD **2015**, http://webbook.nist.gov.
[57] L. Schimka, J. Harl, G. Kresse, *J. Chem. Phys.* **2011**, *134*, 024116.
[58] S. Jana, B. Patra, H. Myneni, P. Samal, *Chem. Phys. Lett.* **2018**, *713*, 1.
[59] M. A. Marques, J. Vidal, M. J. Oliveira, L. Reining, S. Botti, *Phys. Rev. B* **2011**, *83*, 035119.
[60] T. Bredow, M. Lerch, *Z. Anorg. Allg. Chem.* **2004**, *630*, 2262.
[61] B. Grimm, T. Bredow, *Z. Naturforsch., B* **2022**, *77*, 405.

B. Partial substitution of the Mn atoms in $CaMnO_3$ by first row transition metal atoms: Effect on oxygen vacancy formation

Benjamin Grimm[†] und Thomas Bredow[*]

Veröffentlicht von DeGruyter am 27.04.2022

Der Artikel wird im Einverständnis[‡] der Autoren Benjamin Grimm und Thomas Bredow im Appendix B wieder veröffentlicht.

Partial substitution of the Mn atoms in $CaMnO_3$ by first row transition metal atoms: Effect on oxygen vacancy formation, Zeitschrift für Naturforschung B, 2022, 77(6), 405-410. DOI:https://doi.org/10.1515/znb-2022-0025

[†]Address: Mulliken Center for Theoretical Chemistry, Clausius-Institut für Physikalische und Theoretische Chemie, University of Bonn, Beringstr. 4, 53115 Bonn, Germany.
Email Address: grimm@thch.uni-bonn.de

[*]Address: Mulliken Center for Theoretical Chemistry, Clausius-Institut für Physikalische und Theoretische Chemie, University of Bonn, Beringstr. 4, 53115 Bonn, Germany.
Email Address: bredow@thch.uni-bonn.de

[‡]Anfragen zur Genehmigung der Wiederverwendung von Material aus diesem Kapitel sollten an die Walter de Gruyter GmbH gerichtet werden

Benjamin Grimm and Thomas Bredow*

Partial substitution of the Mn atoms in $CaMnO_3$ by first row transition metal atoms: effect on oxygen vacancy formation

https://doi.org/10.1515/znb-2022-0025
Received February 24, 2022; accepted March 18, 2022;
published online April 27, 2022

Abstract: Sustainable hydrogen production is one of the most challenging topics in modern energy economics. Electrochemical and thermal splitting of water are promising techniques, but are highly energy demanding. Efficient hydrogen evolution reaction catalysts can play a key role to lower the electrolysis potential and to make water splitting more feasible. Among other perovskites, $CaMnO_3$ has been identified as efficient electrode material due to its relatively high oxygen vacancy concentrations at elevated temperatures. But this compound needs to be further improved for technical use. In this study, the effect of Mn substitution in $CaMnO_3$ by 3d metals M = Sc, Ti, V, Cr, Fe, Co, Ni, Cu and Zn on the oxygen vacancy formation energy is investigated theoretically at DFT level. Vacancy formation energies, enthalpies and free enthalpies are calculated with a combination of hybrid and GGA density functionals. Configuration entropy is taken into account by calculating all possible configurations of M and oxygen vacancy site in supercell models. The calculated oxygen vacancy formation energies are strongly affected by Mn/M substitution, the most promising heteroelement being Cu. $CaMn_{0.875}Cu_{0.125}O_{2.875}$ and $CaMn_{0.875}Cu_{0.125}O_{2.75}$ are in equilibrium at 537 K, compared to 1231 K for $CaMnO_{2.875}$/$CaMnO_{2.75}$ and 1350 K for $CaMnO_3$/$CaMnO_{2.875}$.

Keywords: $CaMnO_3$; configuration entropy; density functional theory; hydrogen evolution reaction; metal substitution.

Dedicated to Professor Martin Lerch on the occasion of his 60th birthday.

***Corresponding author: Thomas Bredow**, Mulliken Center for Theoretical Chemistry, Institut für Physikalische und Theoretische Chemie, University of Bonn, Beringstr. 4, 53115 Bonn, Germany, E-mail: bredow@thch.uni-bonn.de
Benjamin Grimm, Mulliken Center for Theoretical Chemistry, Institut für Physikalische und Theoretische Chemie, University of Bonn, Beringstr. 4, 53115 Bonn, Germany, E-mail: grimm@thch.uni-bonn.de

1 Introduction

Hydrogen is a promising energy resource [1] whose combustion to water is a sustainable process. However, so far most of the hydrogen used in industry is produced from hydrocarbons by steam reforming, which is not sustainable [2]. It is therefore of fundamental interest to produce hydrogen in alternative ways [3]. Electrolytic splitting of water is a well-established approach to hydrogen production [4]. The potential required for water electrolysis can be significantly reduced by using a redox active anode material. For this purpose, perovskites ABO_3 are considered as suitable materials, due to their stability and their reversible temperature-dependent oxygen vacancy formation (OVF) [5, 6].

$CaMnO_3$ is a well-known perovskite, which forms oxygen vacancies at temperatures above 1450 K [7] but decomposes into $CaMn_2O_4$ and Ca_2MnO_4 at OV concentrations $CaMnO_{3-\delta}$ with $\delta > 0.3$ [8]. Experimentally, substitution of manganese with 3d metals has been attempted to reduce the OVF energy and to prevent decomposition. Galinsky et al. synthesized $CaMn_{1-x}M_xO_3$ ($x \leq 0.5$) for M = Al, V, Fe, Co, Ni and found significant redox activity for M = Fe at temperatures below 700 K and no evidence for decomposition below 1500 K [9].

In a previous paper [10] we theoretically investigated the OVF thermodynamics of $CaMnO_3$ and identified a suitable computational approach to reproduce experimental reference data. The aim of the present study is to investigate the effect of Mn substitution by other transition metals on the OVF energy. For this purpose, Mn was substituted with all 3d metals M = Sc–Zn, also resulting in $CaMn_{1-x}M_xO_3$. We selected $x = 0.125$ in order to be close to the experimental conditions in Ref. 9. Periodic supercell calculations were performed at density functional theory (DFT) level. OVF energies and magnetizations were calculated with a hybrid density functional for $\delta = 0$, $\delta = 0.125$, and $\delta = 0.25$. Vibration contributions to the thermodynamic functions were calculated with a computationally more efficient GGA functional. Configuration entropy was taken into account by a Boltzmann statistics over possible substitute/OV configurations in selected supercells.

2 Computational details

All calculations were performed with CRYSTAL17 (version 1.0.2) [11], a crystal orbital program which uses linear combinations of Gaussian-type atomic orbitals as basis functions. Due to efficient screening, the calculation of Fock exchange is highly computationally efficient in CRYSTAL. The global hybrid functional PW1PW [12] (with 20% Fock exchange) and the optimized rev2-POB-TZVP basis sets [13] were used for energy calculations. A hybrid functional was chosen as these are known to describe electronic and energetic properties of open-shell transition metal oxides more accurately than standard GGA functionals [14]. In our previous study of OVF in $CaMnO_3$ [10], PW1PW provided best agreement with experimental solid-state reaction and OVF energies among a selection of density functionals. Computationally demanding calculations of vibrational frequencies for supercells were performed with the standard GGA functional PBE [15].

The primitive cell of orthorhombic $CaMnO_3$ (space group *Pnma*) contains four formula units. Experimental room-temperature lattice parameters are a = 5.279 Å, b = 7.448 Å, and c = 5.264 Å [16]. Ca occupies the 4*a* Wyckoff site (0.0331, 0.25, 0.9943), Mn the 4*b* site (0.0, 0.0, 0.5), and O the 8*d* (0.2127, 0.5336, 0.2121) and the 4*c* sites (0.0111, 0.75, 0.5659). The lattice parameters and atom positions optimized with PW1PW/rev2-POB-TZVP are in good agreement with experiment, a = 5.262 Å, b = 7.437 Å, and c = 5.256 Å, Ca 4*a* (0.0303, 0.25, 0.9961), O 8*d* (0.2138, 0.5313, 0.2133), and O 4*c* (0.0093, 0.75, 0.5607). $CaMnO_3$ is formally composed of Ca^{2+}, Mn^{4+}, and O^{2-} ions. The d^3 configuration of Mn^{4+} is assumed as a high-spin quartet state (t_{2g}^3). The G-AFM (antiferromagnetic) spin configuration is the magnetic ground state of $CaMnO_3$ [17], consisting of two interpenetrating face centered lattices with opposite spin. Each Mn ion is surrounded by six Mn neighbors with opposite spin. For all subsequent calculations of the perfect $CaMnO_3$ solid this configuration has been used.

For the calculations of Mn/M substitution, $Ca_{16}Mn_{16}O_{48}$ supercells (see Figure 1) were generated from the primitive cell with a ((0,0,2), (0,1,0), (−2,0,0)) transformation matrix.

Two Mn atoms were substituted by M from the 3d series Sc–Zn. The supercells $Ca_{16}Mn_{14}M_2O_{48}$ correspond to $CaMn_{1-x}M_xO_3$ with x = 0.125. All symmetry-inequivalent M configurations were calculated to determine the most stable cation distributions. In some special cases the G-AFM spin configuration had to be modified to ensure the two substituted atoms have opposite spin. For calculations of the OVF energies, two oxygen atoms of the $Ca_{16}Mn_{14}M_2O_{48}$ supercell were removed. The thus obtained $Ca_{16}Mn_{14}M_2O_{46}$ supercells correspond to $CaMn_{1-x}M_xO_{3-\delta}$ with x = 0.125 and δ = 0.125. The number of symmetry-inequivalent configurations of two oxygen vacancies in the $Ca_{16}Mn_{14}M_2O_{46}$ cell is 1128, which makes it impossible to calculate all of them at high computational level.

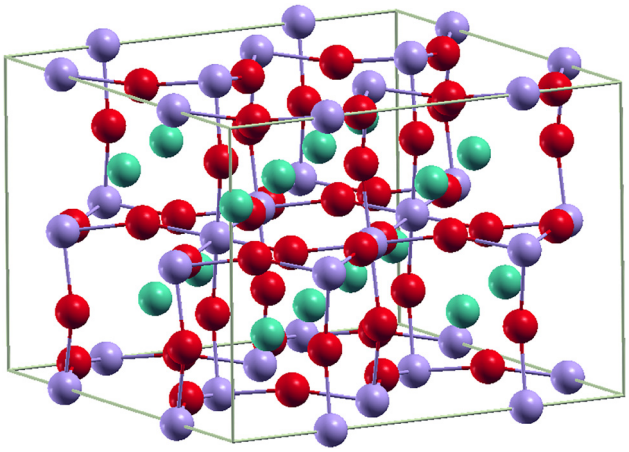

Figure 1: $Ca_{16}Mn_{16}O_{48}$ supercell oxygen (red), manganese (purple), calcium (green).

We therefore followed two strategies to obtain a reasonably large configuration space within the limitations of our computational resources. Strategy 1: all 50 symmetry-inequivalent O vacancy configurations of the unsubstituted $Ca_{16}Mn_{16}O_{46}$ cell were calculated and ordered by energy. Starting from the most stable $Ca_{16}Mn_{16}O_{46}$ configuration all symmetry-inequivalent M configurations in $Ca_{16}Mn_{14}M_2O_{46}$ were calculated. This strategy was adapted for all 3d-atoms with a stable +4 oxidation state (Ti, V, Cr).

Strategy 2 was applied for those 3d metals that are unstable in the +4 oxidation state (Sc, Fe, Co, Ni, Cu, Zn). In these cases only M configurations where both M are next to one oxygen vacancy were selected from the three most stable OV configurations of $Ca_{16}Mn_{16}O_{46}$.

In every defect model an optimization of all atomic positions was performed. For selected cases also the lattice parameters were optimized, but the effect on atomic positions and stability was small.

The calculation of OVF energies for δ = 0.25 (with $Ca_{16}Mn_{14}M_2O_{44}$ cells) is more demanding than for δ = 0.125, since the number of OV configurations is much higher, 6328 for the unsubstituted $Ca_{16}Mn_{16}O_{44}$ cell. We therefore restricted the defect models to those where the two O atoms with the highest magnetization in $Ca_{16}Mn_{14}M_2O_{46}$ were removed. It was assumed that these oxygen atoms are partly oxidized relative to closed-shell O^{2-} and therefore most likely to leave the structure. We are aware that this is a

major simplification and may lead to less accurate results compared to $\delta = 0.125$.

A counterpoise correction was performed for all optimized defect structures by placing ghost atoms at the position of the oxygen vacancies. The OVF energies were calculated with respect to the O_2 molecule in its triplet ground state. For the O_2 reference calculation, the oxygen basis set was converged by adding diffuse functions.

3 Results

3.1 Magnetizations

The magnetizations of the atoms in $CaMn_{0.875}M_{0.125}O_3$ are shown in Table 1.

In all cases, Ca is diamagnetic and Mn has a magnetization of ≈3, corresponding to Ca^{2+} and high-spin Mn^{4+}. The 3d metals with a stable +4 state (Ti, V, Cr) accordingly have magnetizations of approximately zero, one and two. Nevertheless the oxygen magnetization is slightly higher for M = (Ti, V, Cr) compared to the unsubstituted case (Mn). Fe has an average magnetization of 3.4 which is lower than expected for a d^4 high-spin-state of Fe^{4+}. Instead of forming unstable Fe^{4+}, the O^{2-} ions are partly oxidized, as can be seen from their total magnetization 0.9. For Co, a magnetization of 2.5 is calculated, and the total magnetization of the oxygen atoms is 2.2. If we assume that this approximately corresponds to an O-Co charge transfer of two electrons, Co is in a 3+ state. Ni has a magnetization of zero, indicating a d^6 low-spin state. The existence of Ni^{4+} is also confirmed by the relatively small sum of oxygen magnetizations, 0.6. Based on the magnetizations we conclude that Cu and Sc are Cu^{3+}, which is an unusual oxidation state, and Sc^{3+}. For M = Zn, sum of oxygen magnetizations is > 4, in accordance with the expected oxidation state +2 which is formally compensated by oxidation of four O^{2-} to O^-. Analysis of the nearest-neighbor distances d_{O-O}^{min} shows that they are significantly smaller for M = Zn and Sc (2.28 Å for Zn, 2.37 Å for Sc) compared to those of the other M (~2.6 Å). This indicates that the (formal) O^--ions interact with each other to form peroxide ions. d_{O-O} is still larger than in $O^{2-}2$ (1.5–1.6 Å measured in Li_2O_2 [18]), probably because its formation in the substituted oxides is hindered by an activation barrier. Table 2 shows the magnetizations of $CaMn_{0.875}M_{0.125}O_{2.875}$.

For M = Ti, V and Cr, only the Mn magnetization is changed compared to $\delta = 0$ (formally, four Mn^{4+} are reduced to Mn^{3+}). This situation is similar to the unsubstituted case (M = Mn). The average magnetization, however, is only slightly increased from 2.9 to 3.1. For the other cases, the oxygen vacancies are next to the M atoms (strategy 2). That is why in general two Mn atoms and the two M atoms are reduced. For M = Zn, Zn is Zn^{2+}, the neighboring O^{2-} ions are partly oxidized to O^- and the oxidation state of Mn is not altered. Similarly, Sc is Sc^{3+} in $CaMn_{0.875}Sc_{0.125}O_{2.875}$, and two O^{2-} ions are partly oxidized to O^-. Pronounced O^{2-} oxidation is also observed for M = Fe, Co, Ni due to the instability of Fe^{4+}, Co^{4+} and Ni^{4+}. In all cases d_{O-O}^{min} is around 2.55 Å.

3.2 Oxygen vacancy formation energies

Table 3 shows the calculated OVF energies $\Delta_{OVF}E$ for $CaMn_{0.875}M_{0.125}O_3$ and $CaMn_{0.875}M_{0.125}O_{2.875}$, obtained with the supercells $Ca_{16}Mn_{14}M_2O_{48}$, $Ca_{16}Mn_{14}M_2O_{46}$ and $Ca_{16}Mn_{14}M_2O_{44}$, corresponding to $\delta = 0, 0.125$ and 0.25.

Table 1: Average absolute magnetizations μ of the atoms in $CaMn_{0.875}M_{0.125}O_3$ on PW1PW level. The absolute summed, maximal and minimal magnetization of the oxygen atoms are called sum, max and min, d_{O-O}^{min} is minimal O–O distance in Å.

M	μ_{Ca}	μ_{Mn}	μ_M	μ_O	Sum	Max	Min	d_{O-O}^{min}
Sc	0.0	2.89	0.01	0.06	2.87	0.62	−0.58	2.373
Ti	0.0	2.90	0.02	0.01	0.37	0.03	−0.03	2.634
V	0.0	2.89	1.05	0.01	0.67	0.04	−0.04	2.631
Cr	0.0	2.89	2.06	0.01	0.56	0.05	−0.05	2.632
Mn	0.0	2.89	2.89	0.00	0.09	0.00	0.00	2.648
Fe	0.0	2.88	3.44	0.02	0.92	0.13	−0.05	2.596
Co	0.0	2.91	2.45	0.05	2.22	0.18	−0.18	2.606
Ni	0.0	2.88	0.04	0.01	0.61	0.04	−0.04	2.632
Cu	0.0	2.90	0.60	0.04	1.76	0.23	−0.28	2.570
Zn	0.0	2.88	0.01	0.10	4.74	0.62	−0.83	2.281

Table 2: Average absolute magnetizations μ of the atoms in $CaMn_{0.875}M_{0.125}O_{2.875}$ on PW1PW level. The absolute summed, maximal and minimal magnetization of the oxygen atoms are called sum, max and min, d_{O-O}^{min} is minimal O–O distance in Å.

M	μ_{Ca}	μ_{Mn}	μ_M	μ_O	Sum	Max	Min	d_{O-O}^{min}
Sc	0.0	3.02	0.01	0.02	0.85	0.03	−0.04	2.506
Ti	0.0	3.10	0.01	0.01	0.43	0.02	−0.03	2.582
V	0.0	3.09	1.03	0.01	0.60	0.05	−0.05	2.564
Cr	0.0	3.09	2.05	0.01	0.53	0.05	−0.05	2.584
Mn	0.0	3.08	3.08	0.00	0.21	0.01	−0.01	2.299
Fe	0.0	2.98	4.14	0.03	1.36	0.16	−0.17	2.571
Co	0.0	3.02	3.03	0.06	2.92	0.21	−0.21	2.539
Ni	0.0	2.98	0.88	0.02	1.04	0.09	−0.08	2.574
Cu	0.0	3.00	0.07	0.02	0.71	0.05	−0.03	2.518
Zn	0.0	2.89	0.02	0.02	1.06	0.06	−0.06	2.532

Table 3: OVF energies $\Delta_{OVF}E$ (kJ/mol) for $CaMn_{0.875}M_{0.125}O \rightarrow 3\ CaMn_{0.875}M_{0.125}O_{2.875}$ and $CaMn_{0.875}M_{0.125}O_{2.875} \rightarrow CaMn_{0.875}M_{0.125}O_{2.750}$ (kJ/mol) on PW1PW level.

M	$\Delta_{OVF}E_{\delta = 0\rightarrow0.125}$	$\Delta_{OVF}E_{\delta = 0.125\rightarrow0.25}$
Sc	37.0	288.0
Ti	170.2	269.5
V	168.5	326.2
Cr	164.6	180.5
Mn	152.4	143.1
Fe	82.4	238.0
Co	53.0	179.3
Ni	77.6	118.4
Cu	32.0	71.9
Zn	−93.9	180.2

The $CaMnO_3$ OVF energy $\Delta_{OVF}E_{\delta = 0\rightarrow0.125}$ is increased by substitution with M = Ti, V and Cr, while it is decreased with all other 3d metals. This is expected because the latter metals have stable (+2) or (+3) oxidation states which facilitates OVF. For M = Zn $\Delta_{OVF}E_{\delta=0\rightarrow0.125}$ is even negative. We therefore conclude that $CaMn_{0.875}Zn_{0.125}O_3$ does not exist at standard conditions. For Sc and Cu, $\Delta_{OVF}E_{\delta=0\rightarrow0.25}$ is comparably small due to the instability of the oxidation state +4, but still positive. Thus $CaMn_{0.875}Sc_{0.125}O_3$ and $CaMn_{0.875}Cu_{0.125}O_3$ are also expected to be unstable with respect to oxygen loss under ambient pressure. For all compounds except M = Mn (the unsubstituted oxide) and M = Ni, Cu, the second OVF energy ($\delta = 0.125 \rightarrow 0.25$) is much higher than the first. For M = Ti, V, Cr this can be explained by the higher stability of the +4 oxidation state with respect to +3 which is assumed for $\delta = 0.25$. For M = Sc, Fe, Co, Zn the increase is due to the stabilization of the defective structure with $\delta = 0.125$. According to the magnetizations, the Ni and Cu oxidation states are not much different for $\delta = 0.125$ and $\delta = 0.25$ due to partial oxygen reduction. Mn is similarly stable in oxidation states +3 and +4.

3.3 Equilibrium temperatures

To obtain the equilibrium temperature for oxygen loss of the oxides, thermodynamic corrections to the energy must be calculated. As an approximation, the corrections were only calculated for $CaMnO_3$ and $CaMnO_{2.875}$ and transferred to the M-substituted oxides. The harmonic frequency calculations required for this purpose were performed with the standard GGA functional PBE [15] in order to reduce computational cost. In our previous study [10] it was found that PBE and PW1PW provide similar thermodynamic corrections. The free OVF enthalpy $\Delta_{OVF}G$ is calculated from OVF enthalpy $\Delta_{OVF}H$ and OVF entropy $\Delta_{OVF}S$:

$$\Delta_{OVF}G = \Delta_{OVF}H - T\Delta_{OVF}S \tag{1}$$

$\Delta_{OVF}H$ and $\Delta_{OVF}S$ are calculated as the sum of the individual components for translation, rotation, vibration, and electronic excitation. Translation and rotation contributions are not present in solids, and electronic excitations were neglected because the band gaps were larger than the thermal energy RT (between 0.8 and 2.1 eV for the relevant defect configurations and 2.5 eV for the perfect solid on PW1PW level). The OVF free enthalpy was calculated as

$$\Delta_{ODF}E = E^{CaMnO_{3-\lambda}} - E^{CaMnO_3} + \frac{\lambda}{2}E^{O_2} \tag{2}$$

$$\Delta_{therm}H = H^{CaMnO_{3-\lambda}}_{vib} - H^{CaMnO_3}_{vib} + \frac{\lambda}{2}\left(H^{O_2}_{vib} + H^{O_2}_{rot} + H^{O_2}_{trans}\right) \tag{3}$$

$$\Delta_{OVF}H = \Delta_{ODF}E + \Delta_{therm}H \tag{4}$$

$$\Delta_{OVF}S = S^{CaMnO_{3-\lambda}}_{vib} - S^{CaMnO_3}_{vib} + \frac{\lambda}{2}\left(S^{O_2}_{vib} + S^{O_2}_{rot} + S^{O_2}_{trans}\right) \tag{5}$$

The vibrational enthalpy and entropy was calculated from the Boltzmann distribution based on the PBE calculated vibration frequencies ν_i, the temperature T, the pressure p and the cell Volume V (using the Boltzmann constant k and the Planck constant h):

$$H_{vib} = \sum_i \frac{1}{2}h\nu_i + \sum_i \frac{h\nu_i}{e^{\frac{h\nu_i}{kT}} - 1} + pV \tag{6}$$

$$S_{vib} = \frac{1}{T}\left(\sum_i \frac{1}{2}h\nu_i + \sum_i \frac{h\nu_i}{e^{\frac{h\nu_i}{kT}} - 1}\right) + k \cdot \ln\left(\sum_i \frac{e^{\frac{h\nu_i}{2kT}}}{1 - e^{-\frac{h\nu_i}{kT}}}\right) \tag{7}$$

The rotational and translational enthalpy for gas-phase O_2 are calculated from common ideal gas formulas using the ideal gas constant R.

$$H_{rot} = RT \tag{8}$$

$$H_{trans} = \frac{3}{2}RT \tag{9}$$

The entropy of O_2 was taken from the NIST chemical webbook [19] (205.152 kJ/mol at room temperature). For the defect structure, configuration enthalpy and entropy have to be added to the thermal contributions

$$\Delta S_{conf} = -R\sum_i g_i p_i \ln(p_i) \tag{10}$$

$$\Delta H_{conf} = \sum_i (E_i - E_0) g_i p_i, \tag{11}$$

for defect configurations i with their degeneracy g_i due to symmetry equivalence and Boltzmann weight p_i. For

δ = 0.125 all 50 symmetry-independent defect configurations were taken into account, while for δ = 0.25 the computation of 6328 symmetry-independent configurations was too demanding, as mentioned above. Here we assumed that the change in configuration enthalpy and entropy between δ = 0 and 0.125 is comparable to the change between δ = 0.125 and 0.25.

The equilibrium temperature T_{eq} corresponds to the zero of the free enthalpy (Eqn. (1)) and is therefore calculated as

$$T_{eq} = \frac{\Delta_{OVF}H}{\Delta_{OVF}S} \quad (12)$$

Using the OVF energies from Table 3 and Eq. (12), the equilibrium temperatures of $CaMn_{0.875}M_{0.125}O_{2.875}$ were calculated (see Figure 2, Tables 4 and 5).

Mn substitution with Ti, V and Cr leads to increased equilibrium temperatures compared to $CaMnO_3$. Substitution with Fe, Co or Ni leads to equilibrium temperatures of 727, 464 and 684 K, respectively. This fits well with the experimental T_{eq} for Fe, ≈400 °C [9]. With M = Cu or Sc, the equilibrium temperature is 278 (322) K, so oxygen vacancies are already formed near room temperature. Substitution with Zn leads to an unstable solid which does not exist without oxygen vacancies. If δ is increased to 0.25, the equilibrium temperatures for M are in general higher than for Mn (1231 K), except M = Cu (537 K) and M = Ni (900 K). $CaMnO_3$ is a special case where the second equilibrium temperature is smaller than the first. This is related to the fact that δ = 0.25 is already close to the δ threshold for decomposition [8].

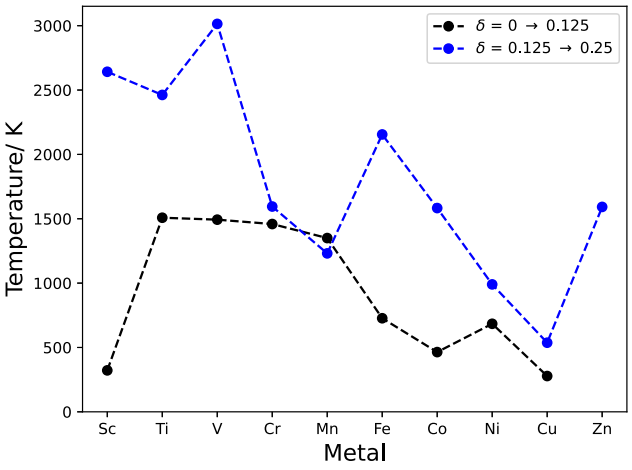

Figure 2: OVF equilibrium temperatures of $CaMn_{0.875}M_{0.125}O_{2.875}$ on PW1PW/PBE level.

Table 4: Thermodynamic corrections for OVF of $CaMnO_3$ on PBE level at 1273 K.

	Δ^{H}_{therm}/kJ/mol	$\Delta_{therm}S$/J/(K* mol)
$\delta = 0 \rightarrow 0.125$	−0.8	112.3
$\delta = 0.125 \rightarrow 0.25$	−16.7	102.7

Table 5: OVF equilibrium temperatures of $CaMn_{0.875}M_{0.125}O_{2.875}$ on PW1PW/PBE level.

M	$T_{eq}/K_{\delta = 0 \rightarrow 0.125}$	$T_{eq}/K_{\delta = 0.125 \rightarrow 0.25}$
Sc	322	2642
Ti	1508	2462
V	1493	3014
Cr	1459	1595
Mn	1350	1231
Fe	727	2155
Co	464	1583
Ni	684	990
Cu	278	537
Zn	–*	1592

*: defect structure already present at 0 K.

4 Summary and conclusions

Quantum-chemical calculations at hybrid DFT level showed that the oxygen vacancy formation energy of $CaMnO_3$ can be significantly reduced by substitution of the Mn atom by 3d metals. The choice of the 3d metal is important, most suitable are 3d metals which prefer the +3 oxidation state over +4. On the one hand, Ti, V and Cr increase the defect formation energy, on the other hand Mn/Sc- and Mn/Zn-substituted $CaMnO_3$ is not stable under ambient conditions. Mn/Fe, Mn/Co, and Mn/Ni substitutions already form oxygen vacancies between 464 and 727 K. Particularly promising is $Ca(Mn,Cu)O_{3-\lambda}$, which already forms oxygen vacancies near room temperature. In addition, due to the high stability of Cu(I) and Cu(II), Mn/Cu substitution may stabilize $Ca(Mn,Cu)O_{3-\lambda}$ with higher amounts of oxygen vacancies, different from Mn/Fe, Mn/Co and Mn/Ni substitutions. This is seen by the significantly smaller $\Delta_{OVF}E_{\delta=0.125\rightarrow0.25}$ compared to Fe, Co and Ni. Thus, based on the present theoretical results, Mn/Cu substitution in $CaMnO_3$ is a promising route for more active perovskites in the hydrogen evolution reaction.

Author contribution: All the authors have accepted responsibility for the entire content of this submitted manuscript and approved submission.
Research funding: None declared.

Conflict of interest statement: The authors declare no conflicts of interest regarding this article.

References

1. Abe J. O., Popoola A., Ajenifuja E., Popoola O. Hydrogen energy, economy and storage: review and recommendation. *Int. J. Hydrogen Energy* 2019, *44*, 15072–15086.
2. Palo D. R., Dagle R. A., Holladay J. D. Methanol steam reforming for hydrogen production. *Chem. Rev.* 2007, *107*, 3992–4021.
3. Dincer I. Green methods for hydrogen production. *Int. J. Hydrogen Energy* 2012, *37*, 1954–1971.
4. Gahleitner G. Hydrogen from renewable electricity: an international review of power-to-gas pilot plants for stationary applications. *Int. J. Hydrogen Energy* 2013, *38*, 2039–2061.
5. Bhalla A., Guo R., Roy R. The perovskite structure—a review of its role in ceramic science and technology. *Mater. Res. Innovat.* 2000, *4*, 3–26.
6. Niu G., Guo X., Wang L. Review of recent progress in chemical stability of perovskite solar cells. *J. Mater. Chem. A* 2015, *3*, 8970–8980.
7. Bulfin B., Vieten J., Starr D., Azarpira A., Zachäus C., Hävecker M., Skorupska K., Schmücker M., Roeb M., Sattler C. Redox chemistry of $CaMnO_3$ and $Ca_{0.8}Sr_{0.2}MnO_3$ oxygen storage perovskites. *J. Mater. Chem. A* 2017, *5*, 7912–7919.
8. Bakken E., Norby T., Stølen S. Nonstoichiometry and reductive decomposition of $CaMnO_{3-\delta}$. *Solid State Ionics* 2005, *176*, 217–223.
9. Galinsky N., Sendi M., Bowers L., Li F. CaMn1- xBxO3- δ (B= Al, V, Fe, Co, and Ni) perovskite based oxygen carriers for chemical looping with oxygen uncoupling (CLOU). *Appl. Energy* 2016, *174*, 80–87.
10. Grimm B., Bredow T. Defect formation thermodynamics of CaMnO3: a closer look, 2022. *ChemPhysChem*. submitted.
11. Dovesi R., Erba A., Orlando R., Zicovich-Wilson C. M., Civalleri B., Maschio L., Rérat M., Casassa S., Baima J., Salustro S. Others Quantum-mechanical condensed matter simulations with CRYSTAL. *Wiley Interdiscip. Rev. Comput. Mol. Sci.* 2018, *8*, e1360.
12. Bredow T., Gerson A. R. Effect of exchange and correlation on bulk properties of MgO, NiO, and CoO. *Phys. Rev. B* 2000, *61*, 5194.
13. Vilela Oliveira D., Laun J., Peintinger M. F., Bredow T. BSSE-correction scheme for consistent Gaussian basis sets of double-and triple-zeta valence with polarization quality for solid-state calculations. *J. Comput. Chem.* 2019, *40*, 2364–2376.
14. Bredow T., Stahl B. Systematic variation of Fock exchange in hybrid functionals: effect on the structural, electronic and energetic properties of VO_2. *Chem. Phys. Lett.* 2018, *695*, 28–33.
15. Perdew J. P., Burke K., Ernzerhof M. Generalized gradient approximation made simple. *Phys. Rev. Lett.* 1996, *77*, 3865.
16. Poeppelmeier K. R., Leonowicz M., Scanlon J., Longo J., Yelon W. Structure determination of $CaMnO_3$ and $CaMnO_{2.5}$ by X-ray and neutron methods. *J. Solid State Chem.* 1982, *45*, 71–79.
17. Wollan E., Koehler W. Neutron diffraction study of the magnetic properties of the series of perovskite-type Compounds [(1- x) La, x Ca] MnO_3. *Phys. Rev.* 1955, *100*, 545.
18. Cota L. G., de la Mora P. On the structure of lithium peroxide. Li_2O_2. *Acta Crystallogr. B* 2005, *61*, 133–136.
19. Linstrom P., W. G. Mallard E., Eds. *NIST Chemistry WebBook, NIST Standard Reference Database Number 69*; Institute of Standards and Technology, 2022.

C. Defect formation thermodynamics of (A, A')(B, B')O_3 (A=Mg,Ca,Sr and B=Ti,Mn,Cr,Fe,Mo) perovskites

Benjamin Grimm[†] und Thomas Bredow[*]

Eingereicht am 02.02.2023, Akzeptiert am 13.03.2023, Online veröffentlicht am 22.03.2023

Der Artikel wird im Einverständnis[‡] der Autoren Benjamin Grimm und Thomas Bredow im Appendix C wieder veröffentlicht.

Defect formation thermodynamics of (A, A')(B, B')O_3 (A=Mg,Ca,Sr and B=Ti,Mn,Cr,Fe,Mo) perovskites, Phys. Status Solidi B,2023,260,202300048. DOI:https://doi.org/10.1002/pssb.202300048

[†]Address: Mulliken Center for Theoretical Chemistry, Clausius-Institut für Physikalische und Theoretische Chemie, University of Bonn, Beringstr. 4, 53115 Bonn, Germany.
Email Address: grimm@thch.uni-bonn.de

[*]Address: Mulliken Center for Theoretical Chemistry, Clausius-Institut für Physikalische und Theoretische Chemie, University of Bonn, Beringstr. 4, 53115 Bonn, Germany.
Email Address: bredow@thch.uni-bonn.de

[‡]Anfragen zur Genehmigung der Wiederverwendung von Material aus diesem Kapitel sollten an die Wiley-VCH GmbH gerichtet werden

RESEARCH ARTICLE

physica status solidi b

www.pss-b.com

Defect Formation Thermodynamics of $(A, A')(B, B')O_3$ (A = Mg,Ca,Sr and B = Ti,Mn,Cr,Fe,Mo) Perovskites

Benjamin Grimm and Thomas Bredow*

In a previous theoretical study [B. Grimm and T. Bredow, Oxygen Defect Formation Thermodynamics of $CaMnO_3$: A Closer Look. Phys. Status Solidi B 2022, https://doi.org/10.1002/pssb.202200427], the structural, thermodynamic, and electronic properties of $CaMnO_3$ have been studied. The present study increases the range of compounds to ternary perovskites in a search for suitable anode materials for high-temperature water electrolysis. $(A, A')(B, B')O_3$ compounds containing the abundant elements A = Mg,Ca,Sr and B = Ti,Mn,Cr,Fe,Mo are studied theoretically on hybrid density functional theory level. Criteria for a suitable electrode material are low-oxygen defect formation energy and high reaction energy for decomposition into other phases. Based on these criteria, the most suitable ABO_3 perovskites are chosen as starting points to create stable mixed compounds. The compound $Ca_{0.5}Sr_{0.5}Fe_{0.25}Mn_{0.75}O_{3-\delta}$ is found to be the optimal choice as electrode material, with an oxygen defect concentration of at least $\delta = 0.1875$ present at 520 K and highly endothermic decomposition reactions.

1. Introduction

Sustainable hydrogen production is fundamental for future energy supply.[1] Its realization is possible, for example, by electrocatalytic water splitting, but this requires a high amount of electric power.[2] A distinction is made between low-temperature (70–90 °C) and high-temperature electrolysis (up to 1000 °C).[3] High-temperature electrolysis requires significantly less electric power and is sustainable if heat is generated by a clean energy source such as sunlight. Additionally, the electrochemical potential can be lowered using an electrochemically active anode material. Perovskites are particularly suitable, since they are structurally and chemically stable, but reversibly exchange oxygen with the environment[4] at higher temperatures.

B. Grimm, T. Bredow
Mulliken Center for Theoretical Chemistry
Clausius-Institut für Physikalische und Theoretische Chemie
University of Bonn
Beringstr. 4, 53115 Bonn, Germany
E-mail: grimm@thch.uni-bonn.de

The ORCID identification number(s) for the author(s) of this article can be found under https://doi.org/10.1002/pssb.202300048.

DOI: 10.1002/pssb.202300048

Bulfin et al. experimentally investigated the redox chemistry of $CaMnO_3$ and $Ca_{0.8}Sr_{0.2}MnO_3$ and found substantial formation of oxygen vacancies at temperatures above 1173 K for $CaMnO_3$ and above 1073 K for $Ca_{0.8}Sr_{0.2}MnO_3$.[5] These temperatures are in the typical range of high-temperature electrolysis.[3] While $CaMnO_3$ decomposes into Ca_2MnO_4 and $CaMn_2O_4$ at higher oxygen defect concentrations, no decomposition was observed for $Ca_{0.8}Sr_{0.2}MnO_3$. Vieten et al. computed thermodynamic properties of 240 $(A_xA'_{1-x})(B_yB'_{1-y})O_{3-\delta}$ compounds using VASP and a combination of generalized gradient approximation density functional theory (DFT) and one-center Hubbard corrections (GGA + U).[6] An empirical model was developed based on these data to compute the amount of oxygen vacancies δ dependent on oxygen partial pressure and temperature. However, they used a strong simplification assuming that all ABO_3 structures have an idealized cubic structure. Their results for oxygen vacancy formation (OVF) formation enthalpies deviate from the experiment by 20–30 kJ mol^{-1} and also some outliers were found.

In this work, thermodynamic properties of ABO_3 compounds with A = Mg, Ca, Sr and B = Ti, Mn, Cr, Fe, Mo were computed on hybrid DFT level. Our aim was to find a compound with a low OVF energy and with endothermic decomposition into the oxides A_2BO_4 and AB_2O_4. We took into account a variety of possible crystal structures for each oxide. To find the most stable polymorph, all ABO_3 polymorphs mentioned in the Materials Project[7] database were considered. For the respective most stable polymorphs of each compound, OVF and decomposition energies into AB_2O_4 and A_2BO_4 were calculated. Binary oxides ABO_3 with lowest defect formation energies were used as basis for generating quaternary $(A, A')(B, B')O_3$ compounds. OVF energies and decomposition energies of selected stable mixtures were computed. From phonon calculations, the vibration contributions to the Gibbs energy $G(T)$ were obtained, in order to estimate the transition temperature of phase transitions. In this way the suitability of the mixed oxides as electrode materials for high-temperature electrolysis was assessed.

2. Computational Details

All calculations were performed with the crystal-orbital program CRYSTAL17 (version 1.0.2),[8] which uses linear combinations of Gaussian-type atomic orbitals as basis functions of the crystal

orbitals. The global hybrid functional PW1PW[9] was used in combination with the pob-TZVP-rev2 solid-state basis sets,[10,11] since this provided the most accurate results for the defect formation thermodynamics of $CaMnO_3$.[12] The Monkhorst–Pack grid was adapted to each crystal structure to ensure sufficiently high k-point density. The integration truncation parameters TOLINTEG were set to 7,7,7,7,14.

For the calculation of ABO_3 compounds all available space groups (SG) for A = Mg, Ca, Sr and B = Ti, Mn, Cr, Fe, Mo were collected from the Materials Project[7] database (SG = 2, 12, 14, 15, 20, 51, 62, 63, 74, 140, 146, 148, 186, 194, and 221). These were then used to create initial structures for full geometry optimizations of all atom positions and lattice parameters. In this way, the most stable polymorph was determined for each of the resulting 15 ABO_3 compounds. In some cases, structures with different space groups converged to the same result during geometry optimization. The SG with highest symmetry was then selected for further calculations. For the calculation of decomposition energies (reaction 1), the most stable polymorphs of AB_2O_4 and A_2BO_4 were determined in the same way.

$$ABO_3 \rightarrow \frac{1}{3}A_2BO_4 + \frac{1}{3}AB_2O_4 + \frac{1}{6}O_2 \quad (1)$$

In the following sections, the investigation of the oxygen defect formation is explained (reaction 2).

$$ABO_3 \rightarrow ABO_{3-\delta} + \frac{\delta}{2}O_2 \quad (2)$$

We only consider neutral unit cells here since our model corresponds to neutral O_2 formation. According to Kröger–Vink notation the oxygen vacancy sites are close to $V_O^{\cdot\cdot}$, since the Mulliken population of ghost functions at the defect site is below 0.3e in all cases. The change in spin population of the neighboring transition metal atoms indicates that they are oxidized, as described in our previous work.[13] As described by Bjørheim et al.[14] charged defects play an important role in $BaZrO_3$. The instability of the Zr(III) state leads to formation of $V_O^{\cdot}$ defects. However, for the compounds in this work, the investigation of neutral defects is sufficient.

The oxygen-deficient ABO_3 structures were created starting from an almost cubic supercell of the most stable polymorph with a side length of ≈10 Å, corresponding to $A_{16}B_{16}O_{48}$. In principle there are 48 different configurations for the $A_{16}B_{16}O_{47}$ cell (corresponding to $\delta = 0.0625$). For the highly symmetric ABO_3 structures, only 2–3 distinct configurations exist since all others are symmetry equivalent. But for the mixed perovskites (with reduced symmetry), we had to consider all 48 configurations. Since geometry optimizations at the hybrid DFT level are demanding for large numbers of configurations of these relatively large cells, two strategies were pursued to find the most stable defect site within the limits of our computational resources.

2.1. Approach 1

The oxygen atom with the largest magnetization in the stoichiometric supercell was removed. In order to increase symmetry, we adopted a ferromagnetic state for all systems instead of more complicated spin configurations. This was mainly relevant for the transition metal atoms, but small magnetizations were also present on the oxygen atoms. Here it was assumed that high magnetization indicates a tendency toward oxygen reduction which is the first step of defect formation.

2.2. Approach 2

Single-point energy calculations were performed for all 48 defect positions, assuming atomic positions of the perfect bulk. For the preselected structures, full geometry optimizations were performed in a second step.

In most cases, approach 2 led to more stable structures. In selected cases, geometry optimization of the second most stable defect configuration was performed, but this did not lead to a change in stability order. Thus we conclude that the present approach is justified. Only in few examples, approach 1 led to a more stable structure than approach 2. In these cases, relaxation of the atoms surrounding the oxygen vacancy is essential, so that single-point energies are not representative.

There are $\binom{48}{2} = 1128$ possible combinations to remove two oxygen atoms from the $A_{16}B_{16}O_{48}$ cell ($\delta = 0.125$). To reduce the number of time-consuming calculations, only the 47 defect positions from the most stable $A_{16}B_{16}O_{47}$ cell were taken into account. The most stable structure of the $A_{16}B_{16}O_{46}$ supercell was determined analogous to the procedure for the first defect. Similarly, only 46 sites were considered for the third oxygen vacancy ($\delta = 0.1875$) starting from the most stable $A_{16}B_{16}O_{46}$ configuration. From selected binary compounds having small OVF and large decomposition energies, mixed compounds with different $(A_xA'_{1-x})$ and $(B_yB'_{1-y})$ ratios (in steps of 0.25 for x, y) were generated. The most stable polymorph for each mixed compound was determined from the most stable polymorphs of the respective binary oxide. Due to the high computational demand, only a selection of the configurations of the primitive cell were calculated.

Mixing energy and mixing entropy were calculated for all mixed oxides. The mixing energy δE_{mix} of a perovskite $A_xA'_{1-x}B_yB'_{1-y}O_3$ is given as (Equation (3))

$$\begin{aligned}\delta E_{mix} = {} & E^{A_xA'_{1-x}B_yB'_{1-y}O_3} \\ & - xyE^{ABO_3} - (1-x)yE^{A'BO_3} \\ & - x(1-y)E^{AB'O_3} - (1-x)(1-y)E^{A'B'O_3}\end{aligned} \quad (3)$$

The configuration mixing entropy δS_{mix} was approximated according to Bulfin et al.[15] as (Equation (4))

$$\delta S_{mix} = -R(x\ln(x) + (1-x)\ln(1-x) + y\ln(y) + (1-y)\ln(1-y)), \quad (4)$$

where R is the ideal gas constant and x is the fraction of defects or substituted atoms. The formulas for mixing energy and entropy were already successfully used by Fuks et al. for computing solid solutions of $(Ba, Sr)(Co, Fe)O_3$ and $Ba_cSr_{1-c}TiO_3$.[16,17]

Neglecting the thermodynamic contributions (see below), the Gibbs energy of mixing was approximated by Equation (5).

$$\delta G_{\mathrm{mix}}^{\mathrm{approx}} = \delta E_{\mathrm{mix}} - T\delta S_{\mathrm{mix}}^{\mathrm{approx}} \tag{5}$$

The most stable mixed compounds are those with the most negative Gibbs energy of mixing. From these, the defect formation energies were calculated in the same way as for the ABO_3 compounds. Higher defect concentrations were then calculated for the mixed compounds with the smallest defect formation energies. Vibrational contributions to the thermodynamic functions were neglected here because we found in recent work that the frequencies are not very sensitive to small structural changes.[12]

The thermodynamic functions of the decomposition reactions into the parent oxides and the defect formation reactions were calculated in a different way. The calculated $G(T)$ is used to compute the stability of the defect structures relative to the perfect solid and with respect to selected decomposition products in the experimentally relevant temperature range. In this case, phonon calculations were performed to obtain the vibration contributions to the Gibbs energy of reaction $\delta_r G$, the reaction enthalpy $\delta_r H$, and reaction entropy $\delta_r S$ (Equation (6)).

$$\delta_r G(T) = \delta_r H(T) - T \cdot \delta_r S(T) \tag{6}$$

From $\delta_r G(T)$, the temperature-dependent equilibrium OV concentration and the stability with respect to decomposition products was calculated. In general, $\delta_r H$ and $\delta_r S$ are the sum of the individual components for translation, rotation, vibration, and electronic excitation. Translation and rotation are not present in solids. Electronic excitations were neglected because the fundamental bandgaps were larger than the thermal energy kT (2.5 eV for $CaMnO_3$ on PW1PW level). For decomposition the Gibbs energy relative to $A_xA'_{1-x}B_yB'_{1-y}O_3$ was obtained via Equation (7).

$$\begin{aligned}\delta_r G(T) = {} & \frac{1}{3} H_{\mathrm{vib}}^{\mathrm{A_xA'_{2-2x}B_yB'_{2-2y}O_4}}(T) + \frac{1}{3} H_{\mathrm{vib}}^{\mathrm{A_{2x}A'_{2-2x}B_yB'_{1-y}O_4}}(T) \\ & + \frac{1}{6} H^{\mathrm{O_2}} - H_{\mathrm{vib}}^{\mathrm{A_xA'_{1-x}B_yB'_{1-y}O_3}}(T) \\ & - T\left(\frac{1}{3} S_{\mathrm{vib}}^{\mathrm{A_xA'_{1-x}B_{2y}B'_{2-2y}O_4}}(T) + \frac{1}{3} S_{\mathrm{vib}}^{\mathrm{A_{2x}A'_{2-2x}B_yB'_{1-y}O_4}}(T)\right. \\ & \left. + \frac{1}{6} S^{\mathrm{O_2}} - S_{\mathrm{vib}}^{\mathrm{A_xA'_{1-x}B_yB'_{1-y}O_3}}(T)\right)\end{aligned} \tag{7}$$

The thermodynamic properties of gas-phase O_2 were taken from the NIST chemical webbook.[18]

For the defect formation reaction, the Gibbs energy is calculated by Equation (8).

$$\begin{aligned}\delta_r G(T) = {} & H_{\mathrm{vib}}^{\mathrm{A_xA'_{1-x}B_yB'_{1-y}O_{3-\delta}}}(T) + \frac{\delta}{2} H^{\mathrm{O_2}} \\ & - H_{\mathrm{vib}}^{\mathrm{A_xA'_{1-x}B_yB'_{1-y}O_3}}(T) \\ & - T\left(S_{\mathrm{vib}}^{\mathrm{A_xA'_{1-x}B_yB'_{1-y}O_{3-\delta}}}(T) + \frac{\delta}{2} S^{\mathrm{O_2}} - S_{\mathrm{vib}}^{\mathrm{A_xA'_{1-x}B_yB'_{1-y}O_3}}(T)\right)\end{aligned} \tag{8}$$

The vibrational enthalpy (Equation (9)) and entropy (Equation (10)) were calculated from the phonon frequencies ν_i, the temperature T, the pressure p, and the cell Volume V (using the Boltzmann constant k and the Planck constant h).

$$H_{\mathrm{vib}} = E_{\mathrm{el}} + \sum_i \frac{1}{2} h\nu_i + \sum_i \frac{h\nu_i}{e^{\frac{h\nu_i}{kT}} - 1} + pV \tag{9}$$

$$S_{\mathrm{vib}} = \frac{1}{T}\left(\sum_i \frac{1}{2} h\nu_i + \sum_i \frac{h\nu_i}{e^{\frac{h\nu_i}{kT}} - 1}\right) + k \cdot \ln\left(\sum_i \frac{e^{\frac{h\nu_i}{2kT}}}{1 - e^{-\frac{h\nu_i}{kT}}}\right) \tag{10}$$

The frequencies were calculated with the GGA functional PBE[19] because hybrid functionals are too demanding for phonon calculations of larger supercells. Test calculations showed that the differences in δ_{therm} between PBE and PW1PW are only a few kJ mol^{-1}. In principle, conformational entropies similar to Equation (4) should be also taken into account. However, the conformational entropies can be neglected in the temperature range (300–800 K) because the Gibbs energies only change about 0.1 kJ mol^{-1}.

3. Results

3.1. ABO_3 Polymorphs

First of all it is necessary to calculate the perfect structures of the ABO_3 compounds with A = Mg,Ca,Sr and B = Ti,Mn,Cr,Fe,Mo. For this purpose it is mandatory to consider several possible phases since in many cases the most stable polymorph has not yet been identified. The Materials Project database[7] provides a large number of possible ABO_3 structures for the compounds of interest. From these structures space groups and initial atom positions and lattice parameters for all 15 compounds were taken. The next step was to determine the most stable phase for all compounds based on the relative energies. **Figure 1** shows the calculated relative energies of the ABO_3 polymorphs.

For $CaFeO_3$ the polymorph with SG 14 is most stable at PW1PW level, in agreement with the experiment,[20] whereas in the Materials Project database, the slightly less stable polymorph with SG 62 is reported as ground state. For $CaMnO_3$, the polymorphs with SG 14, 20, and 62 are quasidegenerate with

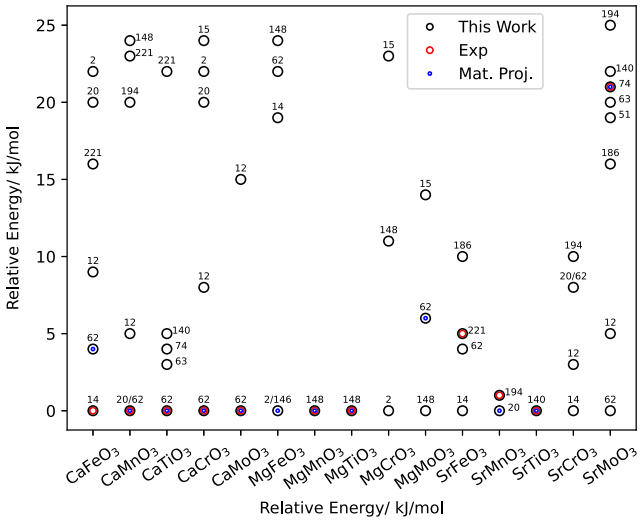

Figure 1. Relative energies of ABO_3 polymorphs calculated with PW1PW. Experimental low-temperature polymorphs in red, most stable polymorphs according to Materials Project[7] in blue.

relative energies 0.2, 0.0X, and 0.1 kJ mol^{-1} (see Table S1, Supporting Information). In such cases the tool FINDSYM was used to check whether the minima are identical within given numerical precision.[21] Here it turned out that the PW1PW optimizations with SG 14 and 62 (but not SG 20) both converged into the same minimum, so only results of the higher SG 62 are reported (which is the experimental ground-state structure).[5] The same was observed for $CaTiO_3$, $CaCrO_3$, and $CaMoO_3$. Thus, for each of these four compounds, the experimentally most stable polymorph with SG 62 was confirmed.[22–24] For $MgMnO_3$ and $MgTiO_3$, SG 2 and 148 polymorphs were optimized into the same minimum. After symmetry analysis we confirm the experimental ground-state structure with SG 148.[25,26] For $SrFeO_3$, SG 14 polymorph is most stable. The experimental structure with SG 221[27] is predicted to be 4.6 kJ mol^{-1} less stable. For $SrMnO_3$, the optimized SG 20 and 186 structures are nearly identical. The experimental structure with SG 194[28] is only slightly less stable. $SrTiO_3$ is a special case where initial structures with SG 12,14, 51, 62, 63, 74, 140, and 221 converged to the same minimum. The experimental low-temperature structure has SG 140, while the cubic perovskite structure (SG 221) occurs at high temperatures.[29] The two structures are energetically and structurally similar, so our theoretical approach cannot distinguish between them. The results for $SrMoO_3$ are in less agreement with experiment. The experimentally reported ground-state structure with SG 74 is 20.7 kJ mol^{-1} less stable than the most stable calculated structure with SG 62.[30] No experimental data are available for $MgFeO_3$, $MgCrO_3$, $MgMoO_3$, and $SrCrO_3$.

3.2. Defect Formation Energies of Most Stable ABO_3 Polymorphs

Defect formation energies δE_{OVF} and decomposition energies $\delta E_{Decompose}$ were calculated for selected ABO_3 compounds. The decomposition reaction (Equaton (1)), which is preferred for $CaMnO_3$,[31] was assumed for all compounds. Similar to the procedures described in the previous section, the most stable polymorph for each of the AB_2O_4 and A_2BO_4 compounds was determined for this purpose (see Supporting Information). The defect formation reaction corresponds to Equation (2). **Table 1** lists the defect formation energies and decomposition energies for the 15 selected ABO_3 perovskites. Furthermore, the size of the supercell used for the defect calculation (according to the procedure described in Computational Details) was given.

The values in Table 1 provide a basis for selecting the most promising binary compounds as candidates for quaternary mixed perovskites. $CaMnO_3$ is our reference compound. It is experimentally known that the defect concentration δ of $CaMnO_{3-\delta}$ is limited by decomposition into AB_2O_4 and A_2BO_4.[31] Its defect formation energy, $\delta E_{OVF} = 184$ kJ mol^{-1}, is 2.7 times larger than the decomposition energy ($\delta E_{Decompose} = 499$ kJ mol^{-1}). An improved electrode material should have a lower OVF energy and a larger decomposition energy than $CaMnO_3$. The lower decomposition energy leads to OVF at lower temperatures and the higher decomposition energy decreases the decomposition rate.

According to the calculated δE_{OVF}, the suitability as electrode material deteriorates when B = Mo or Ti ($\delta E_{OVF} = 309 - 658$ kJ mol^{-1}). For Ti this can be explained by the higher stability of Ti^{4+} compared to Ti^{3+} in the oxide lattice, which disfavors the defect state. For Mo, the larger ionic radius could be problematic for the stabilization of the defects. For the Cr perovskites, the difference between decomposition energy and OVF energy is either very small ($SrFeO_3$), or the decomposition energy is even smaller ($SrCrO_3$ and $CaCrO_3$). The OVF energy is slightly larger compared to $CaMnO_3$, while the decomposition is strongly favored. Therefore, the Cr perovskites are also not suitable as electrode materials. If Mg is used instead of Ca, the decomposition energy becomes even more negative.

Only the elements A = Ca,Sr and B = Mn,Fe remain as suitable candidates, in agreement with previous studies.[6,32] For Fe, both decomposition and OVF are facilitated compared to Mn, while for Sr the OVF energy remains similar compared to Ca, but decomposition is more endothermic. Therefore we conclude that a combination of Ca, Sr, Mn, and Fe may be a good candidate for a suitable electrode material.

Table 1. Defect formation energies (Equation (2), $\delta = 0.0625$) per half mole O_2 in kJ mol^{-1} on PW1PW level. $\delta E_{Decompose}$ is the decomposition energy into AB_2O_4 andA_2BO_4 (Equation (1)).

Compound	Spacegroup	Supercell	δE_{OVF}	$\delta E_{Decompose}$
$SrFeO_3$	14	2 × 2 × 1	4.8	260.8
$CaFeO_3$	14	2 × 2 × 1	46.2	–3.2
$MgFeO_3$	148	2 × 2 × 2	176.9	–742.4
$CaMnO_3$	20	2 × 2 × 1	183.6	499.2
$SrMnO_3$	20	2 × 2 × 1	189.4	977.6
$SrCrO_3$	14	2 × 2 × 1	206.5	224.0
$CaCrO_3$	62	2 × 1 × 2	220.7	44.8
$MgCrO_3$	2	2 × 2 × 2	286.5	–385.6
$MgMnO_3$	148	2 × 2 × 2	299.0	374.4
$SrMoO_3$	62	2 × 1 × 2	309.0	2356.8
$MgMoO_3$	148	2 × 2 × 2	518.9	1526.4
$CaMoO_3$	62	2 × 1 × 2	541.5	2328.0
$SrTiO_3$	140	2 × 2 × 2	600.0	3107.2
$MgTiO_3$	148	2 × 2 × 2	638.9	2268.8
$CaTiO_3$	62	2 × 1 × 2	658.1	2873.6

3.3. Mixing Energies

The next step is to construct unit cells for the mixed compounds consisting of $CaMnO_3$, $CaFeO_3$, $SrMnO_3$ and $SrFeO_3$, which were selected as most promising binary perovskites in the previous section. For this purpose, as explained in Computational Details, the most stable conformations of the individual mixed perovskites were determined and the Gibbs energies of mixing were approximated from the mixing energies and conformational entropies (Equation (3) and (4)). **Table 2** lists the mixing energies and Gibbs energies for the mixed perovskites with the ten lowest Gibbs energies of mixing, all others can be found in the Supporting Information. For the approximated mixing Gibbs energy, a temperature $T = 800$ K was assumed which is typical for the defect formation reactions (see above).

Table 2. Mixing energies per formula unit δE_{mix} (Equation (3)) in kJ mol^{-1} on PW1PW level, mixing entropies δS_{mix} (Equation (4)) in J (K mol)$^{-1}$, and approximated mixing Gibbs energies δG_{mix}^{approx} (Equation (5)) in kJ mol^{-1} at 800 K. The supercell size is 2 × 2 × 1 for all compounds.

Compound	SG	δE_{mix}	δS_{mix}	δG_{mix}^{approx}
$Ca_{0.5}Sr_{0.5}Fe_{0.0}Mn_{1.0}O_3$	20	−2.5	5.8	−7.1
$Ca_{0.75}Sr_{0.25}Fe_{0.0}Mn_{1.0}O_3$	20	−1.0	4.7	−4.8
$Ca_{1.0}Sr_{0.0}Fe_{0.5}Mn_{0.5}O_3$	14	0.7	5.8	−3.9
$Ca_{0.5}Sr_{0.5}Fe_{0.25}Mn_{0.75}O_3$	20	5.4	10.4	−3.2
$Ca_{0.25}Sr_{0.75}Fe_{0.0}Mn_{1.0}O_3$	20	0.7	4.7	−3.1
$Ca_{0.25}Sr_{0.75}Fe_{0.25}Mn_{0.75}O_3$	20	6.2	9.4	−1.3
$Ca_{1.0}Sr_{0.0}Fe_{0.75}Mn_{0.25}O_3$	14	3.4	4.7	−0.4
$Ca_{0.75}Sr_{0.25}Fe_{0.5}Mn_{0.5}O_3$	20	8.5	10.4	0.2
$Ca_{0.25}Sr_{0.75}Fe_{1.0}Mn_{0.0}O_3$	14	4.7	4.7	0.9
$Ca_{0.5}Sr_{0.5}Fe_{0.5}Mn_{0.5}O_3$	20	10.4	11.5	1.2

The SG of the mixed compounds was chosen based on the most stable space groups of $CaMnO_3/SrMnO_3$ (SG 20) and $SrFeO_3/CaFeO_3$ (SG 14). For all compounds with an Fe amount of <0.5, SG 20 was assumed, for all others, the most stable structure was taken. A negative Gibbs energy of mixing δG_{mix}^{approx} is desirable; otherwise, the mixed perovskite would convert back to the respective binary perovskites under the conditions of high-temperature water splitting. As expected, the configuration entropy is largest when four different metals are present in the mixed perovskite. This compensates for the sometimes slightly more positive mixing energy in these cases. All perovskites with $\delta G_{mix}^{approx} < -1\,kJ\,mol^{-1}$ are discussed as possible candidates for an electrode material based on the defect formation energies.

3.4. Defect Formation Energies of the Mixed Perovskites

Table 3 shows the first two defect formation energies and the decomposition energy for the mixed perovskites.

The mixed compound for use as electrode material should have smaller OVF energies and larger decomposition energies than our reference material $CaMnO_3$ in order to have a higher concentration of oxygen vacancies and to be a more stable material with respect to decomposition. The first OVF energy $\delta E_{OVF,1}$ corresponds to $\delta = 0 \rightarrow 0.0625$ and $\delta E_{OVF,2}$ corresponds to $\delta = 0.0625 \rightarrow 0.125$.

Table 3. δE_{OVF} Per half mole O_2 in kJ mol^{-1} on PW1PW level (Equation (2)). $\delta E_{decompose}$ is the decomposition energy into A_2BO_4 and AB_2O_4 (Equation (1)).

Compound	$\delta E_{OVF,1}$	$\delta E_{OVF,2}$	$\delta E_{decompose}$
$Ca_{1.0}Sr_{0.0}Fe_{0.5}Mn_{0.5}O_3$	72.2	19.4	336.0
$Ca_{0.5}Sr_{0.5}Fe_{0.25}Mn_{0.75}O_3$	78.0	79.9	606.4
$Ca_{0.25}Sr_{0.75}Fe_{0.25}Mn_{0.75}O_3$	95.4	93.6	707.2
$Ca_{0.5}Sr_{0.5}Fe_{0.0}Mn_{1.0}O_3$	188.5	171.9	817.6
$Ca_{0.75}Sr_{0.25}Fe_{0.0}Mn_{1.0}O_3$	192.2	178.7	676.8
$Ca_{0.25}Sr_{0.75}Fe_{0.0}Mn_{1.0}O_3$	193.8	185.2	888.0
$CaFeO_3$	46.2	9.8	36.8
$CaMnO_3$	183.6	177.0	499.2
$SrFeO_3$	4.8	61.5	260.8
$SrMnO_3$	189.4	182.2	977.6

The average OVF energy of the first two defects ($\delta = 0 \rightarrow 0.125$) for $CaMnO_3$ (here SG 20) is 180.3 kJ mol^{-1}, which is 27 kJ mol^{-1} larger than $\delta E_{OVF} = 153.3\,kJ\,mol^{-1}$ that was determined previously for $CaMnO_3$ in SG 62.[12] The difference is related to the different structures of the two space groups. It can also be due to the less intensive search for the most stable OV configuration for $\delta = 0.125$. Thus the $\delta E_{OVF,2}$ presented in Table 3 may be overestimated by 10–20 kJ mol^{-1}. But this is not a problem for the present comparison with decomposition energies. The only compounds with smaller OVF energies and larger decomposition energies than $CaMnO_3$ are $Ca_{0.5}Sr_{0.5}Fe_{0.25}Mn_{0.75}O_3$ and $Ca_{0.25}Sr_{0.75}Fe_{0.25}Mn_{0.75}O_3$. Thus, both mixed perovskites are proposed as reasonable candidates for an electrode material of a solar cell. $Ca_{0.5}Sr_{0.5}Fe_{0.25}Mn_{0.75}O_3$ is preferred due to the smaller defect formation energy and is therefore studied in more detail below.

3.5. Reaction Gibbs Energies of $Ca_{0.5}Sr_{0.5}Fe_{0.25}Mn_{0.75}O_3$

Figure 2 shows the OVF Gibbs energies for $Ca_{0.5}Sr_{0.5}Fe_{0.25}Mn_{0.75}O_3$ for δ = 0.0625, 0.125, 0.1875, as well as the free reaction energy for decomposition.

It can be seen that the structure with $\delta = 0.1875$ is more stable at high temperatures than those with $\delta = 0.0625$ and 0.125. Since the equilibrium temperatures for $\delta = 0.0625$ and 0.125 are higher than for $\delta = 0.1875$, we conclude that there are no defects below 520 K. Above 520 K the defect concentration increases to $\delta = 0.1875$. According to the stoichiometric factor, the Gibbs energy has a steeper descend for higher defect concentrations; therefore, it is reasonable that larger defect concentrations than $\delta = 0.1875$ may be even more stable for higher temperatures. These were not studied due to the increasing

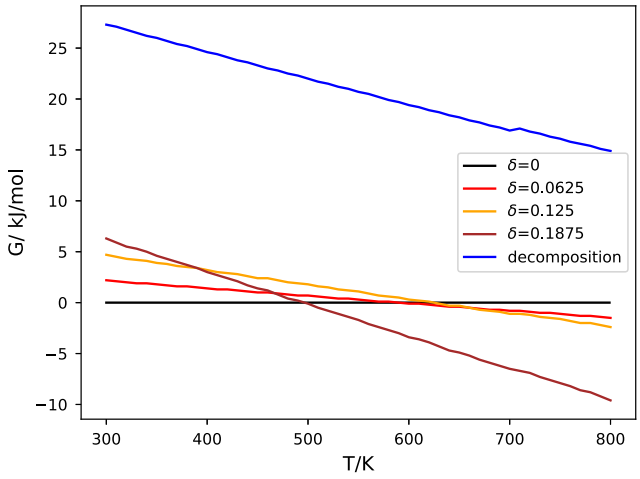

Figure 2. Temperature-dependent OVF Gibbs energy for δ = 0.0625, 0.125, and 0.1875 and Gibbs energy of decomposition ($Ca_{0.5}Sr_{0.5}Fe_{0.25}Mn_{0.75}O_3 \rightarrow \frac{1}{3}Ca_{0.5}Sr_{0.5}Fe_{0.5}Mn_{1.5}O_4 + \frac{1}{3}CaSrFe_{0.25}Mn_{0.75}O_4 + \frac{1}{6}O_2$).

number of defect configurations and limitations of available computational resources.

By varying the oxygen partial pressure, the equilibrium temperature can be adjusted, here $p_{O_2} = 1$ bar was assumed. In practical use oxygen defects can be formed by heating the material over 520 K. After cooling it rapidly reaches below 520 K; the OVs are reversibly refilled with oxygen from the environment which lowers the water electrolysis potential. So the electrolysis will have to be carried out at temperatures below 520 K, which is in the common range for high-temperature water electrolysis. Furthermore, even for higher temperatures, no signs of decomposition can be seen for $\delta = 0.1875$. Therefore, the mixed perovskite $Ca_{0.5}Sr_{0.5}Fe_{0.25}Mn_{0.75}O_3$ can be recommended as electrode material.

4. Conclusion

In this work, we continued our search for improved anode materials for high-temperature water electrolysis. The stability of ABO_3 perovskites with A = Mg,Ca,Sr and B = Ti,Mn,Cr,Fe,Mo with respect to oxygen vacancy formation and decomposition into the binary oxides was calculated on hybrid DFT (PW1PW) level. Only $CaFeO_3$,$CaMnO_3$, $SrFeO_3$, and $SrMnO_3$ have smaller oxygen defect formation energies and higher decomposition energies than the reference compound $CaMnO_3$ which was studied earlier. From these four compounds, various mixed compounds have been constructed and evaluated based on their stability against decomposition. From the most stable mixed compounds $Ca_{0.5}Sr_{0.5}Fe_{0.25}Mn_{0.75}O_{3-\delta}$ was found to be the optimal choice as electrode material, with a defect formation energy of 78.0 kJ mol^{-1} and no decomposition present at temperatures below 1500 K. The temperature-dependent Gibbs energies of reaction showed that $Ca_{0.5}Sr_{0.5}Fe_{0.25}Mn_{0.75}O_{3-\delta}$ has an oxygen vacancy concentration of at least $\delta = 0.1875$ at 520 K which is quite promising.

Supporting Information

Supporting Information is available from the Wiley Online Library or from the author.

Acknowledgements

Open Access funding enabled and organized by Projekt DEAL.

Conflict of Interest

The authors declare no conflict of interest.

Data Availability Statement

Research data are not shared.

Keywords

defect formation, mixing energies, perovskites, phase stability, thermodynamics

Received: February 2, 2023
Revised: March 8, 2023
Published online: March 22, 2023

[1] J. O. Abe, A. Popoola, E. Ajenifuja, O. Popoola, *Int. J. Hydrogen Energy* **2019**, *44*, 15072.
[2] I. Dincer, *Int. J. Hydrogen Energy* **2012**, *37*, 1954.
[3] F. Safari, I. Dincer, *Energy Convers. Manage.* **2020**, *205*, 112182.
[4] J. T. Mefford, X. Rong, A. M. Abakumov, W. G. Hardin, S. Dai, A. M. Kolpak, K. P. Johnston, K. J. Stevenson, *Nat. Commun.* **2016**, *7*, 11053.
[5] B. Bulfin, J. Vieten, D. Starr, A. Azarpira, C. Zachäus, M. Hävecker, K. Skorupska, M. Schmücker, M. Roeb, C. Sattler, *J. Mater. Chem. A* **2017**, *5*, 7912.
[6] J. Vieten, B. Bulfin, P. Huck, M. Horton, D. Guban, L. Zhu, Y. Lu, K. A. Persson, M. Roeb, C. Sattler, *Energy Environ. Sci.* **2019**, *12*, 1369.
[7] A. Jain, S. P. Ong, G. Hautier, W. Chen, W. D. Richards, S. Dacek, S. Cholia, D. Gunter, D. Skinner, G. Ceder, K. A. Persson, *APL Mater.* **2013**, *1*, 011002.
[8] R. Dovesi, A. Erba, R. Orlando, C. M. Zicovich-Wilson, B. Civalleri, L. Maschio, M. Rerat, S. Casassa, J. Baima, S. Salustro, B. Kirtman, *Wiley Interdiscip. Rev.: Comput. Mol. Sci.* **2018**, *8*, e1360.
[9] T. Bredow, A. R. Gerson, *Phys. Rev. B* **2000**, *61*, 5194.
[10] D. Vilela Oliveira, J. Laun, M. F. Peintinger, T. Bredow, *J. Comput. Chem.* **2019**, *40*, 2364.
[11] J. Laun, T. Bredow, *J. Comput. Chem.* **2022**, *43*, 839.
[12] B. Grimm, T. Bredow, *Phys. Status Solidi B* **2023**, *260*, 2200427.
[13] B. Grimm, T. Bredow, *Z. Naturforsch., B: Chem. Sci.* **2022**, *77*, 405.
[14] T. S. Bjørheim, M. Arrigoni, D. Gryaznov, E. Kotomin, J. Maier, *Phys. Chem. Chem. Phys.* **2015**, *17*, 20765.
[15] B. Bulfin, L. Hoffmann, L. de Oliveira, N. Knoblauch, F. Call, M. Roeb, C. Sattler, M. Schmücker, *Phys. Chem. Chem. Phys.* **2016**, *18*, 23147.
[16] D. Fuks, Y. Mastrikov, E. Kotomin, J. Maier, *J. Mater. Chem. A* **2013**, *1*, 14320.
[17] D. Fuks, S. Dorfman, S. Piskunov, E. Kotomin, *Phys. Rev. B* **2005**, *71*, 014111.
[18] P. J. Linstrom, http://webbook.nist.gov **2005** (accessed: September 2022).
[19] J. P. Perdew, K. Burke, M. Ernzerhof, *Phys. Rev. Lett.* **1996**, *77*, 3865.
[20] P. Woodward, D. Cox, E. Moshopoulou, A. Sleight, S. Morimoto, *Phys. Rev. B* **2000**, *62*, 844.
[21] H. T. Stokes, D. M. Hatch, *J. Appl. Crystallogr.* **2005**, *38*, 237.
[22] R. Ali, M. Yashima, *J. Solid State Chem.* **2005**, *178*, 2867.
[23] A. C. Komarek, T. Möller, M. Isobe, Y. Drees, H. Ulbrich, M. Azuma, M. T. Fernández-Díaz, A. Senyshyn, M. Hoelzel, G. André, Y. Ueda, M. Grüninger, M. Braden, *Phys. Rev. B* **2011**, *84*, 125114.
[24] C. de la Calle, J. Alonso, M. Garcia-Hernandez, V. Pomjakushin, *J. Solid State Chem.* **2006**, *179*, 1636.
[25] B. Chamberland, A. Sleight, J. Weiher, *J. Solid State Chem.* **1970**, *1*, 512.
[26] K. Sreedhar, N. Pavaskar, *Mater. Lett.* **2002**, *53*, 452.
[27] T. Takeda, R. Kanno, Y. Kawamoto, M. Takano, S. Kawasaki, T. Kamiyama, F. Izumi, *Solid State Sci.* **2000**, *2*, 673.
[28] P. Battle, T. Gibb, C. Jones, *J. Solid State Chem.* **1988**, *74*, 60.
[29] H. Fujishita, Y. Shiozaki, E. Sawaguchi, *J. Phys. Soc. Jpn.* **1979**, *46*, 581.
[30] R. B. Macquart, B. J. Kennedy, M. Avdeev, *J. Solid State Chem.* **2010**, *183*, 250.
[31] E. Bakken, T. Norby, S. Stølen, *Solid State Ionics* **2005**, *176*, 217.
[32] N. Galinsky, M. Sendi, L. Bowers, F. Li, *Appl. Energy* **2016**, *174*, 80.

D. Effect of surface energetics on phase stability of $CaMnO_3$

Benjamin Grimm[†] und Thomas Bredow[*]

Eingereicht am 20.01.2023, Akzeptiert am 08.05.2023, Online veröffentlicht am 21.05.2023

Der Artikel wird im Einverständnis[‡] der Autoren Benjamin Grimm und Thomas Bredow im Appendix D wieder veröffentlicht.

Effect of surface energetics on phase stability of $CaMnO_3$, Phys. Status Solidi B,2023,260,2300031. DOI:https://doi.org/10.1002/pssb.202300031

[†]Address: Mulliken Center for Theoretical Chemistry, Clausius-Institut für Physikalische und Theoretische Chemie, University of Bonn, Beringstr. 4, 53115 Bonn, Germany.
Email Address: grimm@thch.uni-bonn.de

[*]Address: Mulliken Center for Theoretical Chemistry, Clausius-Institut für Physikalische und Theoretische Chemie, University of Bonn, Beringstr. 4, 53115 Bonn, Germany.
Email Address: bredow@thch.uni-bonn.de

[‡]Anfragen zur Genehmigung der Wiederverwendung von Material aus diesem Kapitel sollten an die Wiley-VCH GmbH gerichtet werden

RESEARCH ARTICLE

physica status solidi b

www.pss-b.com

Effect of Surface Energetics on Phase Stability of $CaMnO_3$

Benjamin Grimm and Thomas Bredow*

$CaMnO_3$ is a promising starting point for the search of perovskites which are suitable as electrode materials for the hydrogen evolution reaction (HER). In a previous theoretical study [*Phys. Status Solidi B* 2022, 260, 2200427], it was established that the global hybrid functional PW1PW is well suited to obtain structural, energetic, and electronic bulk properties. Herein, the focus is extended to surface properties of $CaMnO_3$. All symmetry-inequivalent low-index surfaces of $CaMnO_3$ are investigated with PW1PW. Based on the experience with polar surfaces, it is decided to employ stoichiometric and symmetric models, in some cases with Schottky defects. From the calculated surface energies, the crystal morphologies are predicted based on the Gibbs–Wulff theorem. The (101), (100), (011), (001), and (010) surfaces (space group no. 62) and the (010), (110), (011), and (101) surfaces (space group no. 20) dominate the surfaces of respective single crystals and should be considered in future theoretical calculations of the HER. Furthermore, it is found that the modification with space group no. 20 is significantly more stable than space group no. 62 for nanoparticles with a diameter below 10 nm.

1. Introduction

Perovskites are frequently discussed as anode material for electrolytic water splitting[1–5] due to their structural stability, which allows reversible oxygen exchange with the environment.[6,7] Hydrogen evolution reactions (HERs) with perovskites have also recently studied by Sokolov et al.[8]

In previous work,[9] we theoretically studied bulk properties of $CaMnO_3$, which is considered as a promising catalyst. $CaMnO_3$ allows oxygen defect formation in a typical range for high-temperature electrolysis but has the drawback of decomposing into $CaMn_2O_4$ and Ca_2MnO_4.[10,11] However, the decomposition problem can be solved using solid solutions with other perovskites which makes $CaMnO_3$ a good reference compound for HER catalyst research.[12]

B. Grimm, T. Bredow
Mulliken Center for Theoretical Chemistry
Clausius-Institut für Physikalische und Theoretische Chemie
University of Bonn
Beringstr. 4, 53115 Bonn, Germany
E-mail: grimm@thch.uni-bonn.de

The ORCID identification number(s) for the author(s) of this article can be found under https://doi.org/10.1002/pssb.202300031.

DOI: 10.1002/pssb.202300031

It was shown that the hybrid functional PW1PW[13] provides accurate lattice parameters, electronic properties, and oxygen vacancy formation energies of the bulk. As next step toward future theoretical studies of the HER, the structure and stability of $CaMnO_3$ surfaces needs to be examined. From the experimental side, high-resolution transmission electron (HRTEM) images of $CaMnO_3$ are available. Markovich et al. presented a HRTEM study of $CaMnO_3$ in which the (101) surface is clearly visible.[14] Unfortunately, no information is provided for the other surfaces. The relative abundance of the surface planes remains therefore an open issue. Previous theoretical studies of $CaMnO_3$ surfaces address, e.g., the influence of the magnetic structure on the surface energy of the Mn-terminated (001) surface of $CaMnO_3$.[15] Surface energies calculated for ferromagnetic and antiferromagnetic states differ only by 0.12 eV $Å^{-2}$. This was confirmed by Nguyen et al. who obtained a corresponding energy difference of 0.13 eV $Å^{-2}$.[16] Woodley et al. investigated $La_{1-x}Ca_xMnO_3$ bulk and surface structure using simulation methods based on ionic potentials.[17] They computed surface energies for the (010) and the (110) surface of $CaMnO_3$ and $LaMnO_3$ with La/Ca termination and Mn termination.

However, a systematic study of the relative surface stability of all low-index surfaces is—to the best of our knowledge—missing. This will be addressed in the present study. Many perovskite surfaces are polar according to Tasker's classification[18] and therefore represent a challenge to their theoretical treatment with slab models. Bottin, Finocchi, and Noguera performed a seminal study of perovskite $SrTiO_3$ surfaces.[19] They identified several factors which are essential for a physically correct modeling of the surfaces. First, the surface model should be symmetric with respect to the surface normal in order to prevent the existence of a dipole moment. Furthermore, it should minimize the number of broken metal–oxygen bonds. Moreover, the model should contain a certain minimal number of atomic layers.

Some surface cutting schemes do not automatically lead to stoichiometric slab models. The stoichiometry of the slab models can be achieved by incorporating Schottky defects, as discussed by Bauerfeind et al.[20] In the present study, we follow their suggestions by constructing symmetric and stoichiometric surface models. Also, we check the relevance of nonstoichiometric models and reconstructions as described by Bottin et al.[19]

Based on the calculated surface energies, the minimum energy shape of a single crystal can be constructed applying the Gibbs–Wulff theorem.[21] The most abundant surface planes will have to be taken into account in future theoretical models of

the HER. For this purpose, we calculated the surface energies of all low-index surfaces of the two most stable modification of $CaMnO_3$. For all slab models, convergence of the calculated surface energies with the number of layers was assured.

In our previous study,[9] we identified two orthorhombic polymorphs with space groups (SG) no. 20 and 62 as most stable. The SG 62 polymorph is the experimental low-temperature structure for $CaMnO_3$.[22] Here, the Ca atoms are coordinated by eight oxygen atoms. Mn and O form corner-sharing MnO_6 octahedra with tilt angles 25–26°. There are four longer (1.95 Å) and two shorter (1.94 Å) Mn—O bond lengths.

A polymorph with SG 20 was found for $SrMnO_3$ nanoparticles by González-Jiménez et al.[23] This structure has two inequivalent Sr sites: one Sr atom is coordinated by ten oxygen atoms and the other by 12 oxygen atoms. The corner-sharing MnO_6 octahedra have tilt angles of 12–16° and Mn—O bond distances of 1.90–1.98 Å.

2. Computational Details

All calculations were performed with the CRYSTAL17 code (version 1.0.2).[24] The global hybrid functional PW1PW together with triple-zeta basis sets optimized by our group[25] was used because this combination proved to give the most accurate results for solid-state calculations of $CaMnO_3$.[9] The integral truncations (TOLINTEG) were set to 10^{-7} and 10^{-14} atomic units. Furthermore, a $4 \times 4 \times 4$ Monkhorst–Pack grid was employed for bulk calculations, while a $4 \times 4 \times 1$ grid was used for surface calculations.

The surface lattice parameters were obtained from bulk $CaMnO_3$ optimizations on PW1PW level for the structures with SG 20 and 62. In order to increase symmetry in the surface calculations, only ferromagnetic states were considered. This has a minor effect on the surface energy as discussed previously.[15,16]

Slab models were constructed with the SLABCUT option of CRYSTAL17. The surface models are chosen in a way that the resulting slab contains at least one symmetry element parallel to the surface plane and has the correct stoichiometry. In some cases, atoms from the top and the bottom layers had to be removed to maintain stoichiometry. According to these criteria, slab models were created for the low-index surfaces (100), (010), (001), (101), (011), and (110) of both polymorphs. In most cases, the surfaces can be either Ca- or Mn-terminated. Both terminations were considered. The respective surfaces are denoted (*hkl*)–Ca and (*hkl*)–Mn in the following (where *h*, *k*, and *l* are the Miller indices). The slab construction parameters, the number of the topmost layer and the number of atomic layers, were varied in order to obtain models with smallest number of broken metal–oxygen bonds. The uppermost atomic layers of the resulting slab models usually consist of oxygen atoms, yet the surfaces contain undercoordinated Ca or Mn atoms. The number of layers of the slab models is systematically increased until the surface energy converged.

3. Results and Discussion

3.1. Surface Models

We will first show the structures of the bulk-terminated low-index surfaces of both polymorphs. Each slab model is then fully relaxed within the corresponding symmetry restrictions, keeping the surface cell vectors fixed at their values obtained from bulk optimizations.

3.1.1. SG 62

Figure 1 shows the slab models of the considered surfaces of $CaMnO_3$ (SG 62); the nonstoichiometric models are shown in the Supporting Information.

In the (001) and (100) surfaces, the Ca and Mn atoms lie in the same plane, so the Ca- and Mn-terminated surfaces are identical. These slab models are stoichiometric by construction and no Schottky defects had to be introduced. All layers have the composition $Ca_2Mn_2O_6$; they are two symmetry-equivalent layers alternating.

The high stability of these two surfaces can be explained by the fact that only about one metal–oxygen bond is broken per primitive surface unit cell. This was verified by the change of the oxygen coordination number of the metal atoms C_{M-O} in the first layer relative to the bulk. For both cases, the change of coordination number ΔC_{M-O} is close to −1 (−0.999 to −1.408) per unit cell.

The coordination numbers were computed according to Da Silva[26] as

$$C_{M-O}(i) = \sum_j \exp\left[1 - \left(1 - \frac{d_{ij}}{d^i_{av}}\right)^6\right] \quad (1)$$

where d_{ij} are the M^i–O^j distances and d^{av} is iteratively computed as

$${}^n d^{av} = \frac{\sum_j d_{ij} \exp\left[\left(1 - \frac{d_{ij}}{{}^{n-1}d^i_{av}}\right)^6\right]}{\exp\left[\left(1 - \frac{d_{ij}}{{}^{n-1}d^i_{av}}\right)^6\right]} \quad (2)$$

${}^n d^{av}$ is the value after the *n*th iteration cycle starting with ${}^0 d^{av} = 1$ and converging after ${}^n d^{av} - {}^{n-1} d^{av} < 0.0001$.

In the (010) surface, they are Ca_2O_2 layers and Mn_2O_4 layers alternating.

The topmost layer of the Ca-terminated model is Ca_2O_2. The stoichiometry is not kept in this case. There are two ways how to deal with such models. One strategy is to insert defects to make the model stoichiometric, as successfully done by Bauerfeind et al.[20] In this case, one Ca atom and one O atom are removed on each side. The other possibility is to compute a nonstoichiometric model, as suggested by Bottin et al.[19] In this case, the surface energy is dependent on two chemical potentials μ_{Ca} and μ_O. However is it then not directly comparable to the other surface energies. The comparable value is the so-called cleavage energy of the two complimentary terminations (in this case the Ca_2O_2 termination and the Mn_2O_4 termination). It is given as

$$E_{cl}^{Ca_2O_2+Mn_2O_4} = \frac{1}{4A}\left(E_{Slab}^{Ca_2O_2} + E_{Slab}^{Mn_2O_4} - nE_{bulk}\right) \quad (3)$$

where *n* is the number of bulk formula units in both surface models together and *A* is the surface area. For this model the cleavage energy was calculated to 1.506 J m^{-2}.

For each of such surfaces it was checked which of the above-mentioned surface models is more reasonable. To do so, the cleavage energy was compared to the surface energies of the two complementary defective models. The Mn_2O_4-terminated

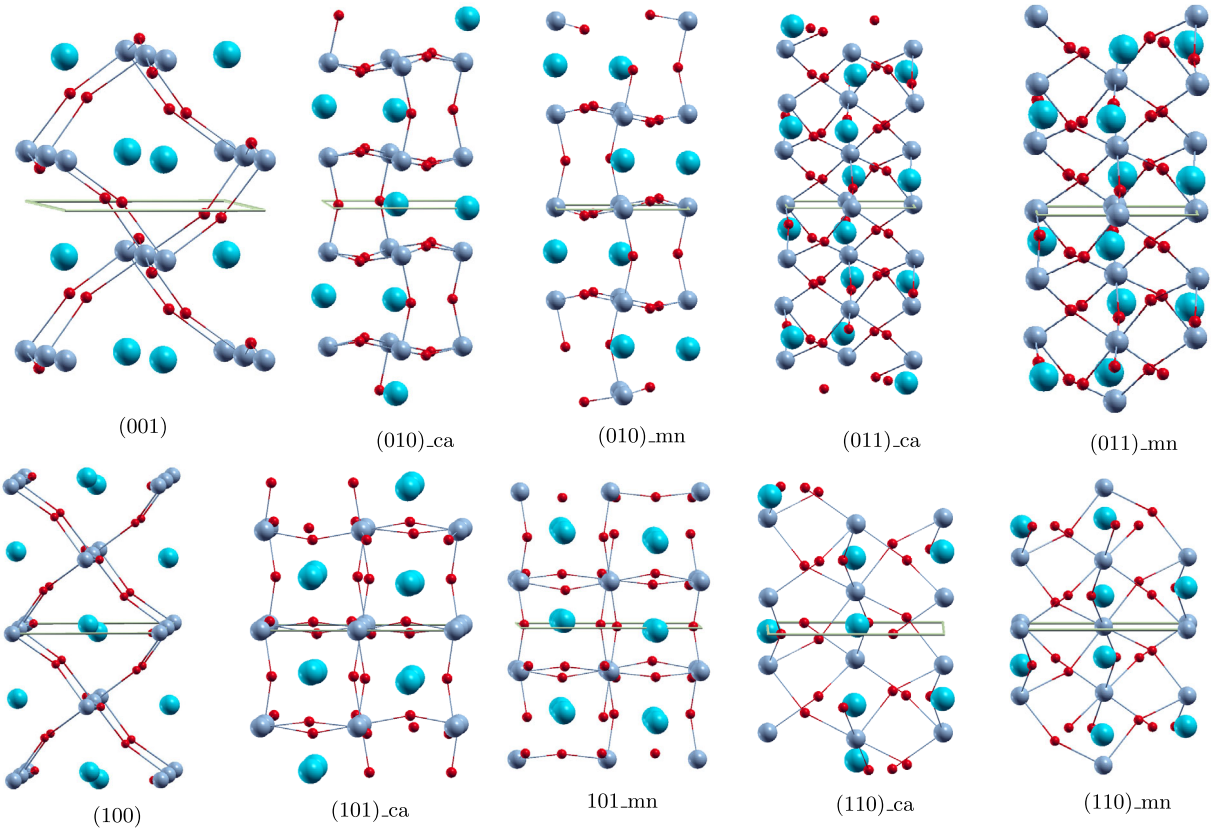

Figure 1. Stoichiometric surface models (SG 62) visualized with XCrysDen[33] (Mn in gray, Ca in cyan, and O in red).

defective model can analogously be created by removing one Mn and two O atoms from both sides. The surface energy is computed as

$$E_s(n) = \frac{E_{Slab}(n) - nE_{Bulk}}{2A} \quad (4)$$

n is the number of formula units according to the number of layers and A is the surface area. The surface energy for the defective Ca_2O_2 model is 2.249 J m^{-2}, while the surface energy of the defective Mn_2O_4 model is 2.000 J m^{-2}. Both values are larger than the cleavage energy; the formation of two complementary nonstoichiometric surfaces is more favorable than the formation of one of these defective models.

The (011) surface has alternating Ca_2O_6 and Mn_2 layers. The defective model for the Ca_2O_6 termination is created by removing three O atoms and one Ca atom each from the top and bottom layer. For the Mn_2 termination, one Mn atom is removed from both sides. The surface energies of the models are 1.733 J m^{-2} for the Ca_2O_6 termination and 2.105 J m^{-2} for the Mn_2 termination. The average cleavage energy for the nonstoichiometric models was computed to 2.432 J m^{-2}. Compared to the surface energies of the defect models, the formation of both defect surface models is more favored than the formation of the two nonstoichiometric surface models.

The (101) surface has alternating Mn_4O_8 and Ca_4O_4 layers. The defective model for the Mn_4O_8 termination by removing two Mn atoms and four oxygen atoms each from the top and the bottom layer. For the defective Ca_4O_4-terminated model, two Ca atoms and two oxygen atoms are removed from both sides. The surface energies of the defective models are 1.359 J m^{-2} for the Mn_4O_8-terminated model and 2.170 J m^{-2} for the Ca_4O_4-terminated model. The cleavage energy for the two nonstoichiometric models is 1.546 J m^{-2} which is slightly larger than the surface energy of the defective Mn_4O_8-terminated model. That means that the formation of the defective Mn_4O_8-terminated model is more favored than the formation of the two nonstoichiometric models.

In the (110) surface, there are alternating Mn_2 and Ca_2O_6 layers. The defective model for the Ca_2O_6 termination is created by removing three O atoms and one Ca atom each from the top and bottom layer. For the Mn_2 termination, one Mn atom is removed from both sides. The surface energies of the models are 1.986 J m^{-2} for the Ca_2O_6 termination and 2.095 J m^{-2} for the Mn_2 termination. The cleavage energy for the nonstoichiometric models was computed to 2.325 J m^{-2}. Compared to the surface energies of the defect models, the formation of both defect surface models is more favored than the formation of the two nonstoichiometric surface models.

3.1.2. SG 20

Figure 2 shows the slab models of the considered surfaces of $CaMnO_3$ (SG 20), the nonstoichiometric models are shown in the Supporting Information.

The (001) surface has alternating Mn and CaO_3 layers. The nonstoichiometric models have a cleavage energy of 2.485 J m^{-2}.

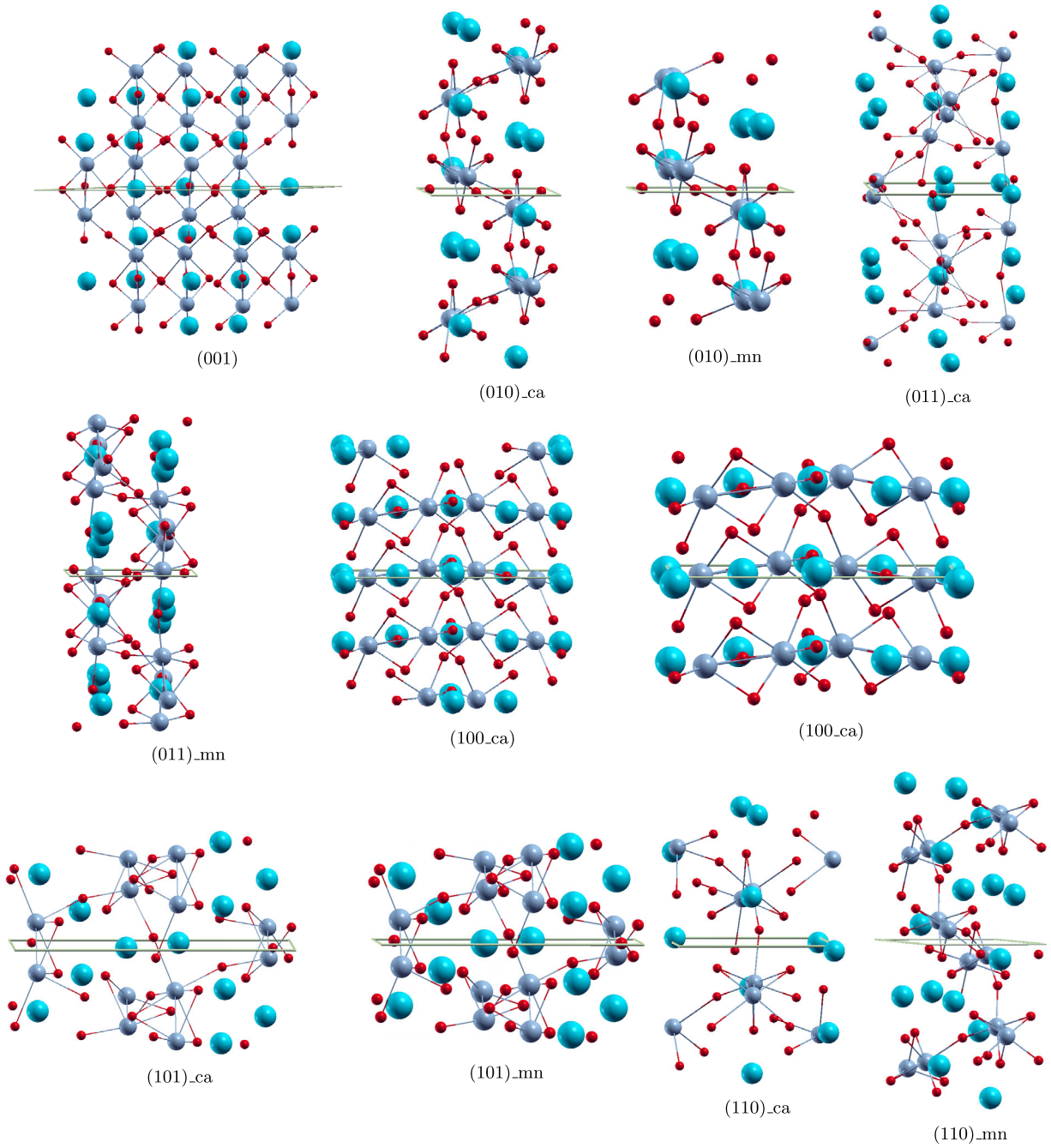

Figure 2. Stoichiometric surface models (SG 20) visualized with XCrysDen[33] (Mn in gray, Ca in cyan, and O in red).

The CaO_3-terminated defect model was created by constructing a ((2,0),(0,2)) supercell. From this, 2 Ca atom and 6 O atoms were removed from both sides to keep stoichiometry. This model was computed for a surface model containing 24 formula units and a surface energy of 2.113 J m^{-2} was obtained. In the same way a Mn-terminated defective model could be constructed using the same supercell and removing two Mn atom from both sides. However, this is not sensible because removing one Mn atom breaks three Mn—O bonds. Breaking the face connected pairing of the MnO_6 octahedra leads to poor convergence and high surface energies. The surface energy of the defective model is smaller than the cleavage energy of the nonstoichiometric models, so it is favored.

The (010) surface has Ca_2O_2 and $CaMn_2O_5$ layers in the way that one Ca_2O_2 layer is followed by two $CaMn_2O_5$ layers. So there are two different ways to cut, between the two $CaMn_2O_5$ layers and between a Ca_2O_2 layer and a $CaMn_2O_5$ layer. Cutting between two $CaMn_2O_5$ layers (see (010)–Mn in Figure 2) leads

automatically to a stoichiometric model without any defects. It has a surface energy of 2.521 J m^{-2}.

Cutting between one Ca_2O_2 and one $CaMn_2O_5$ layer leads to one second $CaMn_2O_5$-terminated model and one Ca_2O_2-terminated model. The two nonstoichiometric models obtained from this cut and have a cleavage energy of 1.445 J m^{-2}. The (010)–Ca model in Figure 2 is the Ca_2O_2 terminated model of this cut, stoichiometrized by removing one Ca and one O atom each from both sides. It is the most stable surface model for this SG and has a surface energy of 1.029 J m^{-2}. As the surface energy is smaller than the cleavage energy, it is more favored to form the defective Ca_2O_2 terminated model than forming the two nonstoichiometric models.

The (011) surface has also Ca_2O_2 and $CaMn_2O_5$ layers in the way that one Ca_2O_2 layer is followed by two $CaMn_2O_5$ layers which leads to the same cleavage scheme. For this surface the (011)–Mn model (obtained by cutting between the two $CaMn_2O_5$ layers) leads to the lowest surface energy (1.399 J m^{-2}). The defective (010)–Ca model has a surface energy of 1.667 J m^{-2}. The cleavage energy of the cut between one Ca_2O_2 and one $CaMn_2O_5$ layer is 1.430 J m^{-2} which is slightly larger than the surface energy of the (011)–Mn model.

The (100), (101), and (110) surfaces have also the same cutting scheme. For the (100) and the (101) surfaces, the models obtained by cutting between the two $CaMn_2O_5$ layers ((100)–Mn and (101)–Mn) are the most stable. The (100)–Mn model has a surface energy of 1.108 J m^{-2} and the (101)–Mn model has a surface energy of 1.457 J m^{-2}.

The cleavage energies between one Ca_2O_2 and one $CaMn_2O_5$ layer are 1.785 J m^{-2} for the (100) surface and 1.530 J m^{-2} for the (101) surface. For both cases, the cleavage energy is larger than the surface energy of the (101)–Mn) or the (100)–Mn model.

For the (110) surface, cutting between the two $CaMn_2O_5$ layers ((110)–Mn) leads to a surface energy of 1.645 J m^{-2}. The cleavage energies between one Ca_2O_2 and one $CaMn_2O_5$ layer are 1.408 J m^{-2} which is smaller than the surface energy. However, the defective Ca-terminated model (110)–Ca is more stable with a surface energy of 1.030 J m^{-2}.

3.2. Surface Energies

Figure 3 shows the convergence behavior of the calculated surface energies with respect to the number of layers for all stoichiometric surface models. Convergence is achieved within 0.1 J m^{-2}, except for some less stable surfaces due to limitations of available computational resources (for a more detailed discussion see below).

For the SG 62 polymorph, the three surfaces (001), (100), and (101)–Mn are most stable (E_s = 1.31, 1.31, and 1.36 J m^{-2}, respectively). The high stability of the (001) and the (100) surface is related to the small number of broken M—O bonds as discussed above. The similarly high stability of the (101)–Mn surface is surprising because four Mn—O bonds are cleaved ($\Delta C_{Mn-O} = -3.01$). Here, it was observed that the relaxation energy (energy difference between relaxed and bulk-terminated structure) is particularly large, although no reconstruction takes place.

For the SG 20 polymorph, the three surfaces (100), (010)–Ca, and (110)–Ca are most stable with surface energies 1.03, 1.03, and 1.11 J m^{-2}, respectively. The stability of the (100) surface can be explained by their small ΔC_{Mn-O} values (Section 3.1.2). The (010)–Ca surface and the (110)_Ca surfaces are stable because of their high relaxation energies.

Some surface energies converge quite slowly (e.g., for SG 62 the (110) and the (101) surface models). We could identify the CRYSTAL BFGS optimization algorithm as one source of this issue. When we optimized selected slab models with the PreconLBFGS optimizer as implemented in the ASE,[27–29] using CRYSTAL17 as calculator, structures with much lower energies resulted, and surface energy convergence with number of layers was considerably improved.

Table 1 shows the converged surface energies as average value of the respective two largest slab models. The surface energy E_s was calculated in the standard way (Equation (5)).

$$E_s(n) = \frac{E_{Slab}(n) - nE_{Bulk}}{2A} \tag{5}$$

n is the number of formula units according to the number of layers and A is the surface area. As discussed in the previous section, there is one case for which the nonstoichiometric model

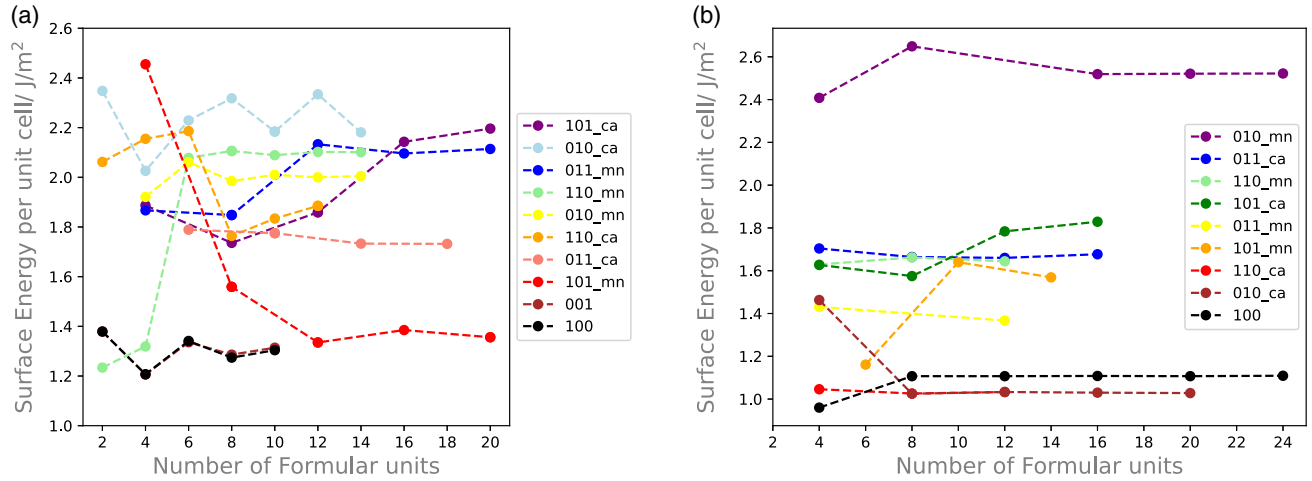

Figure 3. Surface energies of $CaMnO_3$. a) SG 62 polymorph, b) SG 20 polymorph.

Table 1. Converged surface energies E_s in J m^{-2} and their contribution p_{hkl} (%) to the Gibbs–Wulff surface.

Surface	E_s	p_{hkl}
(a) SG 62 polymorph		
(100)	1.306	20.1
(001)	1.312	14.9
(101)–Mn	1.359	30.5
(010)	1.506	27.0
(011)–Ca	1.733	7.5
(110)–Ca	1.986	0.0
(b) SG 20 polymorph		
(010)–Ca	1.029	17.2
(110)–Ca	1.030	36.9
(100)–Mn	1.108	4.3
(011)–Mn	1.399	31.0
(101)–Mn	1.457	10.7
(001)	2.113	0.0

is favored (for the (010) surface of SG62). In this case, the surface energy is approximated as the cleavage energy of the nonstoichiometric models.

Based on these surface energies, a Wulff construction was performed (with the VESTA code[30]) which is shown in **Figure 4**.

In the minimum energy shape of SG 62 polymorph, the {101}–Mn facet is dominating with a percentage of 30.5. This is due to the presence of four symmetry-equivalent surfaces ((101), $\bar{1}0\bar{1}$), $(10\bar{1})$, $(\bar{1}01)$, while there are only two symmetry-equivalent surfaces for the other two stable facets {001} and {100}, respectively. Interestingly the (010) surface has the second-largest contribution (27.0%). Reason is the low contribution of the neighboring surfaces (011) and (110).

The most stable (100) surface has only third-largest contribution with 20.1%. This is explained by the high stability of the (101) surface which cuts the edge between the (001) and the (100) surface. This also explains that the amount of the (001) surface is only 14.9% even if it is almost as stable as the (100) surface. The (011) surface contributes to the total crystal surface by 7.5% and the (110) surface has no contribution to the surface shape.

Overall, the Wulff construction shows that all low-index surfaces except the (110) surface have a significant contribution to the crystal shape, and therefore have to be taken into account in theoretical models of the HER on $CaMnO_3$, if single-crystalline or microcrystalline particles are considered. The overall crystal morphology is typical for an orthorhombic crystal, a cuboid with cut edges.

In the minimum energy shape of the SG 20 polymorph, the (110) surface is dominating with a contribution of 36.8%, followed by (011) (31.0%) and (010) (17.2 %). The reason for the higher contributions of {110} and {011} is that there are more symmetry-equivalent planes than for {010} (as already discussed for the energy shape of SG 62). The (101) surface contributes to the crystal surface by 10.7%. The small contribution of the (100) surface (only 4.3%) is surprising and is related to the vectors [*hkl*] of other stable surfaces. The (001) surface is not contributing to the shape because of its high surface energy.

4. Nanoparticle Energies

As mentioned above, a SG 20 polymorph was experimentally found for $SrMnO_3$ nanoparticles.[23] As far as the authors are aware, a corresponding $CaMnO_3$ polymorph has not yet been synthesized. We therefore investigated if this polymorph can be stabilized in small particles. Navrotsky et al. showed that differences in surface energies of the various polymorphs can lead to a phase change for large surface areas (small particle sizes) for TiO_2.[31] We therefore calculated the relative stability of the SG 62 and SG 20 polymorphs with respect to the particle diameter using the same approach. The particles are approximated as spheres with diameter d. Atoms in the outermost shell with 0.5 nm thickness are assumed to be surface atoms (Equation (6))

$$f_{\text{surf}}(d) = \frac{V(d) - V(d - 1\text{nm})}{V(d)} \quad . \tag{6}$$

$f_{\text{surf}}(d)$ is the fraction of surface atoms in a spherical nanoparticle with diameter d.

Based on the surface energies E_{hkl} and the surface contributions to the Wulff construction p_{hkl} (see Table 1), the average surface energy $\overline{E}_s$ was computed using Equation (7) for both polymorphs

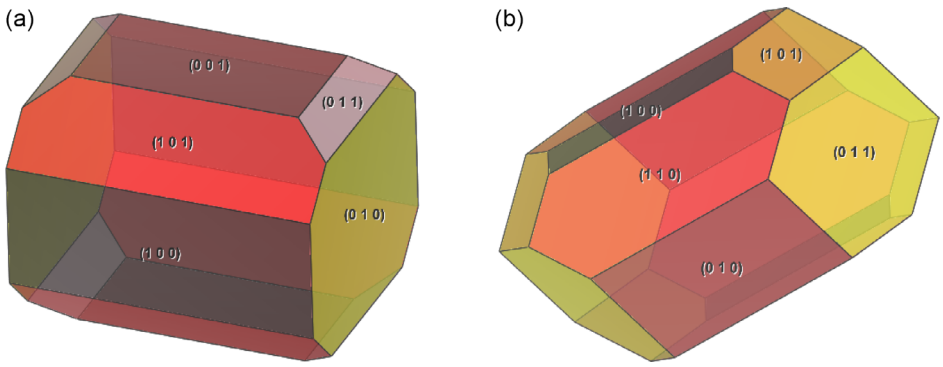

Figure 4. Wulff constructions of $CaMnO_3$. a) SG 62 polymorph, b) SG 20 polymorph.

$$\overline{E}_s = \sum_{\{hkl\}\in \text{Wulff}} p_{hkl} E_{hkl} \quad (7)$$

$\overline{E}_s$ is 1.41 J m^{-2} for the SG 62 polymorph and 1.19 J m^{-2} for the SG 20 polymorph; the difference $\Delta\overline{E}_s$ is therefore −0.34 J m^{-2}. The change ΔE_{surf} (kJ mol^{-1}) of the bulk energy per formula unit of a nanoparticle due to the contribution of the surface energies is given by Equation (8)

$$\Delta E_{surf}(d) = A_{mol}(d) f_{surf}(d) \Delta\overline{E}_s \quad (8)$$

The molar surface area of a nanoparticle with diameter d, $A_{mol}(d)$ (m^2 mol^{-1}), was calculated from the specific surface area A_{sp}, the particle diameter d, and the molar mass M. Paul and Das measured a specific surface area of $A_{sp} = 11.04\,m^2g^{-1}$ for an average $CaMnO_3$ particle size of $d = 414$ nm.[32] For a particle diameter d, A_{mol} is therefore given by Equation (9)

$$A_{mol}(d) = \frac{414}{d(\text{nm})} \times 11.04 \times M_{CaMnO_3} \quad (9)$$

The relative stability of the two polymorphs in nanoparticles with diameter d is given by Equation (10)

$$\Delta E_{nano}(d) = \Delta E_{bulk} + \Delta E_{surf}(d) \quad (10)$$

ΔE_{bulk} was calculated as 0.1 kJ mol^{-1} in our previous study. **Figure 5** shows the change of the energy difference between polymorphs 20 and 62 $\Delta E_{nano}(d)$ as a function of the particle diameter d.

For nanoparticles with a diameter below 10 nm, the SG 20 polymorph is significantly more stable than the experimentally known SG 62 polymorph. This is in line with the experimental observation for $SrMnO_3$ that a polymorph with SG 20 is favored for nanoparticles.[23] A polymorph with SG 20 has not yet been experimentally reported for $CaMnO_3$, possibly due to kinetic hindrance, but based on our present results we propose its thermodynamic stability for small particle sizes.

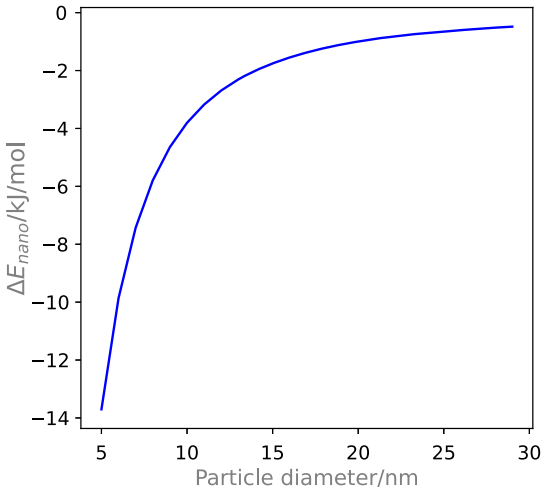

Figure 5. Energy difference $\Delta E_{nano}(d)$ in kJ mol^{-1} between SG 20 and SG 62 as function of the particle diameter d (nm).

5. Conclusion

The stability of low-index surfaces of $CaMnO_3$ was calculated on hybrid DFT (PW1PW) level. The experimentally known low-temperature polymorph with SG 62 and a polymorph with SG 20, known from $SrMnO_3$ nanoparticles, were investigated. Both polymorphs have approximately the same cohesive energy.

Stoichiometric and symmetric slab models were constructed for both polymorphs. Ca- and Mn-terminated models were distinguished where necessary. Wulff constructions were performed for both polymorphs based on converged low-index surface energies. The predicted Wulff shape of the SG 62 polymorph is dominated by the (101) surface. Additionally, (100), (010), (001), (101), and (011) surfaces have significant contributions. For the SG 20 polymorph, the Wulff shape is dominated by the most stable (110) surface. The four surfaces (110), (011), (010), and (101) also contribute to the crystal shape and therefore have to be considered in future theoretical studies of the HER process on $CaMnO_3$.

In general, all surface energies of the SG 20 polymorph are lower than those of the SG 62 polymorph. Therefore, nanoparticles with a diameter below 10 nm prefer the structure corresponding to SG 20. This has been found experimentally for $SrMnO_3$ but not yet for $CaMnO_3$. The present theoretical results suggest that this polymorph might exist under certain preparation conditions.

Supporting Information

Supporting Information is available from the Wiley Online Library or from the author.

Acknowledgements

Open Access funding enabled and organized by Projekt DEAL.

Conflict of Interest

The authors declare no conflict of interest.

Data Availability Statement

Research data are not shared.

Keywords

$CaMnO_3$, hybrid density functional theory, phase stability, surface energies, Wulff construction

Received: January 20, 2023
Revised: May 5, 2023
Published online: May 21, 2023

[1] G. Gahleitner, *Int. J. Hydrog. Energy* **2013**, *38*, 2039.
[2] Y. Rong, Y. Hu, A. Mei, H. Tan, M. I. Saidaminov, S. I. Seok, M. D. McGehee, E. H. Sargent, H. Han, *Science* **2018**, *361*, aat8235.

[3] J.-P. Correa-Baena, M. Saliba, T. Buonassisi, M. Grätzel, A. Abate, W. Tress, A. Hagfeldt, *Science* **2017**, *358*, 739.
[4] H. S. Jung, N.-G. Park, *Small* **2015**, *11*, 10.
[5] D. Wang, M. Wright, N. K. Elumalai, A. Uddin, *Sol. Energy Mater. Sol. Cells* **2016**, *147*, 255.
[6] P. P. Lopes, D. Y. Chung, X. Rui, H. Zheng, H. He, P. Farinazzo Bergamo Dias Martins, D. Strmcnik, V. R. Stamenkovic, P. Zapol, J. F. Mitchell, R. F. Klie, N. M. Markovic, *J. Am. Chem. Soc.* **2021**, *143*, 2741.
[7] J. S. Yoo, X. Rong, Y. Liu, A. M. Kolpak, *ACS Catal.* **2018**, *8*, 4628.
[8] M. Sokolov, Y. A. Mastrikov, G. Zvejnieks, D. Bocharov, E. A. Kotomin, V. Krasnenko, *Catalysts* **2021**, *11*, 1326.
[9] B. Grimm, T. Bredow, *Phys. Status Solidi B* **2023**, *260*, 2200427.
[10] B. Bulfin, J. Vieten, D. Starr, A. Azarpira, C. Zachäus, M. Hävecker, K. Skorupska, M. Schmücker, M. Roeb, C. Sattler, *J. Mater. Chem. A* **2017**, *5*, 7912.
[11] F. Safari, I. Dincer, *Energy Convers. Manag.* **2020**, *205*, 112182.
[12] B. Grimm, T. Bredow, *Phys. Status Solidi B* **2023** https://doi.org/10.1002/pssb.202300048.
[13] T. Bredow, A. R. Gerson, *Phys. Rev. B* **2000**, *61*, 5194.
[14] V. Markovich, I. Fita, A. Wisniewski, R. Puzniak, D. Mogilyansky, L. Titelman, L. Vradman, M. Herskowitz, G. Gorodetsky, *Phys. Rev. B* **2008**, *77*, 054410.
[15] A. Filippetti, W. E. Pickett, *Phys. Rev. Lett.* **1999**, *83*, 4184.
[16] T. T. Nguyen, T. C. Bach, H. T. Pham, T. T. Pham, D. T. Nguyen, N. N. Hoang, *Physica B* **2011**, *406*, 3613.
[17] M. J. Akhtar, C. R. A. Catlow, B. Slater, A. M. Walker, S. M. Woodley, *Chem. Mater.* **2006**, *18*, 1552.
[18] P. W. Tasker, *J. Phys. C: Solid State Phys.* **1979**, *12*, 4977.
[19] F. Bottin, F. Finocchi, C. Noguera, *Phys. Rev. B* **2003**, *68*, 035418.
[20] K. C. L. Bauerfeind, R. Roß, T. Bredow, *J. Phys. Chem. C* **2020**, *124*, 28520.
[21] G. Wulff, *Z. Kristallogr. -Cryst. Mater.* **1901**, *34*, 449.
[22] K. Poeppelmeier, M. Leonowicz, J. Scanlon, J. Longo, W. Yelon, *J. Solid State Chem.* **1982**, *45*, 71.
[23] I. N. González-Jiménez, E. Climent, A. Torres-Pardo, M. Hernando, A. E. Sánchez-Peláez, F. Fernández-Martínez, M. T. F. Díaz, J. M. González-Calbet, A. de Andrés, Á. Varela, M. Parras, *Inorg. Chem.* **2016**, *55*, 3980.
[24] R. Dovesi, A. Erba, R. Orlando, C. M. Zicovich-Wilson, B. Civalleri, L. Maschio, M. Rérat, S. Casassa, J. Baima, S. Salustro, B. Kirtman, *Wiley Interdiscip. Rev. Comput. Mol. Sci.* **2018**, *8*, e1360.
[25] D. Vilela Oliveira, J. Laun, M. F. Peintinger, T. Bredow, *J. Comput. Chem.* **2019**, *40*, 2364.
[26] J. L. Da Silva, *J. Appl. Phys.* **2011**, *109*, 023502.
[27] D. Packwood, J. Kermode, L. Mones, N. Bernstein, J. Woolley, N. Gould, C. Ortner, G. Csányi, *J. Chem. Phys.* **2016**, *144*, 164109.
[28] Atomic Simulation Environment, Main ASE Repo, https://gitlab.com/ase/ase (accessed: October 2022).
[29] Atomic Simulation Environment, ASE Fork, https://gitlab.com/waldlaubsaengernest/ase (accessed: November 2022).
[30] K. Momma, F. Izumi, *J. Appl. Crystallogr.* **2011**, *44*, 1272.
[31] M. R. Ranade, A. Navrotsky, H. Z. Zhang, J. F. Banfield, S. H. Elder, A. Zaban, P. H. Borse, S. K. Kulkarni, G. S. Doran, H. J. Whitfield, *Proc. Natl. Acad. Sci. USA* **2002**, *99*, 6476.
[32] D. Paul, G. Das, *CrystEngComm* **2021**, *23*, 4050.
[33] A. Kokalj, *J. Mol. Graph. Model.* **1999**, *17*, 176.

E. Revisiting $CaMnO_3$ as a Proton Conductor - A Theoretical Perspective

Benjamin Grimm[†] und Thomas Bredow[*]

Eingereicht am 17.11.2023 bei J. Phys. Chem. C, Akzeptiert am 13.03.2024 , Online veröffentlicht am 25.03.2024

Der Artikel wird im Einverständnis [‡] der Autoren Benjamin Grimm und Thomas Bredow im Appendix E wieder veröffentlicht.

Revisiting $CaMnO_3$ as a Proton Conductor - A Theoretical Perspective,J. Phys. Chem. C,2024. DOI:https://doi.org/10.1021/acs.jpcc.3c07594

[†]Address: Mulliken Center for Theoretical Chemistry, Clausius-Institut für Physikalische und Theoretische Chemie, University of Bonn, Beringstr. 4, 53115 Bonn, Germany.
Email Address: grimm@thch.uni-bonn.de

[*]Address: Mulliken Center for Theoretical Chemistry, Clausius-Institut für Physikalische und Theoretische Chemie, University of Bonn, Beringstr. 4, 53115 Bonn, Germany.
Email Address: bredow@thch.uni-bonn.de

[‡]Anfragen zur Genehmigung der Wiederverwendung von Material aus diesem Kapitel sollten an die American Chemical Society gerichtet werden

THE JOURNAL OF PHYSICAL CHEMISTRY C
A JOURNAL OF THE AMERICAN CHEMICAL SOCIETY

pubs.acs.org/JPCC

Article

Revisiting $CaMnO_3$ as a Proton Conductor—A Theoretical Perspective

Benjamin Grimm* and Thomas Bredow*

Cite This: https://doi.org/10.1021/acs.jpcc.3c07594

Read Online

ACCESS | Metrics & More | Article Recommendations | Supporting Information

ABSTRACT: High-temperature water electrolysis is presently discussed as a technique for conversion of electrical energy into chemical energy, which can be employed for renewable energy storage. The proton ceramic electrolysis cell (PCEC) is a promising technique for this, which is hampered by long-term stability and efficiency issues of available electrode materials. $CaMnO_3$ is a promising electrode material due to its stability and the ability of reversibly forming oxygen vacancies. Its stability with respect to decomposition can be further improved by Mn/Fe substitution and Ca/Sr substitution. However, in a previous theoretical study [*Phys. Rev. B* **2010**, *82*, 014103], a rather high proton migration barrier of 1.8 eV was obtained for cubic $CaMnO_3$. This would exclude $CaMnO_3$ as an efficient electrode material. In this work, much lower proton migration barriers of ≈0.2 eV were computed for cubic $CaMnO_3$. For the experimental room-temperature orthorhombic phase, the barriers are only slightly larger (0.2 to 0.5 eV). Mn/Fe and Ca−Sr substitution is essential for negative hydration energies and does not significantly change the barriers. Based on the present theoretical results, we therefore suggest to reconsider substituted $CaMnO_3$ as an PCEC electrode material.

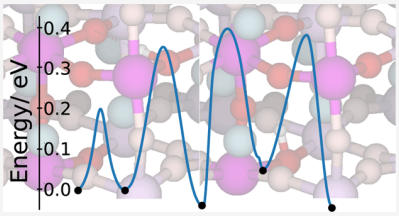

INTRODUCTION

Renewable energies are an increasingly important alternative to fossil fuels and contribute significantly to the reduction of CO_2 emission. The conversion of electrical energy into chemical energy is an important process that enables renewable energy sources, such as wind and solar energy, to be efficiently stored and retrieved when needed. For this purpose, solid oxide electrolysis cells (SOECs), in which oxide ions migrate from the cathode to the anode, were intensively investigated. For example, Hauch et al. reviewed recent advances in solid oxide cell technology.[1] The proton ceramic electrolysis cell (PCEC) is an alternative technique in which protons migrate from the anode to the cathode. Duan et al. reviewed the use of proton conducting oxides for energy conversion and storage.[2] They mentioned that the migration barriers are generally lower for protons than for oxide ions, allowing a lower working temperature, which is a key advantage of PCEC compared to SOEC. Furthermore, dry hydrogen is produced because unlike in SOECs, water is directed to the anode and not to the cathode where the hydrogen is produced.

Poetzsch et al. discussed the thermodynamic and transport kinetics exemplified for protons ($OH_O^{\bullet}$) and oxygen vacancies ($V_O^{\bullet\bullet}$) as charge carriers.[3] The equilibration of a material containing these carriers depends on the oxygenation reaction and the hydration reaction of a metal oxide. The thermodynamics of these reactions can be controlled by the partial pressures p_{H2} and p_{O2}, the temperature, and the material-specific thermodynamic parameters. In the proton ceramic fuel cell (PCFC), the process of the PCEC is inverted. Hydrogen is adsorbed to the anodes, the protons migrate to the cathode and react there with the incoming oxygen to water. Zohourian et al. studied mixed-conducting perovskites as cathode materials for PCFC.[4] They derived hydration enthalpies and entropies for 18 compositions of the $(Ba,Sr,La)(Fe,Co,Zn,Y)O_{3-\delta}$ perovskites and found the highest proton concentration in $Ba_{0.95}La_{0.05}Fe_{0.8}Zn_{0.2}O_{3-\delta}$. Merkle et al. reviewed the recent research on oxides with mixed protonic and electronic conductivity.[5] PCEC and PCFC electrode materials often show the presence of mobile protonic defects (built via hydration of oxygen vacancies), oxygen vacancies, and electronic defects and are therefore often called triple ionic-electronic conductors.[6]

The proton mobility of perovskites was theoretically investigated with the density functional theory. Calculated proton migration barriers are typically between 0.25 and 0.5 eV.[7−11] Recently, Hoedl et al. computed proton migration barriers in $BaFeO_{3-\delta}$ on the PBE level.[12] The calculated migration barriers were between 0.1 and 0.3 eV. Recently, we investigated $CaMnO_3$ in more detail because experimental data show comparably low oxygen vacancy formation enthalpies, which allow reversible defect formation around 1200 K.[13,14] One issue is the decomposition into $CaMn_2O_4$ and Ca_2MnO_4, which limits the oxygen vacancy concentration, but it was already

Received: November 17, 2023
Revised: March 7, 2024
Accepted: March 13, 2024

shown that the decomposition is prevented by Ca/Sr substitution in $Ca_{0.8}Sr_{0.2}MnO_3$.[15] We found that a combined Ca/Sr and Mn/Fe substitution can lower the oxygen vacancy formation Gibbs energy as well as prevent decomposition.[14]

In a benchmark study covering a range of perovskites, Bork et al. computed a proton migration barrier of 1.8 eV for cubic $CaMnO_3$.[16] This value is considerably higher than the typical barriers, 0.25 and 0.5 eV, reported in the literature for other perovskites.[7−11] The aim of this work is to re-examine the proton conductivity of $CaMnO_3$ to check its use as a PCEC material. First, the proton migration barriers are computed for the cubic phase with the computational setup that was derived in our previous studies.[13,14] In order to provide a more realistic model, the barriers are then computed for the experimentally known orthorhombic polymorphs (space group no. 62).[17] Also the influence of Ca/Sr and Ca/Fe substitution on the barriers is investigated.

COMPUTATIONAL DETAILS

All calculations were performed with the crystal-orbital program CRYSTAL17 (version 1.0.2).[18] The global hybrid functional PW1PW[19] together with triple-ζ basis sets optimized by our group[20] were used because this combination proved to give the most accurate results for solid-state calculations of $CaMnO_3$.[13] The integral truncation thresholds (TOLINTEGs) were set to 1×10^{-7} and 1×10^{-14} atomic units, respectively. Furthermore, a $4 \times 4 \times 4$ Monkhorst−Pack grid was employed. A ferromagnetic spin configuration was considered as an approximation of more complicated spin configurations in order to reduce computational cost. The proton migration barriers were computed using the climbing-image nudged-elastic band (NEB) method implemented in the atomic simulation environment (ASE-NEB[21]) with CRYSTAL as a calculator. A modified ASE code[22] was used in order to employ all symmetry options implemented in CRYSTAL during structure optimization.

Here, structure optimization denotes the search for local minima on the energy hypersurface for a given system using the BFGS algorithm.[23−26] The NEB approach computes a minimum energy path (in this case, for the migration of a proton) between two minimum structures. The images connecting the two structures are initially guessed by linear interpolation. After that the geometries of the images are optimized under the constraint that the reaction coordinate must not change.[27] Hydrogen incorporation is modeled by placing a single hydrogen atom on a bulk oxygen atom forming an OH group as a simplification of eq 1.

$$CaMnO_{3-\delta} + \delta H_2O \rightarrow CaMnO_3H_{2\delta} \quad (1)$$

Proton migration barriers are computed for migration pathways between oxygen atoms of the same MO_6 octahedron (intraoctahedral) or of two adjacent MO_6 octahedra (interoctahedral). In order to model macroscopic proton diffusion through the bulk, rotation of the OH group is necessary (Figure 4). During geometry optimizations in an NEB run, only the atom positions are relaxed, and the cell parameters are kept fixed to the optimized values. The optimized initial and final images are linearly interpolated and then optimized by the ASE-NEB code.

The computation of the defect structures needed for the hydration energies is performed by removing one oxygen atom from the unit cell and optimizing atom positions only. After optimization, an oxygen ghost function is added on the position of the removed oxygen for a final single point calculation to correct the basis set superposition error.

RESULTS AND DISCUSSION

Optimization of Lattice Parameters. First, the unit cells of the cubic and orthorhombic $CaMnO_3$ phases are optimized with the standard CRYSTAL optimizer (cell parameters and atom positions). The optimized cell parameters are compared to the available experimental data in Table 1.

Table 1. Comparison of Calculated and Measured Lattice Parameters for Cubic and Orthorhombic $CaMnO_3$

phase	space group	method	a/Å	b/Å	c/Å
cubic	225	PW1PW	3.730		
	225	experiment (ref 28)	3.77		
orthorhombic	62	PW1PW	5.275	7.446	5.261
	62	experiment (ref 17)	5.297	7.448	5.264

Table 2. Change of Lattice Parameters of Orthorhombic $CaMnO_3$ by Mn/Fe and Ca/Sr Substitution

phase	a/Å	b/Å	c/Å
$CaMnO_3$	5.275	7.446	5.261
$CaMn_{0.875}Fe_{0.125}O_3$ (distant Fe)	5.286	7.466	5.269
$CaMn_{0.875}Fe_{0.125}O_3$ (close Fe)	5.290	7.449	5.274
$Ca_{0.75}Sr_{0.25}Mn_{0.875}Fe_{0.125}O_3$ (distant Fe)	5.302	7.519	5.308
$Ca_{0.75}Sr_{0.25}Mn_{0.875}Fe_{0.125}O_3$ (close Fe)	5.297	7.448	5.264

It can be seen that the deviations from the experiment are smaller than 1%, indicating the accuracy of the employed method. However, it has to be mentioned that this good agreement is rather fortuitous for the cubic phase because it is a high-temperature phase which is only stable above 913 °C and as $CaMnO_{3-\delta}$ with $\delta \approx 0.5$.[28] This structure does not exist without defects and is stable at room temperature. The computation of this phase therefore has not the aim to coincide with the experiment but only to compare the migration barriers with the theoretical study of Bork et al.[16] The comparison of the lattice parameter with the experiment is therefore a crude approximation.

A $2 \times 1 \times 2$ orthorhombic supercell containing 80 atoms and a $2 \times 2 \times 2$ cubic supercell containing 40 atoms are used for all calculations.

To model Mn−Fe and Ca−Sr substitution, the unit cell was fully optimized (cell parameters and atom positions). The lattice parameters are shown in Table 2.

Two different Fe configurations are modeled: two neighboring Fe atoms (close Fe) and two Fe atoms with the maximal possible distance (distant Fe). For all considered Ca/Sr and Mn/Fe configurations, the changes of the lattice parameters are small.

Hydration Energies. A negative hydration energy is essential for the proton conductivity. It can be calculated as the reaction energy of

$$CaMnO_{3-\delta} + CaMnO_3 + \delta H_2O \rightarrow 2CaMnO_3H_\delta \quad (2)$$

The δ here equals 0.0625 for the orthorhombic cell, corresponding to one oxygen defect per cell. The results are listed in Table 3.

https://doi.org/10.1021/acs.jpcc.3c07594
J. Phys. Chem. C XXXX, XXX, XXX−XXX

Table 3. Calculated Hydration Energies in kJ/mol[a]

	$CaMnO_3$		$CaMn_{0.875}Fe_{0.125}O_3$				$Ca_{0.75}Sr_{0.25}Mn_{0.875}Fe_{0.125}O_3$			
	orthorhombic		distant Fe		close Fe		distant Fe		close Fe	
	min	max	min	max	min	max	min	max	min	max
structure	(c)	(d)	(c)	(a)	(c)	(d)	(c)	(b)	(c)	(d)
E_{hyd}	40.2	40.9	−55.6	−29.3	−83.5	−55.9	−51.2	9.9	−64.2	−18.1

[a]Minimal and maximal values correspond to the most and less stable hydrogen position. The labels (a) to (d) correspond to the structures in Figure 5, the Fe and Sr positions are shown in Figure 7.

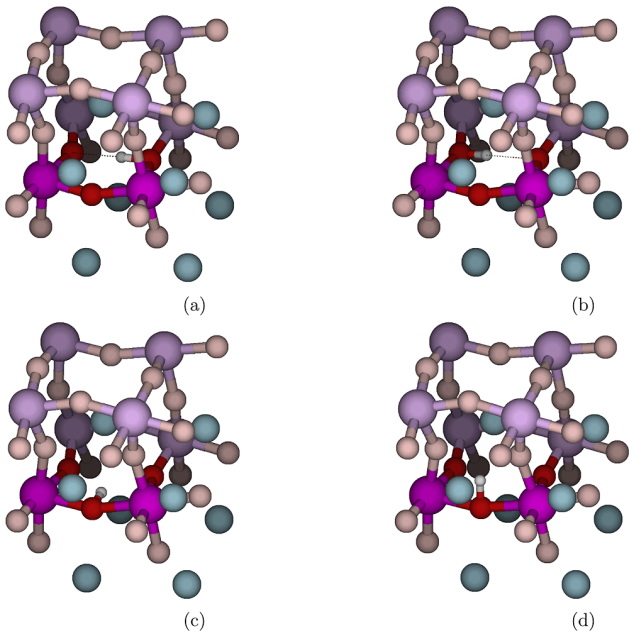

Figure 1. Energetic minima for one adsorbed hydrogen atom on cubic $CaMnO_3$. Mn: pink and light pink; O: red and light red; and Ca: blue; H: white.

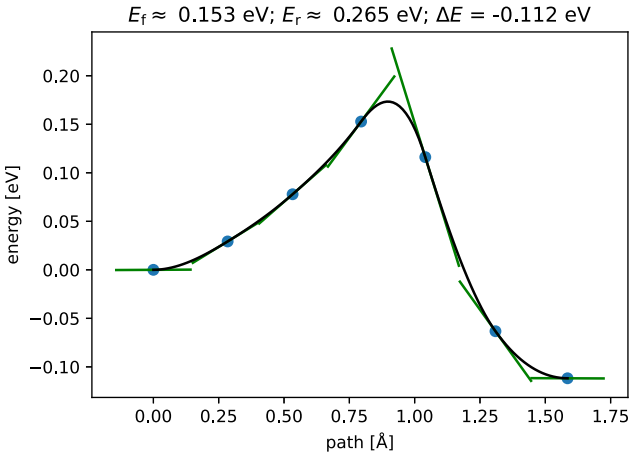

Figure 2. Energy profile for the intraoctahedral jump barrier [from (a) to (c) in Figure 1] for cubic $CaMnO_3$. E_f and E_r are the barriers in forward and reverse directions and ΔE is the energy difference between the minima.

The hydration energies are positive (40.2 to 40.9 kJ/mol) for orthorhombic $CaMnO_3$. Mn/Fe substitution strongly decreases the hydration energy from −55.6 to −29.3 kJ/mol for distant Fe and from −83.5 to −55.9 kJ/mol for close Fe atoms. Ca/Sr substitution increases the hydration enthalpy slightly to −51.2 to 9.9 kJ/mol for distant Fe and to −62.2 to −18.1 kJ/mol for close Fe atoms. Because the hydration enthalpy for unsubstituted orthorhombic $CaMnO_3$ is positive, we conclude that it is not proton conducting; it becomes a proton conductor by Mn/Fe substitution. Ca/Sr substitution only slightly lowers the effect.

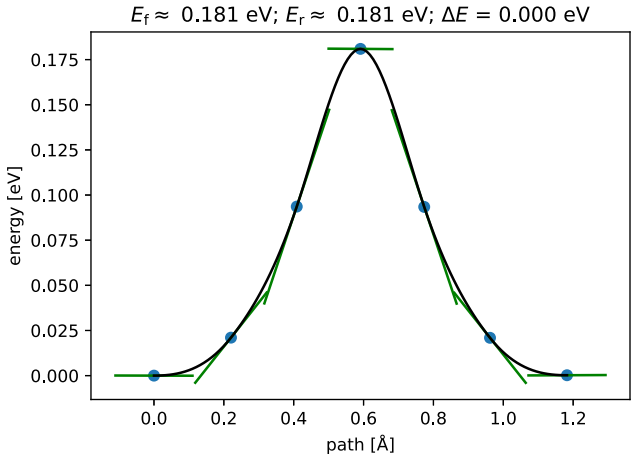

Figure 3. Energy profile for the interoctahedral jump barrier [from (a) to (b) in Figure 1] for cubic $CaMnO_3$. E_f and E_r are the barriers in forward and reverse directions and ΔE is the energy difference between the minima.

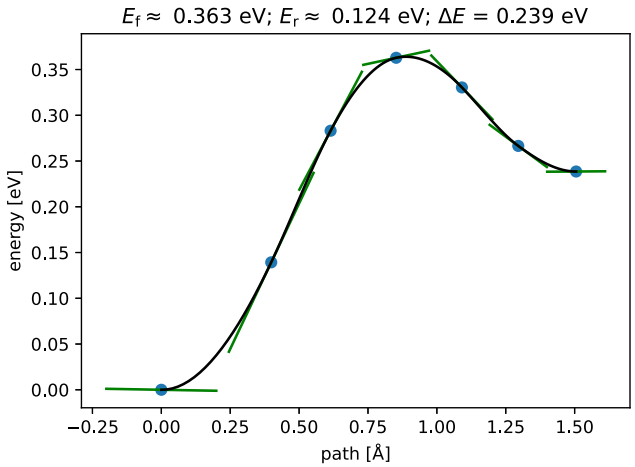

Figure 4. Energy profile for the rotational barrier [from (c) to (d) in Figure 1] for cubic $CaMnO_3$. E_f and E_r are the barriers in forward and reverse directions and ΔE is the energy difference between the minima.

Proton Migration Barriers for Cubic $CaMnO_3$. For computing the intraoctahedral and interoctahedral jump barriers as well as the rotational barrier, energy minima are searched for various proton positions in the unit cell (a more detailed description can be found in the Supporting

https://doi.org/10.1021/acs.jpcc.3c07594
J. Phys. Chem. C XXXX, XXX, XXX−XXX

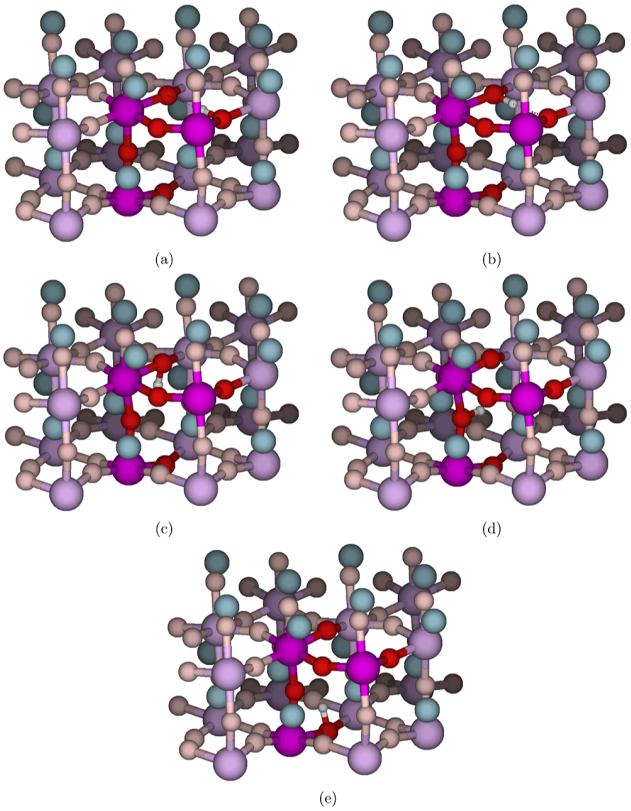

Figure 5. Energetic minima for one adsorbed hydrogen atom in orthorhombic $CaMnO_3$. Mn: pink and light pink; O: red and light red; Ca: blue; and H: white.

Table 4. Proton Migration Barriers for Orthorhombic $CaMnO_3$ in eV[a]

	jump barrier interoctahedral (a) → (b)	rotational barrier downward (b) → (c)	jump barrier intraoctahedral (c) → (d)	jump barrier intraoctahedral (d) → (e)
E_f	0.20	0.35	0.37	0.33
E_r	0.20	0.39	0.28	0.42

[a] E_f and E_r are the barriers in forward and reverse directions, (a) to (f) denote the structures given in Figure 5.

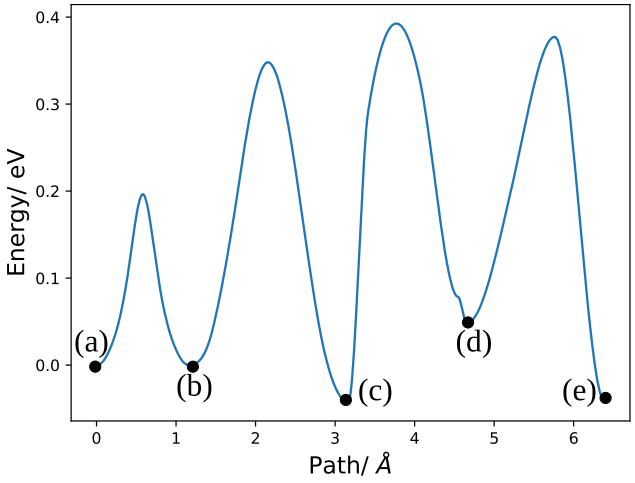

Figure 6. Proton migration path for orthorhombic $CaMnO_3$. (a) to (e) correspond to the structures in Figure 5.

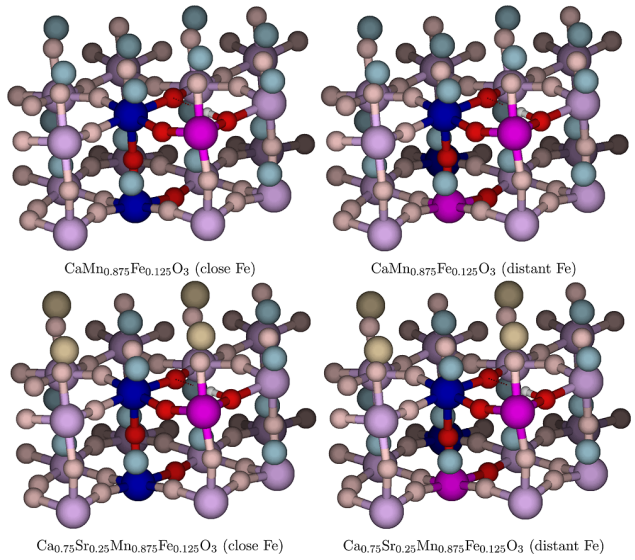

Figure 7. Structure (a) (→ Figure 5) for Mn/Fe- and Ca/Sr-substituted $CaMnO_3$. Mn: pink and light pink; O: red and light red; Ca: light blue; Fe: dark blue; Sr: light yellow; and H: white.

Information). The structures of the minima are shown in Figure 1.

The interoctahedral jump barrier corresponds to the migration barrier of the proton from minimum (a) to (c) in Figure 1. The energy profile is shown in Figure 2.

The intraoctahedral jump barrier is 0.15 eV in the forward direction and 0.27 eV in the reverse direction. Bork et al. computed a much higher value of 1.76 eV[16] for this jump. Regarding the other barriers in their study, it can be noticed that for all materials including Ca ($CaTiO_3$, $CaZrO_3$, and $CaMnO_3$) unusually high barriers are computed. That is indicating that there might be a technically problem for these compounds.

Bork et al.[16] only investigated the intraoctahedral jump barrier [from (a) to (b) in Figure 1]. However, the interoctahedral barrier [from (a) to (b) in Figure 1] looks promising because of the low O−O distance (2.8 Å). The energy profile of the computer interoctahedral jump barrier is shown in Figure 3.

A computed jump barrier of 0.18 eV (Figure 3) is lower than the intraoctahedral jump barrier (0.27 eV), which was expected because the lower O−O distance and the stabilization of the transition state by the hydrogen bond.

The rotational barrier (Figure 4) was computed to be 0.36 eV, which is in agreement with the 0.32 eV computed by Bork et al.[16]

Orthorhombic $CaMnO_3$. The next step is to examine if the low barriers found for the cubic phase are also present in the orthorhombic phase, which is the experimentally known phase at room temperature. The goal is to find a proton migration path through the bulk, which is required for macroscopic proton conduction. For this, different hydrogen adsorption positions have been optimized (Figure 5), their relative energies are given in the Supporting Information. The path starts with an interoctahedral jump from (a) to (b) in Figure 5. After that a rotation has to follow. The downward rotation from (b) to (c) is preferred over upward rotation because here the oxygen ion is blocked by the upper calcium ion. The path continues with two intraoctahedral jumps from (c) to (d) and from (d) to (e). A direct interoctahedral jump from (c) to (e) is not possible

https://doi.org/10.1021/acs.jpcc.3c07594
J. Phys. Chem. C XXXX, XXX, XXX−XXX

Table 5. Proton Migration Barriers for Orthorhombic $CaMnO_3$ Compared with Mn/Fe- and Ca/Sr-Substituted $CaMnO_3$ in eV[a]

		jump barrier inter octahedral (a) → (b)	rotational barrier downward (b) → (c)	jump barrier intraoctahedral (c) → (d)
$CaMnO_3$	E_f	0.20	0.35	0.37
	E_r	0.20	0.39	0.28
$CaMn_{0.875}Fe_{0.125}O_3$	E_f	0.21	0.34	0.25
(close Fe)	E_r	0.21	0.38	0.12
$CaMn_{0.875}Fe_{0.125}O_3$	E_f	0.17	0.33	0.26
(distant Fe)	E_r	0.22	0.42	0.23
$Ca_{0.75}Sr_{0.25}Mn_{0.875}Fe_{0.125}O_3$	E_f	0.24	0.26	0.30
(close Fe)	E_r	0.23	0.49	0.04
$Ca_{0.75}Sr_{0.25}Mn_{0.875}Fe_{0.125}O_3$	E_f	0.25	0.22	0.20
(distant Fe)	E_r	0.20	0.54	0.12

[a] E_f and E_r are the barriers in forward and reverse directions, (a) to (d) are the structures given in Figure 5.

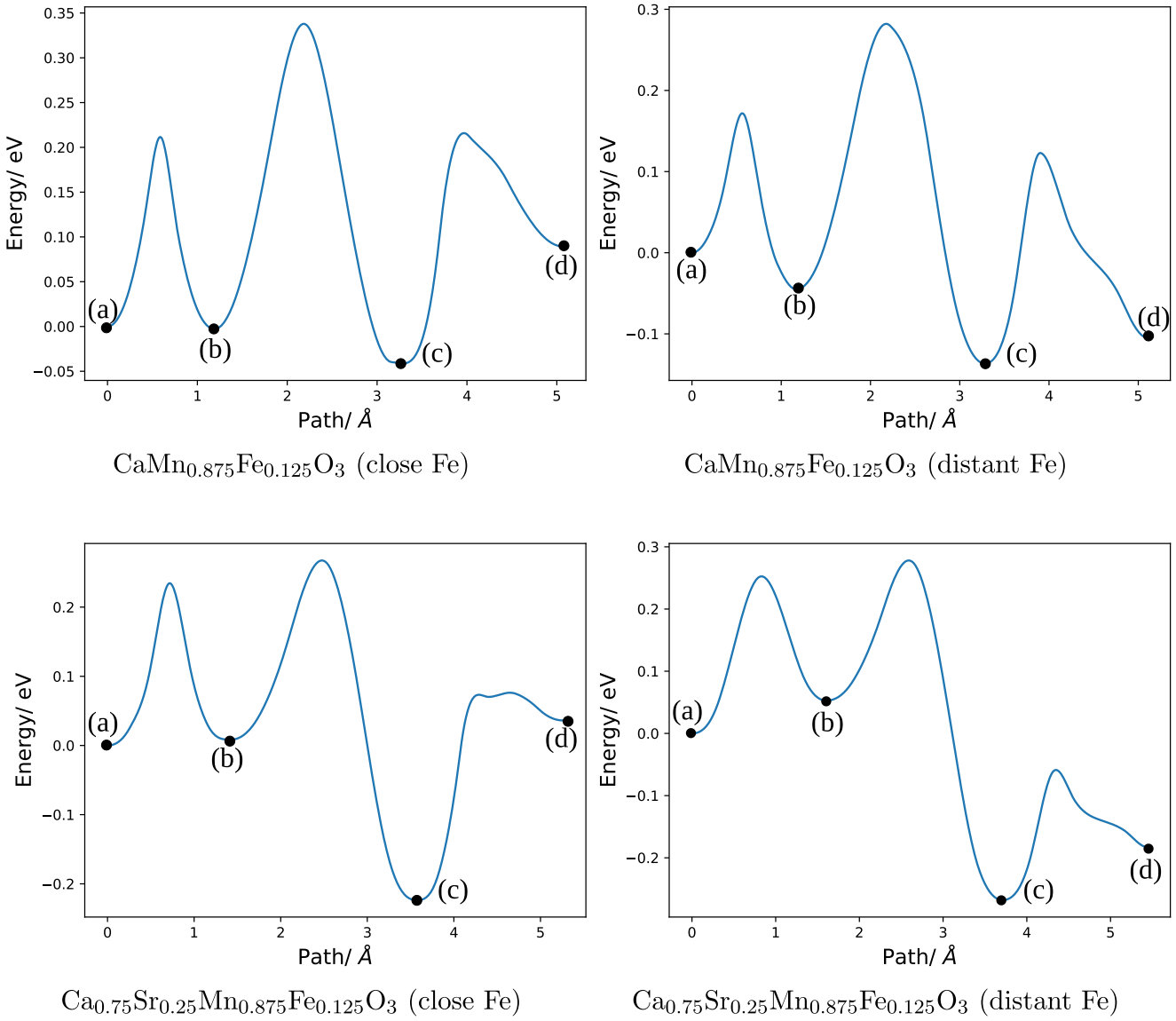

Figure 8. Proton migration path for Mn/Fe- and Ca/Sr-substituted $CaMnO_3$. The labels (a) to (d) correspond to the structures in Figure 5.

because of the large O−O distance (4.2 Å). The barriers are listed in Table 4.

The interoctahedral jump barrier (0.2 eV) is lower than the intraoctahedral jump barriers (0.28 to 0.42 eV). The downward

https://doi.org/10.1021/acs.jpcc.3c07594
J. Phys. Chem. C XXXX, XXX, XXX−XXX

rotation barrier is in between with 0.35 eV in the forward and 0.39 eV in the reverse direction.

The energy profile of the proton migration path from (a) to (e) is given in Figure 6.

Ca/Sr and Mn/Fe Substitution. Because $CaMnO_{3-\delta}$ decomposes into $CaMn_2O_4$ and Ca_2MnO_4 at higher temperatures, the maximum oxygen vacancy concentration is limited.[15] We showed in a previous work that Ca/Sr substitution prevents decomposition and Mn/Fe substitution lowers the oxygen vacancy formation energy.[14] Lower defect formation energies are advantageous because lower temperatures are required for the deoxygenation process (eq 3).

$$CaMnO_3 \rightarrow CaMnO_{3-\delta} + \frac{\delta}{2}O_2 \quad (3)$$

However, the effect of substitution on the migration barriers must be investigated. First, two neighboring Mn atoms have been replaced by Fe ($x_{Fe} = 0.125$). This configuration is a special case, which was considered here even if there are other configurations that might be more stable. The largest effect on the barrier is expected because an oxygen atom is connected to two Fe atoms. For comparison, the barriers for a structure with two distant Fe atoms are also computed. Ca/Sr substitution is modeled by substituting 25% of the Ca atoms by Sr atoms (alternating layers with alternating Ca and Sr chains and with only Ca atoms) in the unit cell. The structures are exemplarily shown in Figure 7 for structure (a).

The proton migration path is computed and compared with the path for the unsubstituted case in Figure 6. It is assumed as sufficient to compute only the path from (a) to (d) because the intraoctahedral barriers from (c) to (d) and from (d) to (e) are quite similar.

The corresponding proton migration barriers are listed in Table 5.

The interoctahedral jump barriers are only slightly changing, for all substitutions the barriers are between 0.17 and 0.24 eV. For the rotational barrier, the tendency that E_f is smaller than E_r remains. For close Fe in $CaMn_{0.875}Fe_{0.125}O_3$, the effect is the same as in $CaMnO_3$, while for distant Fe E_f and E_r already differ by 0.09 eV. For $Ca_{0.75}Sr_{0.25}Mn_{0.875}Fe_{0.125}O_3$, the effect is most pronounced with a difference of 0.23 eV. For the intraoctahedral migration barrier, E_f is larger than E_r because structure (d) is less stable than structure (c). The effect is the smallest for distant Fe in $CaMn_{0.875}Fe_{0.125}O_3$ (0.03 eV) and moderate for $CaMnO_3$ (0.09 eV) and close to Fe in $CaMn_{0.875}Fe_{0.125}O_3$. For $Ca_{0.75}Sr_{0.25}Mn_{0.875}$, a value of only 0.04 eV for E_r is observed, meaning that the energy difference between (c) and (d) is almost as high as the barrier. The reason is probably that the adsorption of the hydrogen to the oxygen atom coordinated to two Fe atoms is unfavored and the effect is increased by Ca/Sr substitution. The energy profiles for proton migration of the substituted structures are shown in Figure 8.

CONCLUSIONS

This theoretical work showed that all proton migration barriers of $CaMnO_3$ are below 0.5 eV, contrary to previous reports. For the experimentally observed orthorhombic phase, a complete proton migration path could be computed, with jump and rotation barriers ranging from 0.2 to 0.5 eV. Ca/Sr and Mn/Fe substitution does not change the barriers significantly but is essential for obtaining negative hydration energies, which is essential for a proton conductor. This in combination with the observed increased stability versus decomposition and the reduced oxygen vacancy formation energy, which indicates that $Ca_{1-x}Sr_xMn_{1-y}Fe_yO_3$ is a promising candidate for a PCEC anode material. It has to be mentioned that this is valid only for relatively small x_{Sr} and x_{Fe} (in our case $x_{Sr} = 0.25$ and $x_{Fe} = 0.125$) because higher amounts may change the structure of the solid. In future work, proton migration from the $CaMnO_3$ surface into the bulk will be studied. If the corresponding migration barriers are reasonably small, this would indicate that substituted $CaMnO_3$ may work as a PCEC electrode material. Also it can be recommended to increase experimental research on this compound.

ASSOCIATED CONTENT

Supporting Information

The Supporting Information is available free of charge at https://pubs.acs.org/doi/10.1021/acs.jpcc.3c07594.

Relative energies, energetic minima and oxygen−oxygen-distances of the jump barriers (PDF)

AUTHOR INFORMATION

Corresponding Authors

Benjamin Grimm − *Mulliken Center for Theoretical Chemistry, Clausius-Institut für Physikalische und Theoretische Chemie, University of Bonn, 53115 Bonn, Germany*; orcid.org/0000-0003-3929-4280; Email: grimm@thch.uni-bonn.de

Thomas Bredow − *Mulliken Center for Theoretical Chemistry, Clausius-Institut für Physikalische und Theoretische Chemie, University of Bonn, 53115 Bonn, Germany*; Email: bredow@thch.uni-bonn.de

Complete contact information is available at: https://pubs.acs.org/10.1021/acs.jpcc.3c07594

Notes

The authors declare no competing financial interest.

ACKNOWLEDGMENTS

We want to thank the Paderborn Center for Parallel Computing (PC^2) for providing substantial computer resources which are absolutely necessary for NEB calculations of our large supercells.

REFERENCES

(1) Hauch, A.; Küngas, R.; Blennow, P.; Hansen, A. B.; Hansen, J. B.; Mathiesen, B. V.; Mogensen, M. B. Recent advances in solid oxide cell technology for electrolysis. *Science* **2020**, *370*, No. eaba6118.

(2) Duan, C.; Huang, J.; Sullivan, N.; O'Hayre, R. Proton-conducting oxides for energy conversion and storage. *Appl. Phys. Rev.* **2020**, *7*, 011314.

(3) Poetzsch, D.; Merkle, R.; Maier, J. Stoichiometry variation in materials with three mobile carriers—thermodynamics and transport kinetics exemplified for protons, oxygen vacancies, and holes. *Adv. Funct. Mater.* **2015**, *25*, 1542−1557.

(4) Zohourian, R.; Merkle, R.; Raimondi, G.; Maier, J. Mixed-conducting perovskites as cathode materials for protonic ceramic fuel cells: understanding the trends in proton uptake. *Adv. Funct. Mater.* **2018**, *28*, 1801241.

(5) Merkle, R.; Hoedl, M. F.; Raimondi, G.; Zohourian, R.; Maier, J. Oxides with mixed protonic and electronic conductivity. *Annu. Rev. Mater. Res.* **2021**, *51*, 461−493.

(6) Papac, M.; Stevanović, V.; Zakutayev, A.; O'Hayre, R. Triple ionic−electronic conducting oxides for next-generation electrochemical devices. *Nat. Mater.* **2021**, *20*, 301−313.

(7) Wang, Z.; Yang, W.; Zhu, Z.; Peng, R.; Wu, X.; Xia, C.; Lu, Y. First-principles study of O 2 reduction on BaZr 1- x Co x O 3 cathodes in protonic-solid oxide fuel cells. *J. Mater. Chem. A* **2014**, *2*, 16707−16714.

https://doi.org/10.1021/acs.jpcc.3c07594
J. Phys. Chem. C XXXX, XXX, XXX−XXX

(8) Munoz-Garcia, A. B.; Pavone, M. First-principles design of new electrodes for proton-conducting solid-oxide electrochemical cells: A-site doped Sr2Fe1. 5Mo0. 5O6- δ perovskite. *Chem. Mater.* **2016**, *28*, 490−500.
(9) Xu, X.; Wang, H.; Ma, J.; Liu, W.; Wang, X.; Fronzi, M.; Bi, L. Impressive performance of proton-conducting solid oxide fuel cells using a first-generation cathode with tailored cations. *J. Mater. Chem. A* **2019**, *7*, 18792−18798.
(10) Lan, C.; Li, H.; Zhao, S. A first-principles study of the proton and oxygen migration behavior in the rare-earth perovskite SmNiO 3. *J. Comput. Electron.* **2020**, *19*, 905−909.
(11) Ding, H.; Wu, W.; Jiang, C.; Ding, Y.; Bian, W.; Hu, B.; Singh, P.; Orme, C. J.; Wang, L.; Zhang, Y.; et al. Self-sustainable protonic ceramic electrochemical cells using a triple conducting electrode for hydrogen and power production. *Nat. Commun.* **2020**, *11*, 1907.
(12) Hoedl, M.; Chesnokov, A.; Gryaznov, D.; Merkle, R.; Kotomin, E.; Maier, J. Proton migration barriers in $BaFeO_{3-\delta}$ − insights from DFT calculations. *J. Mater. Chem. A* **2023**, *11*, 6336−6348.
(13) Grimm, B.; Bredow, T. Oxygen Defect Formation Thermodynamics of CaMnO3: A Closer Look. *Phys. Status Solidi B* **2023**, *260*, 2200427.
(14) Grimm, B.; Bredow, T. Defect Formation Thermodynamics of (A, A')(B, B') O 3 (A= Mg, Ca, Sr and B= Ti, Mn, Cr, Fe, Mo) Perovskites. *Phys. Status Solidi B* **2023**, *260*, 2300048.
(15) Bulfin, B.; Vieten, J.; Starr, D.; Azarpira, A.; Zachäus, C.; Hävecker, M.; Skorupska, K.; Schmücker, M.; Roeb, M.; Sattler, C. Redox chemistry of $CaMnO_3$ and $Ca_{0.8}Sr_{0.2}MnO_3$ oxygen storage perovskites. *J. Mater. Chem. A* **2017**, *5*, 7912−7919.
(16) Bork, N.; Bonanos, N.; Rossmeisl, J.; Vegge, T. Simple descriptors for proton-conducting perovskites from density functional theory. *Phys. Rev. B: Condens. Matter Mater. Phys.* **2010**, *82*, 014103.
(17) Poeppelmeier, K.; Leonowicz, M.; Scanlon, J.; Longo, J.; Yelon, W. Structure determination of CaMnO3 and CaMnO2. 5 by X-ray and neutron methods. *J. Solid State Chem.* **1982**, *45*, 71−79.
(18) Dovesi, R.; Erba, A.; Orlando, R.; Zicovich-Wilson, C. M.; Civalleri, B.; Maschio, L.; Rérat, M.; Casassa, S.; Baima, J.; Salustro, S.; et al. Quantum-mechanical condensed matter simulations with CRYSTAL. *Wiley Interdiscip. Rev.: Comput. Mol. Sci.* **2018**, *8*, No. e1360.
(19) Bredow, T.; Gerson, A. R. Effect of exchange and correlation on bulk properties of MgO, NiO, and CoO. *Phys. Rev. B: Condens. Matter Mater. Phys.* **2000**, *61*, 5194−5201.
(20) Vilela Oliveira, D.; Laun, J.; Peintinger, M. F.; Bredow, T. BSSE-correction scheme for consistent gaussian basis sets of double-and triple-zeta valence with polarization quality for solid-state calculations. *J. Comput. Chem.* **2019**, *40*, 2364−2376.
(21) Atomic Simulation Environment. Main ASE repo. https://gitlab.com/ase/ase (accessed 2022-11-01).
(22) Atomic Simulation Environment. ASE fork. https://gitlab.com/waldlaubsaengernest/ase (accessed 2023-10-01).
(23) Broyden, C. G. The Convergence of a Class of Double-rank Minimization Algorithms 1. General Considerations. *IMA J. Appl. Math.* **1970**, *6*, 76−90.
(24) Fletcher, R. A new approach to variable metric algorithms. *Comput. J.* **1970**, *13*, 317−322.
(25) Goldfarb, D. A family of variable-metric methods derived by variational means. *Math. Comput.* **1970**, *24*, 23−26.
(26) Shanno, D. F. Conditioning of quasi-Newton methods for function minimization. *Math. Comput.* **1970**, *24*, 647−656.
(27) Henkelman, G.; Jónsson, H. Improved tangent estimate in the nudged elastic band method for finding minimum energy paths and saddle points. *J. Chem. Phys.* **2000**, *113*, 9978−9985.
(28) Taguchi, H.; Nagao, M.; Sato, T.; Shimada, M. High-temperature phase transition of CaMnO3- δ. *J. Solid State Chem.* **1989**, *78*, 312−315.

https://doi.org/10.1021/acs.jpcc.3c07594
J. Phys. Chem. C XXXX, XXX, XXX−XXX

F. A theoretical study on proton migration on the $CaMnO_3$ surface

Benjamin Grimm[†] und Thomas Bredow[*]

Eingereicht am 28.03.2024 bei J. Phys. Chem. C

[†]Address: Mulliken Center for Theoretical Chemistry, Clausius-Institut für Physikalische und Theoretische Chemie, University of Bonn, Beringstr. 4, 53115 Bonn, Germany.
Email Address: grimm@thch.uni-bonn.de

[*]Address: Mulliken Center for Theoretical Chemistry, Clausius-Institut für Physikalische und Theoretische Chemie, University of Bonn, Beringstr. 4, 53115 Bonn, Germany.
Email Address: bredow@thch.uni-bonn.de

A Theoretical Study on Proton Migration on the $CaMnO_3$ Surface

Benjamin Grimm* and Thomas Bredow*

Mulliken Center for Theoretical Chemistry, Clausius-Institut für Physikalische und Theoretische Chemie, University of Bonn, Beringstr. 4, 53115 Bonn, Germany.

E-mail: grimm@thch.uni-bonn.de; bredow@thch.uni-bonn.de

Abstract

Recently, it was shown theoretically, that $Ca_{1-x}Sr_xMn_{1-y}Fe_yO_3$ has low proton migration barriers ranging from 0.2 to 0.5 eV [B. Grimm, T. Bredow, J. Phys. Chem C **2024** DOI: 10.1021/acs.jpcc.3c07594]. In this article, the proton migration mechanism from the $CaMnO_3$ surface into the bulk will be investigated theoretically. The process is one of the key steps in proton conducting electrolysis cells (PCEC). In the theoretical models, the (100) and (010) surfaces are considered, which together account for about 50 percent of the total surface area of $CaMnO_3$ single crystals. It turns out that the proton migration mechanism on the (010) surface is feasible and is further improved by Mn/Fe substitution. The (010) surface of $CaMn_{0.75}Fe_{0.25}O_3$ has strongly negative hydration energies of −230 kJ/mol in the first and −191 kJ/mol in inner layers. The largest barrier for proton migration is calculated for the hopping process from the first to the second layer. This is due to the relatively large hydration energy difference of about 1 eV between the two layers, which is also found for the known proton conductor $BaFeO_3$. The lower hydration energies in inner layers for $CaMn_{0.75}Fe_{0.25}O_3$ are leading to low barriers (0.21 and 0.51 eV), predicting the (010) surface of this material as a possible candidate for use in a PCEC electrode.

1. Introduction

Renewable energies are a relevant topic for guaranteeing the future of energy supply and reducing CO_2 emissions. The conversion of electrical energy into chemical energy plays a pivotal role. For this reason, high-temperature electrolysis cells have already been extensively investigated, whereby a distinction is made between the solid oxide electrolysis cell (SOEC)[1] and the proton conducting electrolysis cell (PCEC).[2] While the SOEC is already being used in industrial scale, the PCEC has increasingly become the focus of current research. The PCEC is generally advantageous because of the lower proton migration barriers compared to oxide ions and the production of dry hydrogen. However, proton conducting anode materials have to be found.

Theoretical studies can forecast the proton conductivity of a material by computing proton migration barriers and hydration energies. Several studies have already calculated proton migration barriers of bulk perovskites and obtained values between 0.25 and 0.5 eV.[3–7] Hoedl et al. calculated the proton migration barriers of bulk $BaFeO_{3-\delta}$ and obtained comparable low barriers between 0.1 and 0.3 eV.[8] These low barriers confirm the high proton conductivity in $BaFeO_{3-\delta}$, which is explained by the relatively small O-O and O-H distances.

In recent work, we showed that $CaMnO_3$ has low proton migration barriers between 0.2 and 0.5 eV.[9] However, computing proton migration barriers and hydration energies in the bulk is not sufficient to forecast a material to be suitable for use as a PCEC anode material. Since the surface is the catalytic active center of the solid, defect formation and water adsorption on the surface is the preliminary step for the overall process. Carlotto computed oxygen vacancy formation energies and water adsorption energies of Al, Co and Cu doped $SrTiO_3-\delta$ on the (100) surface.[10] It was shown that dopants lead to lower defect formation energies and influence the stabilization of different water adsorption types (molecular or dissociative). Li et al. computed different proton-migration mechanisms on the (001) surface of perfect and defective $LaMO_3$ (M = Cr, Mn, Fe).[11] For perfect $LaMO_3$ they found that the protons prefer to migrate along the [010] axis in a Grotthus-type mechanism. For

the defect structures a so-called vehicle mechanism is preferred for M=Mn and Fe, in which the protons hop together with the underlying oxide ions. Interestingly, Li et al. only computed proton migration mechanisms perpendicular to the surface normal. The existence of a proton-migration path from the surface into the bulk is absolutely essential for the catalytic activity of proton conductors. The challenge is that the surface OH-groups are favored because the undercoordinated surface atoms are stabilized. Merkle et al. mentioned in a review about mixed protonic and electronic conductivity that this stabilization causes higher proton concentrations on the surface than in the bulk.[12]

To the best of our knowledge, there is no theoretical study yet computing the proton migration path from the surface to the bulk for $CaMnO_3$. In this work, the proton migration from the $CaMnO_3$ surface into the bulk will be investigated in more detail. The (100) and (010) surfaces of the experimentally found orthorhombic polymorph (space group 62) are considered, which together account for about 50 % of the total surface area of $CaMnO_3$ single crystals.[13] First, the oxygen defect formation energies and hydration energies are computed for the first four layers of both surfaces for $CaMnO_3$ and $CaMn_{0.75}Fe_{0.25}O_3$. The proton migration path is then computed with the Nudged-Elastic-Band method for the most promising surface model (with low defect formation energies and a small difference between the hydration energies in the first and inner layers). The energetic differences of the hydrogen positions in the first and inner layers are then compared to the theoretical reference $BaFeO_3$. Since these energy differences are mainly responsible for the migration barriers, this simple procedure allows for a comparison of $CaMnO_3$-based materials to a literature-known good proton conductor.

2. Computational Details

All calculations were performed with the crystal orbital program CRYSTAL17 (version 1.0.2).[14] The hybrid functional PW1PW and the pob-TZVP-rev2 basis sets[15] optimized

by our group were used. This combination provided the most accurate results for the calculation of the defect formation enthalpies of $CaMnO_3$.[16] The integral truncations were set to 10^{-7} and 10^{-14} atomic units and a 4×4×1 Monkhorst-Pack grid was used in the slab calculations. All calculations were performed for a ferromagnetic spin configuration in order to increase symmetry and reduce computational cost. The proton migration barriers were calculated using the nudged-elastic-band (NEB) method implemented in the atomic simulation environment (ASE-NEB[17]) with CRYSTAL as calculator. The supercell volume is fixed and five images are optimized for each NEB. A modified version of the ASE code[18] was used to exploit all symmetry-related features implemented in CRYSTAL in the optimization.

The surface models were constructed in such a way that at least one symmetry element exists parallel to the surface plane. For undoped orthorhombic $CaMnO_3$ the (100) and (010) surfaces were considered, which have the lowest calculated surface energies.[13] For $BaFeO_3$ and the cubic $CaMnO_3$ polymorph the layer sequence does not allow stoichiometric and symmetric models. In this case, a non-stoichiometric but symmetric model was selected and the surface energy was calculated relative to the most stable oxides (BaO and Fe_2O_3 or CaO and MnO_2, respectively). Most slab models consist of seven stoichiometric layers. In our previous study it was found that surface energies are close to convergence with this model size. Due to the symmetry of the surface model, the hydrogen atoms were always adsorbed simultaneously at the top and bottom and therefore all hydration energies and barriers were normalized accordingly.

In the PCEC process two hydrogen atoms are adsorbed on the surface by adsorbing a water molecule into a first layer oxygen vacancy. That is why the presence of first-layer defects as well as negative hydration enthalpies are essential. In order to reduce computational effort, the proton migration mechanism is only computed for one proton, while the second proton stays in the first layer.

3. Results and Discussion

The surfaces of orthorhombic $CaMnO_3$ (space group 62) have already been investigated theoretically.[13] The (100) and (010) surfaces have 20 % and 27% contribution to the calculated Wulff shape of $CaMnO_3$ single crystals, respectively, and are therefore both relevant.[13] It has to be noted that the defective $(101)_m n$ model which has a contribution of 30.5 % to the overall surface is not taken into account, because the defective model is most likely not able to model hydrogen adsorption correctly. For the computation of $CaMn_{0.75}Fe_{0.25}O_3$, a configuration with two distant Fe atoms is chosen because it is statistically more likely than two close Fe atoms. A similar Mn/Fe distribution was used in our previous study.[9]

Defect formation and hydration energies

(100) surface

As mentioned above, two hydrogen atoms are added to the surface by first removing an oxygen atom and then adding a water molecule (Eqs. 1 and 2). It has to be noted, that during optimization one hydrogen atom left the water molecule and moved to a neighboring surface oxygen atom, so that two OH groups are formed.

$$CaMnO_3 \rightarrow CaMnO_{3-\delta} + \frac{\delta}{2}O_2 \quad \text{Defect formation} \tag{1}$$

$$CaMnO_{3-\delta} + \delta H_2O \rightarrow CaMnO_3H_2 \quad \text{Hydration} \tag{2}$$

The seven-layer surface model of the (100) surface is shown in Figure 1. It has to be noted that the (100) surface has a strong surface dipole because of the alternating $(2\,O)^{4-}$ and $CaMnO^{4+}$ layers which might effect the formation energies of charged defects. The use of symmetrical surface models partly minimizes this effect. The seven-layer slab model is justified since the surface energy is already converged.[13] Since there are already 120 atoms in the model the use of even more layers was not feasible due to limitations of computational

resources.

As the primitive surface unit cell is quite small and leads to unwanted adsorbate-adsorbate interaction, a 2×2 supercell was created.

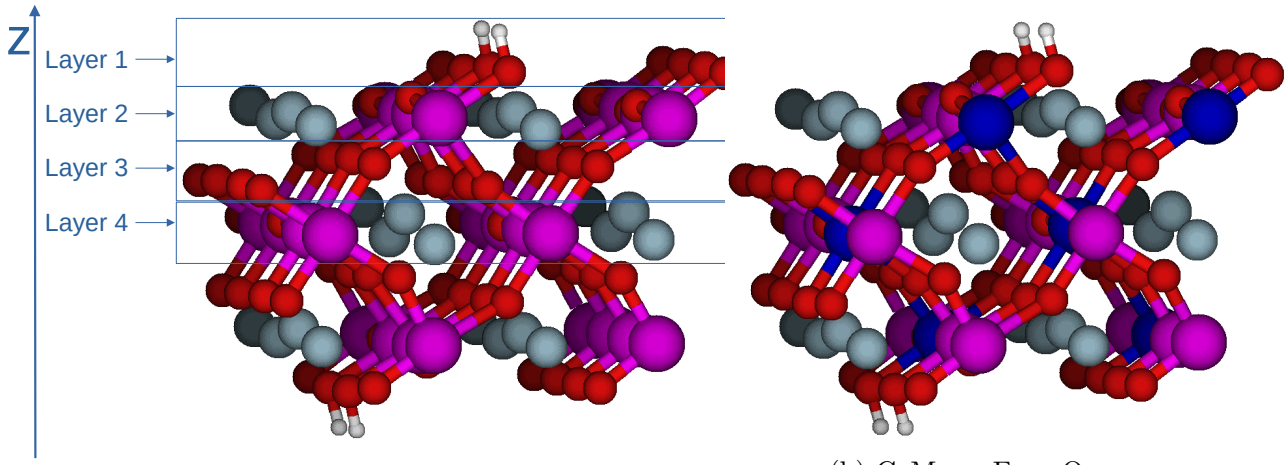

(a) $CaMnO_3$ (b) $CaMn_{0.75}Fe_{0.25}O_3$

Figure 1: Surface models of the (100) surface for $CaMnO_3$ and $CaMn_{0.75}Fe_{0.25}O_3$
Mn: pink ; O: red; Ca: blue

It is assumed that during the PCEC process, one of the upper oxygen atoms in the first layer is removed at elevated temperatures to form an oxygen defect (Eqn. 1). The hydration of the defective structure (Eqn. 2) then formally corresponds to the hydrogenation of the two upper oxygen atoms. The calculated oxygen defect formation energies and hydration energies are listed in Table 1.

Table 1: Oxygen defect formation energies (ΔE_{ODF}) (a) and hydration energies (ΔE_{hyd}) (b) in eV of the (100) $CaMnO_3$ surface compared to bulk $CaMnO_3$. All surface hydration energies are computed with respect to a first-layer defect, hydrogen positions are the Minima shown in the SI.

(a)

Layer	ΔE_{ODF}	
	$CaMnO_3$	$CaMn_{0.75}Fe_{0.25}O_3$
1	1.30	0.23
2	1.87	1.21
3	1.77	1.23
4	1.80	1.40
bulk	1.87	

(b)

Minimum	ΔE_{hyd}	
	$CaMnO_3$	$CaMn_{0.75}Fe_{0.25}O_3$
1	-3.27	-2.40
2	-2.17	-1.39
3	-1.70	-1.07
4	-1.56	-1.00

For $CaMnO_3$ ΔE_{ODF} is relatively small in the first layer (1.30 eV) and rapidly converges towards the bulk value (1.87 eV) in inner layers. This justifies the above assumption that oxygen vacancies are primarily formed in the topmost layer. This trend is even more pronounced in the Mn/Fe substituted system where ΔE_{ODF} is only 0.23 eV in the first layer. During adsorption of H_2O into a vacant O position of the first layer, one hydrogen atom binds to a neighboring surface oxygen atom. This dissociation process is not associated with an activation barrier as it occurs during structure optimization. ΔE_{hyd} is strongly negative in the topmost layers, in line with a strong water affinity of the defective surfaces.

(010) surface

The most stable (010) surface model is non-stoichiometric with a Ca_4O_4 termination (Figure 2. All calculations were performed for a 1×2 supercell corresponding to $Ca_{24}Mn_{20}O_{64}$.

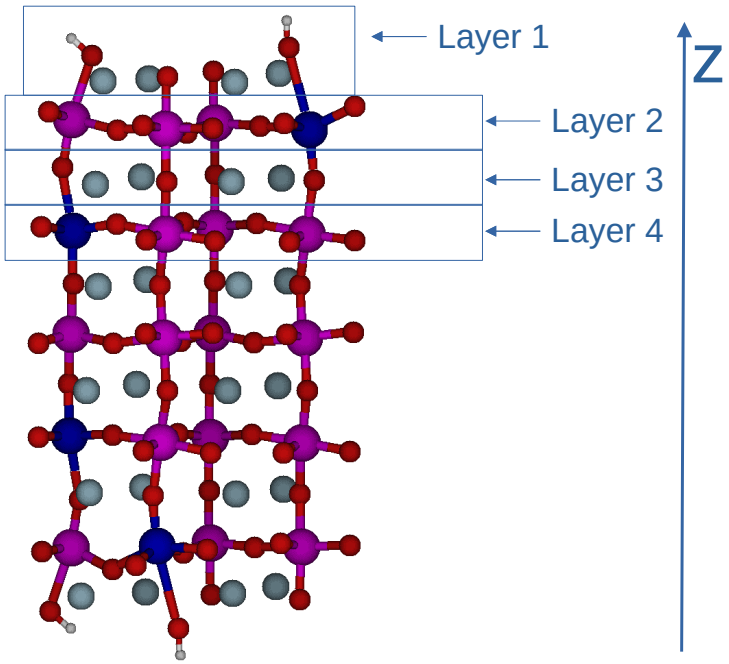

2×1 supercell with two adsorbed H-atoms

Figure 2: Surface model of the (010) surface of $CaMn_{0.75}Fe_{0.25}O_3$.
Mn: pink ; Fe: blue; O: red; Ca: light blue

The oxygen defect formation energies and hydration energies are computed for the first four layers. The results are given in Table 2.

Table 2: Oxygen defect formation energies (ΔE_{ODF}) and hydration energies (ΔE_{hyd}) eV of the (010) $CaMnO_3$ surface compared to bulk $CaMnO_3$. All surface hydration energies are computed with respect to a first-layer defect, hydrogen positions are shown in the SI.

Layer	ΔE_{ODF}		ΔE_{hyd}	
	$CaMnO_3$	$CaMn_{0.75}Fe_{0.25}O_3$	$CaMnO_3$	$CaMn_{0.75}Fe_{0.25}O_3$
1	2.85	0.98	-2.78	-2.38
2	2.37	1.70	-1.26	-1.23
3	2.06	0.98	-1.69	-1.98
4	1.86	1.24	-1.37	-1.91
bulk	1.87			

For undoped $CaMnO_3$, the hydration energies in the first two layers are 0.49 to 0.89 eV

less negative than for the (100) surface, and the oxygen defect formation energies are 0.06 to 1.55 eV larger. This indicates that oxygen vacancies are preferably formed on the (100) surface so the hydration will also take place predominantly there. Also the absolute value of the hydration energy is 7 kJ/mol smaller than the defect formation energy which disfavors hydrogenation.

$CaMn_{0.75}Fe_{0.25}O_3$ shows similar hydration energies in the first layer for both surfaces. In the second layer of the (010) surface the hydration energy is 0.15 eV less negative compared to the (100) surface. However, the hydration energies in the third and fourth layer decrease again (-1.98 and -1.91 eV) while they increase in the (100) surface (-1.07 and -1.01 eV). This indicates a more favorable proton migration mechanism for the (010) surface than for the (100) surface. The first layer defect formation energy is significantly higher for the (010) surface (2.85 eV) than for the (100) surface (1.30 eV). This could lead to preferred oxygen defect formation at the (100) surface rather than on (010). However, this is only valid for the same Fe concentration at both surfaces. Comparison of the calculated results for (100) and (010) surfaces of $CaMnO_3$ shows that for unsubstituted $CaMnO_3$ hydration is only taking place at the (100) surface, while it is possible on both surfaces for $CaMn_{0.75}Fe_{0.25}O_3$. The hydration energies in inner layers indicate that the proton migration from the surface to the bulk is favored for the (010) surface. For better understanding of the proton migration mechanism, the corresponding minimum energy path is computed for the (100) surface of $CaMnO_3$ and the (010) surface of $CaMn_{0.75}Fe_{0.25}O_3$.

Proton migration path

(100)-surface of $CaMnO_3$

The proton migration path from the surface into the bulk is investigated in more detail by performing NEB calculations. The initial and final structures for the hopping processes are shown in Figure 3.

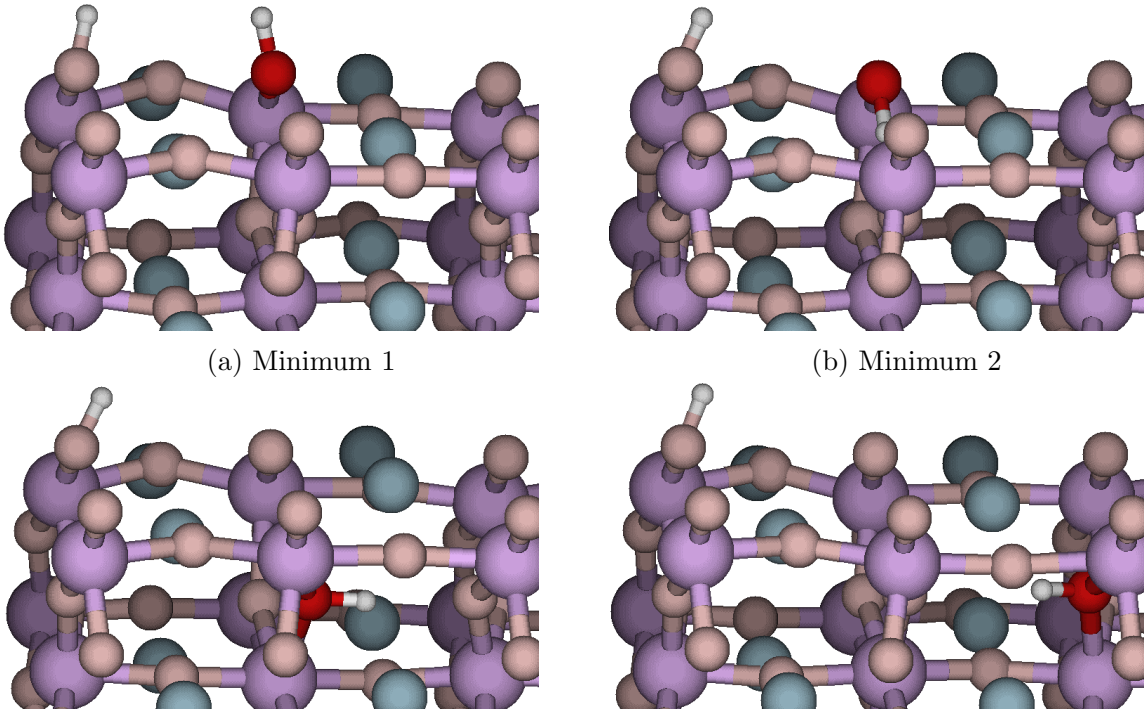

(a) Minimum 1 (b) Minimum 2

(c) Minimum 3 (d) Minimum 4

Figure 3: Energetic minima of the proton migration path for the (100)-surface of $CaMnO_3$. Mn: light pink; O: red and light red; Ca: blue; H: white
Oxygen next to the migrating proton is highlighted in red.

The relative energies of the four minima are listed in Table 3.

Table 3: Relative energies of Minimum 1 to Minimum 4 (eV) in the (100)-surface of $CaMnO_3$; for the corresponding structures see Figure 3

	Minimum 1	Minimum 2	Minimum 3	Minimum 4
E_{rel}	0.00	1.10	1.57	1.71

There is a substantial energy difference of 1.1 eV between Minima 1 and 2. The rotation of the proton away from the surface is unfavorable, since the upper coordination site of the (approximately trigonal-pyramidal) $CaMn_3O$ unit is then unoccupied. At Minimum 3, the proton is no longer bound to the uppermost oxygen atom for the first time, which also leads to a further energy increase. The energy difference between Minimum 3 and Minimum 4 is

then only 0.14 eV, which no longer influences the migration barriers. The calculated energy profile from Minimum 1 to Minimum 4 is shown in Figure 4, the barriers are listed in Table 4.

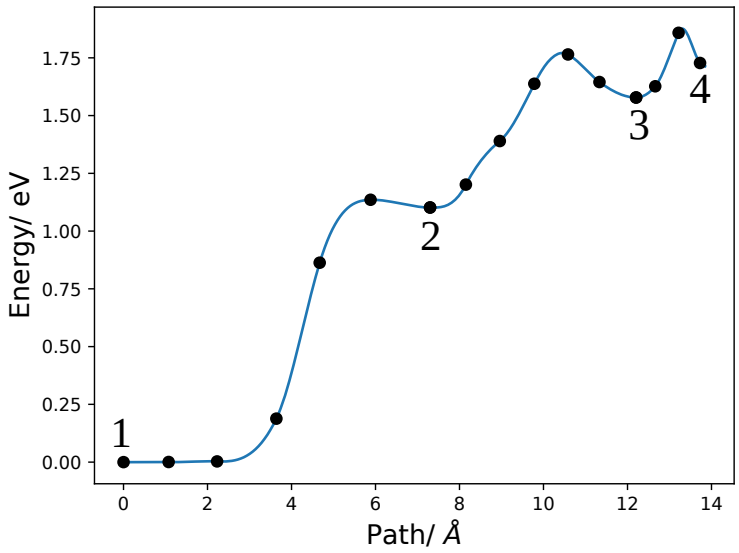

Figure 4: Minimum energy pathway for proton migration from Minimum 1 to Minimum 4 in the (100)-surface of $CaMnO_3$.

Table 4: Barriers for proton migration from Minimum 1 to Minimum 4 in the (100)-surface of $CaMnO_3$ in eV

	Barrier 1 (1→ 2)	Barrier 2 (2→ 3)	Barrier 3 (3→ 4)
forward	1.12	0.66	0.28
backward	0.03	0.19	0.12

The activation energy for rotation of the proton away from the surface (barrier 1) is mainly due to the high energy difference between Minimum 1 and Minimum 2. Therefore there is almost no barrier for back rotation, which means that population of minimum structure 2 is very low. The proton migration from the surface to the next inner oxygen atom (barrier 2) has a barrier of 0.66 eV in the forward direction and 0.19 eV in the backward

direction. This barrier is still significantly larger than the migration barriers calculated in the bulk (0.2-0.5 eV). The next jump barrier (barrier 3) of 0.28 eV is comparable to the jump barriers in the bulk, which suggests that barriers for subsequent hopping processes into the bulk will also be in this range. It can therefore be assumed that when a proton migrates from Minimum 1 to Minimum 3, it will continue to move in a similar way to the bulk. However, this process is strongly hindered by the high energy of Minimum 2. This structure may be stabilized by higher amounts of water on the surface which is a realistic scenario for the PCEC process.

(010)-surface of $CaMn_{0.75}Fe_{0.25}O_3$

The proton migration path has been computed analogously for the (010)-surface of $CaMn_{0.75}Fe_{0.25}O_3$. The initial structures for the three NEB calculations are shown in Figure 5. The relative energies of the minima are listed in Table 5.

Table 5: Relative energies (eV) of Minimum 1 to Minimum 4 in the (010)-surface of $CaMn_{0.75}Fe_{0.25}O_3$; the corresponding structures are shown in Figure 3

	Minimum 1	Minimum 2	Minimum 3	Minimum 4
E_{rel}	0.00	1.15	0.40	0.46

The relative energy of Minimum 2 is significantly higher than the other energies. Correspondingly the activation energy between Minimum 1 to Minimum 2 is the highest barrier of the migration path. The decrease of the energy from Minimum 2 to Minimum 3 favors the proton migration path, since it makes a backwards migration more unlikely.

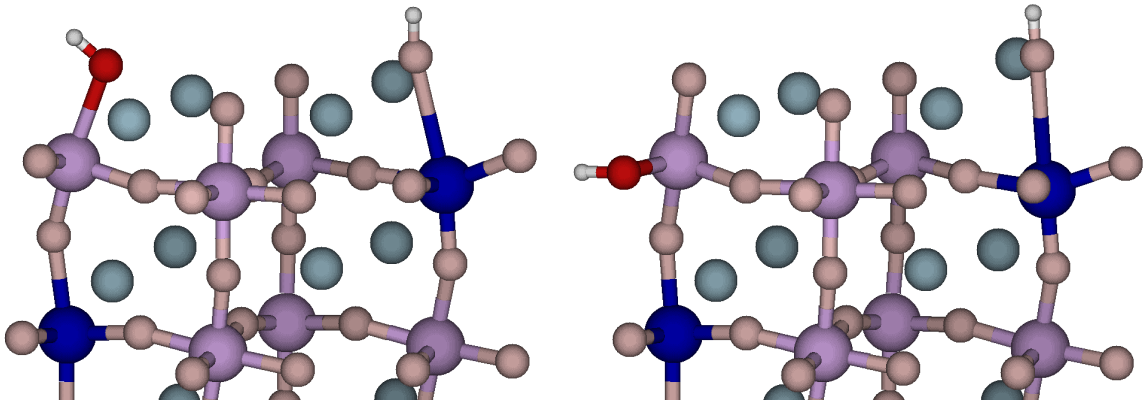

(a) Minimum 1

(b) Minimum 2

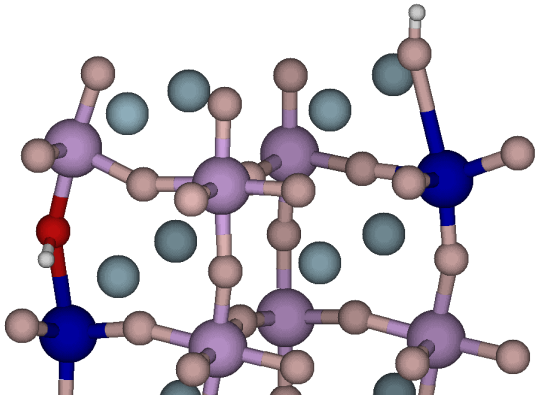

(c) Minimum 3

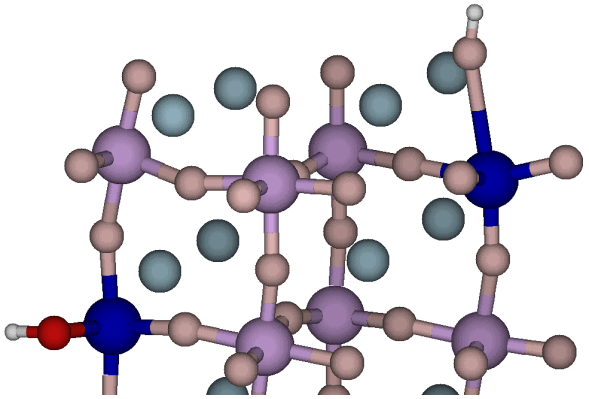

(d) Minimum 4

Figure 5: Energetic minima for the proton migration path in the (010)-surface of $CaMn_{0.75}Fe_{0.25}O_3$. Mn: light pink; Fe: blue; O: red and light red; Ca: blue; H: white Oxygen next to the migrating proton is highlighted in red.

The energy profile for the proton migration from Minimum 1 to Minimum 4 is shown in Figure 6, the barriers are listed in Table 6.

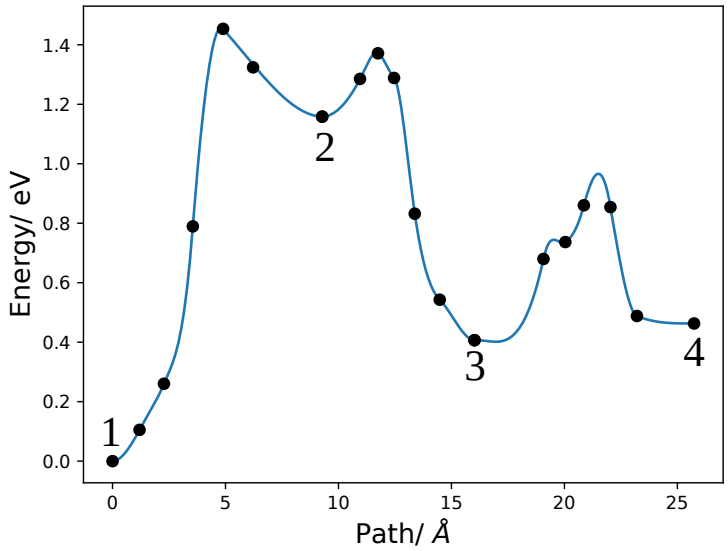

Figure 6: Proton migration path for the (010) surface of $CaMn_{0.75}Fe_{0.25}O_3$ from Minimum 1 to Minimum 4.

Table 6: Barriers for proton migration in the (010) surface of $CaMn_{0.75}Fe_{0.25}O_3$ from Minimum 1 to Minimum 4 in eV

	Barrier 1 (1→ 2)	Barrier 2 (2→ 3)	Barrier 3 (3→ 4)
forward	1.45	0.21	0.46
backward	0.25	0.97	0.40

Comparison with $BaFeO_3$

For $BaFeO_3$, Hoedl et al. calculated small proton migration barriers, ≈ 0.22 eV, in the bulk.[8] The theoretical results are confirmed by the experimental measurements of Zohourian et al. who measured proton concentrations of 10 % per formula unit for $Ba_{0.95}La_{0.05}Fe_{0.8}Zn_{0.2}O_{3-\delta}$ at 250°C.[19] Therefore, $BaFeO_3$ is a suitable theoretical reference to check the significance of the calculated high barrier for surface proton migration, see Table 4.

$BaFeO_3$ crystallizes in the cubic space group 221 with an experimental lattice parameter of

3.971 Å.[20] The geometry optimization resulted in a lattice parameter of 3.970 Å, which is in almost perfect agreement. The most stable (100) surface was calculated, for which two different terminations are possible. For the Ba_4O_4 terminated (100) surface, which is the most stable surface model (see SI), four different positions of two adsorbed hydrogen atoms are calculated for a surface model with 9 layers (Figure 7). The model is therefore slightly thinner than the 11-layered model of the (010)-surface of $CaMnO_3$, which is the closest counterpart.

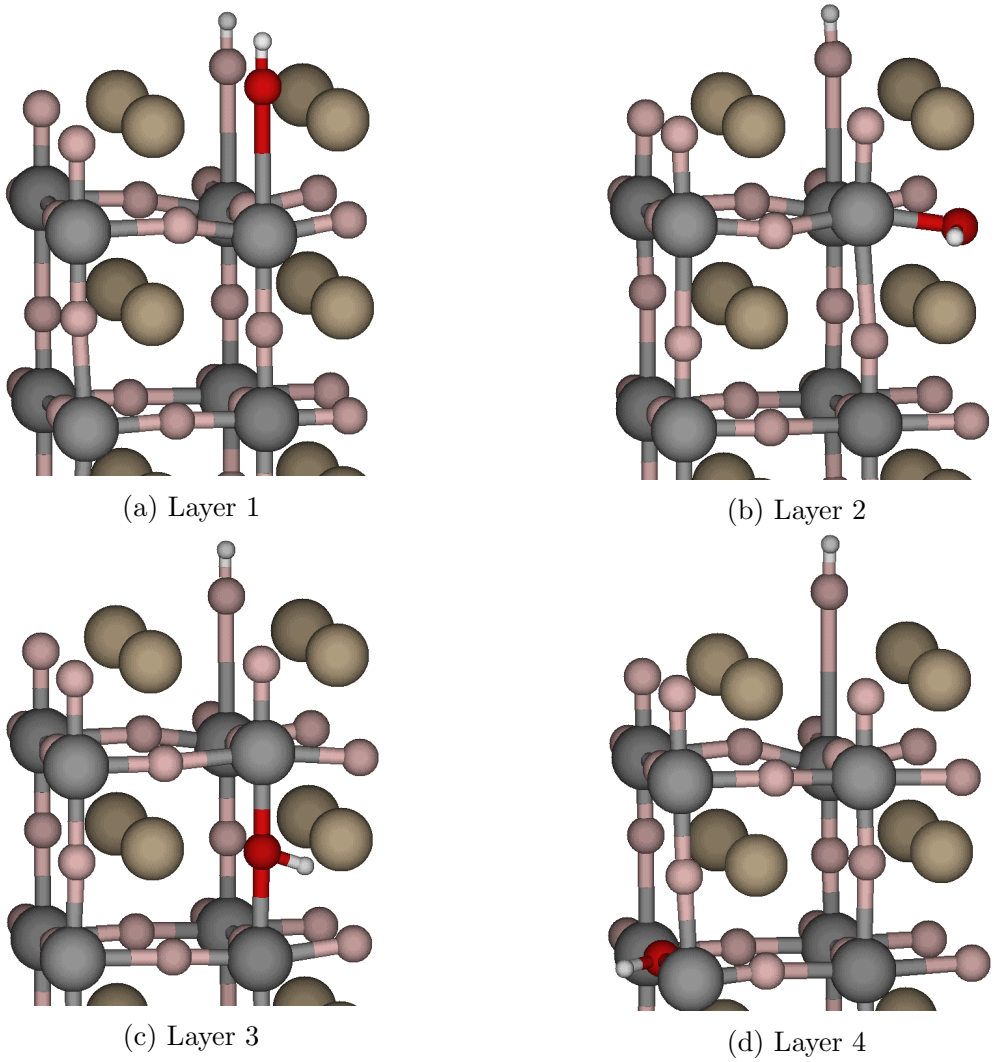

(a) Layer 1

(b) Layer 2

(c) Layer 3

(d) Layer 4

Figure 7: Hydrogen adsorption positions on the (100)-surface of $BaFeO_3$ (one hydrogen in the first layer and the other in layer 1 to 4). Fe: gray; O: red and light red; Ba: light yellow; H: white. Oxygen next to the migrating proton is highlighted in red.

Adsorption of both hydrogen atoms on oxygen atoms in the top layer (Layer 1) leads to strong stretching of the Fe-O bond from 1.9 $\AA$ to 3.1$\AA$. If a hydrogen atom is adsorbed in Layers 2 to 4, the corresponding Fe-O bond is not stretched anymore. This indicates that Fe-O bonds are strongly affected by the formation of a O-H bond and explains the effect of Fe atoms on hydration energies.

The relatives energies for the hydrogen adsorption position in Layers 1 to 4 are compared with the (100) surface of $CaMnO_3$ and the (010) surface of $CaMn_{0.75}Fe_{0.25}O_3$ (see Table 7), the structures for hydrogen adsorption in Layers 1 to 4 are given in the SI.

Table 7: Relative energy E_{rel} for hydrogen adsorption positions in eV for $CaMnO_3$ (100), $CaMn_{0.75}Fe_{0.25}O_3$ (010) and $BaFeO_3$ (100). In all positions, one hydrogen is in the first layer and the other in Layers 1 to 4.

Surface	E_{rel} / eV			
	Layer 1	Layer 2	Layer 3	Layer 4
$CaMnO_3$ (100)	0.00	0.75	1.58	1.93
$CaMnO_3$ (010)	0.00	1.52	1.10	1.41
$CaMn_{0.75}Fe_{0.25}O_3$ (010)	0.00	1.15	0.40	0.46
$BaFeO_3$ (100)	0.00	1.15	0.71	1.16

The relative energies for proton adsorption in the first two layers are comparable for $BaFeO_3$ (100) and $CaMnO_3$ (100) and $CaMn_{0.75}Fe_{0.25}O_3$ (010). For the inner layers, $CaMn_{0.75}Fe_{0.25}O_3$ (010) shows significantly lower relative energies than $BaFeO_3$ (100), while the values for the (100) surface of $CaMnO_3$ are 0.9 to 1.5 eV higher. The high relative energy of 1.15 eV for proton adsorption in the second layer leads to a high activation barrier. However, the fact that the predominant (100) surface of the known proton conductor $BaFeO_3$ has the same E_{rel} as $CaMn_{0.75}Fe_{0.25}O_3$ (010) indicates that the proton migration from the surface to the bulk should be possible in Fe-doped $CaMnO_3$. The stabilization of first layer proton adsorption is reasonable because the smaller coordination numbers of the corresponding oxygen ions.

While the proton migration mechanism on the $CaMnO_3$ (100) surface is affected by high relative energies in layers 3 and 4 (1.58 and 1.93 eV), the (010) surface of $CaMn_{0.75}Fe_{0.25}O_3$

even shows lower relative energies than $BaFeO_3$ for layers 3 and 4, leading to a more feasible proton migration pathway than for $BaFeO_3$. This is a very promising result and therefore the $CaMn_{0.75}Fe_{0.25}O_3$ (010) surface is potentially suitable as a PCEC anode material. However, bulk hydration thermodynamics also have to be taken into account. Comparing the hydration energies and oxygen defect formation energies of different $Ca_{1-x}Sr_xMn_yFe_{1-y}O_3$ compounds with $BaFeO_3$ (Table S5 in the SI) shows that the hydration energy of bulk $CaMn_{0.75}Fe_{0.25}O_3$ is positive. A negative hydration energy is required for proton conduction, therefore $Ca_{0.5}Sr_{0.5}Mn_{0.75}Fe_{0.25}O_3$ is the most promising candidate regarding hydration thermodynamics. To finally evaluate its suitability has PCEC material, the computation of hydration migration barriers in bulk and surface has to be done in future work which is challenging in the less symmetric space group No.20 (found in previous calculations.[21]

4. Conclusion

In this article, the proton migration mechanism from the $CaMnO_3$ surface into the bulk was investigated. The (100) surface and the (010) surfaces were considered, which together account for about 50 % of the total surface area of single-crystal $CaMnO_3$. The calculation of the hydration and defect formation energies showed that the defect formation energy for $CaMnO_3$ in the first two layers on the (010) surface is 0.06 to 1.55 eV higher and the hydration energies 0.49 to 0.89 eV lower than on the (100) surface. Therefore, the hydration mechanism takes place predominantly on the (100) surface, which, however, shows a sharp increase in hydration energy from the first to the fourth layer. The two surfaces were then calculated for $CaMn_{0.75}Fe_{0.25}O_3$ which led to a significant decrease in the defect formation energies on the (010) surface. The $CaMn_{0.75}Fe_{0.25}O_3$ (100) surface has similar hydration energies in the upper layers and even significantly more negative ones in the lower layers. This favors the proton migration mechanism from the topmost layer into the bulk. A comparison with the known proton conductor $BaFeO_3$ showed that the energetic difference of about 1 eV between

the hydrogen positions in first and second layer also occurs for $BaFeO_3$. The (010) surface of $CaMn_{0.75}Fe_{0.25}O_3$ even shows significantly lower relative energies of the hydrogen positions in the third and fourth layer than $BaFeO_3$, which is why the $CaMn_{0.75}Fe_{0.25}O_3$ surface might be suited for use in a PCEC electrode. However, bulk hydration thermodynamics shows that $CaMn_{0.75}Fe_{0.25}O_3$ is not a proton conductor. The compund $Ca_{0.5}Sr_{0.5}Mn_{0.75}$ shows a promising low hydration energy of -1.45 eV and is therefore a promising candidate. Hydration migration barriers in bulk and surface have to be computed in future work, challenging the less symmetric space group No.20.

Supporting Information Available

The following files are available free of charge.

- Filename: SI.pdf (Hydrogen adsorption positions for $CaMnO_3$ and $CaMn_{0.75}Fe_{0.25}O_3$, surface models for $BaFeO_3$)
- Filename: cif.zip (CIF Files of the hydrogen positions 1 to 4 of $CaMnO_3$ ((010) and (100) surface with and without Fe) and $BaFeO_3$)

Acknowledgments

We thank the Paderborn Center for Parallel Computing (PC^2) for providing substantial computer resources which were absolutely necessary for NEB calculations of our large supercells.

References

(1) Hauch, A.; Küngas, R.; Blennow, P.; Hansen, A. B.; Hansen, J. B.; Mathiesen, B. V.; Mogensen, M. B. Recent advances in solid oxide cell technology for electrolysis. *Science* **2020**, *370*, eaba6118.

(2) Duan, C.; Huang, J.; Sullivan, N.; O'Hayre, R. Proton-conducting oxides for energy conversion and storage. *Appl. Phys. Rev.* **2020**, *7*, 011314.

(3) Wang, Z.; Yang, W.; Zhu, Z.; Peng, R.; Wu, X.; Xia, C.; Lu, Y. First-principles study of O_2 reduction on $BaZr_{1-x}Co_xO_3$ cathodes in protonic-solid oxide fuel cells. *J. Mater. Chem. A* **2014**, *2*, 16707–16714.

(4) Munoz-Garcia, A. B.; Pavone, M. First-principles design of new electrodes for proton-conducting solid-oxide electrochemical cells: A-site doped $Sr_2Fe_{1.5}Mo_{0.5}O_{6-\delta}$ perovskite. *Chem. Mater.* **2016**, *28*, 490–500.

(5) Xu, X.; Wang, H.; Ma, J.; Liu, W.; Wang, X.; Fronzi, M.; Bi, L. Impressive performance of proton-conducting solid oxide fuel cells using a first-generation cathode with tailored cations. *J. Mater. Chem. A* **2019**, *7*, 18792–18798.

(6) Lan, C.; Li, H.; Zhao, S. A first-principles study of the proton and oxygen migration behavior in the rare-earth perovskite $SmNiO_3$. *J. Comput. Electron.* **2020**, *19*, 905–909.

(7) Ding, H.; Wu, W.; Jiang, C.; Ding, Y.; Bian, W.; Hu, B.; Singh, P.; Orme, C. J.; Wang, L.; Zhang, Y., et al. Self-sustainable protonic ceramic electrochemical cells using a triple conducting electrode for hydrogen and power production. *Nat. Commun* **2020**, *11*, 1907.

(8) Hoedl, M.; Chesnokov, A.; Gryaznov, D.; Merkle, R.; Kotomin, E.; Maier, J. Proton migration barriers in $BaFeO_{3-\delta}$–insights from DFT calculations. *J. Mater. Chem. A* **2023**, *11*, 6336–6348.

(9) Grimm, B.; Bredow, T. Revisiting $CaMnO_3$ as a Proton Conductor - A Theoretical Perspective. *The Journal of Physical Chemistry C* **2024**, *128*, 5429–5435.

(10) Carlotto, S. The role of the dopant and structural defects on the water absorption and

on the H2 formation in the Al, Co and Cu doped $SrTiO_3$ perovskite steps. *Appl. Surf. Sci.* **2020**, *527*, 146850.

(11) Li, Q.; Yin, Q.; Zheng, Y.-S.; Sui, Z.-J.; Zhou, X.-G.; Chen, D.; Zhu, Y.-A. Insights into hydrogen transport behavior on perovskite surfaces: transition from the grotthuss mechanism to the vehicle mechanism. *Langmuir* **2019**, *35*, 9962–9969.

(12) Merkle, R.; Hoedl, M. F.; Raimondi, G.; Zohourian, R.; Maier, J. Oxides with mixed protonic and electronic conductivity. *Annu. Rev. Mater. Res.* **2021**, *51*, 461–493.

(13) Grimm, B.; Bredow, T. Effect of Surface Energetics on Phase Stability of $CaMnO_3$. *Phys. Status Solidi B* **2023**, *260*, 2300031.

(14) Dovesi, R.; Erba, A.; Orlando, R.; Zicovich-Wilson, C. M.; Civalleri, B.; Maschio, L.; Rérat, M.; Casassa, S.; Baima, J.; Salustro, S., et al. Quantum-mechanical condensed matter simulations with CRYSTAL. *Wiley Interdiscip. Rev. Comput. Mol. Sci.* **2018**, *8*, e1360.

(15) Vilela Oliveira, D.; Laun, J.; Peintinger, M. F.; Bredow, T. BSSE-correction scheme for consistent gaussian basis sets of double-and triple-zeta valence with polarization quality for solid-state calculations. *J. Comp. Chem.* **2019**, *40*, 2364–2376.

(16) Grimm, B.; Bredow, T. Oxygen Defect Formation Thermodynamics of $CaMnO_3$: A Closer Look. *Phys. Status Solidi B* **2023**, *260*, 2200427.

(17) Atomic Simulation Environment. Main ASE repo: Accessed: 2022-11-01, https://gitlab.com/ase/ase.

(18) Atomic Simulation Environment. ASE fork: Accessed: 2023-10-01, https://gitlab.com/waldlaubsaengernest/ase.

(19) Zohourian, R.; Merkle, R.; Raimondi, G.; Maier, J. Mixed-conducting perovskites as

cathode materials for protonic ceramic fuel cells: understanding the trends in proton uptake. *Adv. Funct. Mater.* **2018**, *28*, 1801241.

(20) Hayashi, N.; Yamamoto, T.; Kageyama, H.; Nishi, M.; Watanabe, Y.; Kawakami, T.; Matsushita, Y.; Fujimori, A.; Takano, M. $BaFeO_3$: a ferromagnetic iron oxide. *Angew. Chem., Int. Ed.* **2011**, *123*, 12755–12758.

(21) Grimm, B.; Bredow, T. Defect Formation Thermodynamics of (A, A')(B, B')O_3 (A= Mg, Ca, Sr and B= Ti, Mn, Cr, Fe, Mo) Perovskites. *Phys. Status Solidi B* **2023**, 2300048.